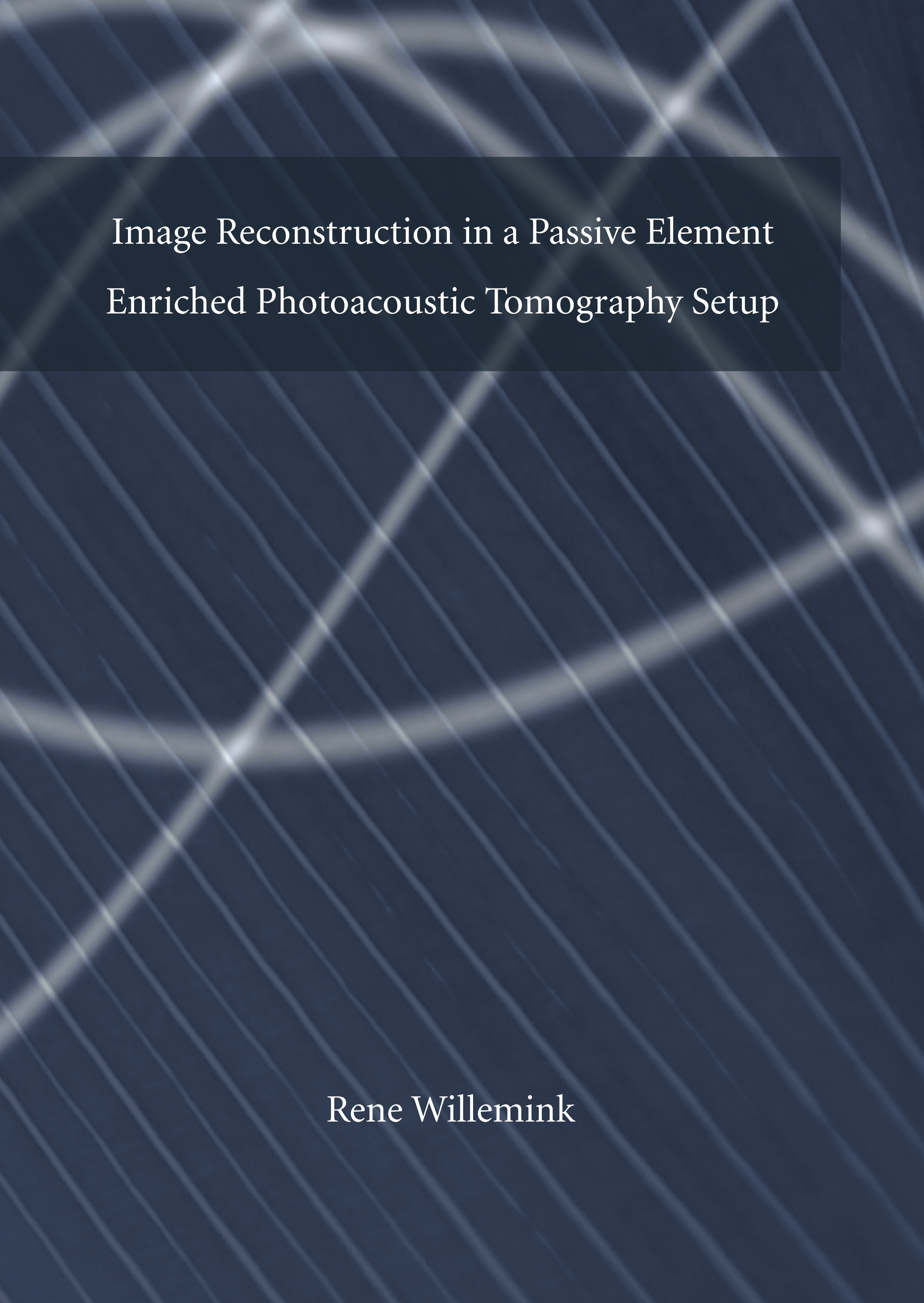

Image Reconstruction in a Passive Element Enriched Photoacoustic Tomography Setup

Rene Willemink

IMAGE RECONSTRUCTION IN A PASSIVE ELEMENT ENRICHED PHOTOACOUSTIC TOMOGRAPHY SETUP

Rene Willemink

De promotiecommissie:

voorzitter en secretaris:	
Prof.dr.ir. A.J. Mouthaan	Universiteit Twente
promotor:	
Prof.dr.ir. C.H. Slump	Universiteit Twente
assistent promotor:	
Dr. S. Manohar	Universiteit Twente
leden:	
Prof.dr. A.G.J.M. van Leeuwen	Universiteit Twente / Universiteit van Amsterdam
Prof.dr.ir. P.H. Veltink	Universiteit Twente
Prof.dr. M. Frenz	Universiteit Bern, Zwitserland
Dr.ir. M. Versluis	Universiteit Twente

This research is financially supported by the speerpunt program NIMTIK of the former BMTI (presently MIRA institute) and the PRESMITT project of the IOP-Photonic Devices program

Signals & Systems group,
EEMCS Faculty, University of Twente
P.O. Box 217, 7500 AE Enschede, the Netherlands

Printed by Gildeprint B.V., Enschede, The Netherlands
Typesetting: LaTeX2e
Cover design by Martin Willemink

ISBN 978-90-365-3042-2
DOI 10.3990/1.9789036530422

IMAGE RECONSTRUCTION IN A PASSIVE ELEMENT ENRICHED PHOTOACOUSTIC TOMOGRAPHY SETUP

PROEFSCHRIFT

ter verkrijging van
de graad van doctor aan de Universiteit Twente,
op gezag van de rector magnificus,
prof.dr. H. Brinksma,
volgens besluit van het College voor Promoties
in het openbaar te verdedigen
op 16 juni 2010 om 16:45h

door

Gerrit Hendrik Willemink
geboren op 21 Maart 1981
te Bramsche, Duitsland

Dit proefschrift is goedgekeurd door:

De promotor: Prof.dr.ir. C.H. Slump

De assistent promotor: Dr. S. Manohar

Summary

Photoacoustic imaging is a relatively new imaging technology, in which an object is illuminated with optical energy and where in return measurements are taken in the acoustical domain. Due to a physical phenomenon, called the photoacoustic effect, the absorption of light leads to the generation of pressure waves. By measuring these generated pressure waves outside of the object it is possible to reconstruct an image of the optical absorption distribution of the imaged object. Several photoacoustic imaging approaches exist, which differ in how to deliver the optical energy to the object, how to measure the generated pressure waves, and how the imaging setup is geometrically laid out. In this thesis we focus on an implementation that is being developed by the Biomedical Photonic Imaging (BMPI) group of the University of Twente. This implementation is coined the Passive Element enRiched PhotoAcoustic Tomography (PER-PAT) imaging setup. It allows not only to image the optical absorption distribution, but also the speed of sound distribution and acoustic attenuation distribution at the same time, by adding carefully positioned passive elements into the setup. These passive elements act as ultrasound point sources when being illuminated with pulsed optical energy. The work that is presented in this thesis deals with the signal processing that is necessary to transform the measured pressure signals with a PER-PAT imaging setup into reconstructions of these three distributions. This work is divided into four parts.

The first part is about the calibration of the imaging setup. Calibration of the setup is necessary because, in order to do a good reconstruction, the exact geometrical parameters of the setup need to be known. To make this possible, two kind of measurements, a calibration and a reference measurement, should be performed on the imaging setup. We presented an analysis on the properties of these two measurements and finally proposed a robust algorithm that automatically determines the geometrical parameters from the two input measurements. Because of the noise and sometimes low amplitude measurements this is a difficult task, which is handled very well by our algorithm on all our performed measurements so far.

The second part is about the pre-processing step which is necessary for the reconstruction of the speed of sound and acoustic attenuation distributions. In this pre-processing step, we extract the time delay and attenuation factors that are encountered by acoustic signals traveling from these passive elements to our ultrasound detector elements. Therefore we investigated the estimation of these two propagation parameters from the raw pressure signals. Two existing approaches were compared to several new approaches, which were all based on performing a maximum likelihood estimate. We found that these new estimators have a wider application area and some of them perform better by making use of more of the information that is available in the measured raw pressure signals.

In the third part we discuss the reconstruction of actual speed of sound and acoustic attenuation distributions from the, in the previous part, extracted time delay and attenuation factors. We propose an algorithm that can be used to reconstruct these distributions from a PER-PAT setup containing one or more passive elements. Experimental validation showed that it is very well possible to use the PER-PAT setup to reconstruct the speed of sound and acoustic attenuation distributions. Furthermore it is shown that when more passive elements are used, less projection are required to maintain the same image quality, resulting in a decrease of the time needed to perform a measurement.

The last part contains our approach and findings on reconstructing the optical absorption distribution. We start with a general investigation of the reconstruction problem and the possible approaches, either direct or iteratively, to perform the reconstruction. The direct approach is a very fast, but approximate, solution to the reconstruction problem. The iterative approach can result in much more accurate solutions, but can be orders of magnitude more demanding in terms of computational complexity. We propose a way to accelerate the convergence speed of the iterative methods by using a pre-conditioner based on 2-d FFT transforms. Furthermore, we looked into the reconstruction of optical absorption in the presence of speed of sound inhomogeneities in the object. Speed of sound inhomogeneities in the object can result in blurred optical absorption reconstructions, when these inhomogeneities are ignored in the reconstruction. We proposed an algorithm to correct for these inhomogeneities and have successfully showed the improvement from the new algorithm using experimental results. In the end of the last part, we look into a motion correction algorithm, that allows for the correction of motion artifacts of a photoacoustic measurement using landmarks attached to the imaged object. Unwanted motion during measurements was a problem that occurred in the first generation PER-PAT imaging, for which we could successfully compensate by using this motion correction algorithm.

The thesis thus describes the complete division of the signal processing into problems and solutions that are necessary for image reconstruction in the PER-PAT imaging setup. Based on the described findings we conclude that we have developed successful algorithms and methods for the image reconstruction problem with the PER-PAT imaging setup.

Samenvatting

Fotoacoustische beeldvorming is een relatief nieuwe beeldvormingstechniek, waarbij een object belicht wordt met optische energie en waarop metingen worden uitgevoerd in het acoustische domein. Door een fysisch verschijnsel, het fotoacoustische effect genaamd, leidt de absorptie van licht tot het ontstaan van drukgolven. Door het meten van deze ontstane drukgolven aan de buitenkant van het object is het mogelijk om een beeld te reconstrueren van de optische absorptiedistributie van het gemeten object. Er bestaan verschillende fotoacoustische beeldvormingstechnieken, welke verschillen in de manier waarop de optische energie naar het object overgebracht wordt, de manier waarop de drukgolven gemeten worden en de manier waarop de beeldvormingsopstelling geometrisch in elkaar zit. In dit proefschrift leggen we de nadruk op een implementatie die ontworpen wordt bij de Biomedical Photonic Imaging (BMPI) groep van de Universiteit Twente. Deze implementatie draagt de naam Passive Element enRiched PhotoAcoustic Tomography (PER-PAT) beeldvormingsopstelling. Met deze opstelling is het niet alleen mogelijk om de optische absorptiedistributie te meten, maar ook tegelijkertijd de geluidssnelheidsdistributie en de acoustische verzwakkingsdistributie door het zorgvuldig plaatsen van een passief element in de opstelling. Deze passieve elementen gedragen zich als ultrageluid punt bronnen wanneer ze belicht worden door gepulseerde optische energie. Het werk dat in dit proefschrift gepresenteerd is houdt zich bezig met de signaalbewerking die nodig is om de gemeten drukgolven met de PER-PAT opstelling om te zetten in beelden van deze drie distributies. Dit werk is opgesplitst in vier delen.

Het eerste deel gaat over de calibratie van de beeldvormingsopstelling. Calibratie van de opstelling is noodzakelijk omdat, om een goede reconstructie te doen, de exacte geometrische parameters van de opstelling bekend moeten zijn. Om dit mogelijk te maken moeten twee soorten metingen, een calibratie- en een referentiemeting, uitgevoerd worden. Wij presenteren een analyse van de eigenschappen van deze twee metingen en komen uiteindelijk met een robuust algorithme dat automatisch deze geometrische parameters bepaalt uit de twee metingen. Door ruis en soms lage signaalintensiteiten was dit een uitdagende taak, die door ons algorithme goed is getest op alle metingen die tot zover gedaan zijn.

Het tweede deel gaat over de voorbewerkingsstap die noodzakelijk is voor de reconstructie van de geluidssnelheids- en acoustische verzwakkingsdistributies. In deze voorbewerkingsstap bepalen we vertragings- en verzwakkingsfactoren die ondergaan worden door acoustische signalen die van de passieve elementen naar de ultrageluidsdetectorelementen reizen. Om dit te kunnen uitvoeren hebben we de schatting van deze twee propagatieparameters van de ruwe signalen onderzocht. Twee bestaande

methoden hebben we vergeleken met een aantal nieuwe methoden, welke allemaal gebaseerd zijn op het doen van een maximale waarschijnlijkheidsschatting. Hier hebben we uit geleerd dat deze nieuwe methoden een breder applicatiegebied hebben en dat sommige van de nieuwe methoden beter konden presteren door gebruik te maken van extra informatie die ook beschikbaar is in de ruwe ultrageluidssignalen.

In het derde deel onderzoeken we uiteindelijk de reconstructie van de geluidssnelheids- en de acoustische verzwakkingsdistributies uit de, in het vorige deel, bepaalde vertragings- en verzwakkingsfactoren. We presenteren een algorithme dat gebruikt kan worden in de reconstructie van deze distributies met de PER-PAT opstelling, die een of meerdere passieve elementen bevat. Door het doen van experimenten hebben we aangetoond dat het zeer goed mogelijk is om de PER-PAT opstelling te gebruiken om de geluidssnelheids- en acoustische verzwakkingsdistributie te reconstrueren. Daarnaast hebben we aangetoond dat, wanneer er meerdere passieve elementen gebruikt worden, er minder projecties nodig zijn om dezelfde beeldkwaliteit te kunnen blijven behouden, wat resulteert in een afname van de tijd die nodig is om een meting uit te voeren.

Het laatste deel bevat onze aanpak en bevindingen over de reconstructie van de optische absorptiedistributie. We beginnen met een algemeen onderzoek naar het reconstructieprobleem en de mogelijke oplossingen, hetzij direct hetzij iteratief, om de reconstructie uit te voeren. De directe aanpak is een erg snelle, maar niet noodzakelijkerwijs nauwkeurige, oplossing. De iteratieve aanpak kan resulteren in veel nauwkeurigere oplossingen, maar kan ordes van grootte langer duren om uit te rekenen. Wij presenteren een manier om de convergentietijd van de iteratieve methoden te versnellen door gebruik te maken van een voorconditionering, gebaseerd op 2-d FFT transformaties. Daarnaast hebben we gekeken naar de reconstructie van optische absorptie onder de aanwezigheid van geluidssnelheidsinhomogeniteiten in het object. Geluidssnelheidsverschillen in het object kunnen leiden tot een vervagende optische absorptiereconstructie, als de inhomogeniteiten verwaarloosd worden in de reconstructie. Wij presenteren een algorithm dat corrigeert voor deze inhomogeniteiten en laten succesvol de verbetering van het nieuwe algorithme op experimentele resultaten zien. Aan het einde van dit laatste deel van het proefschrift onderzoeken we een bewegingscorrectiealgorithme, waarmee bewegingsartifacten in fotoacoustische metingen gecorrigeerd kunnen worden door gebruik te maken van markeringen, aangebracht op het te meten object. Ongevraagde beweging tijdens metingen was een probleem dat optrad in de eerste generatie van de PER-PAT opstelling, waarvoor we succesvol konden compenseren met behulp van dit bewegingscorrectiealgorithme.

Het proefschrift in zijn geheel beschrijft dus de opdeling in problemen en oplossingen van de signaalbewerking die nodig is om beeldreconstructies te kunnen uitvoeren met de PER-PAT beeldvormingsopstelling. Op grond van de beschreven bevindingen concluderen we dat we succesvolle algorithmes en methoden hebben ontwikkeld ten behoeve van beeldreconstructie met de PER-PAT beeldvormingsopstelling.

Contents

1

Introduction

This thesis presents an analysis, description and experimental validation of the signal processing, i.e., calibration, post-processing, image reconstruction, needed in a Passive Element enRiched PhotoAcoustic Tomography (PER-PAT) imaging setup. The thesis consists of four parts, every part in a separate chapter, which are interconnected and will be further introduced after defining the scope and context here in the introduction. But before we start with that, first a motivation and an introduction into photoacoustics and its applications will be given.

1.1 Motivation

Photoacoustic imaging is a modality which has the goal to image the optical absorption distribution inside an object. To reach this goal an object is illuminated with a light source, which introduces a distribution of absorbed optical energy inside the object. The absorbed optical energy is transformed into outward traveling pressure waves (ultrasound waves) via fast heat release and thermal expansion. This transformation is termed the photoacoustic effect. The frequency of the generated pressure wave typically depends on the size of structures present in the object, and the time delay for a generated wave to reach a certain measurement point gives an indication of the distance to the responsible structure in the object. This knowledge allows the reconstruction of the optical absorption distribution from measurements of the photoacoustically generated ultrasound waves.

The combined optical/acoustical properties are the strength of photoacoustic imaging. The contrast is mainly dictated by the absorption of optical energy, light having a reasonable penetration depth in soft tissue of 10 - 100 mm [1]. The absorption of optical energy offers higher contrast than ultrasound imaging, which only detects ultrasound properties of the object. The resolution on the other hand is mainly dictated by the measurement of the generated ultrasound wave and thus depends on the characteristics of the detection system used. Ultrasound propagation through soft tissue has a much lower scattering than pure optical imaging and thus allows higher resolution measurements to be taken. An advantage of using optical energy as input energy, over for example x-ray, is the fact that optical photons provide nonionizing and safe radiation for medical applications[1]. Thus due to the good contrast of optical absorption, the non-ionizing character of light, and a scalable resolution, photoacoustic imaging lends itself as a promising medical imaging modality to image for example cancer. Malignant tumors are characterized by angiogenesis, the formation of a network of blood vessels, resulting in an increased optical absorption at the site of the tumor[2]. Furthermore, photoacoustic imaging can be a valuable tool for other diagnosis based on imaging the (micro-)vascular system, such as monitoring wound healing and optimizing the treatment of portwine stains[3].

1.2 The photoacoustic effect

The photoacoustic effect can be defined as the conversion of absorbed optical (or electromagnetic) energy to acoustic energy. There is a wide literature on photoacoustic signal generation and the physical effects which are responsible for the photoacoustic effect. The thermoelastic effect seems to be[4, 5], among the various sources by which acoustic waves can be generated from illumination with optical energy, by far the most efficient one. The absorption of optical energy leads to heating of the object and subsequent thermal expansion will generate an initial pressure distribution inside the object. This initial pressure distribution finally results in outwards traveling pressure waves.

For efficient generation of pressure waves, a short pulse of optical energy should be emitted. How short this pulse should be is governed by the conditions of thermal confinement and stress confinement[1]. If the condition of thermal confinement is not met, then the effect of heat diffusion is significant on the time scale of the laser pulse duration. If the condition of stress confinement is not met, then the effect of pressure propagation is significant on the time scale of the laser pulse duration. Whether those effects are significant on the laser pulse duration time scale depends on the size of absorbers in the object, the smaller the sizes are, the more significant the effect will be. Having a too long laser pulse duration with respect to these small sizes, results in a low pass filtering effect on the generated pressure wave and thus results in a degradation of the resolution of the system.

The heating of the object, due to the absorption of laser light can be represented in a spatially and time dependent heating function $H(\mathbf{r}, t)$. This heating function represents the amount of absorbed energy per unit volume per unit time. The resulting temperature rise due to heating can be modeled by the heat conduction equation, relating the temperature distribution $T(\mathbf{r}, t)$ [K] to the heating function $H(\mathbf{r}, t)$ [J/(m^3

s)], according to[6]:

$$\rho C_p \frac{\partial T(\mathbf{r},t)}{\partial t} = \lambda \nabla^2 T(\mathbf{r},t) + H(\mathbf{r},t) \tag{1.1}$$

here ρ [kg/m^3] is the density of the material, C_p [J/(K kg)] is the specific heat and λ [J/(K m s)] is the thermal conductivity. Under the condition of thermal confinement heat diffusion can be neglected, so that the heat equation reduces to:

$$\rho C_p \frac{\partial T(\mathbf{r},t)}{\partial t} \approx H(\mathbf{r},t) \tag{1.2}$$

The excess temperature distribution is related to the excess acoustic pressure $p(\mathbf{r},t)$ via the following wave equation:

$$\nabla^2 p(\mathbf{r},t) - \frac{1}{c^2}\frac{\partial^2}{\partial t^2} p(\mathbf{r},t) = -\beta\rho \frac{\partial^2}{\partial t^2} T(\mathbf{r},t) \tag{1.3}$$

where c [m/s] is the speed of sound and β [K^{-1}] is the volume thermal expansion coefficient. This means that under the condition of thermal confinement, using (1.2), the generated excess pressure distribution is related to the heating function according to:

$$\nabla^2 p(\mathbf{r},t) - \frac{1}{c^2}\frac{\partial^2}{\partial t^2} p(\mathbf{r},t) = -\frac{\beta}{C_p}\frac{\partial}{\partial t} H(\mathbf{r},t) \tag{1.4}$$

The heating function can furthermore be seen as the product of a purely spatial function $A(\mathbf{r})$ representing the spatial distribution of the heat and a purely time dependent function $I(t)$ representing the time profile of the illuminating laser source, i.e., $H(\mathbf{r},t) = A(\mathbf{r})I(t)$. Furthermore, under the condition of stress confinement the laser pulse profile can be considered as a delta function, i.e., $I(t) = \delta(t)$. A solution to the generated excess pressure in terms of the absorption distribution $A(\mathbf{r})$ can now be found by the use of the Green's function, see Appendix A, resulting in:

$$p(\mathbf{r},t) = \frac{\beta}{4\pi C_p}\frac{\partial}{\partial t}\left(\frac{1}{t}\iint\limits_{\|\mathbf{r}'-\mathbf{r}\|=ct} A(\mathbf{r}')\mathrm{d}\mathbf{r}'\right) \tag{1.5}$$

This means that the generated pressure is related to the time derivative of the integrated absorption distribution over the surface of a sphere, where the radius of the sphere is proportional to the time that has elapsed since firing the laser source. The initial pressure at $t = 0$, $p_0(\mathbf{r}) = p(\mathbf{r},0)$ is then simply given by:

$$p_0(\mathbf{r}) = \frac{\beta c^2}{C_p} A(\mathbf{r}) = \Gamma A(\mathbf{r}) \tag{1.6}$$

where Γ is the (dimensionless) Grueneisen[1] parameter which characterizes the thermo-acoustic efficiency. The initial pressure distribution is thus directly proportional to the absorption distribution $A(\mathbf{r})$.

This model is a simplification which ignores acoustic attenuation and assumes that the speed of sound is constant throughout the complete object. Including attenuating effects requires a modified wave equation with a modified Green's function. The exact form of the time domain wave equation for acoustic attenuation, with its linear dependence on frequency as encountered in soft tissue, is still an open issue. The question is however to what extent ignoring attenuating effects would degrade the reconstruction. A computer simulation study where homogeneous, soft tissue like, acoustic attenuation was modeled[7] shows that ignoring this effect has a blurring effect on the reconstructed images. This is an interesting observation and a logical direction for future work and especially how to deal with inhomogeneous acoustic attenuation. The assumption of a homogeneous speed of sound distribution is easily violated in soft tissue and having an inhomogeneous speed of sound distribution is one of the topics that will be addressed in this thesis.

1.3 Scope and context

Photoacoustic imaging can be performed in various geometries. A single ultrasound detector can be scanned across the surface of tissue [8, 9, 10, 11] with image reconstructions based on synthetic aperture methods [12, 9, 13]. Linear arrays [14, 15, 16, 17] and 2d planar arrays have been used to achieve largely similar results [18, 19]. In contrast to these methods, which may be classified as measurements of single projections of the subject, acquisition of multiple projections around the tissue in the manner of computed tomography have gained in popularity. These measurements have been performed using point detectors in circular or hemispherical arrays [20, 21, 22], medium aspect-ratio detectors in cylindrical arrays [23, 24, 25, 26, 27] and high aspect-ratios (1-d) [28] and large area 2-d detectors [29, 30].

We have chosen for a setup with a 1-d piezoelectric sensor array for recording the pressure waves and a laser, using side illumination instead of top illumination, to deliver the pulses of optical energy. Both the sensor array and the laser are rotating with respect to the object under investigation and are focused in a 2-d slice through of the object. This allows for 2-d sliced based imaging of the object. The setup is more extensively described in the following subsection.

1.3.1 The measurement Setup

All algorithms and reconstruction techniques introduced in this thesis are specifically targeted to the experimental setup that is being used in the Biomedical Photonic Imaging (BMPI) group of the University of Twente. This setup is a custom made photoacoustic tomography setup, which was designed for the simultaneous imaging of both ultrasound and optical properties of the measured object using only optical energy as input. The setup consists of six components:

Laser source A laser source which is capable of emitting very short pulses is used to generate the optical energy to illuminate the measured object. We use a Q-switched Nd:YAG laser, delivering 10 ns pulses at a selectable wavelength of 532 or 1064 nm. This laser source can generate pulses at a repetition rate of 10 Hz, which is useful when signal averaging is necessary to increase the signal to noise

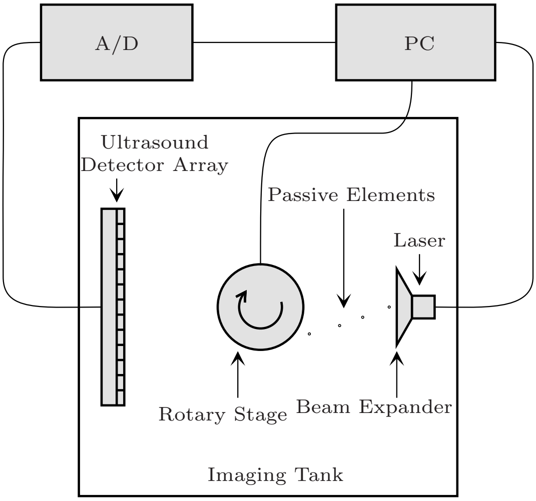

Figure 1.1 Instrumental top view of the passive element enriched photoacoustic tomography (PER-PAT) setup that was used in the experiments shown in this thesis. The algorithms presented in this thesis are targeted to this experimental setup.

(SNR) ratio of the generated signals. A cylindrical lens in combination with a beam expander is used to widen the laser beam in only one axis while focusing it strongly in the second axis to obtain roughly sheet illumination through the object.

Rotary stage The object under investigation is placed on a rotary stage, which allows different measurements to be made with each measurement having the object rotated under a different angle. The same effect can be obtained by allowing the laser source and ultrasound detector array to rotate with respect to a stationary object, which is what our next generation photoacoustic computed tomography imaging setup will use. The rotary stage can also be moved up and down to image difference slices through the object under investigation.

Passive element(s) An array of one or more passive elements was used to allow the imaging of ultrasound properties of the object under consideration. These passive elements are typically hair like structures that are positioned in a vertical direction, thus orthogonal to the imaging slice, that generate a short broadband acoustic pulse when they are illuminated with the laser source. By allowing this generated acoustic pulse to travel through the object, techniques of ultrasound transmission tomography can be used to reconstruct images of the speed of sound distribution and acoustic attenuation distribution of the object.

Ultrasound transducer array An ultrasound transducer array is used to measure the generated photoacoustic signals, which are induced by the photoacoustic effect upon absorption of the incident light. This transducer array consists of a set of piezoelectric sensors that convert the generated pressure signals into electric signals. Two different array configurations have been used for this purpose. The first was a 128-element linear array and the second a 32-element curved array. The piezoelectric detector elements in these arrays are elongated in the vertical direction and narrow in the horizontal direction which makes them especially sensitive in the imaging slice and less sensitive out of the imaging slice.

Imaging tank To make the propagation of ultrasound signals, originating from the object and the passive elements, to the ultrasound transducer array possible, a coupling medium is needed. This coupling medium should have the same acoustic impedance as the object that is being measured. If a medium with a different acoustic impedance, such as air, would be used, there would be a strong reflection of the ultrasound signal on the air/object boundaries and therefore a large reduction in remaining acoustic energy that would reach the detector array. We use water, with a typical speed of sound of about 1500 m/s at room temperature, as a coupling medium.

Amplifier and A/D converter The electric signals from the ultrasound transducer array are processed by an amplifier and A/D converter which convert the continuous analog signals to a sampled digital representation. The 128-element linear array was used in conjunction with a four channel amplifier and A/D converter and a multiplexer, thus being capable of reading out four detector elements per emitted laser pulse. The sampling frequency of this A/D converter was tunable up to 200 MHz. The 32-element curved array was used in conjunction with four sets of eight channel amplifiers and A/D converters, allowing the simultaneous measurement of all 32 detector elements at each emitted laser pulse. The sampling frequency of this A/D converter is fixed at 80 MHz.

Personal computer A personal computer was used to control the laser source and the rotary stage and to do the processing of the digitized ultrasound signals. The reconstruction methods and other algorithms are implemented on this personal computer using Matlab and multi-threaded C++ code compiled as mex libraries.

An instrumental top view of this passive element enriched photoacoustic tomography (PER-PAT) setup is displayed in Figure 1.1.

1.3.2 Measurements

As mentioned before, the goal of our PER-PAT setup is to be able to reconstruct both ultrasound properties and optical absorption of the object under investigation. This requires a set of three different measurements to be performed, all of which are measurements of photoacoustic signals. The first measurement is a calibration measurement, using a calibration object, to determine the speed of sound of the water and the center of rotation of the rotary stage. The second measurement is a reference measurement without any object, to determine the positions of the passive elements. The third measurement is the object measurement where the object under investigation is placed on the rotary stage. All three measurements are illustrated in Figure 1.2. We will come back and refer to these measurements in the different chapters of this thesis.

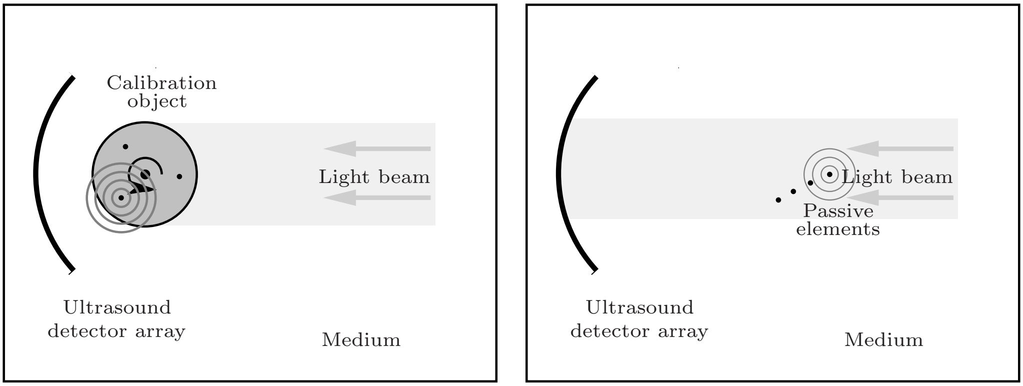

(a) Calibration measurement **(b)** Reference measurement

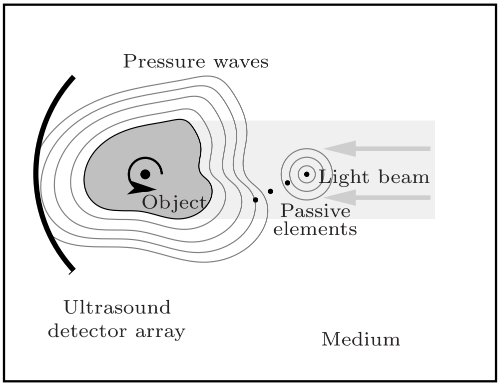

(c) Object measurement

Figure 1.2 Illustration of the three measurements that are necessary for the reconstruction of both the optical and ultrasound properties.

1.4 Thesis overview

In this thesis, four topics related to the image reconstruction in a PER-PAT setup will be discussed. For every topic a separate chapter is used. An overview of the topics/chapters is given in Figure 1.3. Some topics are related to each other as indicated with arrows in the figure and also the relation between the three measurements and the topics are shown.

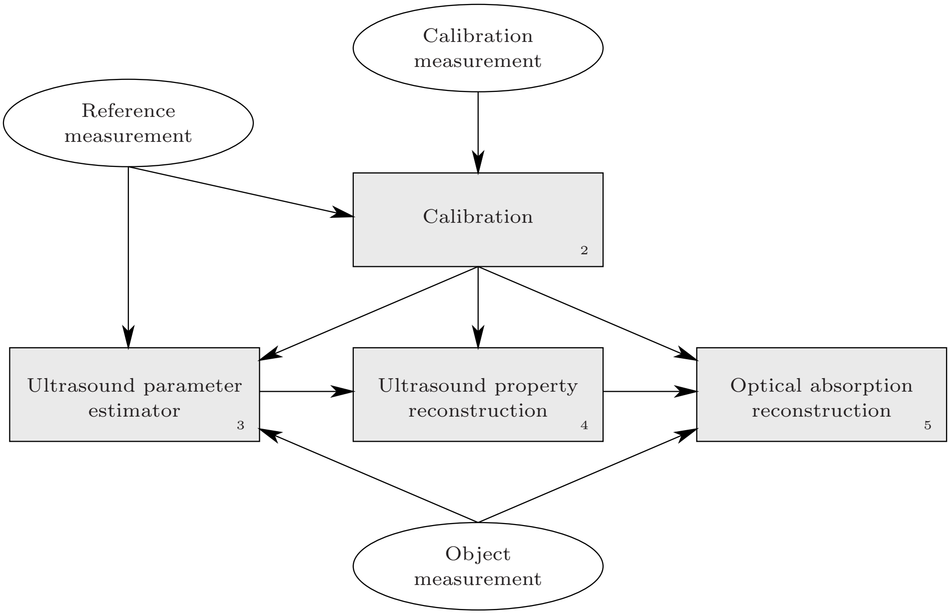

Figure 1.3 An overview of the topics and chapters presented in this thesis. The white balloons indicate the three kind of measurements that need to be taken in order to perform a full hybrid reconstruction. The gray rectangles indicate the four topics and the corresponding chapter number that describes each topic. Arrows show the inter relations between the signals and topics.

1.4.1 Research questions

To structure the research presented in this thesis, several research questions have been proposed for each topic. We will now present a short description of each topic and the associated research questions.

Calibration

The calibration chapter deals with an analysis of the accuracy and the presentation of an algorithm that can be used in the PER-PAT setup to estimate the geometrical parameters needed for image reconstruction. The research questions here are:

- Does the calibration problem have a unique solution and what are the conditions for having a unique solution?

- What accuracy can we theoretically expect from a calibration and how does this depend on the chosen phantom and measurement configuration?
- How does a different speed of sound in the calibration phantom affect the calibration outcome and can we correct for this easily?
- Can we implement a robust calibration algorithm that performs well with a substantial amount of outliers?

Estimation of ultrasound parameters

In this chapter we discuss a pre-processing step necessary before the image reconstruction of acoustic property distributions can take place. This image reconstruction depends on projection measurements which have to be extracted from the reference and object measurements. A maximum likelihood framework that can be used for the extraction of these projection measurement is presented in this chapter. The research questions here are:

- How accurate (with an accuracy possibly below the sampling frequency) can we theoretically extract time of flight measures from photoacoustic point source measurements and can we design a time of flight estimator that attains this accuracy in practice?
- Can we design an estimator that operates on ultrasound transmission mode measurements to estimate frequency dependent attenuation and the corresponding speed of sound dispersion?
- How does including the Kramers-Kronig relation in the model increase the accuracy of the estimate with respect to existing estimator that do not use this extra information?

Reconstruction of ultrasound properties

Here we present our approach and results for the reconstruction of speed of sound and attenuation distributions using our PER-PAT setup. The research questions here are:

- Can we reconstruct speed of sound and acoustic attenuation distributions from single passive element measurements?
- Is there a benefit in using more than one passive element in the setup to increase the spatial resolution of the reconstruction?
- Can we deal with refraction effects, i.e., the bending of rays, that can occur in these ultrasound property measurements?

Reconstruction of optical absorption

Finally, we discuss the image reconstruction of optical absorption which is the main contrast in photoacoustic imaging. We discuss the filtered backprojection method and iterative approaches that can be used. Some improvements, in terms of convergence speed and using the measurement model will be presented here. Also two additions to the reconstruction will be given, being a speed of sound correction algorithm and a motion correction algorithm. The research questions here are:

- How much improvement can we expect from iterative reconstruction algorithms in image quality with respect to the much faster filtered back projection (FBP) type of algorithms?
- How can preconditioning help in improving the convergence speed of iterative reconstruction algorithms and how do we obtain a suitable preconditioner?
- How can we efficiently use an estimated speed of sound map to correct for blurring effects caused by the false assumption of an inhomogeneous speed of sound distribution?
- Is unwanted motion a big problem in optical absorption reconstruction and is there an effective way to correct for this motion in the reconstruction?

2

Calibration algorithms[1]

Abstract

An important part of image reconstruction is the formulation of a measurement model that includes the physics and geometry involved in the imaging problem. Typically this model can be expressed in terms of parameters that describe the physics and geometry. Calibration is the task of accurately determining these parameters in advance so that a correct reconstruction of the unknown image can be made. We present a robust algorithm that can be used in our PER-PAT imaging setup, based on extracting small point source landmarks from the measured photoacoustic ultrasound signals, for which two kind of calibration measurements need to be performed. The two calibration measurements are in depth analyzed in order to setup a calibration model and to get a feeling for the expected accuracy. The presented calibration algorithm has been applied to all our experimental trials, some of which contained a considerable amount of noise, without any problem.

---

[1] Part of this chapter will be communicated as:
G.H. Willemink et al, “Calibration of a photoacoustic CT imager”, IEEE Transactions on Medical Imaging

2.1 Introduction

This chapter describes calibration algorithms which are used to calibrate the geometry of the measurement setup. Calibration is necessary to determine the exact geometrical parameters needed for image reconstruction. The calibration is performed on time of flight (TOF) measurements of small photoacoustic sources. We start this chapter by introducing the calibration parameters and then continue with describing the calibration measurements, which relate the TOF measurements to the calibration parameters. The chapter concludes with the presentation of a robust algorithm to automatically calibrate the geometry of the measurement setup with the proposed measurements.

2.1.1 The calibration parameters

In general we can say that there are internal and external parameters involved in describing the geometrical parameters. The internal parameters describe the measurement array. The external parameters describe the center of rotation of the measurement setup, the speed of sound of the reference medium and the positions of external photoacoustic point sources. An overview of these parameters is displayed in Table 2.1. There can be one or more external point sources, which in our case are passive elements. The position of the external photoacoustic point source is necessary for the reconstruction of the acoustical properties, all other parameters are necessary for the reconstruction of both the acoustical and optical properties. We assume that the internal parameters are fixed and do not change in between measurement sessions and we assume that the external parameters are expected to change in between measurement sessions, but remain fixed in a single measurement session.

Symbol	Name	Type
$\mathbf{T}$	Center of rotation	External
c	Speed of sound of the reference medium	External
$\mathbf{p}_{\mathrm{s}}$	Position of the external photoacoustic point source	External
$\mathbf{p}_{\mathrm{d},i}$	Position of the i^{th} sensor element	Internal
d	Spacing between two detector elements	Internal
l	Length of the linear array	Internal
r	Radius of the curved array	Internal

Table 2.1 Overview of the calibration parameters

2.1.2 Measurement array geometries

We have used two kinds of measurement arrays in our experimental setup. One was a configuration consisting of a linear array with 128 ultrasound detector elements and the other-one was a configuration consisting of a curved array with 32 ultrasound

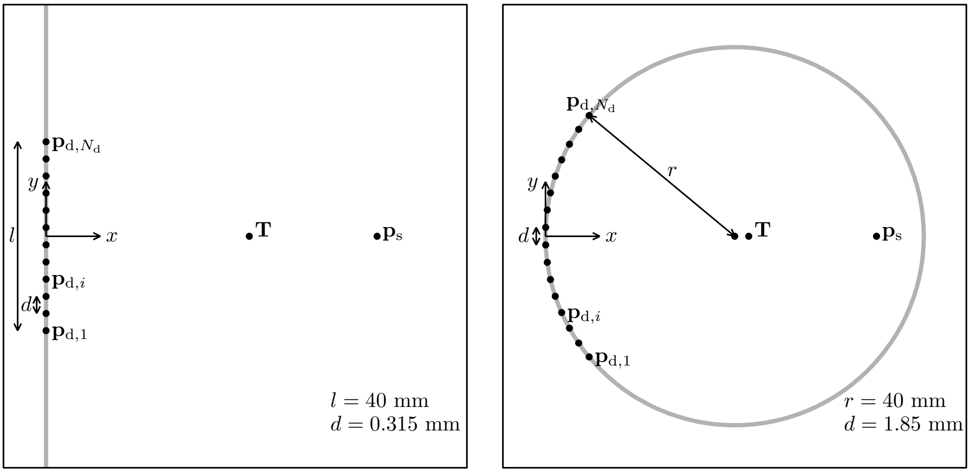

(a) Linear detector array geometry **(b)** Curved detector array geometry

Figure 2.1 Schematic overview of the measurement array geometries used in our setups. The detector elements are depicted on the left in (a) and (b) and labeled by their position $\mathbf{p}_{\mathrm{d},i}$. The center of rotation is labeled with $\mathbf{T}$. An photoacoustic point source is positioned on the right in (a) and (b) and labeled by its position $\mathbf{p}_\mathrm{s}$. The detector spacing, center to center, is indicated with d, the radius of the curved array with r and the length of the linear array with l.

detector elements. A schematic overview of both geometries, together with the calibration parameters, is given in Figure 2.1. The positions of the detector elements in both geometries can be expressed in terms of the number of detector elements N_d, the spacing between the detector elements d and the index of the detector element i ranging from 1 to N_d. For the curved array we also use the curvature radius r in the parametrization. The origin of the coordinate system will be in the middle of the measurement array, between the two center elements. This gives us for the positions of detector elements in the curved array:

$$\mathbf{p}_{\mathrm{d},i} = r \begin{bmatrix} 1-\cos\left(\left(i-\frac{N_\mathrm{d}+1}{2}\right)\dfrac{d}{r}\right) \\ \sin\left(\left(i-\frac{N_\mathrm{d}+1}{2}\right)\dfrac{d}{r}\right) \end{bmatrix} \tag{2.1}$$

The positions of detector elements in the linear array can be derived from the curved array by letting the radius grow to infinity:

$$\mathbf{p}_{\mathrm{d},i} = \lim_{r\to\infty} r \begin{bmatrix} 1-\cos\left(\left(i-\frac{N_\mathrm{d}+1}{2}\right)\dfrac{d}{r}\right) \\ \sin\left(\left(i-\frac{N_\mathrm{d}+1}{2}\right)\dfrac{d}{r}\right) \end{bmatrix} = \begin{bmatrix} 0 \\ \left(i-\frac{N_\mathrm{d}+1}{2}\right)d \end{bmatrix} \tag{2.2}$$

These positions as function of the calibration parameters will be used in subsequent sections when the calibration algorithm is described.

2.2 Calibration measurement models

The input to the calibration measurement models are time of flight (TOF) measurements from photoacoustic point sources. These TOF measurements can be obtained with the techniques described in chapter 3, section 3.3. These measurements are then related to the unknown calibration parameters as introduced in section 2.1.1. For calibration of the external parameters, we have defined two separate measurements:

2.2.1 The reference measurement

The reference measurement allows us to find the position of the external photoacoustic point source and the speed of sound of the reference medium. The measurement consists of measuring the TOF from all external point sources to the detector elements in the measurement array. The measurement array is rigidly connected with the external photoacoustic point source, so there is no rotation involved in the measurement. From the reference measurement we then try to recover the position of the external photoacoustic point source and the speed of sound of the reference medium.

The measurement model used in the reference measurement relates the measured TOF at each detector element $z_{\mathrm{tof},i}$ to the external photoacoustic point source at position $\mathbf{p}_{\mathrm{s}}$ and the speed of sound c of the reference medium via:

$$z_{\mathrm{tof},i} = \frac{1}{c}\|\mathbf{p}_{\mathrm{d},i} - \mathbf{p}_{\mathrm{s}}\| + n_z \tag{2.3}$$

where $\mathbf{p}_{\mathrm{d},i}$ is the position of the i^{th} detector element in the array and n_z represents additive noise. Based on further analysis in section 3.3.3 and Figure 3.8a, we know that the additive noise is Gaussian distributed. The position $\mathbf{p}_{\mathrm{d},i}$ of each detector element is determined by the kind of measurement array that is being used and its internal parameters, as given in (2.1) and (2.2). With this measurement model, we can define the measurement function $h_{\mathrm{tof}}(c, \mathbf{p}_{\mathrm{s}}) = \big(h_{\mathrm{tof},i}(c, \mathbf{p}_{\mathrm{s}})\big)_{i=1}^{N_{\mathrm{d}}}$, consisting of entries:

$$h_{\mathrm{tof},i}(c, \mathbf{p}_{\mathrm{s}}) = \frac{1}{c}\|\mathbf{p}_{\mathrm{d},i} - \mathbf{p}_{\mathrm{s}}\| \tag{2.4}$$

Uniqueness of the measurement function

We want to solve the inverse problem, determining for a given measurement what the unknown parameters are. Therefore it is good to investigate whether distinct parameter settings will always result in distinct measurements, or in other words if the measurement function is an injective function. This requirement is not required on the whole domain of the function, instead it is good enough if the function is injective on the domain defined by parameter values that are realistic and could be expected to occur in practice. A property that can be useful when determining the injectivity of the measurement function is the behavior of the Jacobian matrix. When the rank of the Jacobian matrix is equal to the number of input parameters over the whole domain of interest, we know that the measurement function is injective on that domain. The partial derivatives of the measurement function can be calculated as:

$$\frac{\partial}{\partial c} h_{\mathrm{tof},i} = -\frac{1}{c} h_{\mathrm{tof},i} \tag{2.5}$$

$$\frac{\partial}{\partial \mathbf{p}_{\mathrm{s}}} h_{\mathrm{tof},i} = \left(\mathbf{p}_{\mathrm{s}} - \mathbf{p}_{\mathrm{d},i}\right) \frac{1}{c^2 h_{\mathrm{tof},i}} \tag{2.6}$$

so that the whole Jacobian matrix can be constructed as:

$$\mathbf{H}_{\mathrm{tof}} = \begin{bmatrix} \frac{\partial}{\partial c} h_{\mathrm{tof},1} & \left(\frac{\partial}{\partial \mathbf{p}_{\mathrm{s}}} h_{\mathrm{tof},1}\right)^T \\ \vdots & \vdots \\ \frac{\partial}{\partial c} h_{\mathrm{tof},N_{\mathrm{d}}} & \left(\frac{\partial}{\partial \mathbf{p}_{\mathrm{s}}} h_{\mathrm{tof},N_{\mathrm{d}}}\right)^T \end{bmatrix} \tag{2.7}$$

For this matrix to have a rank of three, the minimum requirement is that we need three measurements or more. This requirement is satisfied for both measurement arrays having 128 and 32 different sensors. We will now investigate the uniqueness of the measurement function for both measurement array geometries by looking at the behavior of the Jacobian matrix. When the Jacobian matrix is not full rank, it will become singular and the condition number will go to infinity. To see if this happens in our situation, we calculated the condition number of the Jacobian matrix for different parameter settings, by moving the photoacoustic point source position around, on both measurement arrays and plotted the results in Figure 2.2a and 2.2b. What we see from these plots is that the Jacobian matrix is not extremely well conditioned, and has a condition number of at least 10^5 over the whole parameter space. This is mainly caused by the fact that the input parameters are not scaled well with respect to each other. To overcome this problem, we applied a different scaling to the speed of sound and the source position. The speed of sound will be represented in [m/s] and the source position not in [m] but in [μm]. This was implemented by multiplying the Jacobian matrix on the right side with a pre conditioning matrix:

$$\mathbf{P} = \begin{bmatrix} 1 & 0 & 0 \\ 0 & 10^{-6} & 0 \\ 0 & 0 & 10^{-6} \end{bmatrix} \tag{2.8}$$

The results of calculating the condition number on the Jacobian matrix with scaled input parameters are displayed in Figure 2.2c and 2.2d. After scaling, the Jacobian matrix is overall much better conditioned. We can now clearly see for both measurement arrays that there is a contour in the parameter space where the Jacobian matrix gets ill-conditioned and is not full rank. These contours coincide with the curve on which the detector elements are positioned, this can be seen by comparing Figure 2.1 with Figures 2.2c and 2.2d. The input domain can be divided into two subdomains, both bounded by these contours, in which the measurement function is injective. Furthermore it could be possible that a parameter setting from one side of input domain has a corresponding parameter setting inside the other domain which, when input to the measurement function, will result in the same measurement. This could be a problem in the curved measurement array, where it is likely that the photoacoustic point source is positioned close to the observed contour, i.e., at a distance roughly eight centimeters away from the measurement array along the x-axis. We will now try to find out if the measurement function indeed has distinct parameter settings in and outside the contour, sharing the same measurement.

Linear array For the linear array we can immediately see that each solution to the measurement function with a source position on the right side of the measurement array, thus on the right of the y-axis, has a symmetric solution with the source position at the left side of the y-axis. Both settings have the same speed of sound c and have mirrored source positions with respect to the y-axis. The symmetry axis is nicely visible by comparing Figures 2.1a and 2.2c. This is however not a problem, since in advance we already know at which side of the measurement array the photoacoustic point source is positioned.

Curved array For the curved array, there is also a symmetry in the geometry, which can be seen from the result of Appendix C. The symmetry is with respect to the imaginary circle spanned by the curved array, see Figures 2.1b and 2.2d. This means there is always a parameter setting with the source positioned inside the imaginary circle and a parameter setting with the source positioned outside the imaginary circle resulting in the same measurement. Both settings have a different speed of sound. The relations between the two corresponding parameter settings $[c_1, \mathbf{p}_{\mathrm{s},1}]^T$ and $[c_2, \mathbf{p}_{\mathrm{s},2}]^T$ are, using Appendix C, given by:

$$\mathbf{p}_{\mathrm{s},2} = \mathbf{p}_0 + \frac{r^2}{\left\|\mathbf{p}_{\mathrm{s},1} - \mathbf{p}_0\right\|^2}\left(\mathbf{p}_{\mathrm{s},1} - \mathbf{p}_0\right) \tag{2.9}$$

$$c_2 = c_1 \frac{\left\|\mathbf{p}_{\mathrm{s},2} - \mathbf{p}_0\right\|}{r} \tag{2.10}$$

where $\mathbf{p}_0 = [r, 0]^T$ is the center of the imaginary circle. As indicated before, this will be a problem when the source is positioned close to the imaginary circle.

Cramer-Rao Lower Bound of the reference measurement

We will now investigate what the theoretical lower bound of the variance of the calibration parameters is for the reference measurement. To calculate this we use the function $h_{\mathrm{tof}}(c, \mathbf{p}_{\mathrm{s}})$ which has a Jacobian matrix $\mathbf{H}_{\mathrm{tof}}$ as given in (2.7). When the time of flight measures of all detectors are identically Gaussian distributed with variance σ^2_{tof} and uncorrelated, the Cramer-Rao Lower Bound (CRLB) can be calculated as[31]:

$$\mathrm{CRLB} = \sigma^2_{\mathrm{tof}}\left(\mathbf{H}^T_{\mathrm{tof}}\mathbf{H}_{\mathrm{tof}}\right)^{-1} \tag{2.11}$$

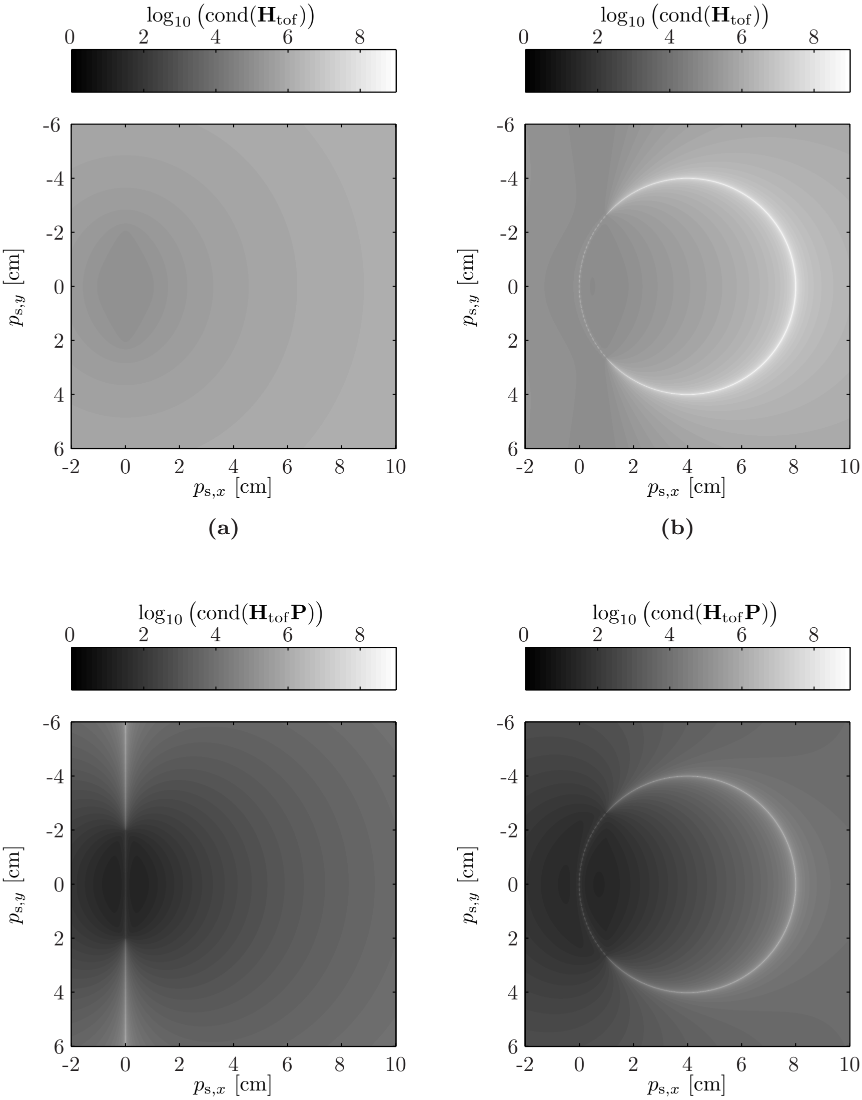

(a) **(b)**

(c) **(d)**

Figure 2.2 The condition number of the Jacobian matrix $\mathbf{H}_{\mathrm{tof}}$ of the reference measurement. Shown are the results for both measurement arrays, the linear array on the left and the curved array on the right, both as introduced in Figure 2.1. The Jacobian matrix was evaluated at different values of $\mathbf{p}_{\mathrm{s}}$ and with a constant speed of sound of $c = 1500$ [m/s]. The top row represents the true condition number and the bottom row the condition number after scaling the inputs.

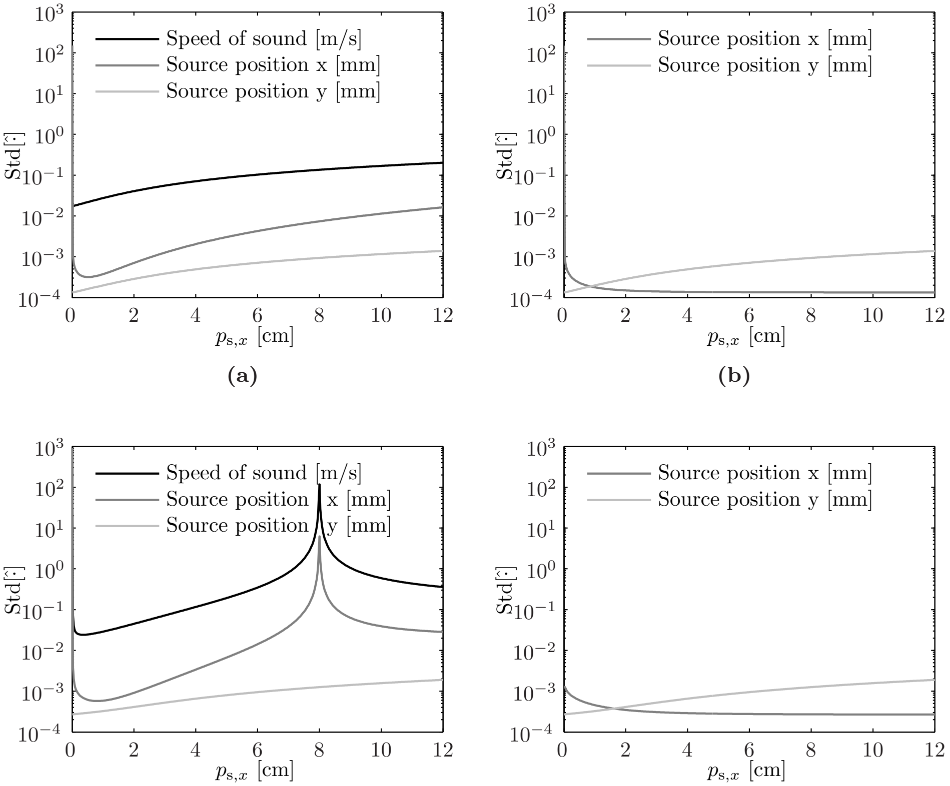

(a) **(b)**

(c) **(d)**

Figure 2.3 This figure shows the CRLB on the parameters of a reference measurement, the measurement function is given in (2.4). The plots on the left (a) and (c) show the results where both speed of sound and the source position are unknown. The plots on the right (b) and (d) show the results where only the source position is unknown. The top row (a) and (b) are for the linear array geometry and the bottom row (c) and (d) are for the curved array geometry. The internal parameters used in the calculation are set to their true values according to the manufacturer as in Figure 2.1. The speed of sound of the reference medium was set to 1500 m/s and the source element was positioned along the x-axis with $p_{s,y} = 0$ cm and $p_{s,x}$ ranging from 0 cm to 12 cm. The uncertainty in the time of flight measurements was set to $\sigma_{\text{tof}} = 10^{-3} \mu$s.

Where the Jacobian matrix $\mathbf{H}_{\mathrm{tof}}$ has to be evaluated at the true value of the speed of sound and source position.

We evaluated the CRLB for both measurement array geometries with the corresponding internal parameters as displayed in Figure 2.1. The speed of sound in the reference medium, which in our PER-PAT setup is water at room temperature, was set to a value of 1500 m/s. The CRLB was then evaluated for different source positions, where the source was moved along the x-axis. The uncertainty in the time of flight measures was set to $\sigma_{\mathrm{tof}} = 10^{-3}\mu\mathrm{s}$, which is reasonable according to Figure 3.7a.

Shown in Figure 2.3a and 2.3c are the extracted minimum standard deviations from the CRLB for the linear and curved measurement array geometry respectively. There is a lot of correlation between the speed of sound and the x-position of the source, which can be seen by calculating the CRLB while assuming that speed of sound is known. The CRLB plots for the source position estimation with known speed of sound are shown in 2.3b and 2.3d. The lower bound on the x-position of the source in that case drops significantly while the lower bound on the y-position of the source does not change. We also see (Figure 2.3c) that when the source is positioned closely to the imaginary circle of the curved array, the lower bound on speed of sound and lower bound on the x-position of the source quickly increase. This effect is caused by the symmetry in the geometry and the rank deficiency of the Jacobian matrix on the line of symmetry. For the reference measurement with the curved array, this will be a problem. We can thus conclude that for certain source position configurations with the curved array, it is not possible to estimate all three parameters from only a reference measurement.

2.2.2 The calibration measurement

The calibration measurement allows us to find the the center of rotation of the detector array and the speed of sound of the reference medium. For this measurement we need a calibration phantom consisting of photoacoustic point sources. In our PER-PAT system, we use a cylindrically shaped calibration phantom made of Agar, in which human or horse hairs are placed to function as photoacoustic point sources. The hairs are aligned in the vertical direction, so that they are placed perpendicular to the measurement plane. The measurement array will rotate stepwise around the calibration phantom and at each step, time of flight measurements from detector elements to the photoacoustic point sources are recorded. From these measurements we then try to recover the center of rotation and the speed of sound of the reference medium.

For a measurement array consisting of N_{d} detector elements, a rotation in N_{R} steps and N_{p} point sources in the calibration phantom, we get $N_{\mathrm{d}} \times N_{\mathrm{R}} \times N_{\mathrm{p}}$ different time of flight measurements. Via a model these measurements are related to the unknown parameters. This model is, besides the unknown parameters, also dependent on the ultrasound properties of the calibration phantom. For a first analysis, we will assume that the speed of sound in the calibration phantom is equal to the speed of sound of the reference medium. In that case, the relation is given by:

$$z_{\text{tof},i,j,k} = \frac{1}{c}\left\|\mathbf{p}_{\text{d},i} - \left(\mathbf{R}_{\phi_j}\mathbf{p}_{\text{s},k} + \mathbf{T}\right)\right\| + n_z \tag{2.12}$$

where i is the index in the detector elements, j is the index in the rotation steps and k is the index in the point sources. For convenience, the positions of the photoacoustic point sources are not given in the measurement array coordinate system, but in a parallel coordinate system with its center defined as the center of rotation $\mathbf{T}$. The complete measurement function for the calibration measurement is given by:

$$h_{\text{tof}}(c, \mathbf{T}, \mathbf{p}_{\text{s},1}, \ldots, \mathbf{p}_{\text{s},N_\text{p}}) = \left(\left(\left(h_{\text{tof},i,j,k}(c, \mathbf{T}, \mathbf{p}_{\text{s},1}, \ldots, \mathbf{p}_{\text{s},N_\text{p}})\right)_{i=1}^{N_\text{d}}\right)_{j=1}^{N_\text{R}}\right)_{k=1}^{N_\text{p}} \tag{2.13}$$

with entries defined as:

$$h_{\text{tof},i,j,k}(c, \mathbf{T}, \mathbf{p}_{\text{s},1}, \ldots, \mathbf{p}_{\text{s},N_\text{p}}) = \frac{1}{c}\left\|\mathbf{p}_{\text{d},i} - \left(\mathbf{R}_{\phi_j}\mathbf{p}_{\text{s},k} + \mathbf{T}\right)\right\| \tag{2.14}$$

Number of rotations and number of sources

In the calibration measurement, we will use a calibration phantom with photoacoustic point sources which rotates around the center of rotation. We will investigate here how many rotation steps and how many sources we need to do a calibration. Without any rotation involved in the measurement, it is clear that we cannot determine the center of rotation, so we need at least $N_\text{R} \geq 2$. The question is however, are two different rotations enough and what kind of effect does increasing the number of rotations have on the calibration accuracy. Similarly we can investigate what kind of phantom configuration works best and what the minimum necessary number of sources N_p is.

We start the analysis again by looking at the Jacobian matrix. In principle, there are three parameters that we want to estimate, the speed of sound c and the x and y position of the center of rotation $\mathbf{T}$. However, also the positions of the photoacoustic point sources in the calibration phantom $\mathbf{p}_{\text{s},k}$ are not known, meaning the total number of unknown parameters is more than three. The partial derivatives of all these parameters are given by:

$$\frac{\partial}{\partial c}h_{\text{tof},i,j,k} = -\frac{1}{c}h_{\text{tof},i,j,k} \tag{2.15}$$

$$\frac{\partial}{\partial \mathbf{T}}h_{\text{tof},i,j,k} = \left(\mathbf{T} + \mathbf{R}_{\phi_j}\mathbf{p}_{\text{s},k} - \mathbf{p}_{\text{d},i}\right)\frac{1}{c^2 h_{\text{tof},i,j,k}} \tag{2.16}$$

$$\frac{\partial}{\partial \mathbf{p}_{\text{s},k}}h_{\text{tof},i,j,k} = \mathbf{R}_{\phi_j}^T\left(\mathbf{T} + \mathbf{R}_{\phi_j}\mathbf{p}_{\text{s},k} - \mathbf{p}_{\text{d},i}\right)\frac{1}{c^2 h_{\text{tof},i,j,k}} \tag{2.17}$$

The complete Jacobian matrix can be formed from these partial derivatives via the recursive creation of the following sub matrices:

$$\mathbf{H}_{c,\mathbf{T},j,k} = \begin{bmatrix} \frac{\partial}{\partial c} h_{\mathrm{tof},1,j,k} & \left(\frac{\partial}{\partial \mathbf{T}} h_{\mathrm{tof},1,j,k}\right)^T \\ \vdots & \vdots \\ \frac{\partial}{\partial c} h_{\mathrm{tof},N_\mathrm{d},j,k} & \left(\frac{\partial}{\partial \mathbf{T}} h_{\mathrm{tof},N_\mathrm{d},j,k}\right)^T \end{bmatrix} \qquad \mathbf{H}_{c,\mathbf{T},k} = \begin{bmatrix} \mathbf{H}_{c,\mathbf{T},1,k} \\ \vdots \\ \mathbf{H}_{c,\mathbf{T},N_\mathrm{R},k} \end{bmatrix}$$

$$\mathbf{H}_{\mathbf{p},j,k} = \begin{bmatrix} \left(\frac{\partial}{\partial \mathbf{p}_{\mathrm{s},k}} h_{\mathrm{tof},1,j,k}\right)^T \\ \vdots \\ \left(\frac{\partial}{\partial \mathbf{p}_{\mathrm{s},k}} h_{\mathrm{tof},N_\mathrm{d},j,k}\right)^T \end{bmatrix} \qquad \mathbf{H}_{\mathbf{p},k} = \begin{bmatrix} \mathbf{H}_{\mathbf{p},1,k} \\ \vdots \\ \mathbf{H}_{\mathbf{p},N_\mathrm{R},k} \end{bmatrix}$$

Which we can use to setup the complete Jacobian matrix of the calibration measurement:

$$\mathbf{H}_{\mathrm{tof}} = \begin{bmatrix} \mathbf{H}_{c,\mathbf{T},1} & \mathbf{H}_{\mathbf{p},1} & \\ \vdots & & \ddots & \\ \mathbf{H}_{c,\mathbf{T},N_\mathrm{p}} & & & \mathbf{H}_{\mathbf{p},N_\mathrm{p}} \end{bmatrix} \tag{2.18}$$

Based on this Jacobian matrix, we found out that for both measurement arrays the minimum number of rotations N_R is two and that one photoacoustic point source in the phantom is enough to get a full rank Jacobian matrix. Of course, the accuracy increases after increasing the number of rotations and the number of photoacoustic point sources. The CRLB can be calculated for the calibration measurement in a similar manner as for the reference measurement, using (2.11) where $\mathbf{H}_{\mathrm{tof}}$ is given by (2.18). For large numbers of N_R and N_p, the CRLB of the calibration parameters gets halved when N_R or N_p is doubled. To get a feeling for the accuracy, the CRLB was calculated with different realistic settings. Two phantom configurations were used, one containing only a single photoacoustic point source and the other one containing four photoacoustic point sources. The sources in the calibration phantom were positioned in a circular configuration at a variable distance r_p from the center of rotation $\mathbf{T}$ and the rotation steps were uniformly distributed over a full 360° rotation. The resulting values of the CRLB are displayed in Figure 2.4. Here indeed we see that with as little as one photoacoustic point source in the phantom and two rotations we can already do a successful calibration.

Effects of a different speed of sound in the calibration phantom

In our simplified model of the calibration measurement, we assumed that the speed of sound inside the calibration phantom was equal to the speed of sound of the reference medium. In practice, this might not be the case. Suppose that the speed of sound in the phantom is different than the speed of sound in the medium, but related to it via the relation $c_{\mathrm{phantom}} = \alpha c_{\mathrm{medium}}$. This is a valid relation when the phantom material responds in a similar way to temperature fluctuations as the medium. Then the measurement function can be seen as to consist of two different parts, one part representing the ultrasound wave traveling through the reference medium and one

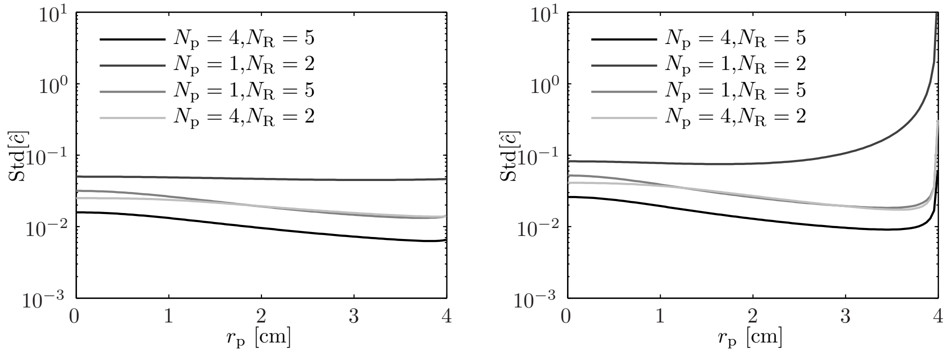

(a) Speed of sound [m/s] (Linear array) **(b)** Speed of sound [m/s] (Curved array)

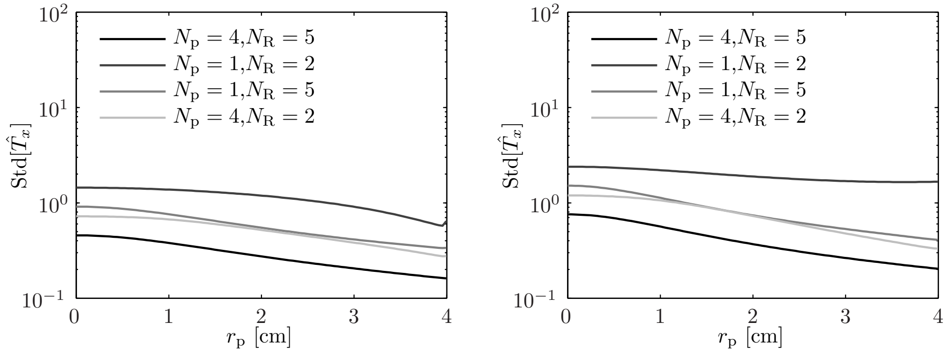

(c) Center of rotation x [μm] (Linear array) **(d)** Center of rotation x [μm] (Curved array)

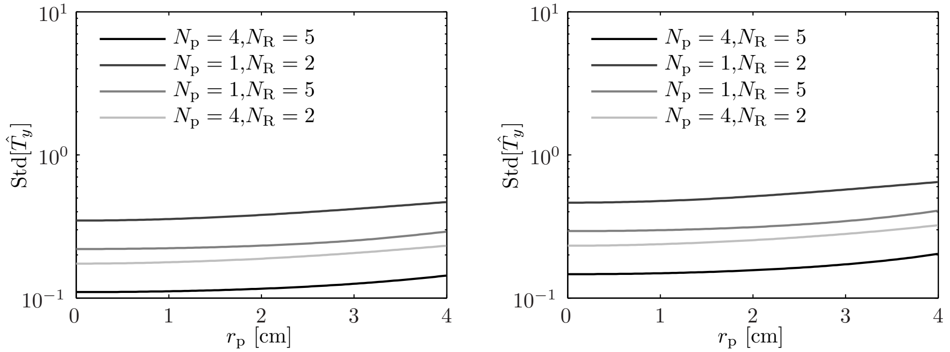

(e) Center of rotation y [μm] (Linear array) **(f)** Center of rotation y [μm] (Curved array)

Figure 2.4 The CRLB for the calibration measurement for different calibration object configurations ($N_p = 1$ and $N_p = 4$) and for a different number of rotations ($N_R = 2$ and $N_R = 5$). The center of rotation was set to $T_x = 4$ cm and $T_y = 0$ cm and the speed of sound to $c = 1500$ m/s.

representing the ultrasound wave traveling through the calibration phantom. The two different paths are illustrated in Figure 2.5 for a circular shaped phantom with a radius of r_c. The paths are connected via the point $\mathbf{p}_\mathrm{c}$ which lies on the boundary of the calibration phantom. The position of that point can be determined from the geometry of the phantom, the speed of sound of the phantom, the speed of sound of the medium, the position of the source $\mathbf{p}_{\mathrm{s},k}$ in the phantom, the position of the detector in the medium $\mathbf{p}_{\mathrm{d},i}$ and is governed by Snell's law. This results in a model that is related to the unknown parameters via:

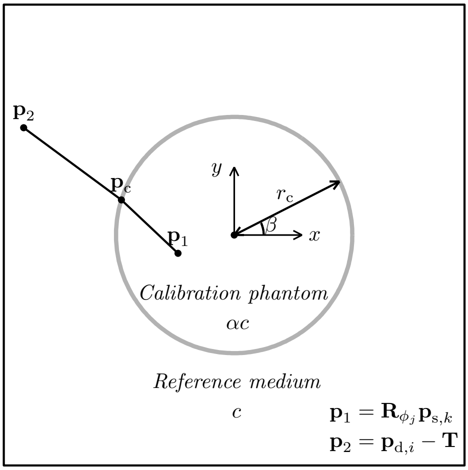

Figure 2.5 Calibration phantom with a different speed of sound as the reference medium

$$h_{\mathrm{tof},i,j,k}(c, \mathbf{T}, \mathbf{p}_{\mathrm{s},1}, \dots, \mathbf{p}_{\mathrm{s},N_\mathrm{p}}) = \frac{1}{c}\left\|\mathbf{p}_2 - \mathbf{p}_c\right\| + \frac{1}{\alpha c}\left\|\mathbf{p}_c - \mathbf{p}_1\right\| \tag{2.19}$$

where $\mathbf{p}_1$ and $\mathbf{p}_2$ are the coordinates respectively of source position k and detector position i in the j^{th} rotation:

$$\begin{aligned} \mathbf{p}_1 &= \mathbf{R}_{\phi_j}\mathbf{p}_{\mathrm{s},k} && (2.20) \\ \mathbf{p}_2 &= \mathbf{p}_{\mathrm{d},i} - \mathbf{T} && (2.21) \end{aligned}$$

Using Snell's law To calculate the point $\mathbf{p}_c$, Snell's law can be enforced by using Fermat's principle of least time, meaning that the path between two points is the path that can be traversed in the least time. By parametrizing the point $\mathbf{p}_c$ as a function of its angular position on the circular boundary β:

$$\mathbf{p}_c = r_\mathrm{c}\mathbf{n}(\beta) = r_\mathrm{c}\begin{bmatrix}\cos(\beta)\\ \sin(\beta)\end{bmatrix} \tag{2.22}$$

we can find the position of $\mathbf{p}_c$ by searching for the angle β which minimizes the traversed time:

$$\beta_{\min} = \arg\min_{\beta} \left(\frac{1}{c} \left\| \mathbf{p}_2 - r_\mathrm{c}\mathbf{n}(\beta) \right\| + \frac{1}{\alpha c} \left\| r_\mathrm{c}\mathbf{n}(\beta) - \mathbf{p}_1 \right\| \right) \tag{2.23}$$

This minimum can be found by taking the derivative with respect to β and equating it to zero. This results in finding a solution for β to the nonlinear equation:

$$\alpha c \frac{r_\mathrm{c} \left(\mathbf{n}_\perp(\beta)\right)^T \left(r_\mathrm{c}\mathbf{n}(\beta) - \mathbf{p}_1\right)}{\left\| r_\mathrm{c}\mathbf{n}(\beta) - \mathbf{p}_1 \right\|} = c \frac{r_\mathrm{c} \left(\mathbf{n}_\perp(\beta)\right)^T \left(\mathbf{p}_2 - r_\mathrm{c}\mathbf{n}(\beta)\right)}{\left\| \mathbf{p}_2 - r_\mathrm{c}\mathbf{n}(\beta) \right\|} \tag{2.24}$$

where $\mathbf{n}_\perp(\beta) = [-\sin(\beta), \cos(\beta)]^T$ is the vector orthogonal to $\mathbf{n}(\beta)$. This nonlinear equation actually represents Snell's law where the two sine terms have already been filled in. Solving this minimization problem to find $\mathbf{p}_\mathrm{c}$ is not straightforward and would result in an iterative approach. But still, we can use it to calculate the true TOF values that would result from a circular calibration phantom with a different speed of sound.

These true TOF values were used as input to determine the bias that is introduced by assuming the model with one speed of sound. The configuration for the bias simulation test consisted of a phantom having a diameter of 1.5 cm with a speed of sound 1% higher than the surrounding medium. The results of this simulation are displayed in Figure 2.6. The bias at different center of rotations have been evaluated. We see that when comparing the bias effect with the CRLB, Figure 2.4, that the bias effect is more severe that the uncertainty due to measurement noise. Therefore it is justified to investigate how the calibration measurement model can be extended in a simple way to model the speed of sound differences.

A simple model ignoring refraction The approach to find the position $\mathbf{p}_\mathrm{c}$ using Snell's law leads to a solution which requires solving a nonlinear equation. This is not very convenient when we want to implement a calibration algorithm based on such a model. However, we have seen that the bias error due to having a different speed of sound in the calibration phantom is larger than the standard deviation on the estimate caused by noise on the TOF measurements. So it can be advantageous to try to correct for the bias by including the two different speeds of sound in the measurement model. We will now explore an approach which includes the effects of different speeds of sound and ignores refraction. We will see that this results in a simple modification to the measurement model.

If we assume that there is no refraction, than the position $\mathbf{p}_\mathrm{c}$ is located on the circle at the intersection point with the line connecting $\mathbf{p}_1$ and $\mathbf{p}_2$. By parameterizing the point $\mathbf{p}_\mathrm{c}$ as a function of its position along this line:

$$\mathbf{p}_\mathrm{c} = \mathbf{p}_1 + \beta \mathbf{v} \tag{2.25}$$

where $\mathbf{v}$ is the unit vector pointing from $\mathbf{p}_1$ to $\mathbf{p}_2$:

$$\mathbf{v} = \frac{\mathbf{p}_2 - \mathbf{p}_1}{\left\| \mathbf{p}_2 - \mathbf{p}_1 \right\|} \tag{2.26}$$

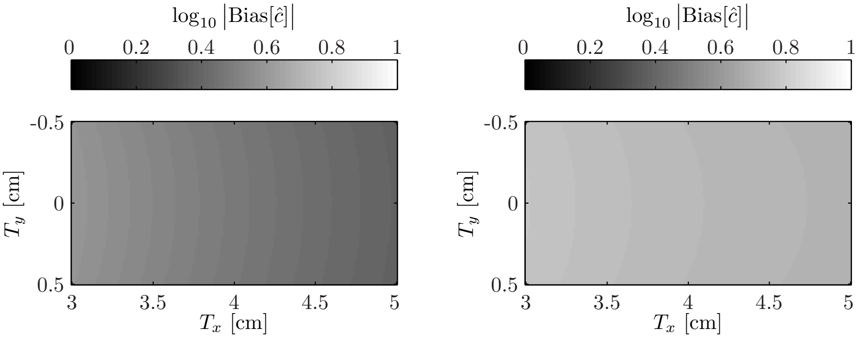

(a) Speed of sound [m/s] (Linear array) **(b)** Speed of sound [m/s] (Curved array)

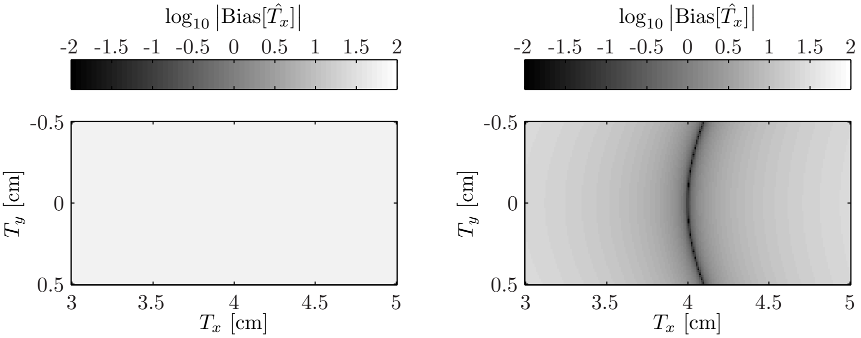

(c) Center of rotation x [μm] (Linear array) **(d)** Center of rotation x [μm] (Curved array)

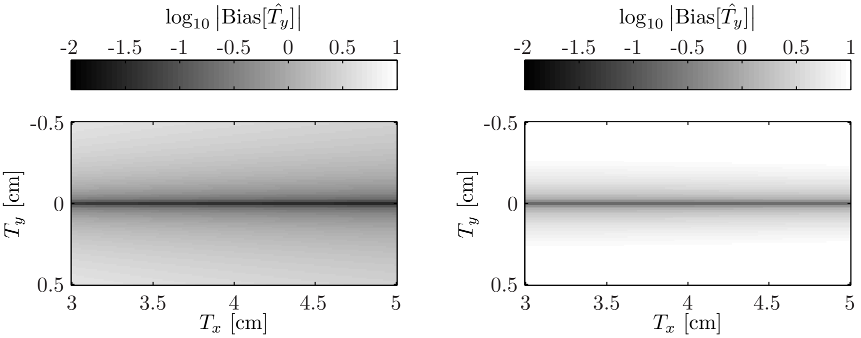

(e) Center of rotation y [μm] (Linear array) **(f)** Center of rotation y [μm] (Curved array)

Figure 2.6 Bias in the calibration measurement estimates due to using a model that assumes equal speed of sound in medium and phantom. The bias values are obtained for a configuration with four sources ($N_\mathrm{p} = 4$), five rotation steps ($N_\mathrm{R} = 5$), a speed of sound in the medium of $c = 1500$ [m/s], a phantom radius of $r_\mathrm{c} = 1.5$ [cm] and sources positioned at a radius of $r_\mathrm{p} = 0.75$ [cm]. The speed of sound in the phantom was set to be 1% higher than the medium, $\alpha = 1.01$.

we can find the position parameter β resulting in the intersection point by requiring that $\mathbf{p}_c$ lies on the circle with radius r_c. Applying this constraint:

$$\left\|\mathbf{p}_1 + \beta \mathbf{v}\right\|^2 = r_\mathrm{c}^2 \tag{2.27}$$

results in a quadratic equation in terms of β:

$$\beta^2 + 2\mathbf{p}_1^T \mathbf{v}\beta + \left\|\mathbf{p}_1\right\|^2 - r_\mathrm{c}^2 = 0 \tag{2.28}$$

When solving this equation, we get two solutions for β. One solution has a negative value and the other one a positive value. The solution with the positive value gives us the correct parameter that results in the point $\mathbf{p}_\mathrm{c}$ on the circle between $\mathbf{p}_1$ and $\mathbf{p}_2$. Applying the *abc*-formula and picking the positive solution gives us:

$$\beta = \sqrt{\left(\mathbf{p}_1^T \mathbf{v}\right)^2 - \left\|\mathbf{p}_1\right\|^2 + r_\mathrm{c}^2} - \mathbf{p}_1^T \mathbf{v} \tag{2.29}$$

So that the point $\mathbf{p}_\mathrm{c}$ can directly be calculated:

$$\mathbf{p}_c = \mathbf{p}_1 + \left(\sqrt{\left(\mathbf{p}_1^T \mathbf{v}\right)^2 - \left\|\mathbf{p}_1\right\|^2 + r_\mathrm{c}^2} - \mathbf{p}_1^T \mathbf{v}\right) \mathbf{v} \tag{2.30}$$

With this result we now have a closed form expression for the measurement model incorporating the two different speeds of sound, but ignoring refraction. The closed form expression of the measurement model can be found by filling this solution for $\mathbf{p}_\mathrm{c}$ in in (2.19):

$$h_{\mathrm{tof},i,j,k}(c, \mathbf{T}, \mathbf{p}_{\mathrm{s},1}, \ldots, \mathbf{p}_{\mathrm{s},N_\mathrm{p}}) = \frac{1}{c}\left\|\mathbf{p}_2 - \mathbf{p}_1\right\| + \frac{1}{c}\left(\tfrac{1}{\alpha} - 1\right)\beta \tag{2.31}$$

The question now is, how much will this simplified model help to get rid of the bias due to the different speeds of sound. This was investigated by again calculating the bias after using the true TOF values which were caused by refraction and two different speeds of sound. The results, for different center of rotations, are displayed in Figure 2.7. When comparing these with the CRLB, Figure 2.4, we see that the bias effect is now much smaller than the uncertainty caused by measurement noise.

2.3 Calibration procedure

Now that the necessary models and measurements required for calibration have been introduced and analyzed, it is time to introduce the calibration procedure. The calibration procedure consists of several parts. First we will pre-process the measured signals, resulting in the extraction of a set of time of flight measurements. Then a classification step is performed, which estimates the number of sources from the set of flight measurements and gives a classification of the measurements into groups identified by the source numbers. Once the measurements are classified to a group, we will introduce an approach to estimate the source positions and speed of sound based on this classification result and the time of flight measurements. The reference

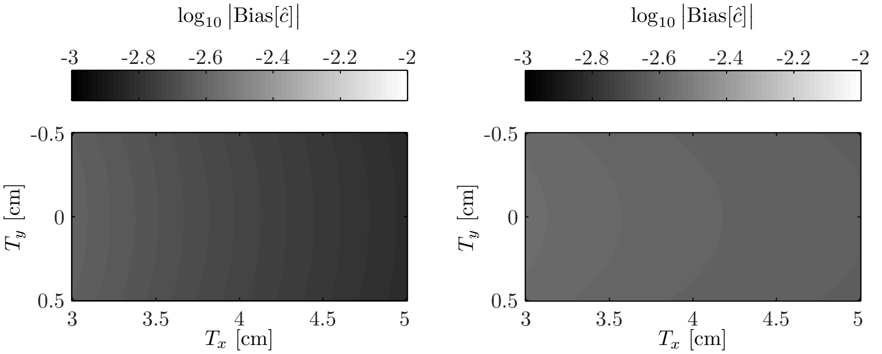

(a) Speed of sound [m/s] (Linear array) **(b)** Speed of sound [m/s] (Curved array)

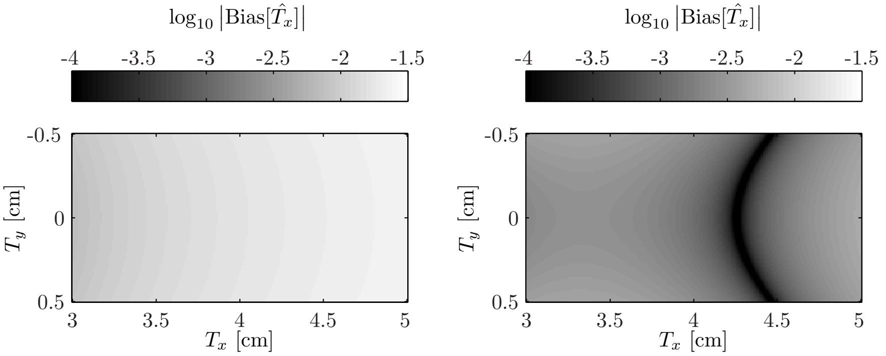

(c) Center of rotation x [μm] (Linear array) **(d)** Center of rotation x [μm] (Curved array)

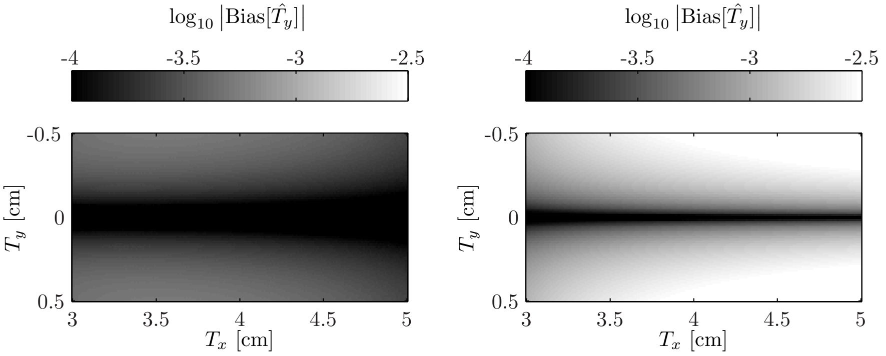

(e) Center of rotation y [μm] (Linear array) **(f)** Center of rotation y [μm] (Curved array)

Figure 2.7 Bias in the calibration measurement when using a model that incorporates speed of sound differences in medium and phantom but ignores refraction. The bias values are obtained for a configuration with four sources ($N_\mathrm{p} = 4$), five rotation steps ($N_\mathrm{R} = 5$), a speed of sound in the medium of $c = 1500$ [m/s], a phantom radius of $r_\mathrm{c} = 1.5$ [cm] and sources positioned at a radius of $r_\mathrm{p} = 0.75$ [cm]. The speed of sound in the phantom was set to be 1% higher than the medium, $\alpha = 1.01$.

measurement calibration problem is then completely solved. The calibration measurement calibration problem requires an extra step such that also the measurements under different rotations are merged and finally result in the estimate of a speed of sound and center of rotation.

2.3.1 Extracting time of flight measures

The first step in the calibration procedure is the extraction of time of flight values from the measured ultrasound signals. The measured signals will contain a time shifted and possibly amplified/attenuated observation of the source signal in the presence of additive noise. The source signal is generated by a small optical absorber via the photoacoustic effect and the shape of this signal is primarily dependent on the size of the absorber. Because the measurement conditions and calibration phantom can change in between different measurement sessions, we might not know the exact source signal beforehand. Therefore we seek a solution to the problem where we simultaneously try to estimate the time of flight values, the source signal and the amplification/attenuation factors from the measured ultrasound signals. A unique solution to this problem cannot be found because of the ambiguity in the phase and amplitude of the source signal with respect to the phases and amplitudes of the measurements. To overcome this problem we will constrain the phase and amplitude of the source signal. The phase will be constrained by enforcing the center of mass of the source signal to be exactly in the center of the signal window. The mass coordinate will be the time and the mass distribution will be the envelope of the source signal, so that the constraint can be written as:

$$\int\limits_{t=t_1}^{t_2} t \frac{h_{\mathrm{env}}(t)}{\int\limits_{t'=t_1}^{t_2} h_{\mathrm{env}}(t')\mathrm{d}t'} \mathrm{d}t = \frac{t_1 + t_2}{2} \tag{2.32}$$

where $h_{\mathrm{env}}(t)$ is the envelope of the source signal $h(t)$, which we take as the magnitude of the analytic signal:

$$h_{\mathrm{env}}(t) = \sqrt{\left(h(t)\right)^2 + \left(\mathcal{H}\left\{h(t)\right\}\right)^2} \tag{2.33}$$

where $\mathcal{H}\{\,\cdot\,\}$ stands for the Hilbert transform. The amplitude of the source signal will be constrained by enforcing the maximum of the signal to be one.

Now given a certain source signal, time of flight values and amplification/attenuation factors it is straightforward to predict the measured signals. We aim to find the maximum likelihood estimate of all these unknown parameters from the observed measurements. In the presence of additive uncorrelated Gaussian noise with equal variance on all measurements, this results in searching for the least square error between the observed signals and predicted signals, subject to the two source signal constraints. The solution to this constrained least squares problem can be found in a simple iterative procedure, which has to be initialized with a rough guess of the source signal. The iterative solution is based on switching between solving for the time of flight and amplification/attenuation factors while keeping the source signal constant and solving for the source signal while keeping the time of flight and amplification/attenuation factors constant. In each iteration, after solving for the source signal, the constraints are applied to the source signal. The implementation of the different steps in the algorithm will now shortly be discussed.

Initialization As initialization for the source signal, a window in one of the source signals can be used which approximately covers the expected source signal.

Applying the source signal constraints First the envelope of the source signal is calculated with the use of the Hilbert transform as shown in (2.33). Then the center of mass is calculated according to (2.32). The source signal is then shifted with the amount of mismatch between the calculated center of mass and the center of the signal window. This shifting is performed using a DFT and an IDFT transform as indicated in (3.50). Next the source signal is scaled by the inverse of its maximum so that the source signal is normalized to have a maximum of one. The result of this step is a source signal which conforms to the constraints.

Time of flight estimation step Given an estimate of the source signal, we can estimate the time of flight and amplification/attenuation factors. This estimation step will be handled with the proposed time of flight estimator as described in section 3.3.3. The time of flight values can be calculated on all measured signals separately. The result of this step are the time of flight values and amplification/attenuation factors for all measured signals.

Source signal estimation step The step of estimating the source signal will be handled by shifting all measured signals with the corresponding estimated time of flight values. Then the maximum likelihood estimate of the source signal is calculated via a weighted average of the shifted measured signals. The weighting factors are calculated based on the previously estimated amplification/attenuation factors. Suppose the amplification/attenuation factors of the measurements are represented in a vector **a** then the weights for averaging the individual measurements is given by:

$$w_i = \frac{a_i}{\|\mathbf{a}\|^2} \tag{2.34}$$

The result of this step is a new estimate of the source signal, on which the constraints still have to be applied.

When after some iterations the results converge to a stable solution, a local minimum to the non-linear least squares problem has been found.

The obtained time of flight values from this procedure are now relative to an arbitrary point in the estimated source signal. In the estimated source signal we can identify the start of the signal, by looking at the amplitude of the envelope of the source signal. When this amplitude is above a certain threshold (based on the noise) we can assume that the first signal from the photoacoustic point source has arrived.

We can then find the time of flight to the center of the source by adding to the signal start time the time necessary to travel to the center of the source. These corrected time of flight values can then be used as input to the calibration procedure.

Extension for multiple source realizations in a single measurement

The described procedure of extracting time of flight measures from the measured ultrasound signals works for single source measurements. Such as is the case with the reference measurement for a single source, section 2.2.1. When a calibration measurement is performed, section 2.2.2 there can be more than one photoacoustic point source, so that this single source approach of extracting time of flight measurements would not work. When there is more than one source, we apply a pre-processing step which identifies the individual source signals in a single measurement and then apply the time of flight/template estimation algorithm on the identified regions in the signal:

Localization based on amplitude information We first identify possible source signals in the measured signals by looking at the envelope of each measured signal. When the envelope exceeds a certain threshold value, we extract a region of the measured signal around that position. On all the collected source signal realizations we perform the previously described time of flight/template estimation algorithm. This gives us an initial estimate of the source signal template which is used in the next step.

Localization based on template filtering With a given initial template estimate, we apply a matched filter to the measured signals and look for local maxima in the resulting filtered signal. Around the obtained local maxima we extract a part of the measured signal. On all the collected source signal realizations we perform the previously described time of flight/template estimation algorithm. The positions of the local maxima are taken into account to calculate the absolute time of flight within the whole measured signal.

This two-step approach will be robust against noisy artifacts in the signal which have a high amplitude, but have a different signal shape than the source signal template.

2.3.2 Classifying time of flight measures

When there is more than one source present in the calibration measurement or when we expect that there could be outliers in the time of flight measurements, we cannot simply find the calibration parameters by directly fitting the (reference or calibration) model to the measurements. First a classification step is necessary in which time of flight measurements are classified as being an outlier or belonging to one of the sources present in the measurement. The number of sources to use in the calibration phantom is a design parameter which can be chosen freely by the user. We have seen in the previous section that more sources result in a more accurate estimate of the calibration parameters but the calibration can in principle work with as little as one source. We would like our classification procedure to be flexible such that it does not require the user to specify the number of sources beforehand but that it is estimated from the measurements automatically. The task of the classification procedure is thus to determine the number of sources present in the measurements and to classify each of the time of flight measurements to one of the possible classes, where the possible classes are all of the sources plus an outlier class for spurious measurements.

In this section we will propose an algorithm to estimate the number of classes and to find the probability that a given measurement is member of a certain class. The approach is based on using a mixture model to represent the measurements and the goal is to obtain a maximum likelihood estimate of the source parameters. In the calibration measurement the measurements are taken by rotating the sensor array at several angles. We limit this procedure to estimate source parameters from each of the rotations separately. The problem that remains to be solved then is finding the correspondences between the sources identified in the different rotations. Also it could be possible that not all sources can be identified in all rotations. These problems will be postponed to a subsequent step, which uses the input of this classification step to solve those problems.

An example of a calibration measurement with estimated time of flight values is displayed in Figure 2.8. As discussed we limit ourselves in this classification step to measurements contained in the same rotation step. The different rotations are separated in Figure 2.8b by vertical bars. In general we can assume that within one rotation step, the time of flight curve for a given photoacoustic point source can approximately be represented with a second order polynomial. We will therefore represent each class (representing a source) by the three parameters that describe a

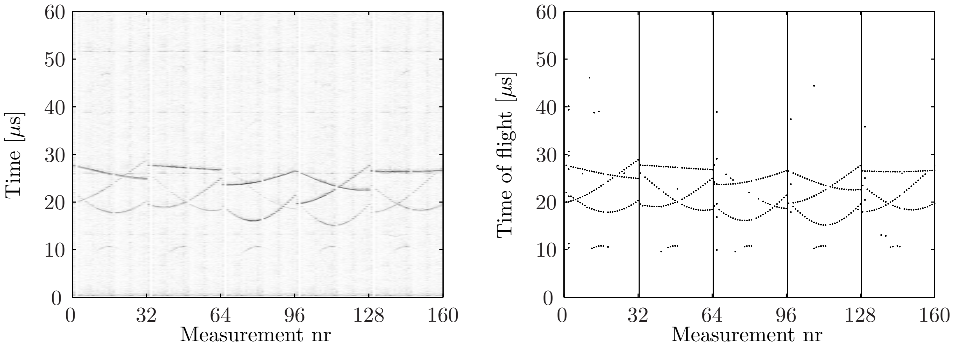

(a) Measured signals **(b)** Estimated time of flight samples

Figure 2.8 Example of a calibration measurement using the 32 element circular array ($N_\mathrm{d} = 32$), measured over five rotation steps ($N_\mathrm{R} = 5$) and containing three photoacoustic point sources ($N_\mathrm{p} = 3$). The discontinuities between the rotation steps are mainly caused by the rotation center not coinciding with the focal center of the circular array.

second order polynomial. We expect the measurement from a certain source to have a small random deviation from this polynomial model which is zero mean Gaussian distributed with variance σ_z^2. Besides the measurements originated from one of the photoacoustic point sources there might be spurious measurements which have to be considered as outliers.

We will now define a model that describes these time of flight measurements. Suppose we have a set of N time of flight measurements $\mathbf{z} = [z_1, \ldots, z_N]^T$. For each measurement, identified by its number i we keep track of the sensor number s_i in the array that measured it. Now if the i^{th} measurement was caused by the photoacoustic point source k with polynomial parameters $\mathbf{x}_k$ then we have:

$$z_i = h_i(\mathbf{x}_k) + n_{i,k} \tag{2.35}$$

where

$$h_i(\mathbf{x}_k) = x_{k,1}s_i^2 + x_{k,2}s_i + x_{k,3} \tag{2.36}$$

is the second order polynomial function that predicts the time of flight measurement at sensor s_i from the photoacoustic point source with polynomial parameters $\mathbf{x}_k$. The measurement is noisy and $n_{i,k}$ is a Gaussian random variable with variance σ_z^2 that represents the noise on the i^{th} measurement. In order to relate each measurement i to the correct photoacoustic point source k we have to know which photoacoustic point source is responsible for which measurement. We can represent this in a membership indicator variable $\boldsymbol{\gamma} = [\gamma_1, \ldots, \gamma_N]^T$ where each γ_i belongs to the i^{th} measurement. If there are N_s photoacoustic point sources then $\gamma_i \in \{0, 1, \ldots, N_\mathrm{s}\}$. A value of $\gamma_i = k$ then indicates that the i^{th} measurement was caused by the k^{th} photoacoustic point source and a value of $\gamma_i = 0$ indicates that the i^{th} measurement was an outlier and is not caused by any of the N_s photoacoustic point sources. In summary, for the i^{th} measurement z_i with membership indicator γ_i we have the relation:

$$z_i = \sum_{k=1}^{N_\mathrm{s}} I_k(\gamma_i)\big(h_i(\mathbf{x}_k) + n_k\big) + I_0(\gamma_i)n_\mathrm{o} \tag{2.37}$$

where $I_k(\gamma_i)$ is an indicator function:

$$I_k(\gamma_i) = \left\{ \begin{array}{ll} 1 & \gamma_i = k \\ 0 & \gamma_i \neq k \end{array} \right. \tag{2.38}$$

and the random variable n_o represents outlier noise, which is uniformly distributed over the measurement space $[z_\mathrm{min}, z_\mathrm{max}]$. The information associated with each measurement z_i is summarized in Table 2.2. Based on this measurement model, we get the following likelihood function:

$$p(z_i|\mathcal{X}, \gamma_i) = \sum_{k=1}^{N_\mathrm{s}} I_k(\gamma_i)\frac{1}{\sqrt{2\pi}\sigma_z}e^{-\frac{1}{2}\frac{r_i^2(\mathbf{x}_k)}{\sigma_z^2}} + I_0(\gamma_i)\frac{1}{v} \tag{2.39}$$

where $\mathcal{X} = (\mathbf{x}_1, \ldots, \mathbf{x}_{\mathrm{N}_s})$ is the set containing the parameters of the photoacoustic point sources, the value of $v = z_\mathrm{max} - z_\mathrm{min}$ is equal to the total size of the measurement

Item	Domain	Description
z_i	$[t_{\min}, t_{\max}]$	Observed time of flight
s_i	$\{1, \ldots, N_\mathrm{d}\}$	Sensor that registered the measurement
γ_i	$\{0, \ldots, N_\mathrm{s}\}$	Source number responsible for this measurement

Table 2.2 Overview of the information that is related to each measurement z_i in the grouping within each rotation step.

space and $r_i(\mathbf{x}) = h_i(\mathbf{x}) - z_i$ represents the residue of the i^{th} measurement. The individual measurements z_i can be combined in a single likelihood function. The combined likelihood of having a set of N_s second order polynomial and membership variables $\boldsymbol{\gamma}$ from an observed measurement $\mathbf{z}$ is given by:

$$p(\mathbf{z}|\mathcal{X}, \boldsymbol{\gamma}) = \prod_{i=1}^{N} p(z_i|\mathcal{X}, \gamma_i) \tag{2.40}$$

A possible solution to the problem of finding the most likely set of second order polynomial functions describing the data can now be found by maximizing this combined likelihood function. By finding this maximum, each measurement will be fully assigned to the group that is most likely. Sometimes however, a measurement might be positioned on the intersection of two polynomial curves, meaning that it could have originated quite well from either one of the two sources. Also it might be possible that a measurement could equally well be an outlier or inlier. To identify these situations in a natural way, we can first find the maximum likelihood estimate of $\mathbf{x}$, independent on $\boldsymbol{\gamma}$ and then find the probability that a certain measurement is member of one of the groups. To find the likelihood function of $\mathbf{x}$, independent on $\boldsymbol{\gamma}$ we have to marginalize over the $\boldsymbol{\gamma}$ variable. For each of the individual measurements z_i we get the marginalized likelihood function:

$$p(z_i|\mathcal{X}) = \sum_{\gamma_i=0}^{N_\mathrm{s}} p(z_i, \gamma_i|\mathcal{X}) = \sum_{\gamma_i=0}^{N_\mathrm{s}} p(z_i|\mathcal{X}, \gamma_i)p(\gamma_i|\mathcal{X}) \tag{2.41}$$

This involves the prior distribution of the membership variables $p(\gamma_i|\mathcal{X})$. If nothing is known in advance about the number of measurements in each of the $N_\mathrm{s} + 1$ groups then we have to use the non-informative prior:

$$p(\gamma_i|\mathcal{X}) = \frac{1}{N_\mathrm{s} + 1} \tag{2.42}$$

The resulting expression for the individual marginalized likelihoods is then:

$$p(z_i|\mathcal{X}) = \frac{1}{(N_\mathrm{s} + 1)\sqrt{2\pi}\sigma_z} \left(\sum_{k=1}^{N_\mathrm{s}} e^{-\frac{1}{2}\frac{r_i^2(\mathbf{x}_k)}{\sigma_z^2}} + \frac{\sqrt{2\pi}\sigma_z}{v} \right) \tag{2.43}$$

And the final marginalized likelihood function involving all measurements is given by the product of all individual marginalized likelihoods:

$$p(\mathbf{z}|\mathcal{X}) = \prod_{i=1}^{N} p(z_i|\mathcal{X}) \tag{2.44}$$

Incorporating different a-priori knowledge on the class distributions is straightforward. An illustration of the obtained likelihood function is displayed in Figure 2.9a and 2.9b for two different settings of v. The figures show a two class situation with one Gaussian inlier class, $N_\mathrm{s} = 1$, and a uniform outlier class. Both likelihoods are displayed together with the marginalized likelihood. For better visualization, the marginalized likelihood is scaled to have the same height as the Gaussian likelihood.

With the help of the a-priori and marginalized likelihood we can calculate the probability of a certain measurement z_i belonging to group γ_i using the estimate of the most likely set of polynomial functions describing the data, $\hat{\mathcal{X}}$:

$$p(\gamma_i|z_i, \hat{\mathcal{X}}) = \frac{p(z_i, \gamma_i|\hat{\mathcal{X}})}{p(z_i|\hat{\mathcal{X}})} = \frac{p(z_i|\hat{\mathcal{X}}, \gamma_i)p(\gamma_i|\hat{\mathcal{X}})}{p(z_i|\hat{\mathcal{X}})} \tag{2.45}$$

For the probability of membership of one of the photoacoustic point source groups $k > 0$ we get:

$$p(\gamma_i = k|z_i, \hat{\mathcal{X}}) = \frac{e^{-\frac{1}{2}\frac{r_i^2(\hat{\mathbf{x}}_k)}{\sigma_z^2}}}{\sum_{k'=1}^{N_\mathrm{s}} e^{-\frac{1}{2}\frac{r_i^2(\hat{\mathbf{x}}_{k'})}{\sigma_z^2}} + \frac{\sqrt{2\pi}\sigma_z}{v}} \tag{2.46}$$

and the probability of a measurement being an outlier $\gamma_i = 0$, thus not being part of one of the N_s photoacoustic point sources, is given by:

$$p(\gamma_i = 0|z_i, \hat{\mathcal{X}}) = \frac{\frac{\sqrt{2\pi}\sigma_z}{w}}{\sum_{k'=1}^{N_\mathrm{s}} e^{-\frac{1}{2}\frac{r_i^2(\hat{\mathbf{x}}_{k'})}{\sigma_z^2}} + \frac{\sqrt{2\pi}\sigma_z}{v}} \tag{2.47}$$

Now the situation when a measurement is obtained at an intersection between the curves of two different photoacoustic point sources can be identified from the membership probability. Both membership probabilities are plotted for a range of residue values in the two class case in Figure 2.9c and 2.9d for two settings of T.

Finding the most likely set of groups of measurements belonging to the same photoacoustic point source comes down to finding the maximum of either the complete likelihood function (2.40) or the marginalized likelihood function (2.44). We will discuss both approaches and finally use the approach based on maximizing the marginalized likelihood function in the proposed algorithm. Maximizing the complete likelihood function means a hard classification of the measurements is performed, i.e., a measurement belong completely to one group and measurements can be outlier or inlier and there is no smooth transition between these classes. Maximizing the marginalized likelihood function gives us a soft classification where the probability can be calculated that a certain measurement belongs to a certain class with (2.46).

Maximizing a likelihood function, involving the product of a set of individual likelihood functions, can equivalently be done by minimizing the cost function which is obtained by applying the $-\log[\cdot]$ operation on the likelihood function. The resulting cost function is a sum of individual cost functions. In the presentation of the cost functions for both approaches we will use a vector of residues at each measurement:

$$\mathbf{r}_i = \begin{bmatrix} r_{i,1} \\ \vdots \\ r_{i,N_\mathrm{s}} \end{bmatrix} \quad \text{with} \quad r_{i,k} = r_i(\mathbf{x}_k) \tag{2.48}$$

We will now discuss the cost functions that result from maximizing the likelihood $p(\mathbf{z}|\mathcal{X},\boldsymbol{\gamma})$ and maximizing the marginalized likelihood $p(\mathbf{z}|\mathcal{X})$. Finding the maximum of the first likelihood function (2.40), can be done in two steps. First the value of $\hat{\boldsymbol{\gamma}}$ that gives the maximum:

$$\hat{\boldsymbol{\gamma}} = \arg\max_{\boldsymbol{\gamma}} p(\mathbf{z}|\mathcal{X},\boldsymbol{\gamma}) \tag{2.49}$$

can be calculated. This has the solution:

$$\hat{\gamma}_i = \begin{cases} k_{\min} & \dfrac{r^2_{i,k_{\min}}}{\sigma^2_z} < T \\[2ex] 0 & \dfrac{r^2_{i,k_{\min}}}{\sigma^2_z} \geq T \end{cases} \tag{2.50}$$

with

$$k_{\min} = \mathop{\arg\min}_{k\in\{1,\ldots,N_\mathrm{s}\}} r^2_{i,k} \tag{2.51}$$

and

$$T = -2\log\left[\frac{\sqrt{2\pi}\sigma_z}{v}\right] \tag{2.52}$$

Filling in this result for $\hat{\boldsymbol{\gamma}}$ in the complete likelihood function and converting it to a cost function gives us:

$$C_1(\mathcal{X}) = -\log\left[p(\mathbf{z}|\mathcal{X},\hat{\boldsymbol{\gamma}})\right] = N\log\left[\sqrt{2\pi}\sigma_z\right] + \sum_{i=1}^{N}\rho_1(\mathbf{r}_i) \tag{2.53}$$

with

$$\rho_1(\mathbf{r}_i) = \begin{cases} \frac{1}{2}\dfrac{r^2_{i,k_{\min}}}{\sigma^2_z} & \dfrac{r^2_{i,k_{\min}}}{\sigma^2_z} < T \\[2ex] \frac{1}{2}T & \dfrac{r^2_{i,k_{\min}}}{\sigma^2_z} \geq T \end{cases} \tag{2.54}$$

This is the cost function of the complete likelihood which now needs to be minimized for $\mathcal{X}$. The cost function thus consists of two parts and has a discontinuity in the first derivative at $r = \sqrt{T}\sigma_z$. Now in the second case, when using the marginalized likelihood function, the cost is simply given by:

$$C_2(\mathcal{X}) = -\log\left[p(\mathbf{z}|\mathcal{X})\right] = N\log\left[(N_\mathrm{s}+1)\sqrt{2\pi}\sigma_z\right] + \sum_{i=1}^{N}\rho_2(\mathbf{r}_i) \tag{2.55}$$

with

$$\rho_2(\mathbf{r}_i) = -\log\left[\sum_{k=1}^{N_\mathrm{s}} e^{-\frac{1}{2}\frac{r_{i,k}^2}{\sigma_z^2}} + \frac{\sqrt{2\pi}\sigma_z}{v}\right] \tag{2.56}$$

The cost function of the marginalized likelihood is a smooth function. Both cost functions are displayed in Figure 2.9e and 2.9f for two settings of T with $N_\mathrm{s} = 1$. In this Figure, we also show the non-robust quadratic cost function that would result from the outlier free assumption. The problem we are facing now is to find the minimum of the cost function. The number of groups N_s is unknown a priori, it needs be estimated as well, and the cost function has local minima which make it a difficult function to optimize. To find the global maximum and the number of groups we propose a strategy based on RANSAC[32].

RANSAC is an algorithm which can be used to fit the parameters of a model to measurements in the presence of outliers. For a given parameter setting, residues to all measurements can be calculated. RANSAC aims to find the parameter setting which minimizes the number of outliers, meaning it minimizes the following cost function:

$$\rho_\mathrm{RANSAC}(r) = \begin{cases} 0 & \dfrac{r^2}{\sigma_z^2} \leq T \\ 1 & \dfrac{r^2}{\sigma_z^2} > T \end{cases} \tag{2.57}$$

the threshold T decides whether a measurement with residue r should be classified as inlier or outlier. The approach to minimize the RANSAC cost function is based on the random sampling of a large number of subsets from the complete measurement set. The size of each sampled subset $N_{\mathcal{S},\min}$ is chosen to be as small as the minimum number of measurements required to obtain a fit to the model. Suppose the measurements participating in the set are given by $\mathcal{S} = \left(i_1, \ldots, i_{N_{\mathcal{S},\min}}\right)$ then we obtain the model fit by solving for $\mathbf{x}$ from $\mathbf{z}_\mathcal{S} = h_\mathcal{S}(\mathbf{x})$. For every sampled set, the obtained parameters from the model fit are used to calculate residues on all measurements. Then the cost function ρ_RANSAC is applied to classify each of the residues and the result is summed. The first encountered set which has a cost lower than a predefined threshold or the set which has the lowest cost (i.e. has the most inliers) over all sampled sets after a maximum number of trials is chosen as the final set. This final set identifies the inliers and outliers in the data. The final inlier set can be used in a subsequent least squares optimization to find the robust parameter estimate of $\mathbf{x}$. Improved algorithms of the RANSAC algorithm have been proposed, such as the MLESAC[33] and MAPSAC[34] algorithms by using different cost functions.

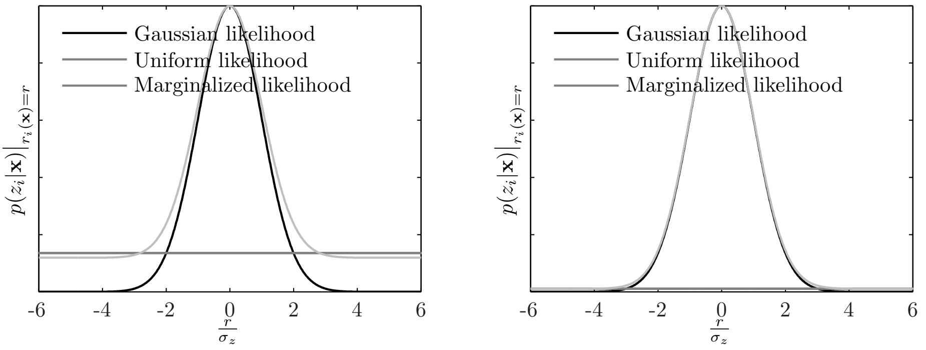

(a) Likelihood functions with $T = 2^2$ **(b)** Likelihood functions with $T = 3^2$

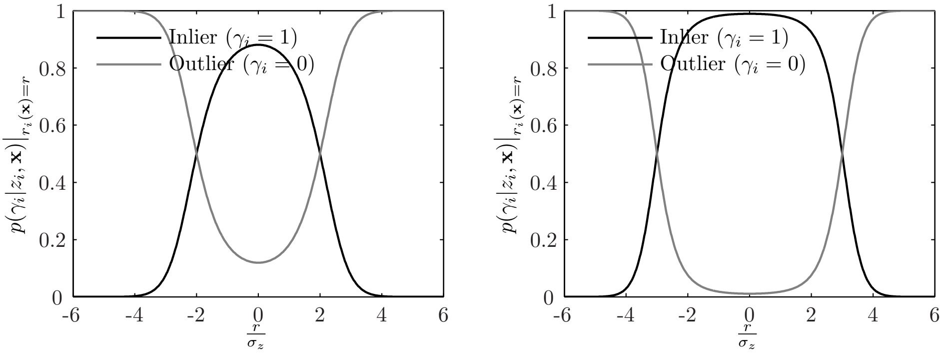

(c) Probability of inlier/outlier with $T = 2^2$ **(d)** Probability of inlier/outlier with $T = 3^2$

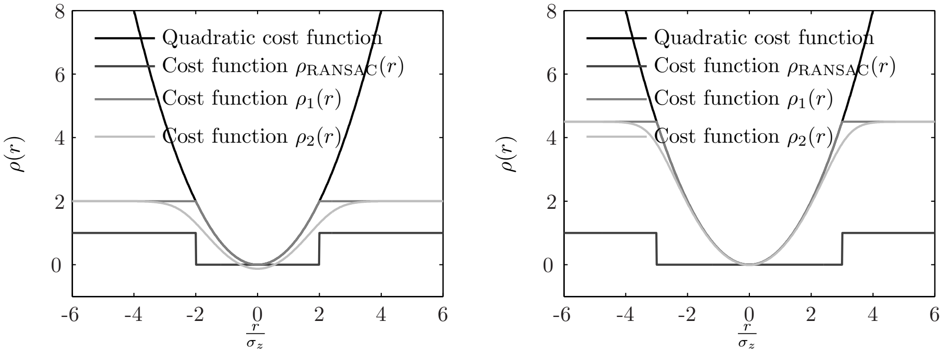

(e) Cost functions with $T = 2^2$ **(f)** Cost functions with $T = 3^2$

Figure 2.9 A two class case with $N_\text{s} = 1$. Illustration of the robust likelihoods, inlier/outlier probabilities and robust cost functions for two different settings of $T = -2\log\left[\frac{\sqrt{2\pi}\sigma_z}{v}\right]$. The distributions and functions are a function of the residue r normalized by the standard deviation σ_z.

To find the number of groups N_s and the global minimum of $C(\mathcal{X})$ we propose to use an incremental procedure, where in each iteration the number of groups N_s is incremented by one, until we find no new groups anymore. We start by setting the number of groups to $N_\mathrm{s} = 1$ and find the global minimum of the resulting cost function $C(\mathcal{X}) = C(\mathbf{x}_1)$ using a RANSAC based approach. In the next iteration N_s is incremented and we have to find the global minimum of $C(\mathcal{X}) = C(\mathbf{x}_1, \mathbf{x}_2)$. We can get very close to this global minimum by using $\hat{\mathbf{x}}_1$ obtained from the previous iteration and minimizing $C(\hat{\mathbf{x}}_1, \mathbf{x}_2)$ only for $\mathbf{x}_2$ using a RANSAC based approach. The global minimum can then be found by minimizing the function with respect to the complete parameter vector $\mathcal{X}$ where we use as an initial estimate the outcome of the RANSAC based approach. This procedure of incrementing N_s can be iterated until there is reason to believe that there are only outliers left in the data set. Some necessary relations that are used in the proposed method are outlined in the next part of the section. An overview of the complete algorithm in pseudo code is given at the end of the section in Figure 2.10.

We will now discuss how we can minimize the cost functions $C_1(\mathcal{X})$ and $C_2(\mathcal{X})$, starting from an initial estimate $\hat{\mathcal{X}}^{(1)}$ in the neighborhood of the minimum. For both cost functions, we will derive a weighted least squares cost function having the form of:

$$Q(\mathcal{X}, \hat{\mathcal{X}}^{(1)}) = \sum_{k=1}^{N_\mathrm{s}} \sum_{i=1}^{N} r_i^2(\mathbf{x}_k) w_{i,k}(\hat{\mathcal{X}}^{(1)}) \tag{2.58}$$

where the difference between minimizing $C_1(\mathcal{X})$ and $C_2(\mathcal{X})$ can be found in the weight function $w_{i,k}(\hat{\mathcal{X}}^{(1)})$. The weight function is dependent on the initial estimate and can be recalculated each time a new estimate has been found from minimizing $Q(\mathcal{X}, \hat{\mathcal{X}})$. From this equation it can be seen that for each group k the minimum of Q can be found independently on the other groups, by minimizing the sum of squared residuals. Suppose we want to find the minimum at the j^{th} iteration. The minimum can be found by equating the gradient of the cost function to zero and solving the resulting system of equations, for the k^{th} group we get for the gradient of the cost function:

$$\frac{\partial Q}{\partial \mathbf{x}_k} = 2 \sum_{i=1}^{N} \frac{\partial r_{i,k}}{\partial \mathbf{x}_k} r_i(\mathbf{x}_k) w_{i,k}(\hat{\mathbf{x}}^{(j)}) \tag{2.59}$$

When the residue function is a linear function of the parameters a closed form solution can be found by solving the linear system of equations:

$$\mathbf{H}_k^T \mathbf{W}_k^{(j)} \mathbf{H}_k \mathbf{x}_k = \mathbf{H}_k^T \mathbf{W}_k^{(j)} \mathbf{z} \tag{2.60}$$

where $\mathbf{H}_k$ is the Jacobian matrix:

$$\mathbf{H}_k = \begin{bmatrix} \left(\frac{\partial r_{1,k}}{\partial \mathbf{x}_k} \right)^T \\ \vdots \\ \left(\frac{\partial r_{N,k}}{\partial \mathbf{x}_k} \right)^T \end{bmatrix} \tag{2.61}$$

and $\mathbf{W}_k^{(j)}$ a diagonal weight matrix:

$$\mathbf{W}_k^{(j)} = \operatorname{diag}\left(w_{1,k}(\hat{\mathcal{X}}^{(j)}), \ldots, w_{N,k}(\hat{\mathcal{X}}^{(j)})\right) \tag{2.62}$$

The closed form solution of the minimum $\hat{\mathbf{x}}_k^{(j+1)}$ of Q is then given by:

$$\hat{\mathbf{x}}_k^{(j+1)} = (\mathbf{H}_k^T \mathbf{W}_k^{(j)} \mathbf{H}_k)^{-1} \mathbf{H}_k^T \mathbf{W}_k^{(j)} \mathbf{z} \tag{2.63}$$

We will now discuss how to obtain the weight function $w_{i,k}(\hat{\mathcal{X}})$. For the cost function $C_1(\mathcal{X})$, when looking at $\rho_2(\mathbf{r}_i)$, we see that for every measurement z_i that only the group k (if any) which has $k = k_{\min}$ and a residue smaller than the threshold T will be of influence and have a weight of one. All groups having a higher residue will have a weight of zero. If we use the result of the previous iteration, $\hat{\mathcal{X}}$ to calculate this threshold T and $k_{\min}$, we get the following weight function:

$$w_{i,k}(\hat{\mathcal{X}}) = \begin{cases} 1 & \text{if } k = k_{\min} \text{ and } \dfrac{r_i^2(\hat{\mathbf{x}}_k)}{\sigma_z^2} < T \\ & \\ 0 & \text{otherwise} \end{cases} \tag{2.64}$$

The marginal likelihood function, with cost function $C_2(\mathcal{X})$ is difficult to optimize, it is a non-convex function. An efficient way to maximize a marginal likelihood function, like the one in our problem, is to use the Expectation Maximization (EM) algorithm. The EM algorithm treats the marginalized variable ($\boldsymbol{\gamma}$ in our case) as an unobserved random variable, whose probability function can be calculated from the observations $\mathbf{z}$ and a guess of the parameter vector $\hat{\mathcal{X}}$. Then the expectation of the likelihood with respect to the unobserved variable is taken. The resulting expression, which is much easier to maximize then the marginal likelihood, is maximized. A useful property of the EM algorithm is that the cost is guaranteed to decrease in every iteration, until a stationary point (local minimum) of the cost function is reached. We will now see how applying the EM algorithm will give us the necessary weight to optimize C_2. We start by calculating the expectation of the log likelihood with respect to the unobserved variable $\boldsymbol{\gamma}$:

$$\begin{aligned} Q_2'(\mathcal{X}, \hat{\mathcal{X}}) &= \mathrm{E}_{\boldsymbol{\gamma}|\mathbf{z},\hat{\mathcal{X}}}\Big[\log\left[p(\mathbf{z}, \boldsymbol{\gamma}|\mathcal{X})\right]\Big] = \sum_{\boldsymbol{\gamma}\in\boldsymbol{\Gamma}} \log\left[p(\mathbf{z}, \boldsymbol{\gamma}|\mathcal{X})\right] p(\boldsymbol{\gamma}|\mathbf{z}, \hat{\mathcal{X}}) && (2.65) \\ &= \sum_{i=1}^{N} \sum_{\gamma_i=0}^{N_\mathrm{s}} \Big(\log\left[p(z_i, \gamma_i|\mathcal{X})\right] p(\gamma_i|z_i, \hat{\mathcal{X}})\Big) && (2.66) \end{aligned}$$

By using the relation $p(z_i, \gamma_i|\mathcal{X}) = p(z_i|\gamma_i, \mathcal{X})p(\gamma_i|\mathcal{X})$, dropping constant terms not dependent on $\mathcal{X}$ or $\hat{\mathcal{X}}$ and taking the negative of the function, we get the equivalent function suitable for minimization:

$$Q_2(\mathcal{X}, \hat{\mathcal{X}}) = \sum_{i=1}^{N} \sum_{k=1}^{N_\mathrm{s}} r_i^2(\mathbf{x}_k) p(\gamma_i = k|z_i, \hat{\mathcal{X}}) \tag{2.67}$$

from which we can identify the weight function resulting from the EM algorithm:

$$w_{i,k}(\hat{\mathcal{X}}) = p(\gamma_i = k|z_i, \hat{\mathcal{X}}) = \frac{e^{-\frac{1}{2}\frac{r_i^2(\hat{\mathbf{x}}_k)}{\sigma_z^2}}}{\sum_{k'=1}^{N_\mathrm{s}} e^{-\frac{1}{2}\frac{r_i^2(\hat{\mathbf{x}}_{k'})}{\sigma_z^2}} + \frac{\sqrt{2\pi}\sigma_z}{v}} \tag{2.68}$$

With these two different implementations of the weight function $w_{i,k}(\hat{\mathcal{X}})$, (2.64) and (2.68), we can perform one step of the iteration in the minimization process of C_1 or C_2 respectively as shown in (2.63). The Jacobian matrix needed in the iteration, belonging to the second order polynomial function $h(\mathbf{x}_k)$, is in our case simply calculated as:

$$\mathbf{H}_k = \begin{bmatrix} s_1^2 & s_1 & 1 \\ \vdots & \vdots & \vdots \\ s_N^2 & s_N & 1 \end{bmatrix} \tag{2.69}$$

A useful quantity to define for the algorithm is the expected number of measurements in a certain class. The expected number of measurements in class k, given the estimated parameter setting $\hat{\mathcal{X}}$ can be calculated as:

$$\hat{N}_k = \mathrm{E}_{\boldsymbol{\gamma}|\mathbf{z},\hat{\mathcal{X}}}\left[\sum_{i=1}^{N} I_k(\gamma_i)\right] = \sum_{i=1}^{N} p(\gamma_i = k|z_i, \hat{\mathcal{X}}) = \sum_{i=1}^{N} w_{i,k}(\hat{\mathcal{X}}) \tag{2.70}$$

The number of outliers, including the measurements which have not been assigned to a certain photoacoustic point source, can then be calculated from $\hat{N}_0$. To guide the sampling procedure in the RANSAC algorithm, we can sample new measurements in a subsequent iteration in a weighted manner, using $\hat{\mathcal{X}}$ from the previous iteration. The probability of sampling the i^{th} measurement, $p(i)$, will then be according to:

$$p(i) = \frac{p(\gamma_i = 0|z_i, \hat{\mathcal{X}})}{\hat{N}_0} \tag{2.71}$$

This ensures that measurements which are not yet likely to be classified as part of an photoacoustic point source group get a higher probability to be selected as model fit candidates in the RANSAC algorithm.

RANSAC is a random procedure with random outcomes. In order to guarantee with a certain probability ϵ that we have found a solution after a limited number of trials, we can calculate the expected number of minimal trials to ensure this probability[32]:

$$\hat{N}_{\mathrm{trials,min}} = \left\lceil \frac{\log(1-\epsilon)}{\log\left(1 - \left(\frac{N_{\mathrm{target}}}{\hat{N}_0}\right)^{N_{\mathcal{S},\mathrm{min}}}\right)} \right\rceil \tag{2.72}$$

Here N_{target} is the number of measurements we would like to be part of the new group and $N_{\mathcal{S},\mathrm{min}}$ is the minimal set size needed to find a fit to the model.

In our case the minimal set size is $N_{\mathcal{S},\min} = 3$ and finding a model fit for a minimal set $\mathcal{S} = (i_1, i_2, i_3)$ is done via:

$$\mathbf{x} = \mathbf{H}_{\mathcal{S}}^{-1}\mathbf{z}_{\mathcal{S}} \quad \text{with} \quad \mathbf{H}_{\mathcal{S}} = \begin{bmatrix} s_{i_1}^2 & s_{i_1} & 1 \\ s_{i_2}^2 & s_{i_2} & 1 \\ s_{i_3}^2 & s_{i_3} & 1 \end{bmatrix} \tag{2.73}$$

Care should be taken because not all combinations of measurements can be used to find an initial parameter estimate. All measurements should come from different sensors, otherwise the matrix $\mathbf{H}_S$ becomes singular and no unique solution exists. Therefore we introduce a degeneracy constraint which states that only sets in which all measurements come from different sensors are valid to be used in the RANSAC procedure:

$$s_{i_1} \neq s_{i_2} \wedge s_{i_1} \neq s_{i_3} \wedge s_{i_2} \neq s_{i_3} \tag{2.74}$$

The resulting algorithm is displayed in Figure 2.10 in pseudo code. The output of the algorithm is the estimated number of sources $\hat{N}_\text{s}$ and the set $\hat{\mathcal{X}}$ consisting of the estimated source parameters $\left(\hat{\mathbf{x}}_1, \ldots, \hat{\mathbf{x}}_{\hat{N}_\text{s}}\right)$. This set is the global maximum of the likelihood $\hat{\mathcal{X}} = \arg\max_{\mathcal{X}} p(\mathbf{z}|\mathcal{X})$. By using this estimate, the classification of a measurement z_i to a class $k \in \{1, \ldots, \hat{N}_\text{s}\}$ can be calculated with the probability measure $p(\gamma_i = k|z_i, \hat{\mathcal{X}})$.

2.3.3 Estimating speed of sound and source positions

From the previous step, we have estimated the number of sources $\hat{N}_\text{s}$ and the classification probability of each measurement into the source classes. We will now continue by showing how to use these results in the calibration procedure.

Reference measurement

In the reference measurement, we want to estimate the speed of sound c and the positions of the $\hat{N}_\text{s}$ passive elements $\mathcal{P} = \left(\mathbf{p}_{\text{s},1}, \ldots, \mathbf{p}_{\text{s},\hat{N}_\text{s}}\right)$. To solve this estimation problem, we setup a likelihood function of these parameters given the measurements, $p(\mathbf{z}|c, \mathcal{P})$, and will use the maximum of this likelihood function as the estimate of our parameters. This likelihood function is very similar to the likelihood function used in the previous step, the only difference is that we change the measurement function h_i from a polynomial function with linear parameters to a function of c and $\mathbf{p}_k$ with non-linear parameters. It could be that in the previous step, we have found an apparent source k which can be well described with a polynomial function, but in fact is not related to a physical photoacoustic point source. In that case, fitting a model using c and $\mathbf{p}_k$ to all of the measurements classified to the apparent source will fail. These apparent sources have to be identified and can be removed in this step of the algorithm, we will come back to this later. Now given the speed of sound and the source position, the residue of the i^{th} measurement assuming membership of the k^{th} class is $r_i(c, \mathbf{p}_k) = h_i(c, \mathbf{p}_k) - z_i$ and the measurement function is given by:

$$h_i(c, \mathbf{p}_k) = \frac{1}{c} \left\| \mathbf{p}_{\text{d},s_i} - \mathbf{p}_k \right\| \tag{2.75}$$

Algorithm Grouping measurements per rotation

```
Initialize by setting $N_{\mathrm{target}} = N_{\mathrm{d}}$, $\hat{N}_{\mathrm{s}} = 0$ and $\hat{\mathcal{X}} = ()$
While $N_{\mathrm{target}}$ is at or above threshold
  Set $k = \hat{N}_{\mathrm{s}} + 1$
  Calculate total number of trials $\hat{N}_{\mathrm{trials,min}}$ using (2.72)
  For $N_{\mathrm{trials}} = 1$ to $\hat{N}_{\mathrm{trials,min}}$
    Sample a minimal set $\mathcal{S}$ of $N_{\mathcal{S},\mathrm{min}}$ measurements, weighted according
     to (2.71) and conform the degeneracy constraint (2.74)
    Estimate model parameters $\hat{\mathbf{x}}_k^{(1)}$ by fitting the minimal set $\mathcal{S}$
     to the model using (2.73)
    Evaluate cost $C_2(\hat{\mathcal{X}}, \hat{\mathbf{x}}_k^{(1)})$ using (2.55)
    If cost is lowest so far
      Calculate local minimum $\hat{\mathbf{x}}_k^{(\mathrm{end})}$ from starting point
      $\left(\hat{\mathcal{X}}, \hat{\mathbf{x}}_k^{(1)}\right)$ via iterations of (2.63) using weights from (2.68)
      Calculate local minimum $\hat{\mathcal{X}}_{\mathrm{best}} = \left(\hat{\mathbf{x}}_1^{(\mathrm{end})}, \ldots, \hat{\mathbf{x}}_k^{(\mathrm{end})}\right)$ from starting
       point $\left(\hat{\mathcal{X}}, \hat{\mathbf{x}}_k^{(\mathrm{end})}\right)$ via iterations of (2.63) using weights from (2.68)
       for all $k \in \{1, \ldots, \hat{N}_{\mathrm{s}}\}$
      Set lowest cost to $C_2(\hat{\mathcal{X}}_{\mathrm{best}})$
      Recalculate $\hat{N}_k$ using (2.70)
    End if
    If reached maximum number of trials and $\hat{N}_k < N_{\mathrm{target}}$
      Decrease $N_{\mathrm{target}}$ by one
      If $N_{\mathrm{target}}$ is below threshold
        Stop the algorithm
      End if
      Recalculate $\hat{N}_{\mathrm{trials,min}}$ using (2.72)
    End if
  End for
  Set $\hat{\mathcal{X}} = \hat{\mathcal{X}}_{\mathrm{best}}$
  Increment $\hat{N}_{\mathrm{s}}$ by one
  Calculate number of unassigned measurements $\hat{N}_0$ using (2.70)
  If $\hat{N}_0 < N_{\mathrm{target}}$
    Set $N_{\mathrm{target}} = \lfloor \hat{N}_0 \rfloor$
  End if
End while
```

Figure 2.10 The measurement grouping algorithm

The likelihood function given a measurement z_i is then:

$$p(z_i|c, \mathcal{P}) = \frac{1}{(\hat{N}_{\mathrm{s}} + 1)\sqrt{2\pi}\sigma_z} \left(\sum_{k=1}^{\hat{N}_{\mathrm{s}}} e^{-\frac{1}{2}\frac{r_i^2(c, \mathbf{p}_{\mathrm{s},k})}{\sigma_z^2}} + \frac{\sqrt{2\pi}\sigma_z}{v} \right) \tag{2.76}$$

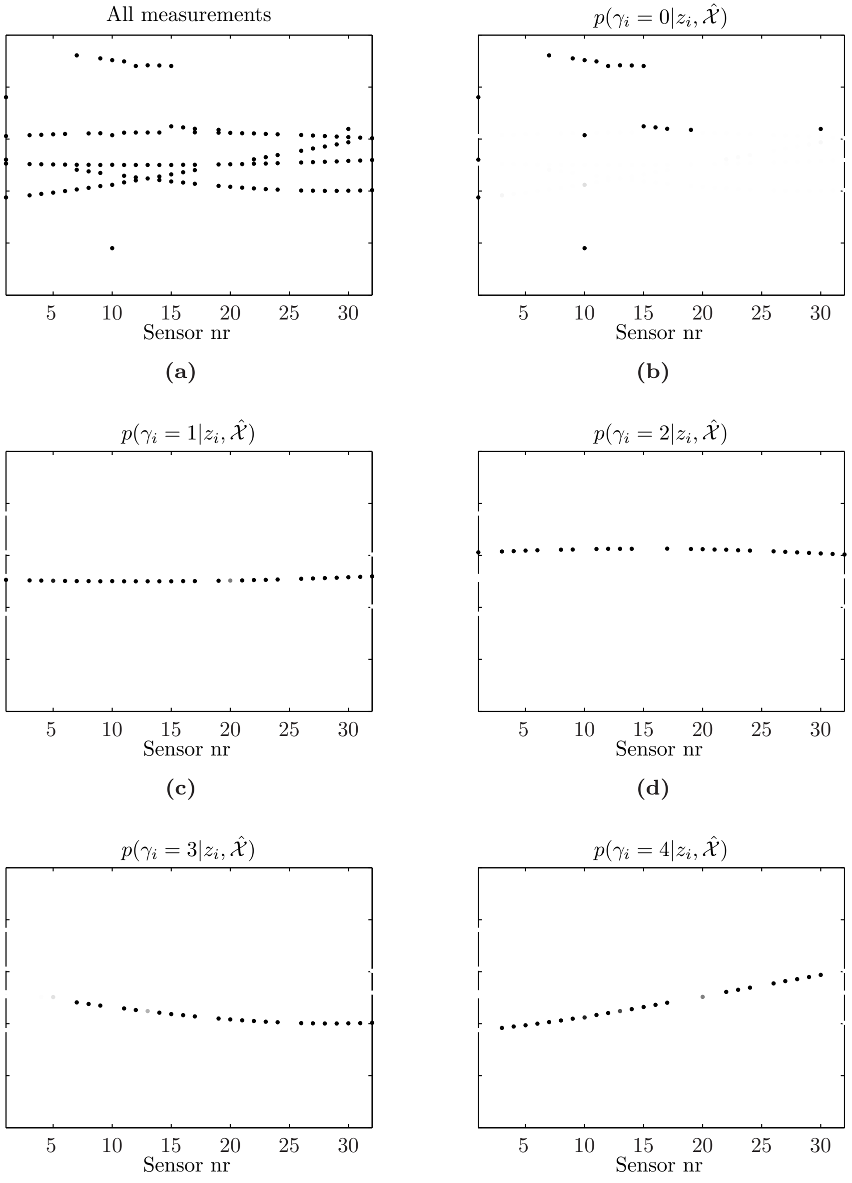

(a) **(b)** **(c)** **(d)** **(e)** **(f)**

Figure 2.11 Example of classification results of the grouping per rotation algorithm. (a) Shows all measurements for a given rotation. The figures (b)-(f) show the probability (intensity coded) of a measurement belonging to that particular class.

The combined likelihood, involving all measurements, is the product of this likelihood function over all measurements. Maximizing the combined likelihood can be done efficiently with the EM-algorithm, which requires an initial estimate of the parameters c and $\mathcal{P}$ to perform the first E-step of the algorithm. This initial estimate is necessary to calculate the probability distribution of the marginalized variable $\boldsymbol{\gamma}$. Instead of calculating this probability distribution given an initial estimate of c and $\mathcal{P}$, we can do a better job by calculating the distribution of $\boldsymbol{\gamma}$ with respect to the final estimate of the polynomial source parameters $\hat{\mathcal{X}}$. We have seen that the polynomial function $h_i(\mathbf{x}_k)$ models the data quite well, meaning that the probability $p(\boldsymbol{\gamma}|\mathbf{z}, \hat{c}, \hat{\mathcal{P}})$ can also be predicted quite well from $p(\boldsymbol{\gamma}|\mathbf{z}, \hat{\mathcal{X}})$. To initialize the EM-algorithm, we will start by finding:

$$\begin{aligned}\left(\hat{c}^{(1)}, \hat{\mathcal{P}}^{(1)}\right) &= \arg\max_{c,\mathcal{P}} \mathrm{E}_{\boldsymbol{\gamma}|\mathbf{z},\hat{\mathcal{X}}}\left[\log\left[p(\mathbf{z}, \boldsymbol{\gamma}|c, \mathcal{P})\right]\right] && (2.77)\\ &= \arg\min_{c,\mathcal{P}} Q(c, \mathcal{P}, \hat{\mathcal{X}}) && (2.78)\end{aligned}$$

where the Q function, or the first E-step of the EM algorithm, is given by:

$$Q(c, \mathcal{P}, \hat{\mathcal{X}}) = \sum_{i=1}^{N}\sum_{k=1}^{\hat{N}_\mathrm{s}} r_i^2(c, \mathbf{p}_k) w_{i,k}(\hat{\mathcal{X}}) \tag{2.79}$$

Once this function is minimized, we can start the EM-algorithm by iteratively minimizing the Q function of the E-step, starting from the initially obtained minimum $\hat{c}^{(1)}$ and $\hat{\mathcal{P}}^{(1)}$:

$$\begin{aligned}\left(\hat{c}^{(j+1)}, \hat{\mathcal{P}}^{(j+1))}\right) &= \arg\max_{c,\mathcal{P}} \mathrm{E}_{\boldsymbol{\gamma}|\mathbf{z},\hat{c}^{(j)},\hat{\mathcal{P}}^{(j)}}\left[\log\left[p(\mathbf{z}, \boldsymbol{\gamma}|c, \mathcal{P})\right]\right] && (2.80)\\ &= \arg\min_{c,\mathcal{P}} Q(c, \mathcal{P}, \hat{c}^{(j)}, \hat{\mathcal{P}}^{(j)}) && (2.81)\end{aligned}$$

where the Q function, obtained with the E-step of the EM algorithm, is given by:

$$Q(c, \mathcal{P}, \hat{c}, \hat{\mathcal{P}}) = \sum_{i=1}^{N}\sum_{k=1}^{\hat{N}_\mathrm{s}} r_i^2(c, \mathbf{p}_k) w_{i,k}(\hat{c}, \hat{\mathcal{P}}) \tag{2.82}$$

The weight function used here, $w_{i,k}(c, \hat{\mathcal{P}})$, is very similar to the weight function used in the classification step $w_{i,k}(\hat{\mathcal{X}})$. Instead of using the residues of the polynomial function the residues of the measurement function with parameters $\hat{c}$ and $\hat{\mathcal{P}}$ is used:

$$w_{i,k}(\hat{c}, \hat{\mathcal{P}}) = \frac{e^{-\frac{1}{2}\frac{r_i^2(\hat{c},\hat{\mathbf{p}}_k)}{\sigma_z^2}}}{\displaystyle\sum_{k'=1}^{\hat{N}_\mathrm{s}} e^{-\frac{1}{2}\frac{r_i^2(\hat{c},\hat{\mathbf{p}}_{k'})}{\sigma_z^2}} + \frac{\sqrt{2\pi}\sigma_z}{v}} \tag{2.83}$$

The M-step of the EM-algorithm now comes down to finding the weighted nonlinear least squares fit for the parameters $\mathbf{x} = \big(c, \mathcal{P}\big)$. When an initial estimate $\mathbf{x}^{(1)}$ is available which is already somewhere close to the minimum, the Gauss-Newton method[35] is the best method, with respect to convergence speed, to solve the minimization problem. In the first iteration of the EM-algorithm however, we have no initial estimate close to the expected minimum. Not much is known on the positions of the sources, $\mathcal{P}$, and only a rough guess is available. A better initial guess can be found for the speed of sound c, which is expected to be somewhere near 1500 m/s. Therefore we propose to start with optimizing a problem of reduced complexity by considering the speed of sound fixed at 1500 m/s and solving only for the source positions. The reduced problem can also be solved with the Gauss-Newton method. The hereby obtained source positions will be used in a subsequent step and optimized together with the speed of sound using the Gauss-Newton method. In order to use the Gauss-Newton method, we need to calculate the Jacobian matrix of the residue vector function, i.e., the function that returns for a given parameter $\mathbf{x}$ all $N \times \hat{N}_\mathrm{s}$ residues. We will define the residue vector function as $r'(\mathbf{x}) = \big(r'_1(c, \mathbf{p}_{\mathrm{s},1}), \ldots, r'_{\hat{N}_\mathrm{s}}(c, \mathbf{p}_{\mathrm{s},\hat{N}_\mathrm{s}})\big)$, where for each source k the residue vector is $r'_k(c, \mathbf{p}_{\mathrm{s},k}) = \big(r'_{1,k}(c, \mathbf{p}_{\mathrm{s},k}), \ldots, r'_{N,k}(c, \mathbf{p}_{\mathrm{s},k})\big)$ and for each source k and measurement i we have $r'_{i,k}(c, \mathbf{p}_{\mathrm{s},k}) = r_i(c, \mathbf{p}_{\mathrm{s},k})\sqrt{w_{i,k}}$. Minimizing the Q function is then equivalent to minimizing $\|r'(\mathbf{x})\|^2$. Constructing the Jacobian matrix of this function $r'(\mathbf{x})$ for a given estimate $\mathbf{x}^{(l)}$, where l is the iteration number of the Gauss-Newton method, is then according to:

$$\mathbf{H}^{(l)}_{c,k} = \begin{bmatrix} \frac{\partial}{\partial c} h^{(l)}_{1,k}\sqrt{w_{1,k}} \\ \vdots \\ \frac{\partial}{\partial c} h^{(l)}_{N,k}\sqrt{w_{N,k}} \end{bmatrix} \quad \mathbf{H}^{(l)}_{\mathbf{p}_k} = \begin{bmatrix} \left(\frac{\partial}{\partial \mathbf{p}_{\mathrm{s},k}} h^{(l)}_{1,k}\right)^T \sqrt{w_{1,k}} \\ \vdots \\ \left(\frac{\partial}{\partial \mathbf{p}_{\mathrm{s},k}} h^{(l)}_{N,k}\right)^T \sqrt{w_{N,k}} \end{bmatrix}$$

$$\mathbf{H}^{(l)} = \begin{bmatrix} \mathbf{H}^{(l)}_{c,1} & \mathbf{H}^{(l)}_{\mathbf{p}_1} & & \\ \vdots & & \ddots & \\ \mathbf{H}^{(l)}_{c,\hat{N}_\mathrm{s}} & & & \mathbf{H}^{(l)}_{\mathbf{p}_{\hat{N}_\mathrm{s}}} \end{bmatrix} \tag{2.84}$$

where the partial derivatives are given by:

$$\frac{\partial}{\partial c} h^{(l)}_{i,k} = \frac{-1}{c^{(l)}} h_i\left(c^{(l)}, \mathbf{p}^{(l)}_{\mathrm{s},k}\right) \tag{2.85}$$

$$\frac{\partial}{\partial \mathbf{p}_{\mathrm{s},k}} h^{(l)}_{i,k} = \left(\mathbf{p}^{(l)}_{\mathrm{s},k} - \mathbf{p}_{\mathrm{d},s_i}\right) \frac{1}{\left(c^{(l)}\right)^2 h_i\left(c^{(l)}, \mathbf{p}^{(l)}_{\mathrm{s},k}\right)} \tag{2.86}$$

and the weights can be obtained from the weight function and the estimate of the parameters in the j^{th} iteration of the EM-algorithm:

$$w_{i,k} = \begin{cases} w_{i,k}(\hat{\mathcal{X}}) & j = 0 \\ w_{i,k}(\hat{c}^{(j)}, \hat{\mathcal{P}}^{(j)}) & j > 0 \end{cases} \tag{2.87}$$

The Gauss-Newton iterations required to optimize the complete parameter vector $\mathbf{x}$ in a given iteration of the EM-algorithm are given by:

$$\hat{\mathbf{x}}^{(l+1)} = \hat{\mathbf{x}}^{(l)} - \left(\mathbf{H}^{(l)T}\mathbf{H}^{(l)}\right)^{-1}\mathbf{H}^{(l)T} r'(\hat{\mathbf{x}}^{(l)}) \tag{2.88}$$

and the Gauss-Newton iterations required to optimize the source position of source k given an initial guess of the speed of sound $c = 1500$ m/s are given by:

$$\hat{\mathbf{p}}_{\mathrm{s},k}^{(l+1)} = \hat{\mathbf{p}}_{\mathrm{s},k}^{(l)} - \left(\mathbf{H}_{\mathbf{p}_k}^{(l)T}\mathbf{H}_{\mathbf{p}_k}^{(l)}\right)^{-1}\mathbf{H}_{\mathbf{p}_k}^{(l)T} r'_k(1500, \hat{\mathbf{p}}_{\mathrm{s},k}^{(l)}) \tag{2.89}$$

As mentioned before, the data could obtain apparent sources. An apparent source is a set of measurement points that can be well described with a polynomial function but does in fact not represent a physical source. We can identify these cases by investigating how well the model $h_i(c, \mathbf{p}_k)$ fits the class measurements. A measure used before to quantify the model fit was the expected number of measurements in a class k, we will use this measure here again, which is now defined as:

$$\hat{N}_k^{(j)} = \mathrm{E}_{\boldsymbol{\gamma}|\mathbf{z},\hat{c}^{(j)},\hat{\mathcal{P}}^{(j)}}\left[\sum_{i=1}^{N} I_k(\gamma_i)\right] = \sum_{i=1}^{N} w_{i,k}(\hat{c}^{(j)}, \hat{\mathcal{P}}^{(j)}) \tag{2.90}$$

When the expected number of measurements in a class are below a threshold, we will remove the corresponding source from the estimation procedure.

The final algorithm to estimate speed of sound c and source positions $\mathcal{P}$ from measurements $\mathbf{z}$, an estimated number of sources $\hat{N}_\mathrm{s}$ and a grouping of measurements into sources described by $\hat{\mathcal{X}}$ is given in Figure 2.12. An example of a reference measurement calibration on a setup with 9 photoacoustic point sources is displayed in Figure 2.13.

Calibration measurement

In the calibration measurement, the goal is to estimate the speed of sound c and center of rotation $\mathbf{T}$ from time of flight measurements $\mathbf{z}$. To accomplish this, a calibration phantom with a number of sources is used. To make the optimization procedure feasible, the positions of the sources in the phantom are added to the optimization problem as unknown parameters. Directly estimating all these parameters without a good initial estimate is not possible due to the many local minima present in the optimization problem. We will discuss here first the task of estimating the relative source positions in each rotation and the speed of sound. In the previous step we have handled all rotations $R \in \{1, \ldots, N_\mathrm{R}\}$ separately. For each rotation we have estimated the number of sources visible in that rotation, $\hat{N}_{\mathrm{s},R}$, and a set of polynomial parameters $\hat{\mathcal{X}}_R = \left(\hat{\mathbf{x}}_1, \ldots, \hat{\mathbf{x}}_{\hat{N}_{\mathrm{s},R}}\right)$ which identify the measurements belonging to each particular source. In this step we will combine the measurements of all rotations and aim to estimate the global speed of sound and relative source positions in each rotation. To each source from each rotation, we assign a unique number and use an indicator variable γ'_i to indicate to which source number a measurement belongs. The

Algorithm Estimation of speed of sound and source positions

```
Set $j = 0$
For $k \in \{1, \ldots, \hat{N}_\mathrm{s}\}$
  Estimate $\hat{\mathbf{p}}_{\mathrm{s},k}$ using (2.89), starting from $\mathbf{p}_{\mathrm{s},k}^{(1)} = \mathbf{p}_{\mathrm{s,guess}}$
End for
Set $\big(\hat{c}^{(1)}, \hat{\mathcal{P}}^{(1)}\big) = \big(1500, \hat{\mathbf{p}}_{\mathrm{s},1}, \ldots, \hat{\mathbf{p}}_{\mathrm{s},\hat{N}_\mathrm{s}}\big)$
While $\big\|\big(\hat{c}^{(j)}, \hat{\mathcal{P}}^{(j)}\big) - \big(\hat{c}^{(j+1)}, \hat{\mathcal{P}}^{(j+1)}\big)\big\| > \epsilon$
  Increment $j$ by one
  Calculate weights using (2.83)
  Remove sources which have $\hat{N}_k^{(j)}$ below a threshold using (2.90)
  If sources have been removed
    Recalculate weights using (2.83)
  End if
  Estimate $\hat{\mathbf{x}}$ using (2.88), starting from $\mathbf{x}^{(1)} = \big(\hat{c}^{(j)}, \hat{\mathcal{P}}^{(j)}\big)$
  Set $\big(\hat{c}^{(j+1)}, \hat{\mathcal{P}}^{(j+1)}\big) = \hat{\mathbf{x}}$
End while
Set $\big(\hat{c}, \hat{\mathcal{P}}\big) = \big(\hat{c}^{(j+1)}, \hat{\mathcal{P}}^{(j+1)}\big)$
```

Figure 2.12 The speed of sound and source positions estimation algorithm

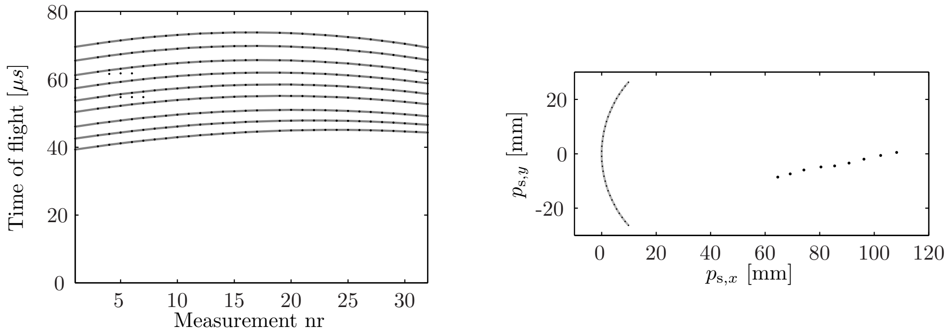

(a) Calibrated fit of the reference measurement model to the time of flight measurements

(b) Estimated source positions of the 9 photoacoustic point sources

Figure 2.13 Example of applying the estimation of speed of sound and source positions algorithm to a reference measurement. The reference measurement was obtained from a setting with 9 photoacoustic point sources.

total number of sources will then be $\hat{N}'_\mathrm{s} = \sum_{R=1}^{N_\mathrm{R}} \hat{N}_{\mathrm{s},R}$. The numbering of source numbers will be such that a group number $\gamma_i = k$ from the previous step, obtained in rotation number R_i, will map to the unique source number $\gamma'_i = k'_{R_i} + k$, where $k'_R = \sum_{R'=1}^{R-1} \hat{N}_{\mathrm{s},R'}$ is an offset number for the R^th rotation. We will stack the relative source positions in the set $\mathcal{P}' = \left(\mathbf{p}'_{\mathrm{s},1}, \ldots, \mathbf{p}'_{\mathrm{s},\hat{N}'_{\mathrm{s}}}\right)$ and use the complete set of source parameters $\hat{\mathcal{X}}' = \left(\hat{\mathcal{X}}_1, \ldots, \hat{\mathcal{X}}_{N_{\mathrm{R}}}\right)$. The information that will be associated to each measurement z_i, where $i \in \{1, \ldots, N \times N_{\mathrm{R}}\}$, in this step is displayed in Table 2.3. Formulating the marginalized likelihood of the global speed of sound c and relative source positions $\mathcal{P}'$ for the calibration measurement can be done in a similar way as finding speed of sound and source positions likelihood of the reference measurement. However, because measurements and sources are strictly related to a single rotation number, the prior distribution on γ_i is a bit different and the resulting marginalized likelihood function becomes:

Item	Domain	Description
z_i	$[t_{\min}, t_{\max}]$	Observed time of flight
s_i	$\{1, \ldots, N_{\mathrm{d}}\}$	Sensor that registered the measurement
R_i	$\{1, \ldots, N_{\mathrm{R}}\}$	Rotation number of this measurement
γ'_i	$\{0, \ldots, \hat{N}'_{\mathrm{s}}\}$	Source number responsible for this measurement

Table 2.3 Overview of the information that is related to each measurement z_i in the global speed of sound/relative position estimation used for the calibration measurement

$$p(z_i|c, \mathcal{P}') = \frac{1}{(\hat{N}_{\mathrm{s},R_i} + 1)\sqrt{2\pi}\sigma_z} \left(\sum_{k \in \mathcal{S}_{R_i}} e^{-\frac{1}{2}\frac{r_i^2(c, \mathbf{p}'_{\mathrm{s},k})}{\sigma_z^2}} + \frac{\sqrt{2\pi}\sigma_z}{v} \right) \tag{2.91}$$

where the set $\mathcal{S}_R = \{k'_R + 1, \ldots, k'_R + \hat{N}_{\mathrm{s},R}\}$ contains the source numbers associated to the rotation number R. Maximizing this likelihood can be done with a similar EM-algorithm as given in Figure 2.12. The only difference will be in the calculation of the weights $w_{i,k}$. The weights used when $j = 0$, i.e., the initialization of the EM-algorithm, are now given by:

$$w_{i,k}(\hat{\mathcal{X}}') = \begin{cases} w_{i,(k-k'_{R_i})}(\hat{\mathcal{X}}_{R_i}) & k \in \mathcal{S}_{R_i} \\ 0 & \text{otherwise} \end{cases} \tag{2.92}$$

and the weights used when $j > 0$ will be:

$$w_{i,k}(\hat{c}, \hat{\mathcal{P}}') = \begin{cases} w_{i,(k-k'_{R_i})}(\hat{c}, \hat{\mathcal{P}}_{R_i}) & k \in \mathcal{S}_{R_i} \\ 0 & \text{otherwise} \end{cases} \tag{2.93}$$

Using these definitions of the weights, we can use the algorithm described in Figure 2.12 to estimate $\hat{c}$ and $\hat{\mathcal{P}}'$. This gives us an intermediate results for the calibration measurement. In the next step we have to determine the absolute source positions and the number of sources by introducing the center of rotation as an extra parameter.

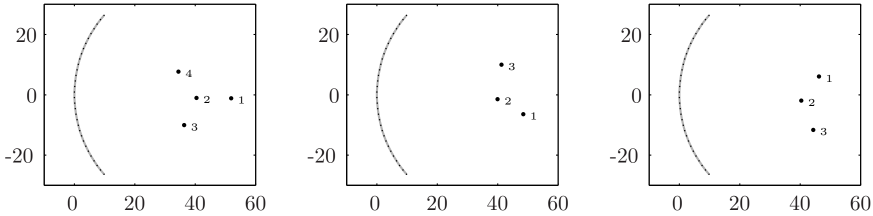

(a) Rotation 1 **(b)** Rotation 2 **(c)** Rotation 3

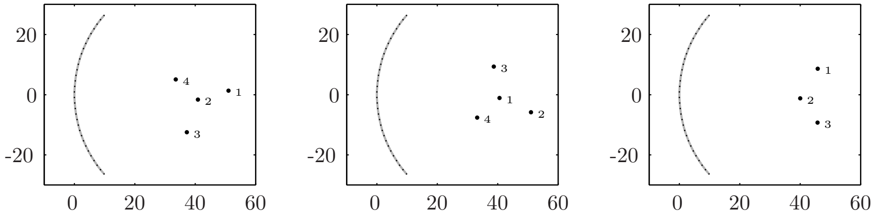

(d) Rotation 4 **(e)** Rotation 5 **(f)** Rotation 6

Figure 2.14 Example of applying the estimation of speed of sound and (relative) source positions algorithm to a calibration measurement. The calibration measurement was obtained from a calibration phantom consisting of 4 photoacoustic point sources. Each figure shows the estimated relative source position using measurements only from that individual rotation step.

Accuracy of calibration

To get an idea of the accuracy of the estimated parameters, we will now find an estimate of the covariance matrix $\mathbf{P_{xx}}$ of the estimated parameters. In the last iteration of the Gauss-Newton procedure in the M-step (2.88), we have linearized the relation between the estimated parameters $\hat{\mathbf{x}}$ and residuals r'. In terms of the weighted measurements $\mathbf{z}'$ this linearized relation is equivalently given by:

$$\begin{aligned} \hat{\mathbf{x}}^{(l+1)} &= \mathbf{b}^{(l)} + \left(\mathbf{H}^{(l)T}\mathbf{H}^{(l)}\right)^{-1}\mathbf{H}^{(l)T}\mathbf{z}' && (2.94) \\ &= \mathbf{b}^{(l)} + \mathbf{A}\mathbf{z}' && (2.95) \end{aligned}$$

where the weighted measurements are related to the observed measurements via $\mathbf{z}' = \mathbf{W}\mathbf{z}$ and the weight matrix is given by:

$$\mathbf{W} = \begin{bmatrix} \operatorname{diag}\left(\sqrt{w_{1,1}}, \ldots, \sqrt{w_{N,1}}\right) \\ \vdots \\ \operatorname{diag}\left(\sqrt{w_{1,\hat{N}_\mathrm{s}}}, \ldots, \sqrt{w_{N,\hat{N}_\mathrm{s}}}\right) \end{bmatrix} \tag{2.96}$$

From this linear transformation of the measurements with known covariance $\mathbf{P_{zz}} = \mathbf{I}\sigma_z^2$ we can obtain an estimate of the covariance matrix of the estimated parameters via:

$$\hat{\mathbf{P}}_{\mathbf{xx}} = \mathbf{A}\mathbf{W}\mathbf{P}_{\mathbf{zz}}\mathbf{W}^T\mathbf{A}^T = \mathbf{A}\mathbf{W}\mathbf{W}^T\mathbf{A}^T\sigma_w^2 \tag{2.97}$$

2.3.4 Estimating speed of sound and the center of rotation

In the calibration measurement, we need to estimate speed of sound and the center of rotation. From the previous step we have obtained a set of relative source positions $\hat{\mathcal{P}}'$ and an estimate of the speed of sound $\hat{c}$. Besides that, we also have an estimate of the covariance matrix describing the uncertainty of the estimated parameter vector. We will now continue by including the center of rotation in the estimate. First an initial guess is calculated based on the estimates from the previous step and finally this initial estimate is used in the optimization procedure of the complete likelihood function $p(\mathbf{z}|c, \mathbf{T}, \mathcal{P})$.

Initial guess

The approach used to find an initial guess is based on selecting pairs of relative source positions from different rotation steps, where the initial guess now consists of the center of rotation, the number of sources and the absolute source positions. Note that the number of sources cannot readily be taken from each of the individual rotation measurements, since not all sources might be visible or detected in every rotation.

The set of all pairs of relative sources from two different rotations is given by $\mathcal{S}_\mathrm{p} = \big\{\big(k_1 \in \mathcal{S}_{R_1}, k_2 \in \mathcal{S}_{R_2}\big) : R_1 \neq R_2\big\}$. Suppose that we are given a pair of relative source positions $\big(\hat{\mathbf{p}}'_{\mathrm{s},k_1}, \hat{\mathbf{p}}'_{\mathrm{s},k_2}\big)$ from two different rotations, i.e., $\big(k_1, k_2\big) \in \mathcal{S}_\mathrm{p}$. If these two relative source positions would belong to the same physical source, then we can estimate the absolute source position and the center of rotation from this pair of relative source positions. To do so, we notice that the relative source position $\mathbf{p}'_{\mathrm{s},k_1}$ is related to the absolute source position $\mathbf{p}_{\mathrm{s},k}$ and center of rotation $\mathbf{T}$ via the relation $\mathbf{p}'_{\mathrm{s},k_1} = \mathbf{R}_{\phi_{R_1}}\mathbf{p}_{\mathrm{s},k} + \mathbf{T}$. If we combine the information from the two relative source positions in the pair we get:

$$\begin{bmatrix}\mathbf{p}'_{\mathrm{s},k_1}\\ \mathbf{p}'_{\mathrm{s},k_2}\end{bmatrix} = \mathbf{A}\begin{bmatrix}\mathbf{p}_{\mathrm{s},k}\\ \mathbf{T}\end{bmatrix} \quad \text{with} \quad \mathbf{A} = \begin{bmatrix}\mathbf{R}_{\phi_{R_1}} & \mathbf{I}\\ \mathbf{R}_{\phi_{R_2}} & \mathbf{I}\end{bmatrix} \tag{2.98}$$

By inverting this relation we can find an estimate of the absolute source position and center of rotation from a pair of relative source positions observed in two different rotations:

$$\begin{bmatrix}\hat{\mathbf{p}}_{\mathrm{s},k}\\ \hat{\mathbf{T}}\end{bmatrix} = \mathbf{A}^{-1}\begin{bmatrix}\hat{\mathbf{p}}'_{\mathrm{s},k_1}\\ \hat{\mathbf{p}}'_{\mathrm{s},k_2}\end{bmatrix} \tag{2.99}$$

Furthermore we can calculate the uncertainty on the estimates $\mathbf{p}_{\mathrm{s},k}$ and $\mathbf{T}$ from the covariance matrix $\hat{\mathbf{P}}_{\mathbf{xx}}$. Therefore we have to extract the intersection of rows and columns associated to either $\mathbf{p}'_{\mathrm{s},k_1}$ or $\mathbf{p}'_{\mathrm{s},k_1}$, resulting in a 4×4 matrix $\mathbf{P}_{k_1,k_2}$. If we decompose the inverted matrix as $\mathbf{A}^{-1} = \begin{bmatrix}\mathbf{A}_\mathrm{p}\\ \mathbf{A}_\mathrm{T}\end{bmatrix}$. Then we can calculate an estimate of the uncertainty of the estimated center of rotation from the involved pair of relative source points using the covariance matrix of $\hat{\mathbf{T}}$:

$$\mathbf{P}_{\mathrm{T}} = \mathbf{A}_{\mathrm{T}} \mathbf{P}_{k_1,k_2} \mathbf{A}_{\mathrm{T}}^T \tag{2.100}$$

Once we have calculated for all possible pairs in $\mathcal{S}_{\mathrm{p}}$ the estimated source position and center of rotation, we can calculate the score of a certain hypothesized center of rotation $\mathbf{T}$. For each pair p we can calculate the squared Mahalanobilis distance:

$$d_p^2(\mathbf{T}) = \left(\hat{\mathbf{T}}_p - \mathbf{T}\right)^T \mathbf{P}_{\mathrm{T}_p}^{-1} \left(\hat{\mathbf{T}}_p - \mathbf{T}\right) \tag{2.101}$$

Now if the pair defined by p describes two relative source positions, both in different rotations, and both from the same physical source point, then we expect that, if the proposed center of rotation $\mathbf{T}$ is the true center of rotation, that the distance d_p^2 will be chi-squared distributed with two degrees of freedom, i.e., $d_p^2 \sim \chi_2^2$. By using the cumulative distribution function of this distribution, $F_{\chi_2^2}(x)$, we can calculate a score $c_p = 1 - F_{\chi_2^2}(d_p^2)$ which gives us a number between 0 and 1. The higher this score, the more likely is the estimated center of rotation, assuming the correspondence of the pair and the true center of rotation are correct. We now propose to find an initial estimate of the center of rotation $\hat{\mathbf{T}}$ using these scores and the calculated translation estimates according to:

$$\hat{\mathbf{T}} = \hat{\mathbf{T}}_{p_{\max}} \quad \text{with} \quad p_{\max} = \underset{p \in \mathcal{S}_{\mathrm{p}}}{\arg\max} \left(\sum_{p' \in \mathcal{S}_{\mathrm{p}}} c_{p'}(\hat{\mathbf{T}}_p) \right) \tag{2.102}$$

Next we setup a graph consisting of vertices representing the relative sources $\mathbf{p}'_{\mathrm{s},k}$. An edge will be created between every pair $p \in \mathcal{S}_{\mathrm{p}}$ of vertices which have a score of $c_p(\hat{\mathbf{T}}) > 0.01$. This means that pairs which are unlikely[2] to satisfy the hypothesis will not be connected. Clusters will then be identified by finding connected components in the graph. A connected component is a set of vertices in the graph which are all connected by paths, i.e., every vertex is connected with every other vertex via zero or more vertices in the set. Only sources which are visible in more than one rotation can be assumed to be part of the calibration phantom and will contribute information about the center of rotation, therefore we will only accept clusters which contain at least two vertices. Now the estimated number of sources in the calibration phantom $\hat{N}_{\mathrm{s}}$ is given by the number of accepted clusters. For each source we can calculate an initial estimate of that source position by averaging over the estimated source positions in the cluster:

$$\hat{\mathbf{p}}_{\mathrm{s},k} = \frac{1}{|\mathcal{C}_k|} \sum_{k' \in \mathcal{C}_k} \mathbf{R}_{\phi_{R_{k'}}}^T \left(\hat{\mathbf{p}}'_{\mathrm{s},k'} - \hat{\mathbf{T}}\right) \tag{2.103}$$

---

[2] By setting the threshold at 0.01 there is only a 1 percent probability of disconnecting a pair which does satisfy the hypothesis but has a lower score

```
**Algorithm** Obtaining an initial estimate for $\mathbf{T}$ and $\mathcal{P}$
For $p \in \mathcal{S}_\mathrm{p}$
  Estimate $\hat{\mathbf{T}}_p$ using (2.99)
  Calculate covariance matrix $\mathbf{P}_{T_p}$ using (2.100)
End for
For $p \in \mathcal{S}_\mathrm{p}$
  Calculate squared Mahalanobilis distances $d^2_{p'}(\hat{\mathbf{T}}_p)$ using (2.101)
   for all $p' \in \mathcal{S}_\mathrm{p}$
  Calculate corresponding scores $c_{p'}(\hat{\mathbf{T}}_p) = 1 - F_{\chi^2_2}\big(d^2_{p'}(\hat{\mathbf{T}}_p)\big)$
   for all $p' \in \mathcal{S}_\mathrm{p}$
End for
Find $\hat{\mathbf{T}}$ using (2.102)
Set $\hat{N}_\mathrm{s} = 0$
For $p \in \mathcal{S}_\mathrm{p}$
  If $c_p(\hat{\mathbf{T}}) > c_\mathrm{th}$
    If $k_1$ or $k_2$ is part of any of the existing clusters
      Inlcude $k_1$ and $k_2$ in the found cluster
    Else
      Increment $\hat{N}_\mathrm{s}$ by one
      Create new cluster $\mathcal{C}_{\hat{N}_\mathrm{s}} = \{k_1, k_2\}$
    End if
  End if
End for
For $k \in \{1, \ldots, \hat{N}_\mathrm{s}\}$
  Estimate $\hat{\mathbf{p}}_{\mathrm{s},k}$ using (2.103)
End for
```

Figure 2.15 The algorithm to obtain an initial estimate of the center of rotation $\mathbf{T}$ and the source positions $\mathcal{P}$

The resulting algorithm is described in pseudo code in Figure 2.15. To illustrate the steps in this algorithm, the calculated scores of each estimated center of rotation for an example measurement are displayed in Figure 2.17. The final clustering result of this example, based on creating graphs of connected components, is displayed in Figure 2.17.

Optimizing the complete likelihood function

Now given the initial estimates $\hat{c}$, $\hat{\mathbf{T}}$, $\hat{\mathcal{P}}$ and the number of sources $\hat{N}_\mathrm{s}$ obtained in the previous step, the final step comes down to actually minimizing the likelihood function $p(\mathbf{z}|c, \mathbf{T}, \mathcal{P})$ which gives us the calibration parameters. The measurement

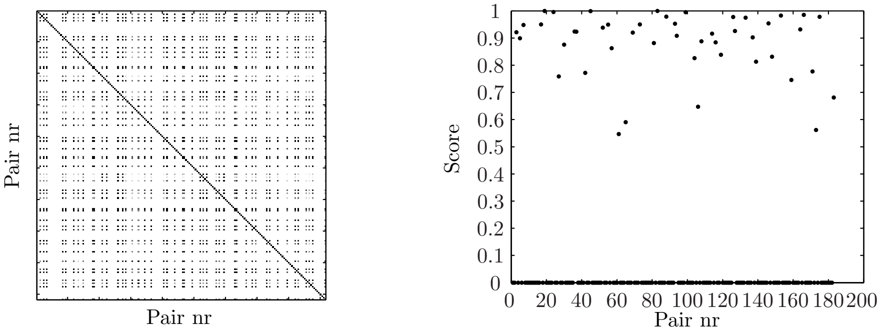

(a) Score matrix consisting of all combinations of possible pairs and the corresponding score c_p

(b) Scores of all possible pairs for the most supported estimated center of rotation

Figure 2.16 Example of score matrix and scores of the best estimated center of rotation for the calibration measurement with relative positions as shown in Figure 2.14 containing four photoacoustic point sources.

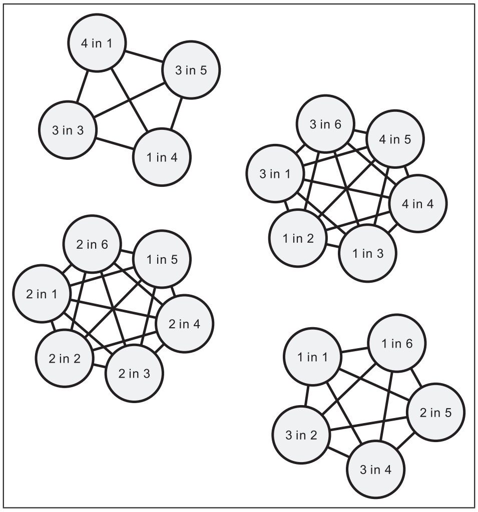

Figure 2.17 Example of connected components formed by applying the clustering operation from the algorithm in Figure 2.15 to the calibration measurement with relative positions as shown in Figure 2.14 containing four photoacoustic point sources. The numbering on the nodes refers to a hair number and a rotation number. The existence of an edge between two vertices means the score c_p of the corresponding pair of vertices is higher than the predefined threshold.

function that we use in setting up this likelihood function is given by:

$$h_i(c, \mathbf{T}, \mathbf{p}_{\mathrm{s},k}) = \frac{1}{c}\|\mathbf{p}_{\mathrm{d},s_i} - \mathbf{R}_{\phi_{R_i}}\mathbf{p}_{\mathrm{s},k} - \mathbf{T}\| \tag{2.104}$$

The residue function is then given by $r_i(c, \mathbf{T}, \mathbf{p}_{\mathrm{s},k}) = h_i(c, \mathbf{T}, \mathbf{p}_{\mathrm{s},k}) - z_i$ and the likelihood for an individual measurement z_i by:

$$p(z_i|c, \mathbf{T}, \mathcal{P}) = \frac{1}{(\hat{N}_\mathrm{s}+1)\sqrt{2\pi}\sigma_z}\left(\sum_{k=1}^{\hat{N}_\mathrm{s}} e^{-\frac{1}{2}\frac{r_i^2(c,\mathbf{T},\mathbf{p}_{\mathrm{s},k})}{\sigma_z^2}} + \frac{\sqrt{2\pi}\sigma_z}{v}\right) \tag{2.105}$$

Maximizing this likelihood requires a similar EM algorithm as implemented before and results in iteratively finding the minimum of the weighted non-linear least squares function Q:

$$Q(c, \mathbf{T}, \mathcal{P}, \hat{c}, \hat{\mathbf{T}}, \hat{\mathcal{P}}) = \sum_{i=1}^{N}\sum_{k=1}^{N_\mathrm{s}} r_i^2(c, \mathbf{T}, \mathbf{p}_{\mathrm{s},k}) w_{i,k}(\hat{c}, \hat{\mathbf{T}}, \hat{\mathcal{P}}) \tag{2.106}$$

where the weights are now given by:

$$w_{i,k}(\hat{c}, \hat{\mathbf{T}}, \hat{\mathcal{P}}) = \frac{e^{-\frac{1}{2}\frac{r_i^2(\hat{c},\hat{\mathbf{T}},\hat{\mathbf{p}}_k)}{\sigma_z^2}}}{\sum_{k'=1}^{\hat{N}_\mathrm{s}} e^{-\frac{1}{2}\frac{r_i^2(\hat{c},\hat{\mathbf{T}},\hat{\mathbf{p}}_{k'})}{\sigma_z^2}} + \frac{\sqrt{2\pi}\sigma_z}{v}} \tag{2.107}$$

2.4 Conclusion

In this chapter, a robust algorithm for the calibration of our PER-PAT setup was described. Input for the algorithm is either a reference measurement, in case of which we are interested in estimating a position and speed of sound, or a calibration measurement, when we want to estimate the center of rotation and speed of sound. These measurements are in principle ultrasound signals, measured with the ultrasound detector array, however as input to the algorithm we use time of flight (TOF) measures obtained from a pre-processing step.

The model that relates the unknown calibration parameters to these TOF measurements is discussed and analyzed in section 2.2. Some interesting properties of the measurement models were learned from this analysis. We found that for the reference measurement, with certain positions of the point source, it is not possible to obtain an unambiguous solution to the calibration problem. This means care needs to be taken when positioning the passive element in the PER-PAT setup. Furthermore we found that the use of a calibration phantom with a slightly different speed of sound than the ultrasound medium, results in biased estimates of the calibration parameters. An effective and relatively simple change in the model was proposed which takes into account the speed of sound difference and the size of the calibration phantom. This new model reduced the biases in the estimated parameters almost completely.

Finally, in section 2.3 a fully automatic calibration algorithm is outlined. The algorithms aims to maximize the likelihood function of the calibration parameters from the observed TOF measurements. Optimizing this likelihood function is not straightforward, the function contains a lot of local maxima, and the key to overcoming this problem is to find a suitable initial guess close to the global maximum. We proposed to divide the problem into smaller subproblems with increasing complexity. Each subproblem is made robust by explicitly adding the notion of outliers and handling them in a natural way by a soft classification of the input measurements. The proposed calibration algorithm was succesfully tested on all our experimentally obtained reference and calibration measurements. Some of these measurements had a substantial amount of noise with a high percentage of outliers, making this a challenging task.

3

Estimation of ultrasound parameters[1]

Abstract

The estimation of integrated ultrasound propagation parameters is important in ultrasound computed tomography and of late also in photoacoustic imaging. We derive and evaluate several maximum likelihood estimators for the measurements of integrated acoustic attenuation and for time of flight. From these estimates, speed of sound and acoustic attenuation images can be reconstructed in a subsequent step. The more accurate this estimate of the propagation parameters is, the better the quality of the reconstructed image can be. We compare our proposed estimators with two existing estimators for acoustic attenuation and show that it is possible to obtain better results by using the maximum likelihood principle and by including phase information in the estimator as well through the Kramers-Kronig causality relations.

---

[1] This chapter is under communication as:
i) G.H. Willemink and S. Manohar et al, "Estimation of integrated ultrasound transmission parameters I: Speed of Sound", Physics in Medicine and Biology
ii) G.H. Willemink and S. Manohar et al, "Estimation of integrated ultrasound transmission parameters II: Acoustic attenuation", Physics in Medicine and Biology

3.1 Introduction

The estimation of acoustic propagation parameters like attenuation and speed of sound are important factors in the fields of ultrasound tissue characterization and non-destructive material testing. An application in medical ultrasound is the reconstruction of distributions of the propagation parameters inside an object from projections [36]. In our PER-PAT imaging setup, we have to estimate time delay and integrated attenuation along paths connecting a passive element with a detector element. These estimates then can be used as input in the next step which is to reconstruct images of speed of sound and acoustic attenuation. The more accurate these projections can be estimated, the more accurate the reconstructed images will be. The accuracy of the estimates depends on the propagation parameters of the object, the signal to noise ratio of the measured signal, as well as on the performance of the estimator that is being used. In this chapter we will focus on the analysis and formulation of an estimator for time of flight and the formulation of accurate estimators of the attenuation parameters. The accuracy will be presented in terms of the bias and variance of the estimators and the resulting root mean square error (RMSE).

The ultrasound propagation estimators proposed in this chapter can be used in ultrasound transmission mode measurements. Measuring in transmission mode means that an input signal is generated at one side of the object and a distorted version of this signal is measured at the opposite side of the object. The distortion of the input signal is caused by the ultrasound propagation parameters of the object. The measured signal is thus a function of the input signal and the unknown ultrasound propagation parameters. The estimation task is now defined as finding an estimate of the unknown ultrasound propagation parameters from the measured signal. This requires the formulation of a measurement model that describes the relation between the parameters and the measured signal.

3.2 The ultrasound propagation parameters

The propagation of an ultrasound signal through an ultrasound medium can be characterized by two effects. First, there is a change in amplitude of the signal and secondly there is a time delay which corresponds to the time the signal travels through the medium. Both, the amplitude and time delay effects, are material properties which can be position and frequency dependent. When looking at the propagated and input signals in the frequency domain, i.e., after a Fourier transform, through a homogeneous object their relation is defined as:

$$Y(\omega) = \exp\left[\left(-\alpha(\omega) - j\frac{\omega}{c(\omega)}\right) d\right] X(\omega) \tag{3.1}$$

here $\omega = 2\pi f$ is the angular frequency, $\alpha(\omega)$ and $c(\omega)$ are the frequency dependent attenuation and speed of sound functions respectively, $Y(\omega)$ is the Fourier transformed propagated signal and $X(\omega)$ is the Fourier transformed input signal. The distance d

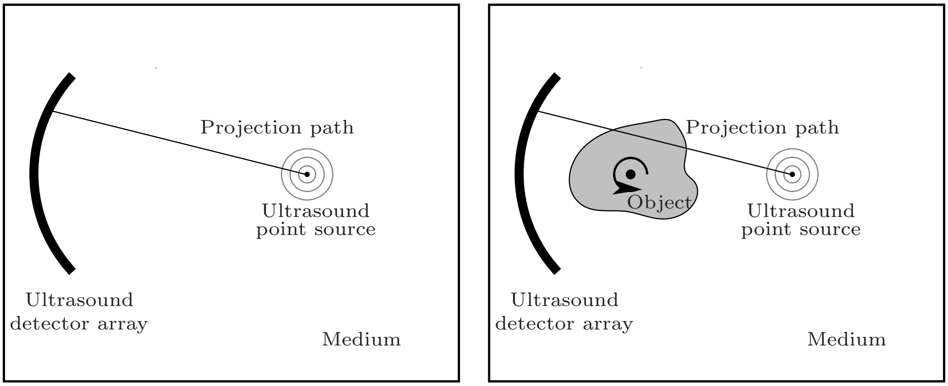

(a) UTT reference measurement **(b)** UTT object measurement

Figure 3.1 Illustration of the ultrasound transmission mode tomography (UTT) setup. Shown here are a reference measurement without any object to obtain a reference measurement and an object measurement with the object in place. By comparing the object measurement to the reference measurement an estimate of the integrated attenuation and time delay along the projection path can be made.

represents the distance traveled through the medium. What we are looking for is a parametrization of the attenuation and speed of sound functions and then to obtain estimates of these parameters from propagated signals.

For a wide variety of materials, the attenuation function obeys a power frequency law[37, 38]:

$$\alpha(\omega) = \alpha_0 |\omega|^y \tag{3.2}$$

The two material dependent parameters in this function are the attenuation constant α_0 and the power factor y. The power factor ranges between 1 and 2 for most materials[39]. The attenuation constant α_0 is one of the parameters that we finally want to estimate. The speed of sound function is directly related to the attenuation function via the Kramers-Kronig relations [40, 41]:

$$\frac{1}{c(\omega)} = \frac{1}{c(\omega_0)} + \alpha_0 \tan\left(\frac{\pi}{2} y\right) \left(|\omega|^{y-1} - |\omega_0|^{y-1}\right) \tag{3.3}$$

where $c(\omega_0)$ is the speed of sound at a chosen reference frequency ω_0. We see here that dispersion vanishes when the parameter $y = 0$ or $y = 2$. The expression for the case of $y = 1$ seems to become indeterminate, however, applying the rule of l'Hopital gives it a well defined limit for $y \to 1$ [42]:

$$\frac{1}{c(\omega)} = \frac{1}{c(\omega_0)} - \alpha_0 \frac{2}{\pi} \big(\ln |\omega| - \ln |\omega_0| \big) \tag{3.4}$$

The speed of sound at the reference frequency, $c(\omega_0)$, is the other parameter that we want to estimate. An overview of the parameters in the model is given in Table 3.1

Parameter	Units	Description
α_0	Np/(rad/s)^y	Power law attenuation constant
y		Power law factor
$c(\omega_0)$	m/s	Speed of sound at a chosen reference frequency

Table 3.1 Overview of the parameters used when describing propagation of ultrasound signals through media having an attenuation function which can be described with a frequency power law.

This parametrization of the propagation parameters in α_0, y and $c(\omega_0)$ is applicable when both the sending and receiving transducer are placed in the medium of interest and the input signal $X(\omega)$ can be observed directly. In practical situations, however, this is not possible and we embed the object of interest in a coupling medium. We can then obtain a reference signal of the input signal by removing the object of interest from the setup as shown in Figure 3.1a. An object signal is obtained by placing the object of interest in between the sending and receiving transducer as shown in Figure 3.1b. This will introduce reflections at the transitions from object to coupling medium and vice versa and also the attenuation and speed of sound of the coupling medium should be taken into account. In terms of transfer functions, we can write the dependency of both the object signal and reference signal on the input signal as:

$$Y_{\mathrm{o}}(\omega) = H_{\mathrm{w}}(\omega)H_{\mathrm{o}}(\omega)H_{\mathrm{refl}}(\omega)H_{\mathrm{rec}}(\omega)X(\omega) \tag{3.5}$$

$$Y_{\mathrm{w}}(\omega) = H_{\mathrm{w}}(\omega)H_{\mathrm{w'}}(\omega)H_{\mathrm{rec}}(\omega)X(\omega) \tag{3.6}$$

where the following transfer functions are defined:

$H_{\mathrm{w}}(\omega)$	Transfer function of the coupling medium (water)
$H_{\mathrm{o}}(\omega)$	Transfer function of the object
$H_{\mathrm{w'}}(\omega)$	Transfer function of the water that replaces the removed object
$H_{\mathrm{refl}}(\omega)$	Transfer function representing reflection
$H_{\mathrm{rec}}(\omega)$	Transfer function of the receiving transducer

By combining these two expressions, we can express the measured object signal as a function of the measured reference signal:

$$Y_{\mathrm{o}}(\omega) = H_{\mathrm{o}}(\omega)H_{\mathrm{refl}}(\omega)H_{\mathrm{w'}}^{-1}(\omega)Y_{\mathrm{w}}(\omega) \tag{3.7}$$

where the individual transfer functions are given by:

$$\ln\big(H_{\mathrm{o}}(\omega)\big) = -\alpha_0|\omega|^y d - j\omega\left(\frac{1}{c(\omega_0)} + \alpha_0 \tan\left(\frac{\pi}{2}y\right)\left(|\omega|^{y-1} - |\omega_0|^{y-1}\right)\right) d \tag{3.8}$$

$$\ln\big(H_{\mathrm{refl}}(\omega)\big) = -\alpha_r \tag{3.9}$$

$$\ln\big(H_{\mathrm{w'}}^{-1}(\omega)\big) = \alpha_w|\omega|^2 d + j\omega\frac{d}{c_w} \tag{3.10}$$

Here we have assumed that the coupling medium is water, i.e. having an attenuation function with a power of 2 and no speed of sound dispersion. Furthermore, because the attenuation in water is very small, $\alpha_w = 2.53 \cdot 10^{-4}$ Np/cm/MHz^2[43], compared to the attenuation expected in the objects to measure, we can ignore the attenuation part of the water transfer function. All parameters can be combined in one single transfer function

$$Y_{\mathrm{o}}(\omega) = H(\omega)Y_{\mathrm{w}}(\omega) \tag{3.11}$$

where

$$H(\omega) = \exp\left[-\alpha_0|\omega|^y d - \alpha_r - j\omega\left(\frac{1}{c(\omega_0)} - \frac{1}{c_w} + \alpha_0 \tan\left(\frac{\pi}{2}y\right)\left(|\omega|^{y-1} - |\omega_0|^{y-1}\right)\right)d\right]$$

The unknown parameters here are the attenuation constant α_0, the reflection coefficient α_r and the speed of sound $c(\omega_0)$. If also the distance d is not known, the integrated attenuation, $\alpha_0 d$, and time delay $\frac{d}{c(\omega_0)-c_w}$ can be chosen as unknown parameters. This is the case in ultrasound transmission tomography measurements, where we want to extract the integrated attenuation and time delay, in order to reconstruct attenuation and speed of sound maps. We assume that the power factor y is known beforehand.

3.2.1 Obtaining the water and object signals

Both the water and object measurements will be available as sampled data in the time domain. A realistic model for noise on the measurements is additive Gaussian white noise. The water measurement has a higher signal to noise ratio due to the absence of an attenuating object than a typical object measurement. In an application like ultrasound transmission mode tomography, where we want to obtain measures of integrated attenuation/time of flight over different paths through the sample, the water measurement can be reused for every individual object measurement, so that it is worth the effort to take multiple water measurements and decrease the noise by averaging. This leads to the assumption from now on that the signal to noise ratio on the the water measurement is high enough to ignore the influence of noise on the water measurement.

Suppose now that we observe the time domain object measurement with additive Gaussian white noise of variance $\sigma_{z_t}^2$, sampled at a frequency of f_{s} and with a length of n samples. An FFT of this time domain object measurement would give us a frequency domain representation where the following frequency components can be calculated:

$$\omega_i = \begin{cases} 2\pi f_{\mathrm{s}}\dfrac{i-1}{n} & i \leq \lceil \frac{n+1}{2} \rceil \\ 2\pi f_{\mathrm{s}}\dfrac{i-1-n}{n} & i > \lceil \frac{n+1}{2} \rceil \end{cases} \tag{3.12}$$

The index i ranges from 1 to n. If we use the complex FFT matrix $\mathbf{W}$ [44] to represent the FFT operation, then the time domain measurements are related to the actual components of $\mathbf{Y}_{\mathrm{o}}(\omega)$ according to:

$$\mathbf{z}_{\mathrm{t}} = \mathbf{V} \begin{bmatrix} Y_o(\omega_1) \\ \vdots \\ Y_o(\omega_n) \end{bmatrix} + \mathbf{n}_{z_t} \tag{3.13}$$

Where the matrix $\mathbf{V} = \mathbf{W}^{-1} = \frac{1}{n}\mathbf{W}^*$ represents the inverse FFT operation. The vector $\mathbf{n}_{z_t}$ represents the additive zero mean white Gaussian noise with variance of $\sigma^2_{z_t}$. We will make use of this relation later to derive the attenuation estimators.

3.3 Estimating time of flight

We start with the estimation of time of flight alone. We do not yet include any dispersion, i.e., frequency dependent behavior, in the estimation procedure. What we are interested here is only the time of flight between a source and detector. In the section on the estimation of attenuation, we will include frequency dependent behavior, and the time of flight estimate will be refined by making use of the relation between time delay dispersion and attenuation dispersion. This section will start by investigating the photoacoustic source signal on which the TOF estimation has to be performed. After that we continue with investigating what kind of accuracy we can expect and present a method to extract TOF measurements from measured signals.

3.3.1 The photoacoustic source signal

The signals used in the calibration procedure are photoacoustically induced ultrasound signals from small optical absorbers incorporated in a calibration phantom. Such a small optical absorber will, as a result of the photoacoustic effect, generate a short bi-polar ultrasound pulse. This bi-polar pulse is then measured with an ultrasound transducer, which will be the input to the calibration procedure. Due to the limited bandwidth of a typical ultrasound transducer we will in general not measure a bi-polar pulse. When the size of the optical absorber is small with respect to the theoretical resolution which depends on the bandwidth of the ultrasound transducer, the shape of this pulse will only be dependent on the impulse response of the ultrasound transducer. The measured signal is the convolution of the short bi-polar pulse with the impulse response of the transducer.

Suppose that the bi-polar pulse has a short duration on the scale of the impulse response. In that case the convolution operation can be seen as taking the time derivative of the impulse response. Thus what we find is that measuring a short bi-polar pulse with the ultrasound transducer results in measuring the time derivative of the impulse response of the ultrasound transducer. If we assume that the transfer function of the transducer is Gaussian with a certain bandwidth and center frequency, then taking the time derivative will still result in a Gaussian transfer function. This translates, in the time domain, to a sine wave of a certain frequency modulated with a Gaussian envelope. Time and frequency domain representations of such a signal are displayed in Table 3.2 and an example realization is plotted in Fig. 3.2. The signal is parametrized with an angular center frequency ω_c and an angular bandwidth ω_b. The angular bandwidth is related to the bandwidth B defined as the frequency range between the two -6 dB cut-off frequencies via:

$$\omega_\mathrm{b} \approx \frac{\pi B}{\sqrt{2\ln 2}} \tag{3.14}$$

We have also shown the representation of a typical bi-polar pulse, as the derivative of an unmodulated Gaussian time domain signal, in Table 3.2 and an example realization in Figure 3.3. An interesting observation here is that, in the limit, when the center frequency is much smaller than the bandwidth, the Gaussian pulse source converges, up to a scale factor, to the bi-polar pulse.

	Time domain	Frequency domain
Gaussian pulse	$-\sin(\omega_\mathrm{c}t)e^{-\frac{1}{2}\omega_\mathrm{b}^2t^2}$	$\sqrt{\frac{\pi}{2}}\frac{j}{\omega_\mathrm{b}}\left(\exp\left[\frac{-(\omega-\omega_\mathrm{c})^2}{2\omega_b^2}\right]-\exp\left[\frac{-(\omega+\omega_\mathrm{c})^2}{2\omega_b^2}\right]\right)$
Gaussian deriv.	$-\omega_\mathrm{b}te^{-\frac{1}{2}\omega_\mathrm{b}^2t^2}$	$\frac{j\omega}{\omega_\mathrm{b}}\exp\left[\frac{-\omega^2}{2\omega_b^2}\right]$

Table 3.2 Time domain and frequency domain representations of two frequency band limited and compactly supported in the time domain functions.

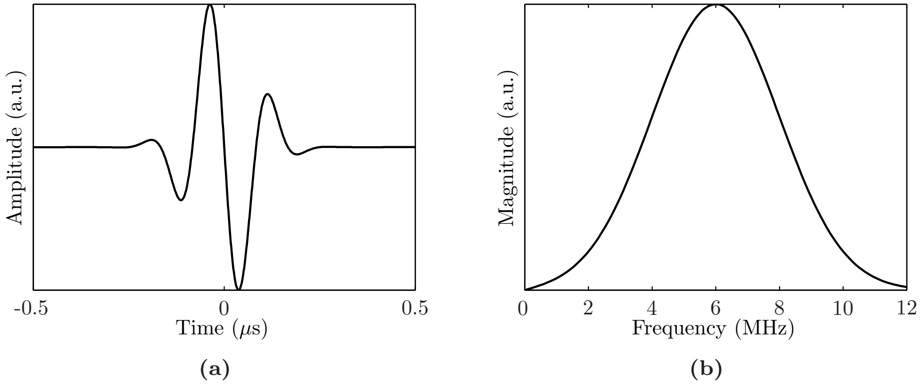

Figure 3.2 A Gaussian pulse source signal with $\frac{\omega_\mathrm{b}}{2\pi} = 2$ MHz and a center frequency of 6 MHz. The time domain representation is shown in (a) and the magnitude of the frequency domain representation in (b).

Normalizing the source signal

For a fair comparison of the influence of the bandwidth and center frequency on the TOF estimation accuracy, we will scale the amplitude of the input signals. Our

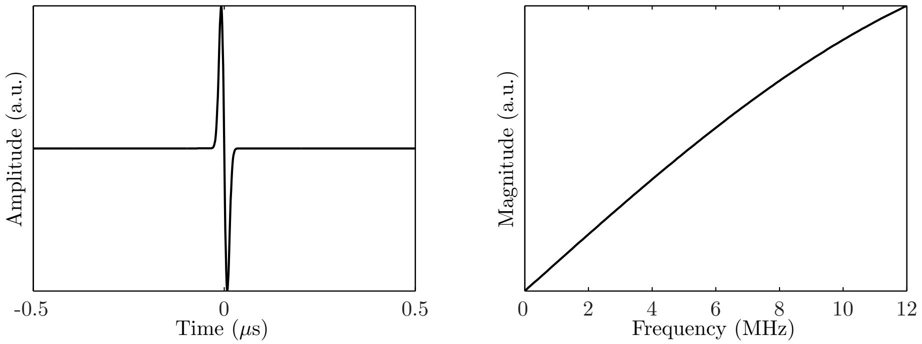

Figure 3.3 A bi-polar pulse, obtained as the derivative of a Gaussian, with $\frac{\omega_\mathrm{b}}{2\pi} =$ 20 MHz. The time domain representation is shown in (a) and the magnitude of the frequency domain representation in (b).

scaling will normalize the total energy in the signal averaged over (a measure of) the signal duration. The parameter ω_b is inversely related to the time duration of the corresponding pulse. For a signal $f(t)$ with the bandwidth related parameter ω_b, we will normalize to the expression:

$$\sqrt{\omega_\mathrm{b}\int_{-\infty}^{\infty} f^2(t)\mathrm{d}t} = 1 \tag{3.15}$$

This ensures that the total energy of the signal scaled by the duration of the signal will be constant for different realizations of the signals.

Applying this normalization will result in a normalizing scale factor of:

$$k = \frac{1}{\sqrt{\omega_\mathrm{b}\int_{-\infty}^{\infty}\sin^2(\omega_\mathrm{c}t)e^{-\omega_\mathrm{b}^2t^2}\mathrm{d}t}} \tag{3.16}$$

The integral term in the denominator can be calculated using Table B.3 from Appendix B:

$$\int_{-\infty}^{\infty}\sin^2(\omega_\mathrm{c}t)e^{-\omega_\mathrm{b}^2t^2}\mathrm{d}t = \frac{\sqrt{\pi}}{2\omega_\mathrm{b}}\left[1 - e^{-\left(\frac{\omega_\mathrm{c}}{\omega_\mathrm{b}}\right)^2}\right] \tag{3.17}$$

which gives the normalizing scale factor for the Gaussian modulated signal:

$$k = \sqrt{\frac{2}{\sqrt{\pi}}\frac{1}{1 - e^{-\left(\frac{\omega_\mathrm{c}}{\omega_\mathrm{b}}\right)^2}}} \tag{3.18}$$

Figure 3.4 shows the resulting amplitude of the source signal after the proposed normalization as a function of the $\frac{\omega_\mathrm{c}}{\omega_\mathrm{b}}$ ratio.

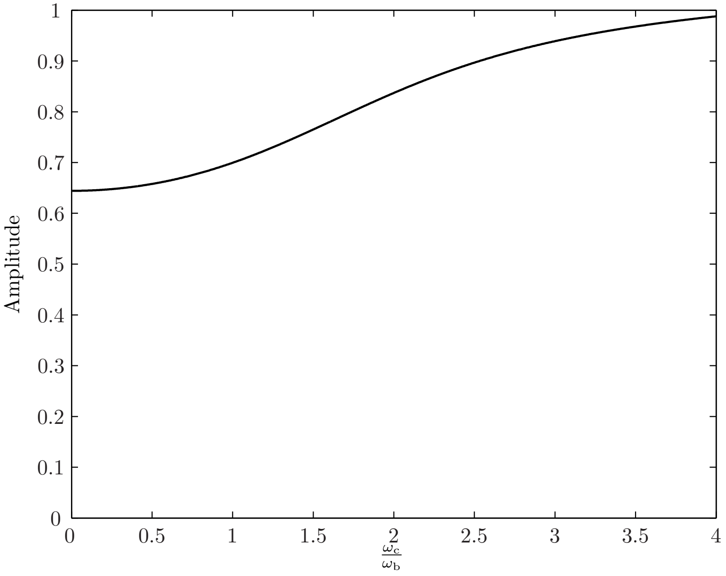

Figure 3.4 Amplitude of the Gaussian modulated pulse after normalization of the total energy over the signal duration as a function of the $\frac{\omega_c}{\omega_b}$ ratio.

Sampling the source signal

In our problem, the continuous time domain signals are available as discrete sampled measurements. We will now proceed with describing the sampled measurements in detail. For a given sampling frequency of f_s (Hz) and a window size of T_w (s), we can take N_s samples inside the measurement window:

$$N_\mathrm{s} = \lceil T_\mathrm{w} f_\mathrm{s} + 1 \rceil \tag{3.19}$$

If the measurement window is centered around the received signal, the distribution of time steps relative to this center will be given by:

$$t_i = \frac{1}{f_s}\left(i - \frac{N_\mathrm{s}+1}{2}\right) \tag{3.20}$$

where $i \in [1, \ldots, N_\mathrm{s}]$ represents the sample number. We can then obtain a vector $\mathbf{z} = [z_1, \ldots, z_{N_\mathrm{s}}]^T$ containing the sampled measurements. If we assume that the measurement is corrupted with additive noise, the elements in the vector are defined as:

$$z_i = h(t_i + \tau) + n_{\mathrm{z},i} \tag{3.21}$$

Here τ is the unknown time delay (within the centered window) and $n_{\mathrm{z},i}$ is additive measurement noise. The measurement function $h(t)$ here is the time domain representation of the source signal (examples of source signals are given in Table 3.2).

3.3.2 The Cramer-Rao Lower Bound

The question now is, how accurately can we estimate the time delay from a set of discrete sampled measurements. To investigate this we look at how the available information (measurement) is related to the unknown time delay, which will help us to find an expression for the uncertainty of the time delay. This accuracy can depend on several factors, such as the sampling frequency, the window size of the measurements, the noise on the measurements and the kind of source signal that is being used. When the measurements are uncorrelated and identically Gaussian distributed with variance σ_z^2, then the Cramer-Rao Lower Bound (CRLB) of the unknown time delay is given by[31]:

$$\mathrm{CRLB} = \frac{\sigma_z^2}{\displaystyle\sum_{i=1}^{N_\mathrm{s}} \left(\frac{\partial}{\partial t} h(t)\big|_{t_i} \right)^2} \tag{3.22}$$

This expression gives us the minimum variance (for unbiased estimators) on the time delay estimate that can be obtained from the described measurements. Which means we have an expression to evaluate the uncertainty of the unknown time delay. From this expression we see that increasing the window size (i.e. taking more samples) will lower the CRLB. However, because we are using signals that have compact support in the time domain, this will approach a limiting value. In the limit, increasing the window size will not decrease the CRLB because the time derivative of the source signal will be zero at both ends of the window.

We will now proceed with showing how this works out for the measured photoacoustic source signal. Applying the time derivative to the source signal and using the CRLB formula (3.22) gives us the necessary expressions. The measurement function is given in the top row of Table 3.2. We will also apply the normalizing scale factor k. The variance of any unbiased estimator of the time delay from a normalized Gaussian modulated signal will have a lower bound of:

$$\mathrm{Var}[\hat{\tau}] \geq \frac{\sigma_z^2}{\displaystyle\sum_{i=1}^{N_\mathrm{s}} k^2 \Big(\omega_c \cos(\omega_c t_i) - \omega_b^2 t_i \sin(\omega_c t_i) \Big)^2 \exp\left[-\omega_b^2 t_i^2 \right]} \tag{3.23}$$

CRLB for an infinitely wide window

As mentioned before, the CRLB approaches a limiting lower bound when the window size becomes infinitely long. We will now investigate what this limiting lower bound is for an infinitely long window size by applying the limit of $N_s \to \infty$ to (3.23). To calculate this limit we make use of the following relation:

$$\int_{-\infty}^{\infty} f(t)\mathrm{d}t \approx \lim_{N_\mathrm{s}\to\infty} \sum_{i=1}^{N_\mathrm{s}} f(t_i)\Delta t = \frac{1}{f_\mathrm{s}} \lim_{N_\mathrm{s}\to\infty} \sum_{i=1}^{N_\mathrm{s}} f(t_i) \tag{3.24}$$

This approximation holds when the sampling frequency is high enough, so that the time spacing between two samples $\Delta t = \frac{1}{f_\mathrm{s}}$ will be small on the scale of $f(t)$. By using this relation we can evaluate the infinite sum as an integral equation for which we can obtain a closed form solution.

For the Gaussian modulated signal we have to evaluate (3.23). The denominator term in that equation can now be rewritten as:

$$\lim_{N_\mathrm{s}\to\infty}\sum_{i=1}^{N_\mathrm{s}} k^2\Big(\omega_c\cos(\omega_c t_i)-\omega_b^2 t_i\sin(\omega_c t_i)\Big)^2\exp\left[-\omega_b^2 t_i^2\right] \tag{3.25}$$

$$\approx\quad f_\mathrm{s}\int_{-\infty}^{\infty} k^2\Big(\omega_c\cos(\omega_c t)-\omega_b^2 t\sin(\omega_c t)\Big)^2\exp\left[-\omega_b^2 t^2\right]\mathrm{d}t \tag{3.26}$$

By expanding the square and using the results from Table B.3, we can calculate the integral:

$$f_\mathrm{s}\int_{-\infty}^{\infty} k^2\Big(\omega_c\cos(\omega_c t)-\omega_b^2 t\sin(\omega_c t)\Big)^2\exp\left[-\omega_b^2 t^2\right]\mathrm{d}t \tag{3.27}$$

$$=\quad f_\mathrm{s}k^2\frac{\sqrt{\pi}}{\omega_\mathrm{b}}\left[\frac{1}{2}\omega_\mathrm{c}^2+\frac{1}{4}\omega_\mathrm{b}^2\left(1-e^{-\left(\frac{\omega_\mathrm{c}}{\omega_\mathrm{b}}\right)^2}\right)\right] \tag{3.28}$$

$$=\quad f_\mathrm{s}\left[\frac{1}{1-e^{-\left(\frac{\omega_\mathrm{c}}{\omega_\mathrm{b}}\right)^2}}\frac{\omega_\mathrm{c}^2}{\omega_\mathrm{b}}+\frac{1}{2}\omega_\mathrm{b}\right] \tag{3.29}$$

Applying this result to (3.23) gives us the CRLB for normalized Gaussian modulated signals measured with an infinitely long window size:

$$\mathrm{Var}[\hat{\tau}]\geq\frac{\sigma_z^2}{f_\mathrm{s}\omega_\mathrm{b}\left[\frac{\left(\frac{\omega_\mathrm{c}}{\omega_\mathrm{b}}\right)^2}{1-e^{-\left(\frac{\omega_\mathrm{c}}{\omega_\mathrm{b}}\right)^2}}+\frac{1}{2}\right]} \tag{3.30}$$

It is interesting to look at the behavior of the term in the denominator. This term converges to different expressions for $\frac{\omega_\mathrm{c}}{\omega_\mathrm{b}}\ll 1$ and $\frac{\omega_\mathrm{c}}{\omega_\mathrm{b}}\gg 1$ as can be seen in Figure 3.5. When $\frac{\omega_\mathrm{c}}{\omega_\mathrm{b}}<\frac{1}{2}$ we get the low center frequency CRLB:

$$\mathrm{Var}[\hat{\tau}]\geq\frac{\sigma_z^2}{f_\mathrm{s}\omega_\mathrm{b}\frac{3}{2}} \tag{3.31}$$

and when $\frac{\omega_\mathrm{c}}{\omega_\mathrm{b}}>2$ we get the high center frequency CRLB:

$$\mathrm{Var}[\hat{\tau}]\geq\frac{\sigma_z^2}{f_\mathrm{s}\omega_\mathrm{b}\left[\left(\frac{\omega_\mathrm{c}}{\omega_\mathrm{b}}\right)^2+\frac{1}{2}\right]} \tag{3.32}$$

Effect of window size

The signals that we encounter in practice have limited support in the time domain, therefore it is convenient to use a limited window over which the two delayed signals

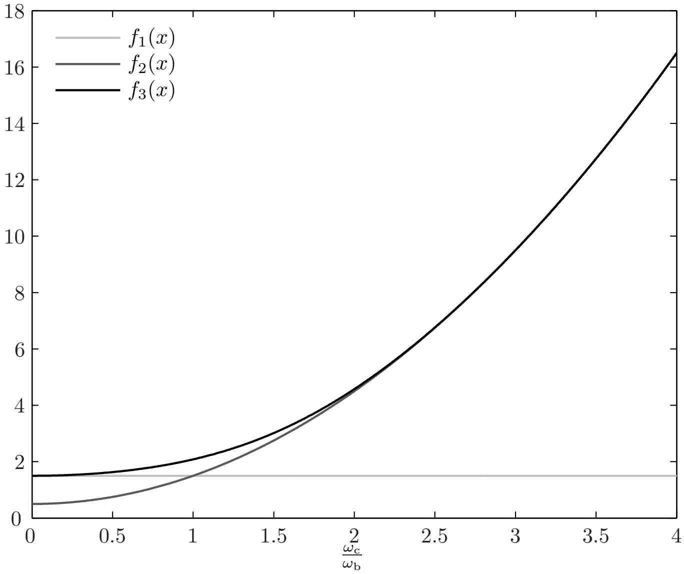

Figure 3.5 Illustration of limit approximations of the denominator term in (3.30). The functions displayed are the low $\frac{\omega_c}{\omega_b}$ ratio approximation $f_1(\frac{\omega_c}{\omega_b})$, the high $\frac{\omega_c}{\omega_b}$ ratio approximation $f_2(\frac{\omega_c}{\omega_b})$ and the original term $f_3(\frac{\omega_c}{\omega_b})$. The functions are given by: $f_1\left(\frac{\omega_c}{\omega_b}\right) = \frac{3}{2}$, $f_2\left(\frac{\omega_c}{\omega_b}\right) = \left(\frac{\omega_c}{\omega_b}\right)^2 + \frac{1}{2}$ and $f_3\left(\frac{\omega_c}{\omega_b}\right) = \frac{\left(\frac{\omega_c}{\omega_b}\right)^2}{1-e^{-\left(\frac{\omega_c}{\omega_b}\right)^2}} + \frac{1}{2}$

have to be compared. The wider this window, the more information that can be used and thus the higher the accuracy of the time delay estimate. However, a wide window is undesirable in practice, since we the probability of measuring echoes and other unwanted signals will increase. We have already seen that the time delay estimate accuracy will converge to a limiting value for infinitely long windows and we will now investigate from what window size on this convergence occurs. To investigate this, we have calculated the CRLB for a whole range of window sizes and for different settings of the ω_c and ω_b parameters. In Figure 3.6 the results of these calculations are displayed. We see there that a window size of $T_w = \frac{6}{\omega_b}$ is sufficient to get as close to 0.1% to the CRLB of the infinite window size for any setting of ω_c and ω_b that we expect to encounter in practice.

Scaling of the source signal

Until now we have assumed that the measured signal and the assumed source signal have the same amplitude. These amplitudes are displayed in Figure 3.4 and are a result of the normalization convention we use as described earlier this section. The

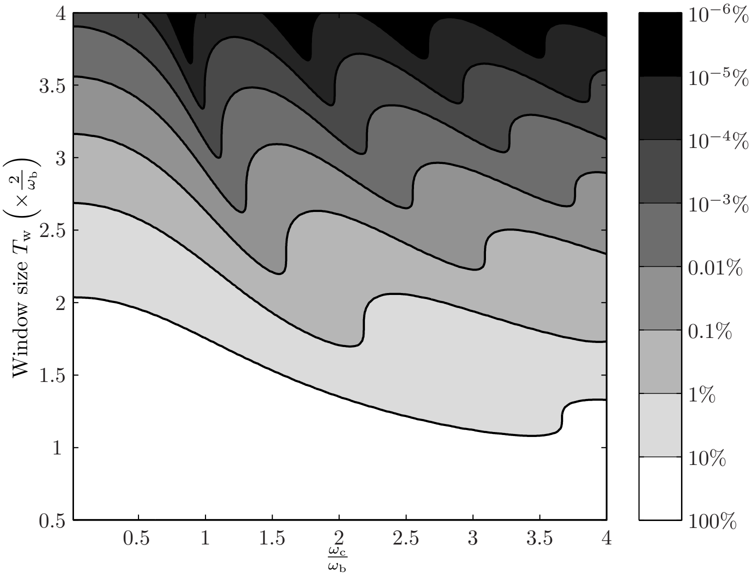

Figure 3.6 This image shows the relative increase in the CRLB that results from using a finite window size with respect to the CRLB that would have been obtained in case of an infinitely long window size. The x-axis indicates the different settings of the ω_c and ω_b parameters. On the y-axis the window size is shown. This window size is relative to the length $\frac{2}{\omega_c}$. The iso-contour lines show the locations of the boundaries for certain CRLB increase ratios. For example, to get an increase in the CRLB of less than 0.1% for all possible settings of ω_c and ω_b a window size of at least $3 \times \frac{2}{\omega_b}$ should be used.

use of a different amplitude in the measured signal can easily be incorporated in the CRLB expression. Suppose the measured signal is scaled with a factor A with respect to the amplitude as shown in Figure 3.4. The measurements are then related to the source signal via:

$$z_i = A \cdot h(t_i + \tau) + n_{z,i} \tag{3.33}$$

The constant A propagates in the CRLB (3.30) by a multiplication with $\left(\frac{1}{A}\right)^2$, so that the CRLB for the TOF in this case becomes:

$$\mathrm{Var}[\hat{\tau}] \geq \frac{\left(\frac{\sigma_z}{A}\right)^2}{f_s \omega_b \left[\frac{\left(\frac{\omega_c}{\omega_b}\right)^2}{1-e^{-\left(\frac{\omega_c}{\omega_b}\right)^2}} + \frac{1}{2}\right]} \tag{3.34}$$

It might however occur, that only the shape and not the scaling of the source signal is known in advance when the signal is measured. In that case, the measurement model has to be extended with the unknown A parameter and the CRLB will be in the form of a covariance matrix. The question is whether the element in the CRLB matrix of the variance of the TOF would still be the same as in the case of an a-priori known A-parameter. To investigate this, we notice that for the multivariate case with uncorrelated identically distributed additive Gaussian noise, the CRLB is given by:

$$\text{CRLB} = \sigma_z^2 \left(\mathbf{H}^T \mathbf{H}\right)^{-1} \tag{3.35}$$

Where $\mathbf{H}$ is the Jacobian matrix of the measurement function, which in our case is given by:

$$\mathbf{H} = \begin{bmatrix} A\frac{\partial}{\partial t} h(t_1 + \tau) & h(t_1 + \tau) \\ \vdots & \vdots \\ A\frac{\partial}{\partial t} h(t_{N_\mathrm{s}} + \tau) & h(t_{N_\mathrm{s}} + \tau) \end{bmatrix} \tag{3.36}$$

so that the expression of the CRLB can be written as:

$$\text{CRLB} = \sigma_z^2 \begin{bmatrix} A^2 \sum\limits_{i=1}^{N_\mathrm{s}} \left(\frac{\partial}{\partial t} h(t_i + \tau)\right)^2 & A \sum\limits_{i=1}^{N_\mathrm{s}} \frac{\partial}{\partial t} h(t_i + \tau) \cdot h(t_i + \tau) \\ A \sum\limits_{i=1}^{N_\mathrm{s}} \frac{\partial}{\partial t} h(t_i + \tau) \cdot h(t_i + \tau) & \sum\limits_{i=1}^{N_\mathrm{s}} h^2(t_i + \tau) \end{bmatrix}^{-1} \tag{3.37}$$

When the cross terms in the matrix in this expression are zero, so that matrix becomes diagonal, the matrix inverse can immediately be calculated. Only in that case, the CRLB of the TOF, which is the upper left element in (3.37), is equal to the earlier found expression (3.22). To see when this is the case, we recall that, using a modified version of (3.24), we can approximate the cross terms with a continuous integral as:

$$\sum_{i=1}^{N_\mathrm{s}} \frac{\partial}{\partial t} h(t_i + \tau) \cdot h(t_i + \tau) \approx f_\mathrm{s} \int\limits_{-\frac{1}{2}T_\mathrm{w}}^{\frac{1}{2}T_\mathrm{w}} \frac{\partial}{\partial t} h(t + \tau) \cdot h(t + \tau) \mathrm{d}t \tag{3.38}$$

where T_w is the window size which related to N_s via (3.19). By using partial integration, we can rewrite this expression as:

$$f_\mathrm{s} \int\limits_{-\frac{1}{2}T_\mathrm{w}}^{\frac{1}{2}T_\mathrm{w}} \frac{\partial}{\partial t} h(t + \tau) \cdot h(t + \tau) \mathrm{d}t = \frac{1}{2} f_\mathrm{s} h^2(t + \tau) \Big|_{t=-\frac{1}{2}T_\mathrm{w}}^{\frac{1}{2}T_\mathrm{w}} \tag{3.39}$$

The question now is, will this expression evaluate to zero. If the window size T_s is chosen wide enough, so that evaluating the source function $h(t)$ at both ends of the window evaluates to zero, the above expression also evaluates to zero. We can say that in that case the source function and its time derivative are orthogonal. This means that when the window is chosen wide enough, the cross terms in (3.37) become zero and the CRLB of the TOF will not be different when the scaling of the source signal A is not known a-priori.

Summary

We will now summarize the effects that the different parameters have on the accuracy of our TOF estimate:

Additive noise variance (σ_z^2) An increase of the additive noise with a certain factor is directly related to an increase with the same factor in the CRLB of the time delay estimate.

Scaling of the source signal (A) Doubling the amplitude scaling of the source signal will result in half of the standard deviation of the time delay estimate. When the scaling of the source signal is not known a-priori and when the window size is chosen wide enough, the CRLB expression is not affected by this extra uncertainty.

Sampling frequency (f_s) Doubling the sampling frequency will lead to a decrease of the CRLB by a factor two. In terms of the standard deviation of the time delay estimate this results in a decrease of a factor $\sqrt{2}$.

Source signal (ω_c and ω_b) The ratio $\frac{\omega_\text{c}}{\omega_\text{b}}$ determines the number of oscillations in the source signal. Increasing this ratio increases the number oscillations and decreases the CRLB as can be seen by the trend of $f_3(\frac{\omega_\text{c}}{\omega_\text{b}})$ in Figure 3.5. The parameter ω_b itself determines the duration of signal in the time domain. Increasing this parameter decreases the signal duration and decreases the CRLB.

Window size (N_s) A large enough window size (and thus large enough number of samples) should be used to ensure that the CRLB approaches the limiting value of an infinitely long window close enough. From Figure 3.6 we see that a typical window size of at least $\frac{6}{\omega_\text{b}}$ should be used, which means a minimum number of samples $N_\text{s} = \lceil 6\frac{f_\text{s}}{\omega_\text{b}} + 1 \rceil$ according to (3.19).

3.3.3 Implementation of a time of flight estimator

Now that we have fully described the source signals, how these are related to the unknown TOF parameter and what kind of accuracy we can expect, it is time to introduce a practical implementation of a TOF estimator.

In general, when there is a time shift τ and a scaling A, a source signal $h(t)$ and a shifted signal $f(t)$ are related as:

$$f(t) = A \cdot h(t + \tau) \tag{3.40}$$

A relation which also can be represented as:

$$f(t) = \mathcal{F}^{-1}\left\{Ae^{j\omega\tau}\mathcal{F}\left\{h(t)\right\}\right\} = \mathcal{F}^{-1}\left\{Ae^{j\omega\tau}H(\omega)\right\} \tag{3.41}$$

Based on these two relations, we will propose an estimator for the time delay τ from discrete sampled time domain signals. The discrete time domain signals will be sampled with a sampling frequency f_s over a certain time window with time steps given by (3.20). This means that for time delays which are an integer multiple of $\Delta t = \frac{1}{f_s}$ we can simply use a matched filter to estimate the time delay. In general, the time delay will not exactly be an integer multiple of Δt and applying the matched filter technique will result in an estimate whose accuracy is already limited by Δt. However, as we have seen in the previous section, the theoretically obtainable accuracy is not limited by the sampling frequency. The matched filter can give us an initial guess of the TOF τ, which is already quite close to the actual value and can be used as initialization in a subsequent estimator.

To proceed with the introduction of the TOF estimator, we start by writing how the sampled measurements $\mathbf{z}$ are related to the source signal $h(t)$ via a measurement function $h_{\mathrm{z}}(\tau)$:

$$\mathbf{z} = h_{\mathrm{z}}(\mathbf{x}) + \mathbf{n}_{\mathrm{z}} = A \begin{bmatrix} h(t_1 + \tau) \\ \vdots \\ h(t_{N_{\mathrm{s}}} + \tau) \end{bmatrix} + \mathbf{n}_{\mathrm{z}} \tag{3.42}$$

where the parameter vector $\mathbf{x} = [\tau, A]^T$ is used. When the additive noise $\mathbf{n}_{\mathrm{z}}$ can be seen as Gaussian white noise with variance σ_{z}^2, a maximum likelihood estimate of the parameter vector $\mathbf{x}$ can be calculated by solving:

$$\hat{\mathbf{x}}_{\mathrm{ML}} = \arg\min_{\mathbf{x}} \|\mathbf{z} - h_{\mathrm{z}}(\mathbf{x})\|^2 \tag{3.43}$$

Because the measurement function is a non-linear function of $\mathbf{x}$ and because we already have an initial estimate $\mathbf{x}^{(1)} = [\hat{\tau}^{(1)}, \hat{A}^{(1)}]^T$ close to the final solution, from our matched filter, we can find the final solution via the Gauss-Newton optimization method[35]. This method is based on iteratively linearizing the measurement function around our current estimated parameter value resulting in a quadratic cost function. The minimum of the cost function is then used as the next estimate and the iteration is repeated:

$$\begin{aligned} \hat{\mathbf{x}}^{(i+1)} &= \arg\min_{\mathbf{x}} \left\| \mathbf{z} - \left(h_{\mathrm{z}}(\hat{\mathbf{x}}^{(i)}) + \mathbf{H}_{\mathrm{z}}^{(i)} \left(\mathbf{x} - \hat{\mathbf{x}}^{(i)} \right) \right) \right\|^2 && (3.44) \\ &= \hat{\mathbf{x}}^{(i)} + \left(\mathbf{H}_{\mathrm{z}}^{(i)T} \mathbf{H}_{\mathrm{z}}^{(i)} \right)^{-1} \mathbf{H}_{\mathrm{z}}^{(i)T} \left(\mathbf{z} - h_{\mathrm{z}}(\hat{\mathbf{x}}^{(i)}) \right) && (3.45) \end{aligned}$$

Here $\mathbf{H}_{\mathrm{z}}^{(i)} = \begin{bmatrix} \hat{A}^{(i)} \mathbf{b}_1^{(i)} & \mathbf{b}_2^{(i)} \end{bmatrix}$ is the Jacobian matrix with the two vectors defined as:

$$\mathbf{b}_1^{(i)} = \begin{bmatrix} \frac{\partial}{\partial t} h(t_1 + \hat{\tau}^{(i)}) \\ \vdots \\ \frac{\partial}{\partial t} h(t_{N_{\mathrm{s}}} + \hat{\tau}^{(i)}) \end{bmatrix} \quad \mathbf{b}_2^{(i)} = \begin{bmatrix} h(t_1 + \hat{\tau}^{(i)}) \\ \vdots \\ h(t_{N_{\mathrm{s}}} + \hat{\tau}^{(i)}) \end{bmatrix} \tag{3.46}$$

Furthermore we know, from (3.38), that when the window size is long enough, the two vectors $\mathbf{b}_1^{(i)}$ and $\mathbf{b}_2^{(i)}$ will be orthogonal. Applying this to (3.44) results in:

$$\hat{\tau}^{(i+1)} = \hat{\tau}^{(i)} + \frac{1}{\hat{A}^{(i)}} \frac{\mathbf{b}_1^{(i)T}\mathbf{z}}{\left\|\mathbf{b}_1^{(i)}\right\|^2} \tag{3.47}$$

$$\hat{A}^{(i+1)} = \frac{\mathbf{b}_2^{(i)T}\mathbf{z}}{\left\|\mathbf{b}_2^{(i)}\right\|^2} \tag{3.48}$$

If we look at these two equations, we see that we can find an expression for the TOF $\hat{\tau}^{(i+1)}$, without explicitly calculating the estimate of the amplitude scaling:

$$\hat{\tau}^{(i+1)} = \hat{\tau}^{(i)} + \frac{\left\|\mathbf{b}_2^{(i)}\right\|^2}{\mathbf{b}_2^{(i)T}\mathbf{z}} \frac{\mathbf{b}_1^{(i)T}\mathbf{z}}{\left\|\mathbf{b}_1^{(i)}\right\|^2} \tag{3.49}$$

In order to use this estimator, we have to specify how we are able to evaluate the function $h_{\mathrm{z}}(\tau)$ and its derivative $\frac{\partial}{\partial\tau}h_{\mathrm{z}}(\tau)$ at arbitrary values of τ. To do this we use relation (3.41). In the discrete sampled case we can write this as:

$$\begin{bmatrix} h(t_1+\tau) \\ h(t_2+\tau) \\ \vdots \\ h(t_{N_{\mathrm{s}}}+\tau) \end{bmatrix} = \mathrm{IDFT}\left\{ \begin{bmatrix} e^{j\omega_1\tau}H(\omega_1) \\ e^{j\omega_2\tau}H(\omega_2) \\ \vdots \\ e^{j\omega_{N_{\mathrm{s}}}\tau}H(\omega_{N_{\mathrm{s}}}) \end{bmatrix} \right\} \tag{3.50}$$

where the elements $H(\omega_i)$ represent the discrete fourier transform (DFT) of the sampled time domain original source signal $h(t_i)$. The components ω_i represent the angular frequency that results from the DFT:

$$\omega_i = \begin{cases} 2\pi f_{\mathrm{s}}\dfrac{i-1}{N_{\mathrm{s}}} & i \leq \lceil \frac{N_{\mathrm{s}}+1}{2} \rceil \\ 2\pi f_{\mathrm{s}}\dfrac{i-1-n}{N_{\mathrm{s}}} & i > \lceil \frac{N_{\mathrm{s}}+1}{2} \rceil \end{cases} \tag{3.51}$$

The time derivative of the measurements function is then given by:

$$\begin{bmatrix} \frac{\partial}{\partial t}h_{\mathrm{z}}(t_1+\tau) \\ \frac{\partial}{\partial t}h_{\mathrm{z}}(t_2+\tau) \\ \vdots \\ \frac{\partial}{\partial t}h_{\mathrm{z}}(t_{N_{\mathrm{s}}}+\tau) \end{bmatrix} = \mathrm{IDFT}\left\{ \begin{bmatrix} j\omega_1 e^{j\omega_1\tau}H(\omega_1) \\ j\omega_2 e^{j\omega_2\tau}H(\omega_2) \\ \vdots \\ j\omega_{N_{\mathrm{s}}} e^{j\omega_{N_{\mathrm{s}}}\tau}H(\omega_{N_{\mathrm{s}}}) \end{bmatrix} \right\} \tag{3.52}$$

By using this measurements function and derivative of the measurements function, together with the iterative relation (3.49) the time delay estimator is fully described.

Monte-Carlo simulation of TOF Estimator

We know what the CRLB of the TOF estimate, given these source signals is. It is interesting to see how close the TOF estimator can get to this lower bound. To investigate this, we performed a Monte-Carlo simulation. As source signal we used a Gaussian pulse with a center frequency ($\frac{\omega_c}{2\pi}$) of 6 MHz and a bandwidth (B) of 4.7 MHz, which corresponds to $\frac{\omega_c}{2\pi} = 2$ MHz. These values correspond to the frequency content of a typical photoacoustic point source, measured with our ultrasound transducer. A realization of this source signal is displayed in Figure 3.2. Furthermore the sampling frequency (f_s) was set to 80 MHz which corresponds to the setting of our A/D converter. For each run in the Monte-Carlo simulation a random time delay was applied to the source signal and additive noise was added. The additive noise variance was ranged from $\sigma_z = 10^{-3}$ to $\sigma_z = 1$ over 100 steps on a logarithmic scale. For each step a simulation with 100.000 runs was performed.

As mentioned before, an initial time delay estimate was obtained by applying a Matched Filter on the measurements. This initial estimate was subsequently used as initialization for the Gauss-Newton based estimator. The accuracy of the Matched Filter is in principle limited by the sampling frequency. The time delay will then be uniformly distributed around the true time delay over the range $[-\frac{1}{2f_s}, \frac{1}{2f_s}]$. However, the accuracy can never be better than the CRLB, so what we expect is that the lower bound of the Matched Filter is given by the sum of CRLB and the limited sampling frequency effect:

$$\mathrm{Var}[\hat{\tau}] = \frac{\left(\frac{1}{f_s}\right)^2}{12} + \mathrm{CRLB} \tag{3.53}$$

The results of the Monte-Carlo simulation are displayed in Figure 3.7. Figure 3.7a shows the performance of the Matched Filter and Gauss-Newton based method together with the CRLB and the predicted Matched Filter Bound. We see that up to additive noise of $\sigma_z = 0.4$ the Gauss-Newton method is very close to the CRLB. The Matched Filter has a constant standard deviation on the estimate for this range as predicted and is outperformed by the Gauss-Newton based estimator. When the additive noise reaches a value $\sigma_z > 0.4$ we see that the Gauss-Newton based estimator starts to deviate from the CRLB and the Matched Filter starts to deviate from its predicted lower limit. This behavior can be explained by looking at the probability density functions that can be estimated from the results of the Monte-Carlo simulation. For low additive noise values, the pdf of the time delay estimate obtained with the Gauss-Newton based estimator is Gaussian distributed with its variance equal to the CRLB. This is illustrated in Figure 3.8a, for $\sigma_z = 0.01$, where a Gaussian distribution is plotted together with the pdf that can be reconstructed from the Monte-Carlo simulation. Also the pdf of the Matched Filter estimator is plotted and we see that it this pdf can be seen as the convolution of the Gaussian pdf based on the CRLB with the uniform pdf based on the limited sampling frequency. For higher additive noise values, both estimators do not follow their predicted lower bound and outliers are starting to occur, which is illustrated in Figure 3.8b. The percentage of outliers as a function of σ_z is displayed in Figure 3.7b. The average number of iterations required

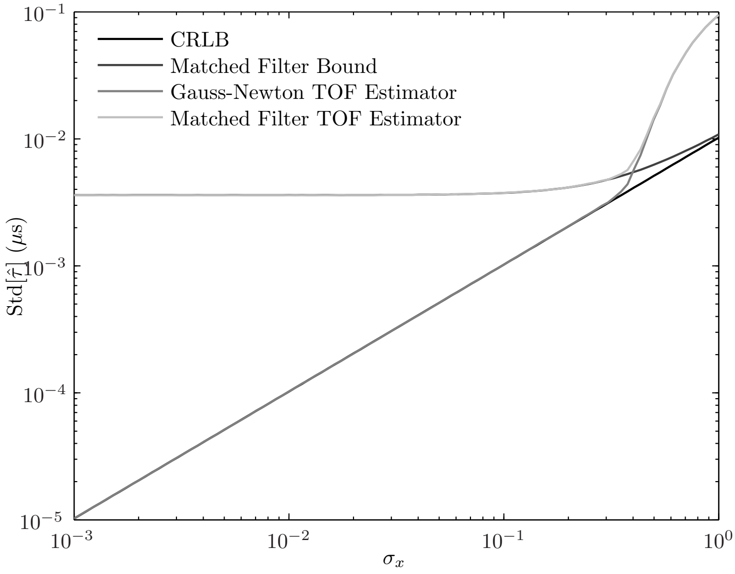

(a) Results of the estimator performance measured as the standard deviation of the estimated parameter and the theoretical lowest possible standard deviation on the parameter for this setting.

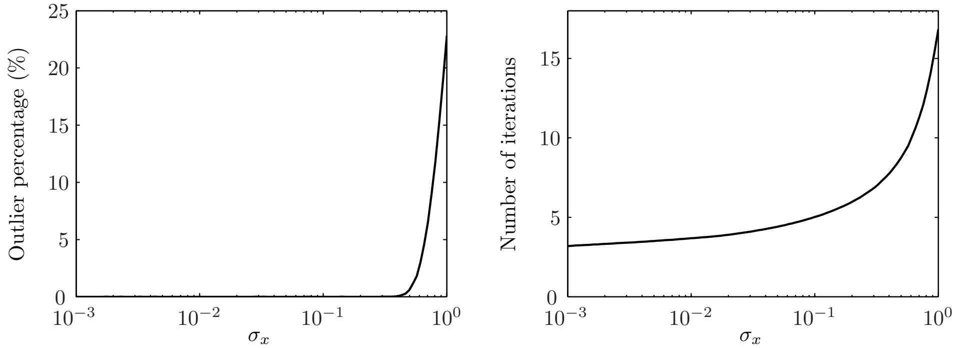

(b) Percentage of outlier occurances in the parameter estimate

(c) Average number of iterations required for convergence of the Gauss-Newton TOF estimator

Figure 3.7 Monte-Carlo simulation results of the Gauss-Newton and Matched Filter time delay estimators. The source signal used has a setting of $\frac{\omega_c}{2\pi} = 6\mathrm{MHz}$ and $\frac{\omega_b}{2\pi} = 2\mathrm{MHz}$. The sampling frequeny was $f_s = 80\mathrm{MHz}$. A realization of the signal is displayed in Figure 3.2. The simulation was carried out over a range of different additive noise variance (σ_z^2) values.

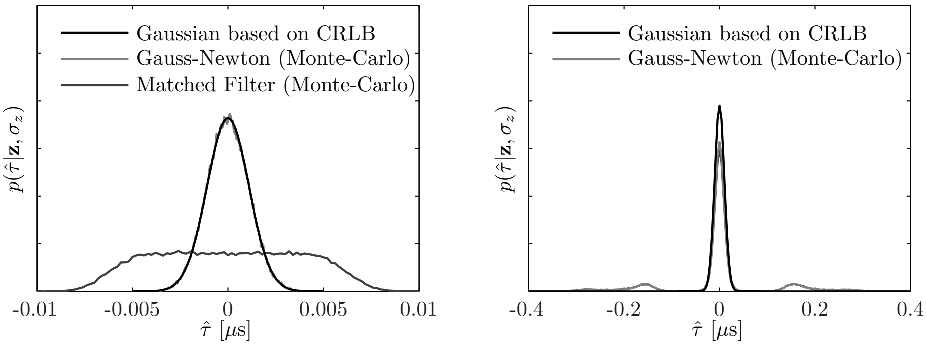

(a) pdf when $\sigma_\mathrm{z} = 0.01$

(b) pdf when $\sigma_\mathrm{z} = 1$

Figure 3.8 Probability density functions of the estimated time delay $\hat{\tau}$, obtained from Monte-Carlo simulations with two different values of additive noise σ_z.

for convergence was also investigated and is displayed in Figure 3.7c. The convergence was tested by comparing the difference between the last two iterations. When the difference becomes smaller than a pre-defined threshold convergence is reached. In the figure we see that when the amount of additive noise is increased, the number of iterations that is required for convergence also increases.

3.3.4 Conclusion

We have analyzed the problem of estimating the unknown TOF from the measurement of a photoacoustic source signal with an ultrasound transducer. The measured photoacoustic signal was represented as a sampled sine wave of a certain frequency modulated with a Gaussian envelope of a certain bandwidth. An estimator was derived which, for high SNR, equals the CRLB. Furthermore, an expression for the CRLB has been obtained, so that the CRLB can be predicted based parameters like the sampling frequency, the noise level, the transfer function center frequency and transfer function bandwidth.

3.4 Estimating acoustic attenuation

We now continue by including the frequency dependent part of the ultrasound propagation parameters. First two existing attenuation estimators will be introduced. These existing estimators, however, do not use the phase information, which can be used to estimate time delay dispersion and improve the accuracy of the attenuation estimate. After this introduction we will continue with our proposed attenuation estimators, where we also use the phase information.

3.4.1 Existing estimators

Spectral shift estimator

The spectral shift estimator [45, 46] is based on the fact that the magnitude of the spectrum of the input signal has a Gaussian distribution. The assumption is made that after propagation of a Gaussian modulated signal through a medium with a linear with frequency increasing attenuation function, i.e., $y = 1$, an output signal will result which still has a Gaussian distribution in the frequency domain. The signal will have the same bandwidth but a lower center frequency. The amount of down shift in center frequency is a measure for the attenuation constant α_0. Suppose the magnitude spectrum of the reference signal is given as:

$$|Y_\mathrm{w}(\omega)| = K_\mathrm{w} \exp\left[-\frac{1}{2}\frac{(\omega-\omega_\mathrm{c})^2}{\sigma^2}\right] \tag{3.54}$$

where ω_c is the angular center frequency of the Gaussian, σ is its bandwidth in the angular frequency domain and K_w is the magnitude of the Gaussian. If we measure an object signal with a linear attenuation function $\alpha(\omega) = \alpha_0|\omega|$, we get for the magnitude of the object measurement spectrum:

$$|Y_\mathrm{o}(\omega)| = K_\mathrm{o} \exp\left[-\frac{1}{2}\frac{(\omega-(\omega_\mathrm{c}-\alpha_0 d\sigma^2))^2}{\sigma^2}\right] \tag{3.55}$$

with

$$K_\mathrm{o} = K_\mathrm{w} \exp\left[-\alpha_r - \omega_\mathrm{c}\alpha_0 d + \tfrac{1}{2}\alpha_0^2 d^2\sigma^2\right] \tag{3.56}$$

The center frequency of the object signal after propagation through an object with a linear attenuation function is thus given by:

$$\omega_{\mathrm{c}'} = \omega_\mathrm{c} - \alpha_0 d\sigma^2 \tag{3.57}$$

From this we can observe that the resulting shift in center frequency is related to the attenuation constant α_0 according to:

$$\alpha_0 = \frac{1}{d}\frac{\omega_\mathrm{c}-\omega_{\mathrm{c}'}}{\sigma^2} \tag{3.58}$$

and to the reflection constant α_r:

$$\alpha_\mathrm{r} = \ln\left(\frac{K_\mathrm{w}}{K_\mathrm{o}}\right) - \frac{\omega_\mathrm{c}^2-\omega_{\mathrm{c}'}^2}{2\sigma^2} \tag{3.59}$$

where $\omega_{\mathrm{c}'}$ is the center frequency in the measured output spectrum. The question that now remains is, how do we estimate the center frequency of the measured signal.

There are several possibilities here:

Frequency of maximum For example one could take the frequency at which the magnitude spectrum attains a maximum.

$$\omega_{\mathrm{c}'} = \arg\max_\omega |Y_\mathrm{o}(\omega)| \tag{3.60}$$

First moment Another possibility is to calculate the center frequency by looking at the spectrum as a (Gaussian) probability density function (pdf) and calculating its first moment, which corresponds to the mean of the pdf:

$$\omega_{\mathrm{c}'} = \sum_i \omega_i \frac{|Y_{\mathrm{o}}(\omega_i)|}{\sum_j |Y_{\mathrm{o}}(\omega_j)|} \tag{3.61}$$

Correlation with Gaussian template A third possibility is to estimate the center frequency by making use of the information that the spectrum is Gaussian shaped with known variance but unknown mean. The mean (center frequency) can then be estimated by cross correlation of the spectrum with a Gaussian template and finding out the frequency that maximizes the cross correlation:

$$\omega_{\mathrm{c}'} = \arg\max_{\omega} \left(\sum_i \exp\left[\frac{-(\omega_i - \omega)^2}{\sigma^2} \right] |Y_{\mathrm{o}}(\omega_i)| \right) \tag{3.62}$$

Finally, when the new center frequency $\omega_{\mathrm{c}'}$ is estimated, the attenuation constant α_0 and reflection constant α_r can be calculated.

Log spectral difference method

Another commonly used estimator is based on fitting a parametrized curve through the difference in logarithm of the magnitude of the sample spectrum with the water spectrum[46, 47]. If we look at the log spectral difference expression:

$$\ln|Y_{\mathrm{o}}(\omega)| - \ln|Y_{\mathrm{w}}(\omega)| = -\alpha_0 |\omega|^y d - \alpha_{\mathrm{r}} \tag{3.63}$$

We see that this linearly relates the attenuation constant α_0 and the reflection constant α_{r} to the log spectral differences. In the log spectral difference method, we try to fit this linear function to the data in a least squares sense. We will stack the data in a vector:

$$\mathbf{z} = \begin{bmatrix} \ln|Y_{\mathrm{o}}(\omega_1)| - \ln|Y_{\mathrm{w}}(\omega_1)| \\ \vdots \\ \ln|Y_{\mathrm{o}}(\omega_n)| - \ln|Y_{\mathrm{w}}(\omega_n)| \end{bmatrix} \tag{3.64}$$

and relate the unknown parameters to the data via the matrix:

$$\mathbf{H} = \begin{bmatrix} -|\omega_1|^y d & -1 \\ \vdots & \vdots \\ -|\omega_n|^y d & -1 \end{bmatrix} \tag{3.65}$$

The unknown parameters are contained in the vector:

$$\mathbf{x} = \begin{bmatrix} \alpha_0 \\ \alpha_{\mathrm{r}} \end{bmatrix} \tag{3.66}$$

The solution to the problem is obtained by minimizing the least squares function:

$$\mathbf{x} = \arg\min_{\mathbf{x}} ||\mathbf{z} - \mathbf{H}\mathbf{x}||^2 \tag{3.67}$$

Which is equivalent (after setting the gradient to zero) to solving the linear system:

$$\mathbf{H}^T\mathbf{H}\mathbf{x} = \mathbf{H}^T\mathbf{z} \tag{3.68}$$

Due to noise on the data, we have to limit the frequency components of the spectrum that will be used in the estimation. Typically, we select frequency components which are above the noise level.

When the distance d is not known, the $\mathbf{H}$ matrix will be modified to not include d and the estimated parameters will then be the integrated attenuation $\alpha_0 d$ and α_r.

3.4.2 Proposed estimators

Based on the measurement relation defined in (3.13), we will now continue with the derivation of several estimators of the ultrasound propagation parameters. We will use the following parameterization of the propagation parameters:

$$\mathbf{x} = \begin{bmatrix} \alpha_0 \\ \alpha_r \\ \tau_0 \end{bmatrix} \tag{3.69}$$

being the attenuation constant, the reflection coefficient and the time delay per unit distance difference between the object and water respectively. The time delay per unit distance is related to the speed of sound in the object and the speed of sound in the water via:

$$\tau_0 = \frac{1}{c(\omega_0)} - \frac{1}{c_w} \tag{3.70}$$

We now define an attenuation and phase function, which are linearly dependent on the unknown parameters, and are contained in the time domain measurement function (3.13). The attenuation function will we define as, see (3.11):

$$h_{\text{att},i}(\mathbf{x}) = -x_1|\omega_i|^y d - x_2 \tag{3.71}$$

and the phase function as, see (3.11):

$$h_{\text{phase},i}(\mathbf{x}) = -\omega_i \left(x_3 + x_1 \tan\left(\frac{\pi}{2}y\right) \left(|\omega_i|^{y-1} - |\omega_0|^{y-1}\right) \right) d \tag{3.72}$$

When the distance d is not known, the measurement model can be changed so that $d = 1$. The resulting unknown parameters will be the integrated attenuation $\alpha_0 d$, the reflection α_r and the time delay $\tau_0 d$.

Using these functions we can write the frequency domain relation between the water and object signals as:

$$Y_{\text{o}}(\omega) = Y_{\text{w}}(\omega) \exp\left[h_{\text{att}}(\mathbf{x}) + jh_{\text{phase}}(\mathbf{x})\right] \tag{3.73}$$

We will use this relation on a limited frequency range and assume that the magnitude of the water signal $Y_{\mathrm{w}}(\omega)$ is zero for all frequencies above our Nyquist frequency $\frac{1}{2}\omega_{\mathrm{s}}$. Due to the limited transducer bandwidth this assumption will be realized. If furthermore, we assume that there is no DC component on the signal, we can use the frequencies between DC and half the sampling frequency $\frac{1}{2}\omega_{\mathrm{s}}$ to construct a time domain measurement function. The time domain measurement function is given by:

$$h_{\mathrm{t}}(\mathbf{x}) = \mathbf{V} \begin{bmatrix} Y_{\mathrm{w}}(\omega_1) \exp\left[h_{\mathrm{att},1}(\mathbf{x}) + j h_{\mathrm{phase},1}(\mathbf{x})\right] \\ \vdots \\ Y_{\mathrm{w}}(\omega_n) \exp\left[h_{\mathrm{att},n}(\mathbf{x}) + j h_{\mathrm{phase},n}(\mathbf{x})\right] \end{bmatrix} \tag{3.74}$$

Due to conjugate symmetry in the DFT operation and the fact that $Y_{\mathrm{w}}(\omega)$ is zero for the DC and half the sampling frequency, we write the equivalent relation:

$$h_{\mathrm{t}}(\mathbf{x}) = \mathrm{Re}\left\{ 2\tilde{\mathbf{V}} \begin{bmatrix} Y_{\mathrm{w}}(\omega_2) \exp\left[h_{\mathrm{att},2}(\mathbf{x}) + j h_{\mathrm{phase},2}(\mathbf{x})\right] \\ \vdots \\ Y_{\mathrm{w}}(\omega_m) \exp\left[h_{\mathrm{att},m}(\mathbf{x}) + j h_{\mathrm{phase},m}(\mathbf{x})\right] \end{bmatrix} \right\} \tag{3.75}$$

where

$$\tilde{\mathbf{V}} = \mathbf{V}_{(:,2:m)} \tag{3.76}$$

and where m is chosen so that it does not include the Nyquist frequency $\frac{1}{2}\omega_{\mathrm{s}}$:

$$m = \left\lceil \frac{n}{2} \right\rceil \tag{3.77}$$

As mentioned before, these time domain measurements are corrupted with additive white Gaussian noise $\mathbf{n}_{\mathrm{z_t}}$ with a variance of $\sigma_{z_t}^2$:

$$\mathbf{z}_{\mathrm{t}} = h_{\mathrm{t}}(\mathbf{x}) + \mathbf{n}_{\mathrm{z_t}} \tag{3.78}$$

The time domain measurement vector $\mathbf{z}_{\mathrm{t}}$ can now directly be used to formulate an estimator of the ultrasound propagation parameters or we can use several transforms to obtain different measurement vectors and construct different ultrasound propagation parameter estimators. In the following subsections we will investigate the different possibilities and formulate a maximum likelihood estimator for each of them. An overview of the possible transformations on $\mathbf{z}_t$ is displayed in Figure 3.9.

Time domain measurements

We start by exploring the possibility of formulating an estimator, directly based on the time domain measurements $\mathbf{z}_{\mathrm{t}}$. For these measurements, the noise is additive white Gaussian with equal variance $\sigma_{z_t}^2$ on all samples in $\mathbf{z}_{\mathrm{t}}$. The model that predicts the measurements from the parameters, $h_{\mathrm{t}}(\mathbf{x})$, is given in (3.75). The maximum likelihood estimate is in this case simply obtained by minimizing the function:

$$\hat{\mathbf{x}}_{\mathrm{ML}} = \arg\min_{\mathbf{x}} ||\mathbf{z}_{\mathrm{t}} - h_{\mathrm{t}}(\mathbf{x})||^2 \tag{3.79}$$

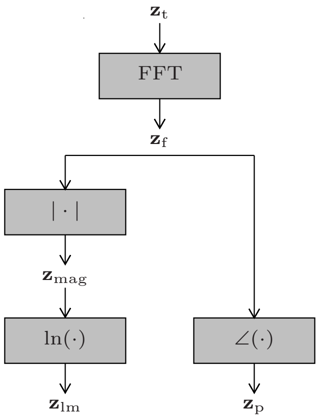

Figure 3.9 Overview of the possible transformations to different measurement domains.

Since the time domain measurement function $h_t(\mathbf{x})$ is nonlinear, we recognize here the nonlinear least squares problem [35]. We will solve this problem via the Gauss-Newton method, which means a linear approximation of $h_t(\mathbf{x})$ is made at a point $\hat{\mathbf{x}}^{(k)}$:

$$h_\mathrm{t}(\mathbf{x}) \approx h_\mathrm{t}(\hat{\mathbf{x}}^{(k)}) + \mathbf{H}_\mathrm{t}^{(k)}(\mathbf{x} - \hat{\mathbf{x}}^{(k)}) \tag{3.80}$$

where $\mathbf{H}_\mathrm{t}^{(k)}$ is the Jacobian matrix which can be calculated as:

$$\mathbf{H}_\mathrm{t}^{(k)} = \mathrm{Re}\left\{ 2\tilde{\mathbf{V}} \begin{bmatrix} Y_\mathrm{w}(\omega_2)\exp\left[h_{\mathrm{mag},2}(\hat{\mathbf{x}}^{(k)}) + jh_{\mathrm{phase},2}(\hat{\mathbf{x}}^{(k)})\right](\nabla h_{\mathrm{mag},2} + j\nabla h_{\mathrm{phase},2})^T \\ \vdots \\ Y_\mathrm{w}(\omega_m)\exp\left[h_{\mathrm{mag},m}(\hat{\mathbf{x}}^{(k)}) + jh_{\mathrm{phase},m}(\hat{\mathbf{x}}^{(k)})\right](\nabla h_{\mathrm{mag},m} + j\nabla h_{\mathrm{phase},m})^T \end{bmatrix} \right\}$$

where gradients of $h_{\mathrm{mag},i}(\mathbf{x})$ and $h_{\mathrm{phase},i}(\mathbf{x})$ are simply given by:

$$\nabla h_{\mathrm{mag},i} = \begin{bmatrix} |\omega_i|^y d \\ -1 \\ 0 \end{bmatrix} \tag{3.81}$$

$$\nabla h_{\mathrm{phase},i} = \begin{bmatrix} -\omega_i d \\ 0 \\ -\omega_i d \tan\left(\frac{\pi}{2}y\right)\left(|\omega_i|^{y-1} - |\omega_0|^{y-1}\right) \end{bmatrix} \tag{3.82}$$

A solution to the nonlinear least squares problem is then found by iteratively minimizing the quadratic function:

$$\hat{\mathbf{x}}^{(k+1)} = \arg\min_{\mathbf{x}} ||h_\mathrm{t}(\hat{\mathbf{x}}^{(k)}) + \mathbf{H}_\mathrm{t}^{(k)}(\mathbf{x} - \hat{\mathbf{x}}^{(k)}) - \mathbf{z}_t||^2 \tag{3.83}$$

This process is iterated until convergence is obtained. In each iteration, the solution to the quadratic function is found by finding an expression of the gradient of this function and setting it to zero. Doing this results in a linear system that has to be solved for $\mathbf{x}$:

$$\mathbf{H}_{\mathrm{t}}^{(k)T}\mathbf{H}_{\mathrm{t}}^{(k)}\mathbf{x} = \mathbf{H}_{\mathrm{t}}^{(k)T}\left(\mathbf{z}_t + \mathbf{H}_{\mathrm{t}}^{(k)}\hat{\mathbf{x}}^{(k)} - h_{\mathrm{t}}(\hat{\mathbf{x}}^{(k)})\right) \tag{3.84}$$

Solving the linear system of equations gives the new solution $\hat{\mathbf{x}}^{(k+1)}$. The process is repeated iteratively until convergence is obtained. To start the algorithm, an initial solution $\hat{\mathbf{x}}^{(0)}$ is required.

Complex frequency domain measurements

The time domain measurements can be converted to the frequency domain via a DFT operation. Applying this transformation on the time domain measurements will result in a new measurement vector, $\mathbf{z}_f$. This new vector contains a DC component, possibly a Nyquist component (when n is even) and two conjugate symmetric complex parts. The Nyquist component cannot be used, because it contains a phase ambiguity and does not contain any information on our parameters. We assume that the signals are DC free, so the DC component will also not be used. Furthermore, the two conjugate symmetric parts contain duplicate information, so we need only one of these parts. The remaining frequency components can be calculated via a cropped DFT transform:

$$\mathbf{z}_{\mathrm{f}} = \tilde{\mathbf{W}}\mathbf{z}_{\mathrm{t}} \quad \text{with} \quad \tilde{\mathbf{W}} = \mathbf{W}_{(2:m,:)} \tag{3.85}$$

which can also efficiently calculated using the FFT and afterwards leaving out the elements we are not interested in. These obtained vector $\mathbf{z}_{\mathrm{f}}$ with frequency domain measurements is related to the parameters via:

$$\mathbf{z}_{\mathrm{f}} = h_{\mathrm{f}}(\mathbf{x}) + \mathbf{n}_{\mathrm{f}} \tag{3.86}$$

where the frequency domain measurement function here is:

$$h_{\mathrm{f}}(\mathbf{x}) = \begin{bmatrix} Y_{\mathrm{w}}(\omega_2)\exp\left[h_{\mathrm{att},2}(\mathbf{x}) + jh_{\mathrm{phase},2}(\mathbf{x})\right] \\ \vdots \\ Y_{\mathrm{w}}(\omega_m)\exp\left[h_{\mathrm{att},m}(\mathbf{x}) + jh_{\mathrm{phase},m}(\mathbf{x})\right] \end{bmatrix} \tag{3.87}$$

Due to the linearity of the DFT transform, the obtained complex noise vector $\mathbf{n}_{\mathrm{f}}$ is Gaussian distributed. Because the time domain measurements are white with equal variance $\sigma_{z_{\mathrm{t}}}^2$, and because $\mathrm{Re}(\tilde{\mathbf{W}})\mathrm{Re}(\tilde{\mathbf{W}})^T = \mathrm{Im}(\tilde{\mathbf{W}})\mathrm{Im}(\tilde{\mathbf{W}})^T = \frac{n}{2}\mathbf{I}$, the real and complex part of $\mathbf{z}_{\mathrm{f}}$ are also Gaussian distributed with equal variance:

$$\sigma_{z_{\mathrm{f}}}^2 = \frac{n}{2}\sigma_{z_{\mathrm{t}}}^2 \tag{3.88}$$

Obtaining a maximum likelihood estimate from $\mathbf{z}_{\mathrm{f}}$ is similar to the approach used on the time domain measurements. The Jacobian of the measurement function $h_f(\mathbf{x})$

is similar to the time domain Jacobian, but now is complex valued:

$$\mathbf{H}_\mathrm{f}^{(k)} = \begin{bmatrix} Y_\mathrm{w}(\omega_2)\exp\left[h_{\mathrm{mag},2}(\hat{\mathbf{x}}^{(k)}) + jh_{\mathrm{phase},2}(\hat{\mathbf{x}}^{(k)})\right](\nabla h_{\mathrm{mag},2} + j\nabla h_{\mathrm{phase},2})^T \\ \vdots \\ Y_\mathrm{w}(\omega_m)\exp\left[h_{\mathrm{mag},m}(\hat{\mathbf{x}}^{(k)}) + jh_{\mathrm{phase},m}(\hat{\mathbf{x}}^{(k)})\right](\nabla h_{\mathrm{mag},n} + j\nabla h_{\mathrm{phase},n})^T \end{bmatrix}$$

The linear system of equations in each iteration consists of stacking the real and imaginary parts together and thus creating a system of equations having only real valued entries. To illustrate this we calculate a real valued Jacobian matrix $\mathbf{A}^{(k)}$ and a real valued residue vector $\mathbf{b}^{(k)}$:

$$\mathbf{A}^{(k)} = \begin{bmatrix} \mathrm{Re}\{\mathbf{H}_\mathrm{f}^{(k)}\} \\ \mathrm{Im}\{\mathbf{H}_\mathrm{f}^{(k)}\} \end{bmatrix} \tag{3.89}$$

$$\mathbf{b}^{(k)} = \begin{bmatrix} \mathrm{Re}\{\mathbf{z}_\mathrm{f} - h_\mathrm{f}(\hat{\mathbf{x}}^{(k)})\} \\ \mathrm{Im}\{\mathbf{z}_\mathrm{f} - h_\mathrm{f}(\hat{\mathbf{x}}^{(k)})\} \end{bmatrix} \tag{3.90}$$

The linear system of equations that has to be solved in each iteration is then given by:

$$\mathbf{A}^{(k)T}\mathbf{A}^{(k)}\mathbf{x} = \mathbf{A}^{(k)T}(\mathbf{b}^{(k)} - \mathbf{A}^{(k)}\hat{\mathbf{x}}^{(k)}) \tag{3.91}$$

The resulting estimator is mathematically equivalent to the time domain estimator and we expect exactly the same performance for both estimators. The advantage however of the frequency domain estimator is that its computationally more efficient. In the frequency domain estimator, the DFT only has to be calculated once on the measurements instead of in every iteration on the Jacobian.

Magnitude spectrum measurements

From the complex frequency domain measurements, we can go to magnitude measurements in the frequency domain by taking the absolute value of the complex data vector $\mathbf{z}_\mathrm{f}$. This is the same domain in which the previously discussed spectral shift estimator operates. We will now investigate how a maximum likelihood estimator can be obtained for these measurements and how this compares to the spectral shift estimator. By working in this domain, we will only be able to estimate attenuation and not the speed of sound, since phase information is discarded. The magnitude measurements are obtained from the complex frequency domain measurements via:

$$\mathbf{z}_\mathrm{mag} = \begin{bmatrix} |z_{\mathrm{f},1}| \\ \vdots \\ |z_{\mathrm{f},m}| \end{bmatrix} \tag{3.92}$$

Since the noise on those real and imaginary parts of $\mathbf{z}_\mathrm{f}$ is additive and independently Gaussian distributed with variance $\sigma_{z_f}^2$, taking the absolute value will result in measurements having a Rice distribution[48], with a pdf of:

$$p(z_{\mathrm{mag},i}|\nu_i,\sigma) = \frac{z_{\mathrm{mag},i}}{\sigma^2}\exp\left[\frac{-(z_{\mathrm{mag},i}^2 + \nu_i^2)}{2\sigma^2}\right] I_0\left(z_{\mathrm{mag},i}\frac{\nu_i}{\sigma^2}\right) \tag{3.93}$$

with $\nu_i = |Y_{\mathrm{w}}(\omega_i)| \exp\left[h_{\mathrm{att},i}(\mathbf{x})\right]$ and $\sigma = \sigma_{z_f}$. For measurement elements with a large signal to noise (SNR) ratio, the distribution of the noise on the measurements converge to a Gaussian distribution. The SNR is defined as:

$$\mathrm{SNR} = \frac{|Y_{\mathrm{w}}(\omega_i)| \exp\left[h_{\mathrm{att},i}(\mathbf{x})\right]}{\sigma_{z_f}} \tag{3.94}$$

A SNR of three or higher already approximates the Gaussian distribution quite well. The variance in that case can be approximated with:

$$\sigma^2_{z_{\mathrm{mag}}} \approx \sigma^2_{z_{\mathrm{f}}} = \frac{n}{2}\sigma^2_{z_{\mathrm{t}}} \tag{3.95}$$

The mean of the random variable $z_{\mathrm{mag},i}$ approximates the value of $\nu_i = |Y_{\mathrm{w}}(\omega_i)| \exp\left[h_{\mathrm{att},i}(\mathbf{x})\right]$. Thus for large SNR values we can say that the magnitude measurement function can be approximated as:

$$\mathbf{z}_{\mathrm{mag}} \approx \begin{bmatrix} |Y_{\mathrm{w}}(\omega_2)| \exp\left[h_{\mathrm{att},2}(\mathbf{x})\right] \\ \vdots \\ |Y_{\mathrm{w}}(\omega_m)| \exp\left[h_{\mathrm{att},m}(\mathbf{x})\right] \end{bmatrix} + \mathbf{n}_{z_{\mathrm{mag}}} \tag{3.96}$$

where $\mathbf{n}_{z_{\mathrm{mag}}}$ is additive Gaussian white noise with variance $\sigma^2_{z_{\mathrm{mag}}} = \sigma^2_{z_{\mathrm{f}}} = \frac{n}{2}\sigma^2_{z_{\mathrm{t}}}$.

Finding an approximate maximum likelihood solution then comes down to minimizing yet another non-linear least squares problem. The problem now only involves the parameters and $\alpha_0 = x_1$ and $\alpha_r = x_2$, since phase information is discarded when using magnitude spectrum measurements. The non-linear least squares expression can be written as:

$$\hat{\mathbf{x}}_{\mathrm{ML}} \approx \arg\min_{\mathbf{x}} \|\mathbf{z}_{\mathrm{mag}} - e^{-x_2} h_{\mathrm{mag}}(x_1)\|^2 \tag{3.97}$$

where the vector function $h_{\mathrm{mag}}(x_1)$ is defined as:

$$h_{\mathrm{mag}}(x_1) = \begin{bmatrix} |Y_w(\omega_2)| \exp[-x_1|\omega_1|^y] \\ \vdots \\ |Y_w(\omega_m)| \exp[-x_1|\omega_m|^y] \end{bmatrix} \tag{3.98}$$

Finding the minimum of this function can be split into two parts. First solving for the parameters x_2, i.e., the parameter that models the frequency independent attenuation, and later on using that result and then solve for the remaining parameters x_1. We will see that this gives a nice comparison with the approach of the spectral shift estimator in this approximated maximum likelihood framework.

Finding the minimum of (3.97) for x_2, by setting the partial derivative of the function with respect to x_2 to zero, gives us:

$$-2e^{-2x_2}||h_{\mathrm{mag}}(x_1)||^2 + 2e^{-x_2}\mathbf{z}^T_{\mathrm{mag}} h_{\mathrm{mag}}(x_1) = 0 \tag{3.99}$$

which can be solved for x_2:

$$\hat{x}_{\mathrm{ML},2} = -\ln\left(\frac{\mathbf{z}^T_{\mathrm{mag}} h_{\mathrm{mag}}(x_1)}{||h_{\mathrm{mag}}(x_1)||^2}\right) \tag{3.100}$$

We have now found an expression for x_2 at the position of the minimum. If we substitute this expression in the function we want to minimize we obtain an expression dependent only on x_1:

$$\hat{x}_{\mathrm{ML},1} = \arg\min_{x_1} \left(||\mathbf{z}_{\mathrm{mag}}||^2 - \left(\mathbf{z}_{\mathrm{mag}}^T \frac{h_{\mathrm{mag}}(x_1)}{||h_{\mathrm{mag}}(x_1)||} \right)^2 \right) \tag{3.101}$$

Finding the minimum of this equation is equivalent to finding the maximum of:

$$\hat{x}_{\mathrm{ML},1} = \arg\max_{x_1} \left(\mathbf{z}_{\mathrm{mag}}^T \frac{h_{\mathrm{mag}}(x_1)}{||h_{\mathrm{mag}}(x_1)||} \right) \tag{3.102}$$

This is justified because the first term is independent of x_1 and in the second term both vectors $\mathbf{z}_{\mathrm{mag}}$ and $h_{\mathrm{mag}}(x_1)$ contain only positive elements meaning we can eliminate the square. The final expression for x_1 now shows that we can solve this problem via a correlation/matched filter approach. The measurement vector $\mathbf{z}_{\mathrm{mag}}$ has to be correlated with different (normalized) realizations of the predicted measurements $\frac{h_{\mathrm{mag}}(x_1)}{||h_{\mathrm{mag}}(x_1)||}$. The value of x_1 which generates the maximum correlation value is the value which gives the maximum likelihood solution based on magnitude measurements. This result suggests that, when using the spectral frequency shift method, it is best to use it with the matched filtering approach with a Gaussian template to find the center frequency, since that is confirm the approximate likelihood solution that we have obtained here.

The corresponding value of x_2 can be calculated from x_1 via (3.100). Finding the value for x_1 is a one-dimensional optimization problem, which we will solve using Brent's method [49]. Brent's method is an efficient method to solve scalar optimization problems and is a combination of a golden section search and inverse quadratic interpolation. As initial bounds of the problem we use 0 as lower bound and an upper bound which can be chosen based on the object and maximum expected attenuation.

Log magnitude spectrum measurements

Applying a log function on the magnitude spectrum measurements gives us an expression which is, after subtraction of a remaining constant offset, linear dependent on the unknown parameters. This is the same domain in which the previously discussed log spectral difference method operates. Linear problems are easier to solve than non-linear problems so we will investigate how this affects our problem and how taking the measurement noise explicitly into account can improve the accuracy of the estimate with respect to the log spectral difference method.

Taking the log of the magnitude (lm) and removing the offset gives us the log magnitude measurements:

$$\mathbf{z}_{\mathrm{lm}} = \begin{bmatrix} \ln|z_{f,2}| \\ \vdots \\ \ln|z_{f,m}| \end{bmatrix} - \begin{bmatrix} \ln|Y_w(\omega_2)| \\ \vdots \\ \ln|Y_w(\omega_m)| \end{bmatrix} \tag{3.103}$$

Applying this transformation will lead to measurements with a noise distribution which is not Gaussian. However, for high SNR values the noise can be approximated as additive Gaussian noise. The measurement transformation function from the complex frequency domain to the log magnitude frequency domain is given by:

$$z_{\mathrm{lm}} = g_{\mathrm{lm}}(z_{\mathrm{f,Re}}, z_{\mathrm{f,Im}}) = \ln\left(\sqrt{z_{\mathrm{f,Re}}^2 + z_{\mathrm{f,Im}}^2}\right) - \ln|Y_w(\omega)| \tag{3.104}$$

By linearizing this equation, we can propagate the noise resulting in a variance on the log magnitude measurements of:

$$\sigma_{z_{\mathrm{lm}},i}^2 = \left(\frac{\sigma_{z_{\mathrm{f}}}}{|Y_w(\omega_i)|\exp[h_{\mathrm{att},i}(\mathbf{x})]}\right)^2 = \frac{1}{\mathrm{SNR}^2} \tag{3.105}$$

Meaning that the variance of the log magnitude measurements is frequency dependent and also dependent on the actual value of the parameters that we want to estimate (x_1 and x_2). The standard deviation of the log magnitude measurements is actually the inverse of the SNR. If we want to use the Gaussian assumption on the distribution of the noise, we have to limit ourselves in the estimation procedure to frequency components which have a signal above the noise floor. Suppose we have made a selection of frequency components with a high enough SNR, we will come back to chosing this set later, $\boldsymbol{\omega}_{\mathrm{s}} = \{\omega_1, \ldots, \omega_k\}$. Using this set we can setup the linear measurement relation:

$$\mathbf{z}_{\mathrm{lm}} \approx \mathbf{H}_{\mathrm{lm}}\mathbf{x} + \mathbf{n}_{\mathrm{lm}} \tag{3.106}$$

where the matrix $\mathbf{H}_{\mathrm{lm}}$ is given by:

$$\mathbf{H}_{\mathrm{lm}} = \begin{bmatrix} -|\omega_1|^y d & -1 \\ \vdots & \vdots \\ -|\omega_k|^y d & -1 \end{bmatrix} \tag{3.107}$$

and the noise vector $\mathbf{n}_{\mathrm{lm}}$ contains additive zero mean Gaussian noise with a covariance matrix equal to:

$$\mathbf{P}_{z_{\mathrm{lm}}z_{\mathrm{lm}}} = \begin{bmatrix} \sigma_{z_{\mathrm{lm}},1}^2 & 0 & 0 \\ 0 & \ddots & 0 \\ 0 & 0 & \sigma_{z_{\mathrm{lm}},k}^2 \end{bmatrix} \tag{3.108}$$

We have to keep in mind here that the covariance matrix is also dependent on the parameter vector $\mathbf{x}$, as is shown in (3.105). Obtaining a maximum likelihood expression is then defined by maximizing the function:

$$\mathbf{x}_{\mathrm{ML}} \approx \arg\max_{\mathbf{x}} \frac{1}{|2\pi\mathbf{P}_{z_{\mathrm{lm}}z_{\mathrm{lm}}}|^{\frac{1}{2}}} e^{-(\mathbf{H}_{\mathrm{lm}}\mathbf{x}-\mathbf{z}_{\mathrm{lm}})^T\mathbf{P}_{z_{\mathrm{lm}}z_{\mathrm{lm}}}^{-1}(\mathbf{H}_{\mathrm{lm}}\mathbf{x}-\mathbf{z}_{\mathrm{lm}})} \tag{3.109}$$

A biased estimate of $\mathbf{x}_{\mathrm{ML}}$ can be obtained by ignoring the normalizing term and minimizing the function:

$$\mathbf{x}_{\mathrm{ML}} = \arg\min_{\mathbf{x}}(\mathbf{H}_{\mathrm{lm}}\mathbf{x} - \mathbf{z}_{\mathrm{lm}})^T\mathbf{P}_{z_{\mathrm{lm}}z_{\mathrm{lm}}}^{-1}(\mathbf{H}_{\mathrm{lm}}\mathbf{x} - \mathbf{z}_{\mathrm{lm}}) \tag{3.110}$$

The solution can be found after setting the gradient of this function to zero, and results in solving the linear system:

$$\mathbf{H}_{\mathrm{lm}}^{T}\mathbf{P}_{z_{\mathrm{lm}}z_{\mathrm{lm}}}^{-1}\mathbf{H}_{\mathrm{lm}}\mathbf{x} = \mathbf{H}_{\mathrm{lm}}^{T}\mathbf{P}_{z_{\mathrm{lm}}z_{\mathrm{lm}}}^{-1}\mathbf{z}_{\mathrm{lm}} \tag{3.111}$$

This might look like an ordinary weighted least squares problem at first, however the weights (residing on the diagonal of the inverse covariance matrix) and the the selection of the frequency components $\boldsymbol{\omega}_{\mathrm{s}}$ are both dependent on the unknown parameters $\mathbf{x}$. Solving this problem requires an iterative approach at which in each iteration, the previous solution of $\mathbf{x}$ is used in the evaluation of the covariance matrix and the selection of valid frequency components.

Determining the set of frequencies with a high enough SNR If the full vector of available positive frequencies is given by $\boldsymbol{\omega}_{\mathrm{pos}} = \{\omega_2, \ldots, \omega_m\}$, then the frequency components which are above the noise floor are given by:

$$\boldsymbol{\omega}_{\mathrm{s}} = \left\{ \omega_i : \omega_i \in \boldsymbol{\omega}_{\mathrm{pos}} \wedge \frac{|Y_w(\omega_i)| \exp[h_{\mathrm{att},i}(\mathbf{x})]}{\sigma_{z_{\mathrm{f}}}} > \mathrm{SNR}_{\mathrm{th}} \right\} \tag{3.112}$$

A good value of the selection threshold $\mathrm{SNR}_{\mathrm{th}}$ has to be determined and will be discussed during the evaluation of the algorithm. In the first iteration, there is no previous solution of $\mathbf{x}$ available. This is not a big problem, since what we actually are interested in are the selection of parameters $\boldsymbol{\omega}_{\mathrm{s}}$ and the weights. We can get initial estimates of both quantities based on the magnitude measurements $\mathbf{z}_{\mathrm{mag}}$:

$$\boldsymbol{\omega}_{\mathrm{s}} = \left\{ \omega_i : \omega_i \in \boldsymbol{\omega}_{\mathrm{pos}} \wedge \frac{z_{\mathrm{mag},i}}{\sigma_{z_{\mathrm{f}}}} > \mathrm{SNR}_{\mathrm{th}} \right\} \tag{3.113}$$

and for the variance used in the weight calculation:

$$\sigma_{z_{\mathrm{lm}},i}^{2} = \left(\frac{\sigma_{z_{\mathrm{f}}}}{z_{\mathrm{mag},i}} \right)^{2} \tag{3.114}$$

For relative high SNR, taking the actual measurement $\mathbf{z}_{\mathrm{mag}}$ will work, but for lower SNR the measurement can be too noisy to get a robust initial estimate of $\boldsymbol{\omega}_{\mathrm{s}}$ and $\sigma_{z_{\mathrm{lm}},i}^{2}$. The robustness can be improved by removing some of the noise from $\mathbf{z}_{\mathrm{mag}}$ and use the noise filtered measurement instead to calculate the initial estimates of $\boldsymbol{\omega}_{\mathrm{s}}$ and $\sigma_{z_{\mathrm{lm}},i}^{2}$. The filtered measurement will be obtained by incorporating prior knowledge on the expected magnitude measurements. This prior knowledge comes mainly from the known input magnitude signal $|Y_w(\omega)|$:

1. We know that the object magnitude measurement has an amplitude not higher, but probably lower, than the reference magnitude signal.

2. The reference magnitude signal has a certain degree of smoothness which will also be present in the object magnitude measurement. Due to the bandwidth limitations of the received transducer, it will be a unimodal smooth function.

If we look at the noise that is present on the object magnitude measurement and the amplitudes of the reference magnitude signal, we can restrict the frequency region of interest, $\boldsymbol{\omega}_{\mathrm{s}}$ already by:

$$\boldsymbol{\omega}_{\mathrm{s,w}} = \left\{ \omega_i : \omega_i \in \boldsymbol{\omega}_{\mathrm{pos}} \wedge \frac{|Y_{\mathrm{w}}(\omega_i)|}{\sigma_{z_{\mathrm{f}}}} > \mathrm{SNR}_{\mathrm{th}} \right\} \tag{3.115}$$

The region of interest of the object magnitude measurement, which only consists of the frequency components $\boldsymbol{\omega}_{\mathrm{s,w}}$ will be refered to as $\mathbf{z}_{\mathrm{mag,roi}}$. The object magnitude signal will have the same amount of smoothness as the reference magnitude signal. We can express this smoothness by assuming that the reference magnitude signal can approximately be represented by a second order polynomial. This means that the third order derivative will be very small and can be added as a constraint for our filter. The approximate expected mean squared value of the third order derivative of the object magnitude signal can be calculated by calculating the third order derivative of the reference magnitude signal. The calculation will be carried out over the selected region of interest:

$$\mathbf{y}_{\mathrm{mag}} = \left\{ |Y(\omega_i)| : \omega_i \in \boldsymbol{\omega}_{\mathrm{pos}} \wedge \frac{|Y_{\mathrm{w}}(\omega_i)|}{\sigma_{z_{\mathrm{f}}}} > \mathrm{SNR}_{\mathrm{th}} \right\} \tag{3.116}$$

with a third order derivative matrix:

$$\mathbf{G}_3 = \left(\frac{1}{2}\right)^3 \begin{bmatrix} -1 & 3 & -3 & 1 & 0 & \dots & 0 \\ 0 & -1 & 3 & -3 & 1 & \dots & 0 \\ \vdots & \vdots & \ddots & \ddots & \ddots & \ddots & \vdots \\ 0 & 0 & \dots & -1 & 3 & -3 & 1 \end{bmatrix} \tag{3.117}$$

The mean squared value of the third order derivative of the reference magnitude signal is then given by:

$$\sigma^2_{G_3,\mathrm{w}} = \frac{1}{k_{\mathrm{roi}}} \left(\mathbf{G}_3 \mathbf{y}_{\mathrm{mag}}\right)^T \mathbf{G}_3 \mathbf{y}_{\mathrm{mag}} \tag{3.118}$$

where k_{roi} represents the number of elements in the vector $\mathbf{y}_{\mathrm{mag}}$. This value has to be scaled down due to the attenuating effects of the object. An approximate scaling factor can be calculated by considering the ratio of the reference magnitude signal to the object magnitude signal. We will obtain this ratio by dividing the maximum of the reference magnitude signal with the maximum of the object magnitude measurement:

$$\sigma^2_{G_3} = \left(\frac{\max\left(\mathbf{z}_{\mathrm{mag,roi}}\right)}{\max\left(\{|Y_{\mathrm{w}}(\omega_i)| : \omega_i \in \boldsymbol{\omega}_{\mathrm{s,w}}\} \right)} \right)^2 \sigma^2_{G_3,\mathrm{w}} \tag{3.119}$$

Finally, the filtered object magnitude measurement can be calculated by maximizing:

$$\mathbf{z}_{\mathrm{mag,f}} = \arg\min_{\mathbf{z}} \left(\frac{1}{\sigma^2_{z_{\mathrm{mag}}}} ||\mathbf{z} - \mathbf{z}_{\mathrm{mag}}||^2 + \frac{1}{\sigma^2_{G_3}} ||\mathbf{G}_3 \mathbf{z}||^2 \right) \tag{3.120}$$

The first term is a likelihood cost function maximizing the measurement fit and the second term is a regularizing cost function which maximizes the smoothness of the solution. The maximum of this optimization function can be obtained by setting its gradient to zero, resulting in:

$$\mathbf{z}_{\mathrm{mag,f}} = \left(\mathbf{I} + \frac{\sigma^2_{z_{\mathrm{mag}}}}{\sigma^2_{G_3}} \mathbf{G}_3^T \mathbf{G}_3 \right)^{-1} \mathbf{z}_{\mathrm{mag}} \tag{3.121}$$

where $\mathbf{I}$ is the identiy matrix. The resulting filtered object magnitude measurement $\mathbf{z}_{\mathrm{mag,f}}$ can now be used in the initialization to calculate $\boldsymbol{\omega}_{\mathrm{s}}$ and $\sigma^2_{z_{\mathrm{lm}},i}$.

Log magnitude and phase spectrum measurements

In the previous linear estimator, we were able to estimate only the attenuating parameters α_0 and α_r. If we add the phase of the object measurement, we have observations of the time delay per unit distance τ_0 as well. The phase measurements can be obtained from the complex frequency domain measurements $\mathbf{z}_{\mathrm{f}}$ by calculating the argument. Care should be taken when calculating the argument, since it is a quantity which ranges between -π and π. To deal with this problem, we use the phase of the reference measurement Y_w and an initial estimate of the parameters $\alpha_0^{(k)}$ and $\tau_0^{(k)}$ in the phase calculation:

$$z_{\mathrm{p},i} = \arg \left\{ \frac{z_{\mathrm{f},i}}{Y_w(\omega_i)} \exp\left[-jh_{\mathrm{phase},i}(\hat{\mathbf{x}}^{(k)}) \right] \right\} + h_{\mathrm{phase},i}(\hat{\mathbf{x}}^{(k)}) \tag{3.122}$$

The phase measurements $\mathbf{z}_{\mathrm{p}} = [z_{\mathrm{p},1}, \ldots, z_{\mathrm{p},m}]^T$ are linearly related to the attenuation parameters α_0 and the time delay per unit distance τ_0. However, again the noise distribution on these measurements is not Gaussian. But also here, for high enough SNR values the noise can be approximated as additive Gaussian noise. Obtaining the argument from the complex frequency domain measurements can be performed by the transformation:

$$z_{\mathrm{p}} = g_{\mathrm{p}}(z_{\mathrm{f,Re}}, z_{\mathrm{f,Im}}) = \arctan\left(\frac{z_{\mathrm{f,Re}}}{z_{\mathrm{f,Im}}} \right) \tag{3.123}$$

Via linearization the noise can be propagated, resulting in a variance of:

$$\sigma^2_{z_{\mathrm{p}}} = \left(\frac{\sigma_{z_{\mathrm{f}}}}{|Y_w(\omega)| \exp[h_{\mathrm{att}}(\mathbf{x})]} \right)^2 \tag{3.124}$$

Which conveniently is exactly the same variance that we have on the log magnitude measurements. We can thus use the same selection procedure for $\boldsymbol{\omega}_{\mathrm{s}}$, being the frequency components with a high enough SNR. For this selection of frequencies, the phase measurement relation is given by:

$$\mathbf{z}_{\mathrm{p}} = \mathbf{H}_{\mathrm{p}}\mathbf{x} + \mathbf{n}_{\mathrm{p}} \tag{3.125}$$

Where the matrix $\mathbf{H}_{\mathrm{p}}$ is given by:

$$\mathbf{H}_{\mathrm{p}} = \begin{bmatrix} -\omega_1 \tan\left(\frac{\pi}{2}y\right)\left(|\omega_1|^{y-1} - |\omega_0|^{y-1}\right)d & 0 & -\omega_1 d \\ \vdots & \vdots & \vdots \\ -\omega_k \tan\left(\frac{\pi}{2}y\right)\left(|\omega_k|^{y-1} - |\omega_0|^{y-1}\right)d & 0 & -\omega_k d \end{bmatrix} \tag{3.126}$$

and the noise vector $\mathbf{n}_{\mathrm{p}}$ contains the additive white Gaussian noise with covariance matrix:

$$\mathbf{P}_{z_{\mathrm{p}}z_{\mathrm{p}}} = \begin{bmatrix} \sigma^2_{z_{\mathrm{p}},1} & 0 & 0 \\ 0 & \ddots & 0 \\ 0 & 0 & \sigma^2_{z_{\mathrm{p}},k} \end{bmatrix} \tag{3.127}$$

By combining the log magnitude and phase measurements, we can formulate a linear estimator for all three parameters, α_0, α_r and τ_0, simultaneously. To do so, we stack the measurements together:

$$\mathbf{z}_{\mathrm{lmp}} = \begin{bmatrix} \mathbf{z}_{\mathrm{lm}} \\ \mathbf{z}_{\mathrm{p}} \end{bmatrix} \tag{3.128}$$

Stack the measurement matrices together:

$$\mathbf{H}_{\mathrm{lmp}} = \begin{bmatrix} \mathbf{H}_{\mathrm{lm}} \\ \mathbf{H}_{\mathrm{p}} \end{bmatrix} \tag{3.129}$$

And combine both covariance matrices:

$$\mathbf{P}_{z_{\mathrm{lmp}}z_{\mathrm{lmp}}} = \begin{bmatrix} \mathbf{P}_{z_{\mathrm{lm}}z_{\mathrm{lm}}} & 0 \\ 0 & \mathbf{P}_{z_{\mathrm{p}}z_{\mathrm{p}}} \end{bmatrix} \tag{3.130}$$

Obtaining a maximum likelihood estimate is now defined as minimizing the function:

$$\hat{\mathbf{x}}_{\mathrm{ML}} = \arg\min_{\mathbf{x}} (\mathbf{H}_{\mathrm{lmp}}\mathbf{x} - \mathbf{z}_{\mathrm{lmp}})^T \mathbf{P}^{-1}_{z_{\mathrm{lmp}}z_{\mathrm{lmp}}} (\mathbf{H}_{\mathrm{lmp}}\mathbf{x} - \mathbf{z}_{\mathrm{lmp}}) \tag{3.131}$$

Here again, the covariance matrix is dependent on the parameters. For a given covariance matrix, calculated from an initial guess of the parameters, the minimum can be found by setting the gradient of this function to zero, which results in solving the linear system:

$$\mathbf{H}^T_{\mathrm{lmp}} \mathbf{P}^{-1}_{z_{\mathrm{lmp}}z_{\mathrm{lmp}}} \mathbf{H}_{\mathrm{lmp}}\mathbf{x} = \mathbf{H}^T_{\mathrm{lmp}} \mathbf{P}^{-1}_{z_{\mathrm{lmp}}z_{\mathrm{lmp}}} \mathbf{z}_{\mathrm{lmp}} \tag{3.132}$$

By repeatedly solving this linear system and using the newest solution $\hat{\mathbf{x}}^{(k)}$ to calculate a new covariance matrix, we can converge to the minimum of this function.

Summary

We have proposed a set of ultrasound parameter estimators, all set in a different measurement domain, derived by some operation from the original input time domain measurements $\mathbf{z}_{\mathrm{t}}$. Two of these domains, $\mathbf{z}_{\mathrm{mag}}$ and $\mathbf{z}_{\mathrm{lm}}$ correspond with the measurement domains on which the, previously reported spectral shift and log spectral difference methods operate. The obtained expressions in these domains show how the spectral shift and the log spectral difference estimators would have to be modified to make them approximate maximum likelihood estimators. An overview of all discussed measurement domains is displayed in Table 3.3.

Symbol	Model	Noise variance^2	Parameters
$\mathbf{z}_{\mathrm{t}}$	Non-linear	$\sigma^2_{z_{\mathrm{t}}}$	$\alpha_0,\ \alpha_r,\ \tau_0$
$\mathbf{z}_{\mathrm{f}}$	Non-linear	$\frac{n}{2}\sigma^2_{z_{\mathrm{t}}}$	$\alpha_0,\ \alpha_r,\ \tau_0$
$\mathbf{z}_{\mathrm{mag}}$	Non-linear	$\frac{n}{2}\sigma^2_{z_{\mathrm{t}}}$	$\alpha_0,\ \alpha_r$
$\mathbf{z}_{\mathrm{lm}}$	Linear	$\frac{n}{2\lvert Y_w(\omega_i)\rvert^2 \exp[2h_{\mathrm{att},i}(\mathbf{x})]}\sigma^2_{z_{\mathrm{t}}}$	$\alpha_0,\ \alpha_r$
$\mathbf{z}_{\mathrm{p}}$	Linear	$\frac{n}{2\lvert Y_w(\omega_i)\rvert^2 \exp[2h_{\mathrm{att},i}(\mathbf{x})]}\sigma^2_{z_{\mathrm{t}}}$	$\alpha_0,\ \tau_0$

Table 3.3 Overview of the measurement domains that can be used in ultrasound propagation parameter estimation. In this chapter, for each of the measurement domains a suitable estimator is derived.

3.4.3 Evaluation

The evaluation consists of two parts, checking the measurement model by applying it to experimentally obtained measurements on an attenuating phantom and the second part is about the investigation of the performance of the proposed ultrasound propagation parameter estimators.

Measurement model validation

The experimental setup to investigate the measurement model is displayed in Figure 3.10. It consists of a sending ultrasound transducer and a receiving needle hydrophone transducer. The hydrophone transducer was connected to a digital oscilloscope which

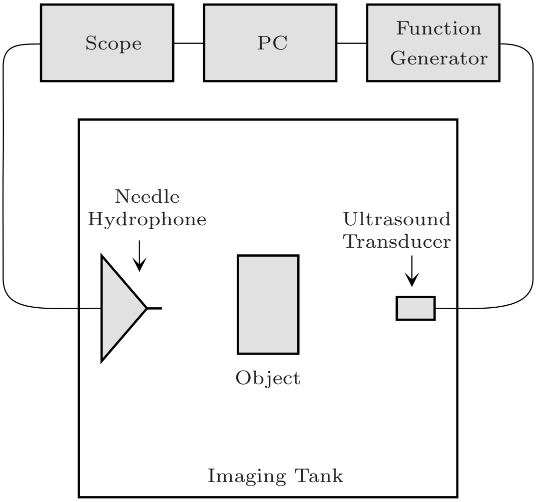

Figure 3.10 Instrumental top view of the measurement model validation setup.

samples the data at a frequency of 500 MHz. An object can be placed in the path between sender and receiver. This is a typical scenario that would occur in a ultrasound transmission tomography setup. Using this setup we have performed two sets of measurements to investigate the measurement model, each with a different reference signal.

First reference signal The first reference signal was created by setting the function generator to a two-period sine wave of a frequency of 5 MHz. The ultrasound transducer used in this case had a center frequency of 5 MHz. As object an Agar/Milk based attenuation object, having a thickness of 48 mm, was used. The resulting signal, as it was measured with the hydrophone and sampled with the oscilloscope, is displayed in Figure 3.11a. Because a two-period sine wave was user here, the resulting reference signal is not very broadband. The ideal measurement would be as broadband as possible, so that the measurement model can be verified over a wide range of frequencies. The attenuating effects of the Agar/Milk object are clearly visible in both the time and frequency domain plots. An obvious signal distortion due to the attenuation, which would have to be caused by dispersion in attenuation over the dominant frequency range is not immediately visible. Using this measured object signal and the input reference signal, we can try to predict the object signal that results from the parameters obtained by fitting the measurement model to the measurements. Three different models were used, in order of increasing complexity. The first model assumes a frequency independent attenuation and its fit is shown in Figure 3.12a. The second model assumes dispersion in the attenuation according to a linear power law, but no dispersion in the speed of sound. The results of this second model are shown in Figure 3.12b. The final model assumes a frequency power law for the attenuation and dispersion in speed of sound according to the Kramers-Kronig relations. This is the measurement model that we assume for the propagation of ultrasound signals

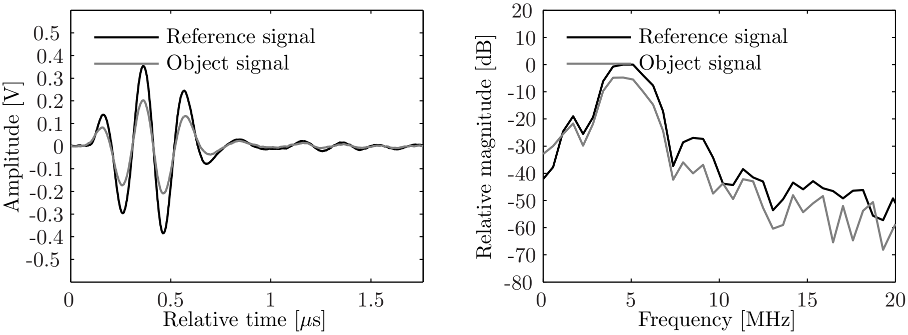

(a) Time domain signals **(b)** Power spectra

Figure 3.11 Experimentally obtained signals with a two-period sine wave with a frequency of 5 MHz. Only the interesting part of the power spectrum is shown.

in the derivation of the estimators. The fit of this final model is shown in Figure 3.12c. From these fits we can conclude that the measurement model, based on the

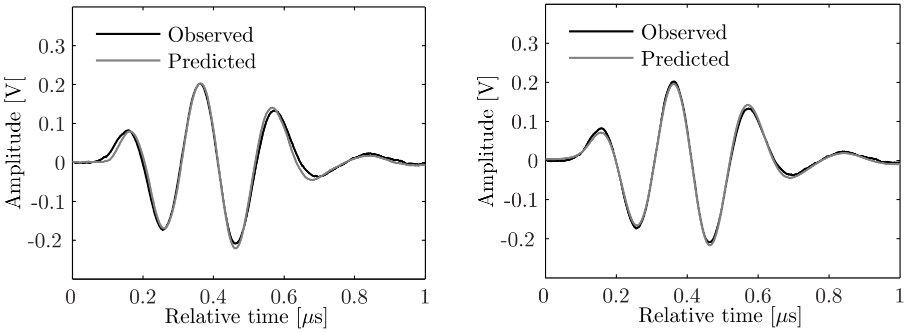

(a) Ignoring dispersion. RMSE = 8.0 mV

(b) Assuming dispersion in attenuation, but no dispersion in speed of sound (without Kramers-Kronig). RMSE = 4.3 mV

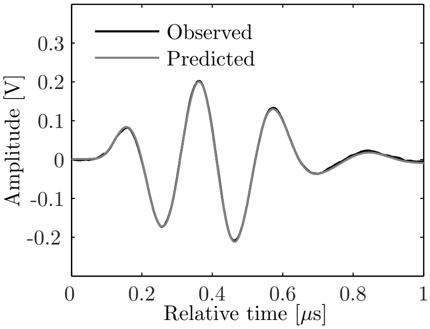

(c) Assuming dispersion in both attenuation and speed of sound (with Kramers-Kronig). RMSE = 2.5 mV

Figure 3.12 Experimentally obtained object signals and predicted object signals from measurements on a reference signal created from a two-period sine wave with a frequency of 5 MHz.

Kramers-Kronig relations, holds in practice and can be well predicted. We also have to add that for this, not very broadband reference signal and not highly attenuating object, the fit that was obtained with the simple model of assuming no dispersion was also quite satisfactory. To illustrate the attenuation dispersion and the corresponding phase relation, we have included the attenuation and phase function and how they compare to the measurements in Figure 3.13. The error bars shown here, derived from the variance expressions in Table 3.3 for $\mathbf{z}_{\mathrm{lm}}$ and $\mathbf{z}_{\mathrm{p}}$, show the 99.7% interval in which the prediction of the measurement should be contained. Both the attenuation function and time delay function are most of the time within this interval.

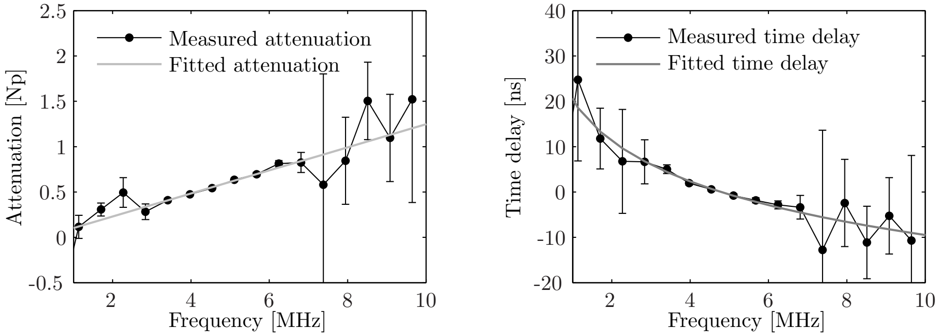

(a) Attenuation function $h_{\text{att}}(\mathbf{x})$ evaluated for several frequencies and the corresponding measurement $\mathbf{z}_{\text{lm}}$

(b) Phase function $\frac{1}{\omega}h_{\text{phase}}(\mathbf{x})$ and the corresponding measurement $\frac{1}{\omega}z_{\text{p}}$

Figure 3.13 Illustration of the measured and fitted attenuation and phase functions in the frequency domain.

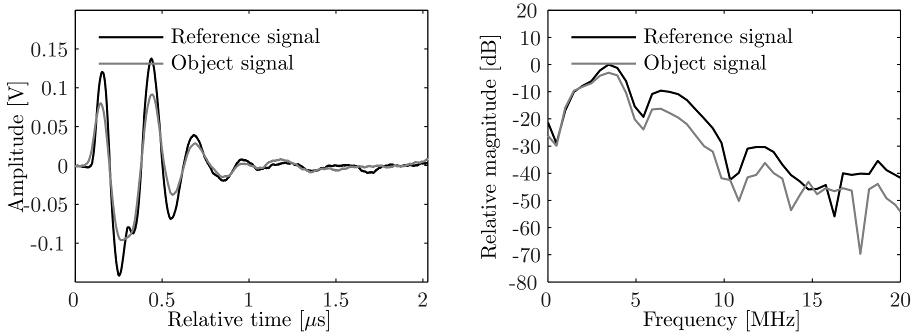

(a) Time domain signals

(b) Power spectra

Figure 3.14 Experimentally obtained signals with a one-period sine wave with a frequency of 5 MHz. Only the interesting part of the power spectrum is shown.

Second reference signal The second reference signal was obtained by setting the function generator to a one-period sine wave, see Figure 3.14a for the resulting pulse. This gives a pulse with a somewhat higher bandwidth, as can be seen from the power spectrum in Figure 3.14b. Also with this reference signal an object measurement with an attenuating object was performed. Due to the typical frequency content of the reference signal, the pulse significantly changes shape after propagating through the object. The results of fitting the measurement model to this measurement are displayed in Figure 3.15. From these results we can conclude that the model measurement model can accurately predict the change in pulse shape due to propagation through an attenuating measurement. Ignoring the phase information leads to a reasonable fit, much better than completely ignoring dispersion. However, including the Kramers-Kronig relation increases the model fit substantially, supporting the conclusion that our measurement model is valid in practice.

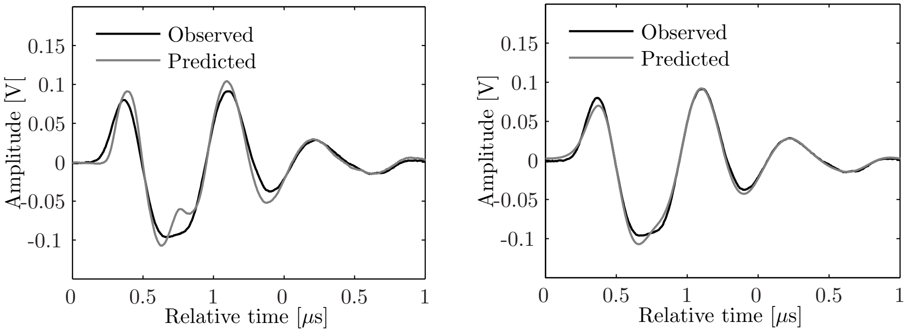

(a) Ignoring dispersion. RMSE = 7.9 mV

(b) Assuming dispersion in attenuation, but no dispersion in speed of sound (without Kramers-Kronig). RMSE = 3.9 mV

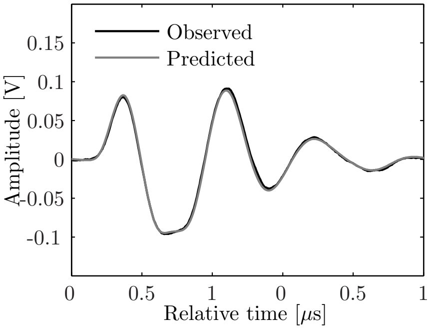

(c) Assuming dispersion in both attenuation and speed of sound (with Kramers-Kronig). RMSE = 3.0 mV

Figure 3.15 Experimentally obtained object signals and predicted object signals from measurements on a reference signal created from a two-period sine wave with a frequency of 5 MHz.

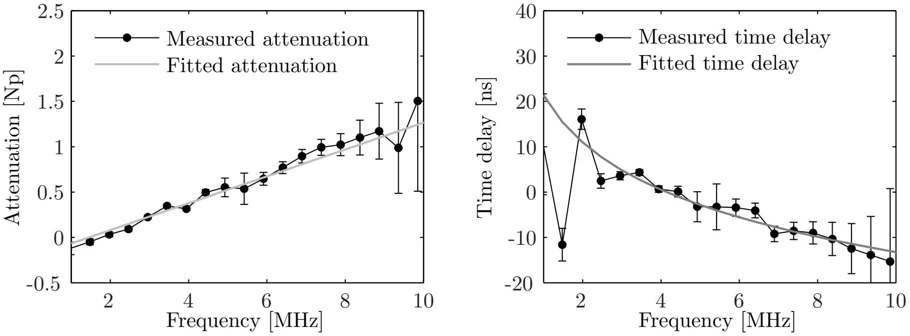

(a) Attenuation function **(b)** Phase function

Figure 3.16 Illustration of the measured and fitted attenuation and phase functions in the frequency domain.

Estimator performance evaluation

For the evaluation of the proposed estimators we have chosen an approach based on a Monte-Carlo computer simulation. This allows controlled circumstances with different signal to noise ratios and simulated distances through the attenuation object. Also by repeating the simulation a high number of times with a different noise realization each run, i.e., the Monte-Carlo method, an accurate description of the performance of the estimators in terms of bias and variance can be obtained. Furthermore, we use the Cramer-Rao Lower Bound (CRLB) to get an indication of the efficiency of the proposed estimators. The CRLB is the lowest variance that any unbiased parameter estimator, given the measurement model and measurement noise distribution, can theoretically attain.

In this evaluation of the different estimators, we will refer to the estimators using abbreviations. A list of the estimators, both existing and proposed, together with their abbreviations, is displayed in Table 3.4.

The Cramer-Rao Lower Bound Let us first look how the CRLB can be calculated for this measurement model. The measurements are taken in the time domain, corrupted with uncorrelated additive Gaussian noise having a variance of $\sigma_{z_\mathrm{t}}^2$. This results in the following pdf of the measurements $\mathbf{z}_\mathrm{t}$:

$$\mathbf{z}_\mathrm{t} \sim \mathcal{N}(h_\mathrm{t}(\mathbf{x}), \sigma_{z_\mathrm{t}}^2 \mathbf{I}) \tag{3.133}$$

The CRLB can simply be calculated in this case by looking at the Jacobian of the measurement function, $\mathbf{H}_\mathrm{t}$, which has been presented in (3.4.2). By evaluating the Jacobian at the true value of the parameters, we can calculate the CRLB of this estimation problem according to[31]:

$$\mathbf{C} = (\mathbf{H}_\mathrm{t}^T \mathbf{H}_\mathrm{t})^{-1} \mathbf{H}_\mathrm{t}^T \sigma_{z_\mathrm{t}}^2 \mathbf{I} \mathbf{H}_\mathrm{t} (\mathbf{H}_\mathrm{t}^T \mathbf{H}_\mathrm{t})^{-1} = (\mathbf{H}_\mathrm{t}^T \mathbf{H}_\mathrm{t})^{-1} \sigma_{z_\mathrm{t}}^2 \tag{3.134}$$

Abbreviation	Method description	Measurement
FSMax	Spectral shift, using frequency of maximum	$\mathbf{z}_{\mathrm{mag}}$
FSFM	Spectral shift, using first moment	$\mathbf{z}_{\mathrm{mag}}$
FSMF	Spectral shift, using Gaussian matched filter	$\mathbf{z}_{\mathrm{mag}}$
CFMag	Log spectral difference, i.e., curve fitting withouth weighting	$\mathbf{z}_{\mathrm{lm}}$
MLTDomain	Maximum likelihood on the time domain measurements	$\mathbf{z}_{\mathrm{t}}$
MLFFT	Maximum likelihood on the complex frequency domain measurements	$\mathbf{z}_{\mathrm{f}}$
MagCorr	Maximum likelihood on the magnitude frequency domain measurements	$\mathbf{z}_{\mathrm{mag}}$
MLMag	Maximum likelihood on the log-magnitude frequency domain measurements	$\mathbf{z}_{\mathrm{lm}}$
MLMagPhase	Maximum likelihood on the log-magnitude and phase frequency domain measurements	$\left(\mathbf{z}_{\mathrm{lm}}, \mathbf{z}_{\mathrm{p}}\right)$

Table 3.4 Overview of the estimators and their abbreviating names.

The obtained matrix **C** is the covariance matrix with the lowest attainable variance for any unbiased estimator.

Monte-Carlo simulation The accuracy of the results obtained with a Monte-Carlo simulation depends on the number of samples that is involved in calculating the results. The outcome of an estimator can be seen as a random variable with a certain mean and variance. We are trying to get an estimate this mean and the corresponding standard deviation (square root of the variance) for each estimator. In order to guarantee a certain accuracy on the Monte-Carlo simulation results, we will set the number of samples N to such a value that the estimated mean and standard deviation are both, in at least 95% of the cases, at most 1% away from their true values. With the help of Appendix D the relation between the estimation accuracy and the number of samples (runs) N and the true variance σ_x^2 is given by:

$$\mathrm{Std}\left[\hat{\mu}_x\right] \approx \frac{1}{\sqrt{N}}\sigma_x \tag{3.135}$$

$$\mathrm{Std}\left[\hat{\sigma}_x\right] \approx \frac{1}{\sqrt{2N}}\sigma_x \tag{3.136}$$

Now in order to have an estimate which is in accordance with our accuracy requirement we set the number of samples so that $2 \times \mathrm{Std}\left[\hat{\mu}_x\right] \leq 0.01\sigma_x$ and $2 \times \mathrm{Std}\left[\hat{\sigma}_x\right] \leq 0.01\sigma_x$ are both valid. This results in the following value of N:

$$N = \left(\frac{2}{0.01}\right)^2 = 40.000 \tag{3.137}$$

meaning that we need 40.000 runs to reach the chosen level of accuracy.

Simulation conditions We have chosen to simulate the propagation through an attenuation object with an attenuation constant of $\alpha_0 = 0.1$ Np/cm/MHz and a power law constant of $y = 1$. This is similar to the conditions as they typically are in soft-tissue. In soft-tissue the attenuation can vary between 0.3 and 3 dB/cm/Mhz[50], where the conversion between Nepers and Decibel is given by 1 Np = 8.69 dB. The reference signal that we have used in the simulation was a Gaussian modulated pulse with a center frequency of $f_0 = 5$ MHz and standard deviation of $\sigma_f = 1.6$ MHz. Two levels of additive Gaussian noise were simulated. A relative low noise scenario with SNR = 100 and a high noise scenario with SNR = 10, where the SNR is defined as the ratio between maximum signal amplitude of the reference signal and the standard deviation of the Gaussian noise σ_{z_t}. The SNR is thus related to the conditions in the reference measurement, the effective SNR on the object measurement would be lower due to the attenuation of the object.

The spectral shift estimator Since there are several ways to estimate the frequency shift on which the spectral shift method is based, we will first determine which method is best and use that in the comparison with the other methods. We have proposed three ways of calculating this shift. The first method was based on simply using determining the frequency at which the maximum occurs and using that frequency to determine the shift (FSMax). The second method was based on calculating the first moment of the magnitude spectrum and to use that as the frequency to determine the shift (FSFM). The last method was to use a matched filter with the Gaussian template obtained from the magnitude spectrum of the reference measurement and use a matched filter to calculate the frequency shift (FSMF).

The results of the Monte-Carlo simulation for the different spectral shift estimators are displayed in Figure 3.17. We see that in both the low and high noise scenario the matched filtering based approach (FSMF) works best. This is not surprisilingly if we recall the conclusion from section 3.4.2. In that section a maximum likelihood estimator is derived for the magnitude spectrum domain with $\mathbf{z}_{\text{mag}}$, on which the spectral shift estimator also operates. The resulting maximum likelihood estimator looks like a matched filter approach with the predicted magnitude spectrum. For the rest of the evaluation, we will continue with the FSMF estimator in the comparison with the other estimators, and henceforth use the term spectral shift estimator synonymous to the FSMF estimation of spectral shift.

Now let us see how the FSMF estimator compares against the MagCorr estimator, both working on the magnitude spectrum measurement. This is interesting to see, because the MagCorr estimator is derived in the maximum likelihood framework. The results of this comparison are displayed in Figure 3.18. We see that in the low noise scenario, the performance of the two estimators is almost equal. In the high noise scenario, however, at a certain moment the RMSE of the spectral shift estimator starts to deviate from the RMSE of the magnitude correlation estimator. The biases are also indicated in these plots to show that they are of minor importance, the estimates are not very biased compared to the standard deviation.

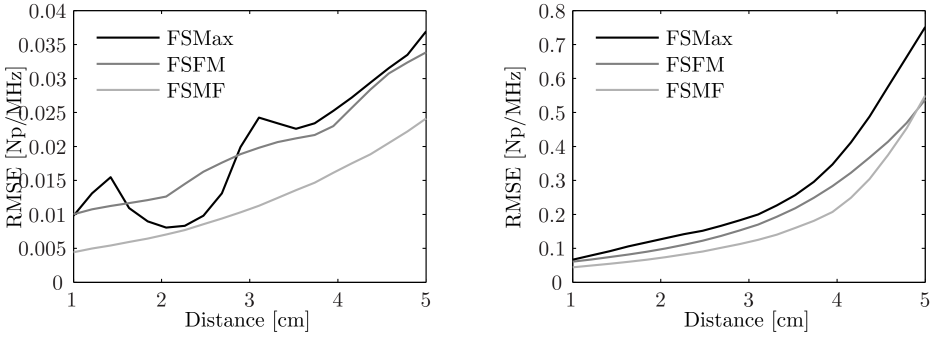

(a) SNR = 100 **(b)** SNR = 10

Figure 3.17 Estimator simulation of spectral shift implementations for SNR

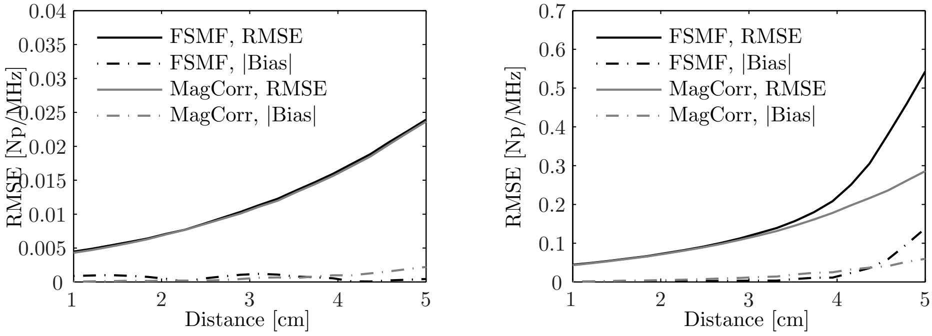

(a) SNR = 100 **(b)** SNR = 10

Figure 3.18 Comparison between two estimators set in the magnitude spectrum domain for a low noise (left) and high noise (right) scenario.

The log spectral difference estimator The log spectral difference estimator (CFMag) can be compared to the maximum likelihood MLMag estimator, since they are both set in the log magnitude domain, $\mathbf{z}_{\text{lm}}$. The estimators are very similar, the only difference is that the MLMag estimator, based on the maximum likelihood framework, takes a different weighting of each frequency component into account, whereas the CFMag estimator treats each frequency component the same. Both estimators only operate on a certain range of the spectrum, the boundaries of this range are selected based on the SNR of each frequency component, indicated with SNR_{th} in the method descriptions. Evaluation of both algorithms turned out that for the CFMag estimator a value of $\text{SNR}_{\text{th}} = 2$ works best and for the MLMag estimator a value of $\text{SNR}_{\text{th}} = 1$ works best. The results of comparing both estimators in a high and low noise scenario to each other are displayed in Figure 3.19. From these results we clearly see that including the weighting that results from using the maximum likeli-

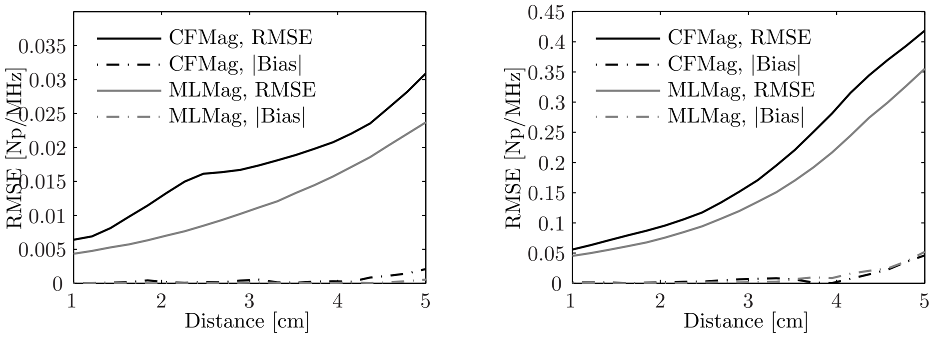

(a) SNR = 100

(b) SNR = 10

Figure 3.19 Comparison between two estimators set in the log magnitude spectrum domain for a low noise (left) and high noise (right) scenario.

hood framework (MLMag) instead of ordinary least squares fitting (CFMag) gives a substantial improvement in the estimator performance.

Comparison of the maximum likelihood estimators Finally we will compare the four maximum likelihood estimators to each other. The results of this comparison are displayed in Figure 3.20. In the low noise scenario, Figure 3.20a, there is a distinct separation visible between the methods that do incorporate speed of sound dispersion through the Kramers-Kronig relations (MLMagPhase and MLFFT/MLTDomain) and those methods that do not (MagCorrelation and MLMag). Obviously, adding this extra information results in a slightly improved, i.e., with a lower RMSE, estimate of the attenuation constant. Also the CRLB was calculated and shown here for comparison. Both the MLMagPhase and MLFFT/MLTDomain estimators reach this lower bound in the low noise scenario.

In the high noise scenario, Figure 3.20b, we see that especially at the longer distances the results of the different estimators start to diverge. The overall winner here are the MLFFT/MLTDomain estimators, which follow the CRLB very well up to a distance of 3.5 cm. And also interestingly to see is that the MagCorrelation estimator turns out to be very robust. It outperforms both the MLMag and MLMagPhase estimators in high noise scenarios.

3.4.4 Conclusion

In this section, the topic of ultrasound propagation parameter estimation, useful as a pre-processing step in ultrasound transmission tomography, was analyzed. We first investigated two existing techniques, the spectral shift method and the log spectral difference method and after that derived five estimators using the maximum likelihood framework on different measurement domains.

The implementation of the spectral shift method can be done in various ways,

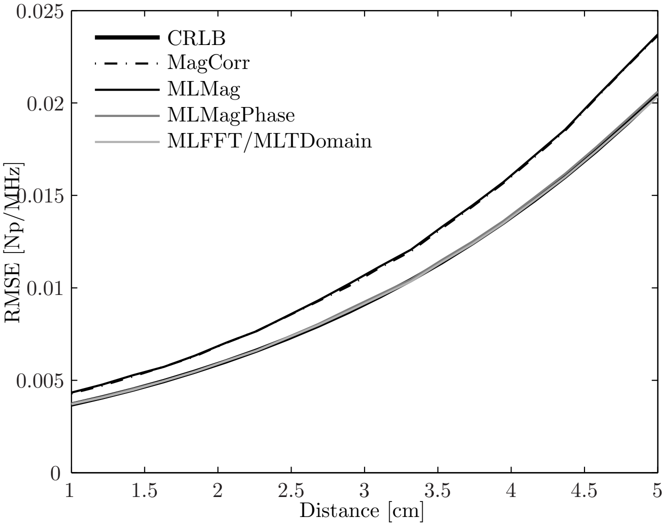

(a) SNR = 100

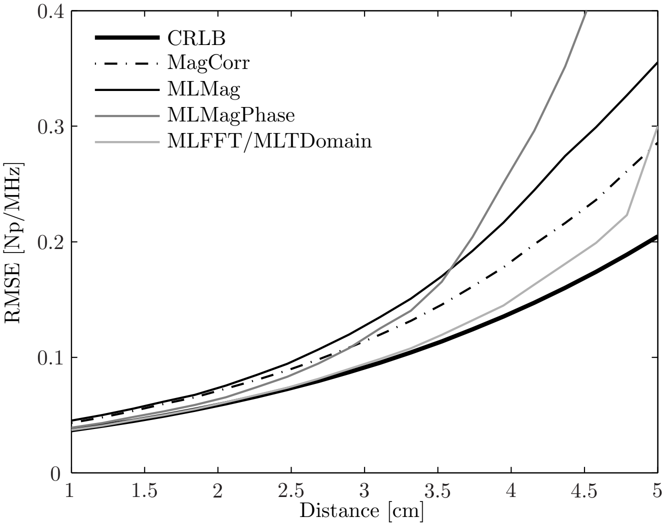

(b) SNR = 10

Figure 3.20 Performance plots of the four proposed maximum likelihood estimators, together with the Cramer-Rao Lower Bound. Shown are a high (left) and a low (right) noise scenario.

which all result in a spectral shift estimate from which the attenuation parameter can be determined. We found that a matched filter technique works best to determine the spectral shift. A very nice result is that when we try to derive a maximum likelihood estimator on the same measurement domain, the magnitude domain, we also end up with an estimator involving some sort of correlation with a custom template shape. In the spectral shift estimator this template is Gaussian shaped, but in our maximum likelihood framework derived estimator it has a shape that is dictated by the input signal and depedent on the actual parameter value.

The log spectral difference method comes down to fitting a straight line to a set of measurement points. A similar estimator can be derived in the maximum likelihood framework, on the log magnitude domain, with the difference that a weighted least squares fit of the measurement points to a straight line needs to be done. Adding weights to the fitting procedure helps a lot in improving the performance of the estimator as can be seen from Figure 3.19.

With our proposed estimators, we went one step further by also using the phase information from the measurements. The Kramers-Kronig relations gives us a relation between the attenuation function and the phase information. This phase information is implicitly available in time domain measurements and can be made explicit by performing an FFT and extracting magnitude and phase measurements from this. We found that the best way of using this extra information is by using just the original time domain measurements, i.e., without applying any non-linear transformations to go to another measurement domain. This difference in estimator performance is especially noticeable in high noise scenarios, the time domain measurements gives then much better results as can be seen from Figure 3.20. The reason why the estimator derived on the original time domain measurements works best is because on this domain the measurement errors are truly Gaussian distributed, any non-linear transform will propagate to another noise distribution, with the effect being larger in the higher noise scenarios.

4

Reconstruction of speed of sound and acoustic attenuation[1]

Abstract

A problem that typically occurs in ultrasound transmission tomography, and which is also encountered in our PER-PAT imaging setup, is the reconstruction of acoustic property distributions from projections through these distributions along ray paths. The acoustic property distributions, being the speed of sound and acoustic attenuation, can be reconstructed by setting up a measurement model that relates the projection measurements to the source distributions. This comes down to tracing the correct ray paths through the image for all combinations between passive elements (the sources) and ultrasound detector elements in our transducer array (the receivers). We propose an algorithm which takes into account the bending of ray paths, caused by speed of sound inhomogeneities, and which is capable of working with multiple passive element in our PER-PAT setup. A numerical analysis and experimental evaluation show that a substantial reduction in measurement time is possible by using multiple passive elements while maintaining a similar level of image reconstruction quality.

---

[1] Parts of this chapter are under communication as:
i) J. Jose, G.H. Willemink et al, "Passive element enriched photoacoustic computed tomography (PER-PACT) for hybrid imaging", Optics Express
ii) S. Resink, J. Jose, G.H. Willemink et al, "Multiple passive element enriched photoacoustic computed tomography (multi PER-PACT)", Journal of Biomedical Optics

4.1 Introduction

In photoacoustic imaging, depending on the object that is being imaged and the required resolutions, it might be necessary to take speed of sound inhomogeneities in the object into account in the reconstruction. See also further in chapter 5, section 5.3. We obtain this speed of sound map from photoacoustic measurements. This is possible because in our PER-PAT system we have placed one or more passive elements, which act as ultrasound point sources. This allows us to take ultrasound transmission mode tomography (UTT) measurements. Due to the geometrical placement of the passive elements opposite to the ultrasound detectors, the generated ultrasound signals do not interfere with the simultaneously generated photoacoustic signals from our object. We have developed a method to obtain accurate projections of both acoustic attenuation and (inverse) speed of sound through the object in a maximum likelihood framework from these ultrasound measurements (see chapter 3). These projections are the integration of the quantity of interest over a path between a source and detector. When speed of sound is the quantity of interest, the projection is given as a time delay and when acoustic attenuation is the quantity of interest, the projection is given as the total attenuation along the path. With our PER-PAT setup it is thus possible to reconstruct two acoustic property distributions, being the speed of sound distribution and the acoustic attenuation distribution of the object. In this chapter we will present a method to reconstruct these acoustic property distributions from the obtained projection measurements.

4.2 Measurement model

The measurement model of UTT is very similar to what is seen in X-ray CT Imaging. Every measurement is a projection along a path between a source and detector pair. The path, however, is not necessarily a straight line. Also, in our PER-PAT setup, there can be multiple sources when more than one passive element is being used. For speed of sound, a single projection measurement, which represents a time delay over the path, is given by:

$$t_f(\mathbf{r}_\mathrm{d}, \mathbf{r}_\mathrm{s}) = \int\limits_{l(\mathbf{r}_\mathrm{d}, \mathbf{r}_\mathrm{s}, c)} \tau(\mathbf{r}) \mathrm{d}\mathbf{r} \tag{4.1}$$

where $\tau(\mathbf{r}) = \frac{1}{c(\mathbf{r})} - \frac{1}{c_0}$ is the time delay per unit distance and c_0 is the speed of sound in the reference medium. The path, from source position $\mathbf{r}_\mathrm{s}$ to detector position $\mathbf{r}_\mathrm{d}$, is represented with the expression $l(\mathbf{r}_\mathrm{d}, \mathbf{r}_\mathrm{s}, c)$, showing that the path can also depend on the (unknown) speed of sound distribution $c(\mathbf{r})$. Notice that in fact the speed of sound measurement model relates the measurement to the time delay per unit distance $\tau(\mathbf{r})$. This is the distribution that will be reconstructed at first, and can then simply be converted to the actual speed of sound distribution via:

$$c(\mathbf{r}) = \frac{c_0}{1 + \frac{c_0}{\tau(\mathbf{r})}} \tag{4.2}$$

For acoustic attenuation we have a very similar measurement relation:

$$a(\mathbf{r}_\mathrm{d}, \mathbf{r}_\mathrm{s}) = \int\limits_{l(\mathbf{r}_\mathrm{d}, \mathbf{r}_\mathrm{s}, c)} \alpha_0(\mathbf{r})\mathrm{d}\mathbf{r} \tag{4.3}$$

where $\alpha_0(\mathbf{r})$ is the unknown attenuation distribution. As mentioned before, the path between source and detector is not necessarily a straight line. In the absence of refraction, or when refraction is so small that it can be ignored, the path would be a straight line. In general, however, the path can be bent and curved[51, 52] which complicates the reconstruction. The only information that is always known in advance about a projection path are its starting point and its end point.

The complete set of measurements consists of different projections, each obtained with the object rotated to a different projection angle. In such a projection are measurements at all the different sensors (detectors) arising from each source. For the single passive element scenario there would be one source and the geometry of a single projection then looks like Figure 4.1a. For the multiple passive element scenario there are more sources in a single projection (rotation) and the geometry will look like Figure 4.1b. These figures show that using multiple sources has the advantage that more information about the unknown object (speed of sound/acoustic attenuation) can be obtained in a single projection. We hope that this results in an increased resolution or better signal to noise ratio.

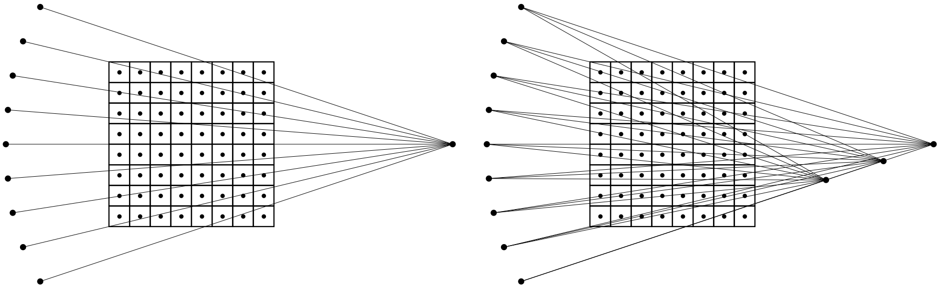

(a) (b)

Figure 4.1 Geometry overview of the ray paths in a single projection (rotation). On the left (a) the scenario with a single passive element is shown and on the right (b) the scenario with multiple passive elements is shown. The rays are drawn here as straight lines, but in reality they can be bent. The grid represents the underlying unknown acoustic property distribution.

4.2.1 Discretizing the measurement model

The projection paths have to be numerically evaluated over the discretized acoustic property distribution. We will represent the acoustic property distribution on a rectangular grid as displayed in Figure 4.1. The off-grid points will be calculated by 2-D bilinear or bicubic interpolation. Once the projection paths are known, the problem of reconstructing the acoustic property distribution is a linear problem. Each projection measurement is a weighted sum of the pixels representing the acoustic property distribution. We use a ray driven approach to numerically calculate the projections over the paths, meaning that we sample along segments of each ray/path. Every sample of the ray can be expressed as a linear combination of one (using nearest neighbor) or more (using bilinear or bicubic interpolation) pixels around the sample. Subsequent sampling of the ray then gives us the weighted sum of pixels for each projection. If we represent the unknown pixels in a parameter vector $\mathbf{x}$, the ray driven discretized measurement model with a projection matrix $\mathbf{H}$ and the projection measurements in a measurement vector $\mathbf{z}$, we have the linear model:

$$\mathbf{z} = \mathbf{H}\mathbf{x} \tag{4.4}$$

which relates the acoustic property distribution to the measurements. Everything, from the number of projections to the number of passive elements is contained in the projection matrix $\mathbf{H}$. The reconstruction problem, assuming the paths are known, is then defined as solving the linear system of equations.

4.2.2 Passive element positioning

The positioning of the passive elements is bound by four constraints. The first constraint is that the passive element has to be properly illuminated by the laser light. The second constraint is that the signal generated by the passive element should not overlap with any of the PA signals from inside the object. The third constraint is that the signals from different passive elements should not interfere with each other. The final constraint is that at all passive elements should be positioned on or outside, but not inside, a line of sight between the detector array and passive element that does not pass through the object. These constraints are nicely visualized in Figure 4.2. A complete area is marked here in which it is possible to position passive elements. The reason for having the first three constraints is straightforward and has to do with the detection/extraction of the projection measurements. When signals start to overlap it is not possible anymore, or more difficult, to extract the attenuation and correct time delay. The reason behind having the final constraint is that a line of sight with one of the detectors can be used as a reference indicator. Along the line of sight we expect zero time delay or attenuation between reference and object measurements. This allows us to correct for small temperature changes in the imaging tank or small position changes of the passive elements between the object and reference measurement.

To get an idea of the effect of the number of passive elements and to investigate the optimal geometrical arrangement of the passive elements, we conducted a study of the projection matrix $\mathbf{H}$. The behavior of this matrix, defined by its singular values, as a function of the number and placement of the passive elements tells us what geometrical configuration is optimal.

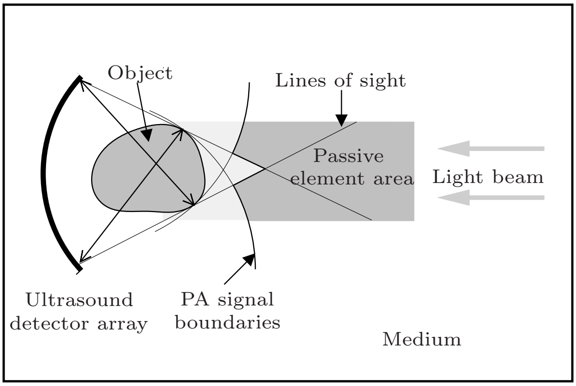

Figure 4.2 Overview of the passive element positioning possibilities.

Optimal single passive element position

First we have investigated what the optimal position of a single passive element would be. A projection matrix **H** was created for different passive element positions, with 90 projections and 32 detector elements consistent with the geometry of the setup and the typical measurement protocol used. An overview of the geometry that was used is displayed in Figure 4.3a. The passive element was positioned within the area marked as PE trial area. For every position the condition number[53] of the matrix, which is an indication for the stability of the solution to the inverse problem, was calculated. A low condition number indicates that the inverse problem is well-conditioned whereas a high condition number indicates the problem is ill-conditioned. The results are shown in Figures 4.3b and 4.3c. In Figure 4.3b, where an image size of 32 × 32 was used, we see an irregular pattern in the condition number plot. The irregular pattern shows that the condition number is very sensitive to the actual ray paths through the object, which means that the grid spacing could be too small for a good reconstruction without any regularization. Therefore, an image size of 16 × 16 was also investigated and displayed in Figure 4.3c which does not show this irregular pattern. Note however, that in an actual reconstruction, regularization will be used to stabilize the reconstruction, meaning that the irregular pattern has no negative effect on the reconstruction. A trend can obviously be identified from both figures, showing that the passive element should not be positioned too close to the object. Surprisingly, these results can well be combined with the bounds that we have defined based on line of sight and PA signal boundaries, as shown in Figure 4.2. From these results we can thus conclude that, within the bounds sketched in Figure 4.2, the position of the passive element is not very critical for the stability of the inverse problem.

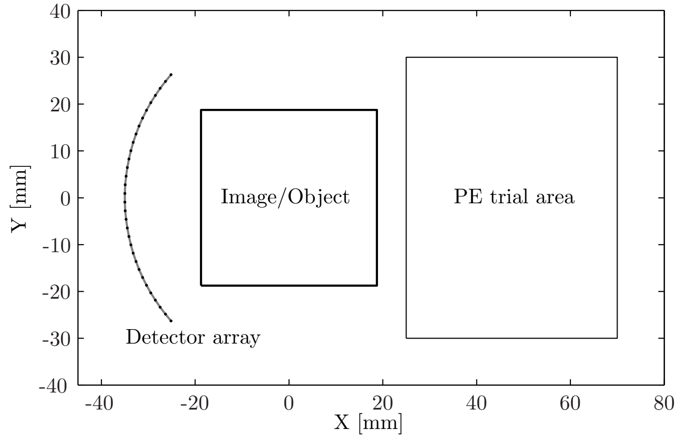

(a) Geometrical overview of detector array, image area and the passive element trial area

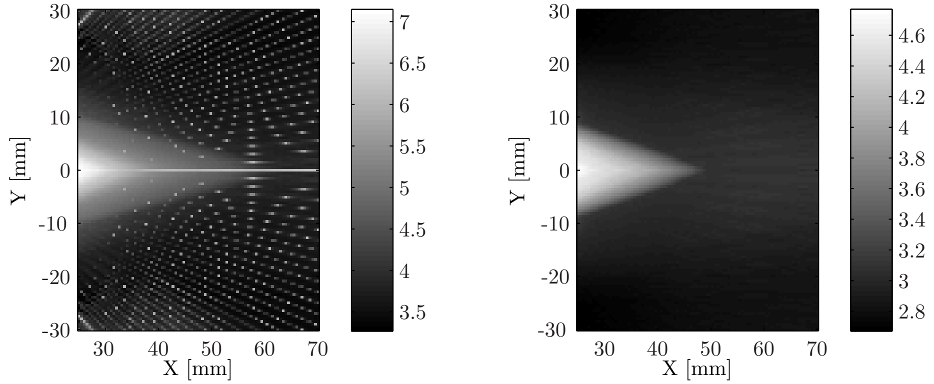

(b) Condition number, $\log_{10}\left(\text{cond}\left(\mathbf{H}^T\mathbf{H}\right)\right)$, with an image grid size of 32 × 32

(c) Condition number, $\log_{10}\left(\text{cond}\left(\mathbf{H}^T\mathbf{H}\right)\right)$, with an image grid size of 16 × 16

Figure 4.3 Investigation of the optimal position of the passive element for image reconstruction based on the condition number of the projection matrix $\mathbf{H}$. The top figure shows an overview of the geometry and the bottom two images show plots of the condition number for two different image grid sizes.

The number and positioning of more passive elements

Based on the analysis just presented and the earlier mentioned bounds on passive element positioning, we will line our passive elements up on a line. This line is in sight with the bottom detector element. The passive elements will be evenly distributed on this line. To find out what the effect of having more passive elements is, we again investigated the condition number of the projection matrix. This time an image grid size of 32 × 32 pixels and 64 × 64 pixels were used, so that the resolution effects of having more than one passive element can also be studied. The calculated condition numbers for these configurations are displayed in Figure 4.4. From these results it can be seen that, for the low resolution case, when going from one to two passive elements there is a substantial improvement in the conditioning of the problem to be expected. Furthermore we see that when a higher resolution is chosen, there is improvement to be expected by adding even more passive elements. We could thus conclude that, the higher the resolution of the reconstruction, the more beneficial it will be to use more passive elements.

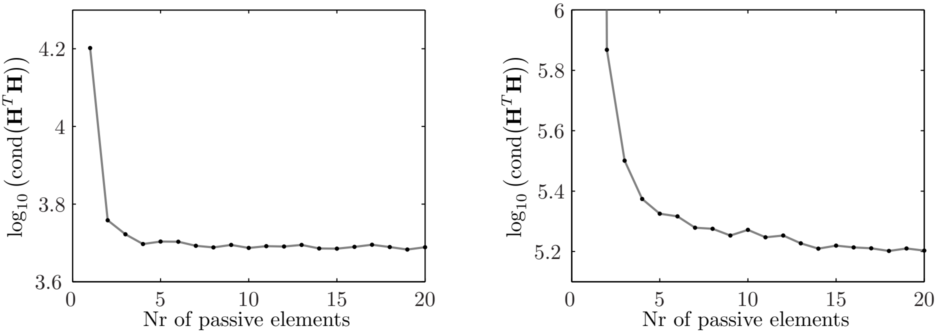

(a) Grid size of 32 × 32 pixels

(b) Grid size of 64 × 64 pixels

Figure 4.4 Plots of the condition number as a function of the number of passive elements. The passive elements are positioned on a line of sight with the bottom detector element, the distance between the first and last passive element is 40 mm and the spacing between the elements is evenly distributed. Two different grid sizes for the reconstruction are shown.

4.3 Approach

To solve the reconstruction problem, essentially a non-linear system of equations needs to be solved. It is, however, very easy to formulate this as iteratively solving a linearized linear system of equations. The non-linearity in the model stems from the curved acoustic ray paths which are a-priori unknown and dependent on the speed of sound sound distribution. The approach we will follow, is to start by assuming a model based on straight ray propagation and then to use the reconstruction result from this simple model to calculated curved ray paths for the next step. This procedure can be iterated until the solution converges.

4.3.1 Solving the linear system

Once the projection has been discretized in a sparse matrix **H**, the reconstruction is fairly straightforward. A direct method, however, to solve the linear system is not possible because the matrix can be quite large, depending on the image size that has been chosen. We will use an iterative method, LSQR[54], to solve the linear system of equations. The matrix **H** can become ill-conditioned, as we have seen already in the previous section in Figure 4.3b for relatively small image sizes. This means regularization, the use of prior information on the solution, mostly in the form of a smoothness assumption, has to be added to the problem. In chapter 5, section 5.2.4, the regularization topic is more extensively discussed and three different regularization methods are described there. These regularization methods will be used here in the reconstruction of the acoustic properties as well. We quickly address the three regularization methods:

Tikhonov In the well-known Tikhonov regularization method the following solution is calculated:

$$\hat{\mathbf{x}}_{\text{Tik}} = \arg\min_{\mathbf{x}} \|\mathbf{Hx}\|^2 + \lambda\|\mathbf{Lx}\|^2 \tag{4.5}$$

here **L** is an operator typically representing a high-pass filter which penalizes the high frequencies in the solution more than the low frequencies. The parameter λ controls the smoothness of the solution.

Total variation With total variation (TV) regularization, an L^1 norm criterion, instead of a quadratic criterion as used in Tikhonov regularization, is used to penalize the high frequencies in the solution. The total variation regularized solution is calculated as:

$$\hat{\mathbf{x}}_{\text{TV}} = \arg\min_{\mathbf{x}} \|\mathbf{Hx}\|^2 + \lambda\text{TV}(\mathbf{x}) \tag{4.6}$$

where $\text{TV}(\mathbf{x}) = \sum_i \sqrt{(\partial_x x_i)^2 + (\partial_y x_i)^2 + \beta^2}$, i.e., the norm of the gradient of the image. Adding the constant $\beta > 0$ offers computational advantages, such as differentiability when the gradient approaches zero[55].

Krylov-subspace iteration number Regularization can also be obtained by constraining the solution to lie in a lower dimensional subspace[56] $\mathcal{S}$:

$$\hat{\mathbf{x}}_{\text{Constr}} = \arg\min_{\mathbf{x}\in\mathcal{S}} \|\mathbf{Hx}\|^2 \tag{4.7}$$

this is effectively what happens when a Krylov-subspace method is used such as LSQR. The solution space is then governed by the iteration number j and the associated Krylov subspace, i.e., $\mathcal{S} = \mathcal{K}_j\big(\mathbf{H}^T\mathbf{H},\, \mathbf{H}^T\mathbf{z}\big)$.

4.3.2 Calculating the ray paths

In the first iteration the ray paths are straight and not dependent on an assumed speed of sound distribution. In the next iterations, we will use the current estimate of the speed of sound distribution to calculate the curved ray paths from each passive element position to each detector position. To trace these rays we will make use of a solution to the Eikonal equation:

$$|\nabla t(\mathbf{r})| = \frac{1}{c(\mathbf{r})} \tag{4.8}$$

numerically calculated with the Fast Marching Method (FMM) [57]. For every passive element and for every projection this equation has to be solved for $t(\mathbf{r})$, given the estimated speed of sound map $c(\mathbf{r})$, with the initial condition set to $t(\mathbf{r}_\mathrm{s}) = 0$. This results in a time of flight map $t(\mathbf{r})$, which contains for every spatial position the shortest time of flight through the speed of sound map to the starting point $\mathbf{r}_\mathrm{s}$, being the location of the passive element. With this approach, we have thus a way to calculate the fastest arrival times of the wave front starting at a passive element, to each of the detector element positions. There are other refraction effects, such as the formation of multiple wave fronts with possibly slower arrival times, which are not taken into account using this method. It is, however, a very quick method to find the first arrival times. From the obtained time of flight map $t(\mathbf{r})$ it is then possible to trace back the ray path belonging to the shortest arrival time via a gradient descent approach through the time of flight map. This ray tracing starts at the position of a detector element and the traced ray will naturally end in the valley which is the location of the passive element. Ray tracing will be performed by parametrizing the ray path l as a function of τ, setting $l(0) = \mathbf{r}_\mathrm{d}$ and solving:

$$\frac{\mathrm{d}l}{\mathrm{d}\tau} = -\nabla t\Big(l(\tau)\Big) \tag{4.9}$$

To solve this equation we use the fourth order Runge-Kutta[58] (RK4) method. The RK4 method is iterated, until we are at a predefined distance from the final point $\mathbf{r}_\mathrm{p}$. We then step in a straight path from there to the final point in order to avoid strange behavior close to the final point where the gradient of $t(\mathbf{r})$ might not be well defined.

FMM implementation

The FMM uses first order derivatives to find the solution to the differential equation, to obtain a high accuracy we use a second order accurate scheme to calculate these first order derivatives. Using FMM with these second order accurate finite differences is called the high accuracy fast marching method (HAFMM)[59, 57].

4.4 Results

We have conducted a simulation study and several experiments with our PER-PAT setup. The goal was to test our approach on curved ray corrections and acoustic property reconstructions and also to find out the effects in practice of using more then one passive elements.

4.4.1 The linear 128 element array

Our first generation PER-PAT setup was equipped with a single passive element and a 128 element linear array, as mentioned in chapter 1. The geometry of this array was described in chapter 2 and displayed in Figure 2.1a. Taking measurements with this setup took relatively long time, because reading out the complete 128 element array using the 4-way multiplexer requires 32 different excitations of the laser. Also there were problems with accurate synchronisation between the laser excitation and detector array measurements, which led to a substantial amount of correlated noise in both the time of flight and attenuation measurements. Nevertheless, we will show the results obtained with this first generation system, since noise filtering on this specific correlated noise pattern has been shown to work very well. Overall, reasonable reconstructions have been obtained with this system. Because the sensor spacing in the 128 element array is smaller than in the curved 32 element array, Figure 2.1b, potentially higher resolution images can be reconstructed with it.

We will show the result on an Agar phantom, with a circular inhomogeneity of Agar doped with 2% carbon, and a rectangular inhomogeneity of Agar doped with of 1% carbon[60], as displayed in Figure 4.5.

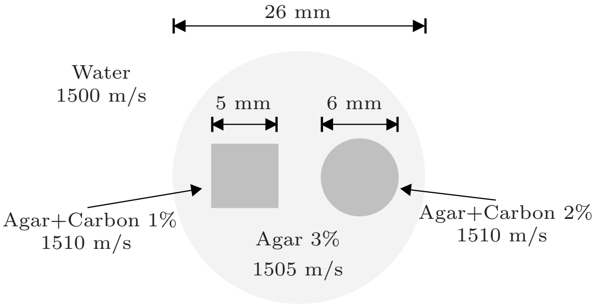

Figure 4.5 Geometrical layout of the phantom used 128 element linear array setup.

The result of extracting the projection data of the integrated attenuation constant is displayed, in the form of a sinogram, in Figure 4.6a and the sinogram with the extracted time delays is displayed in Figure 4.6b. The attenuation that is estimated here is the frequency independent attenuation, because with this setup it was not possible to measure a stable signal from the passive element. We come back to using frequency dependent and frequency independent attenuation in the section on experimental evaluation of the curved 32 element array setup. Inspection of the results shows that there is quite some noise in the sinogram. However, if we look closely, we see that the measurements in groups of four, due to the 4-way multiplexer, are all similarly corrupted with an additive noise term working on all four sensors

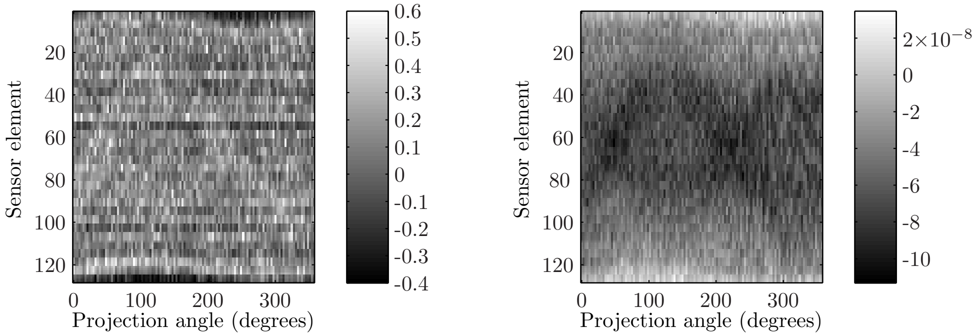

(a) Raw acoustic attenuation projection measurements

(b) Raw time of flight projection measurements

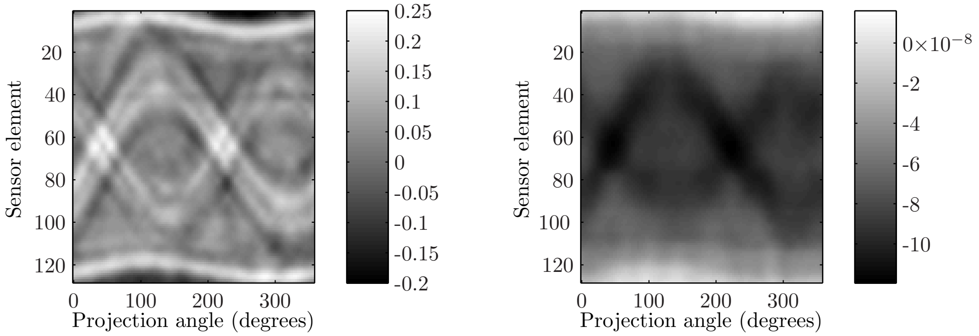

(c) Filtered acoustic attenuation projection measurements

(d) Filtered time of flight projection measurements

Figure 4.6 Raw and filtered sinograms of acoustic attenuation and time delay for an experiment with the phantom displayed in Figure 4.5 on the 128 element linear array setup.

simultaneously. The fact that the noise on the sinogram measurements is correlated can be exploited in a noise filtering algorithm. To filter out some of the noise, we make use of the covariance matrix that describes these correlations. A maximum a-posteriori (MAP) framework can be used to realize the filtering. The unknown true sinogram can assumed to be smooth (prior information) and a noisy observation (with known covariance matrix) of the true sinogram is available. Filtering can then be performed by maximizing:

$$\mathbf{x}_{\text{filt}} = \arg\max_{\mathbf{x}} p(\mathbf{z}|\mathbf{x})p(\mathbf{x}) \tag{4.10}$$

Here $\mathbf{x}$ represents the true sinogram without noise and $\mathbf{z}$ is the noisy observation of this sinogram. The pdf $p(\mathbf{z}|\mathbf{x})$ represents the relation of the observed sinogram to the true sinogram. We assume that the observation, as displayed in Figure 4.6a and

Figure 4.6b, is directly related to the true sinogram plus an additive Gaussian noise term:

$$p(\mathbf{z}|\mathbf{x}) \propto \exp\left[-\frac{1}{2}(\mathbf{z}-\mathbf{x})^T\mathbf{P}_{zz}^{-1}(\mathbf{z}-\mathbf{x})\right] \tag{4.11}$$

where $\mathbf{P}_{zz}$ is the covariance matrix which correctly represents the correlation in the measurement data. For the prior information on the true sinogram, represented by the pdf $p(\mathbf{x})$, we assume a certain degree of smoothness on the sinogram. We do this by assuming that a higher order gradient of the sinogram should be small

$$p(\mathbf{x}) \propto \exp\left[-\frac{1}{2\sigma_G^2}(\mathbf{G}\mathbf{x})^T(\mathbf{G}\mathbf{x})\right] \tag{4.12}$$

where $\mathbf{G}$ represents the gradient operator on the sinogram $\mathbf{x}$ and σ_G^2 represents the variance on the gradient and should be set to a low value that corresponds to the expected smoothness of the true sinogram. Since a sinogram is periodic along the projection angle direction, the gradient operator will be made periodic along that direction as well. Maximization of the pdf in (4.10) comes down to minimizing the quadratic function:

$$\mathbf{x}_{\text{filt}} = \arg\min_{\mathbf{x}}\left[(\mathbf{z}-\mathbf{x})^T\mathbf{P}_{zz}^{-1}(\mathbf{z}-\mathbf{x}) + \frac{1}{\sigma_G^2}(\mathbf{G}\mathbf{x})^T(\mathbf{G}\mathbf{x})\right] \tag{4.13}$$

This can be minimized by setting the gradient of the quadratic function to zero and solving the resulting linear system. The number of unknowns in this linear system is quite high, it equals the number of sensor elements times the number of projection angles. But due to the sparsity of the linear system we can efficiently solve the system using the LSQR algorithm[54]. The results of noise filtering are displayed in Figures 4.6c and 4.6d, showing the effectiveness of the noise filtering.

Reconstruction Results

Finally, after obtaining both the (filtered) integrated attenuation sinogram and the (filtered) time delay sinogram, acoustic attenuation and speed of sound distributions can be reconstructed. For the reconstruction, we use the reconstruction method with iteration number regularization as earlier described. The sensor array used in our experimental setup contains 128 elements, of which 8 elements are defect. The reconstruction is based only on the 120 working sensor elements and the projection matrix $\mathbf{H}$ is adjusted to include only measurements of the working sensors.

Reconstructions were performed on both the raw sinograms and noise filtered sinograms. The reconstruction results for acoustic attenuation are displayed in Figures 4.7a and 4.7c and the reconstruction results for speed of sound are displayed in Figures 4.7b and 4.7d. From this we can conclude that noise filtering improves the reconstruction result by a large amount and that our approach of acoustic property reconstruction works. An artifact that is very prominent, especially in the attenuation reconstruction, is the circular interface surrounding the phantom. This artifact is introduced by by false attenuation estimates on rays passing along the boundary

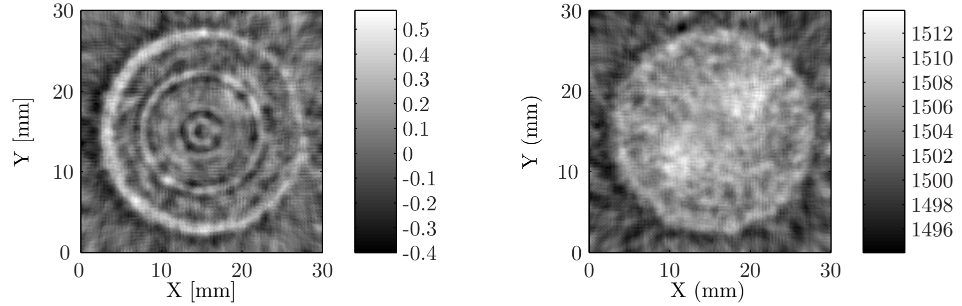

(a) Reconstructed acoustic attenuation distribution using the raw projection measurement

(b) Reconstructed speed of sound distribution using the raw projection measurement

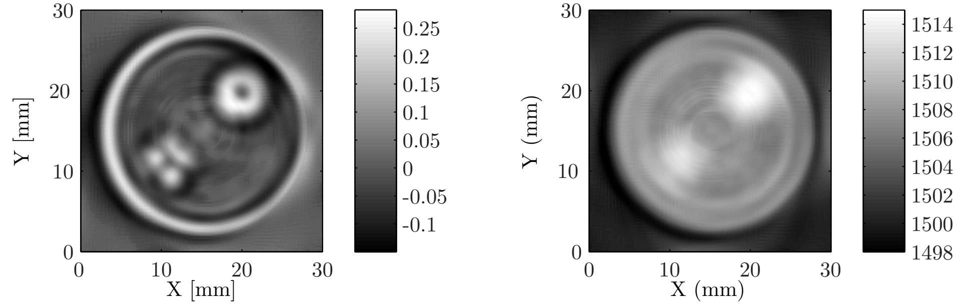

(c) Reconstructed acoustic attenuation distribution using the filtered projection measurement

(d) Reconstructed speed of sound distribution using the filtered projection measurement

Figure 4.7 Raw and filtered reconstruction results of acoustic attenuation and speed of sound for an experiment with the phantom displayed in Figure 4.5 on the 128 element linear array setup.

of the Agar object, caused by ray refraction. These false attenuation estimates are clearly visible in the sinogram in Figure 4.6c. We will come back to this artifact in the section on experimental results of the 32 element curved array.

4.4.2 Simulation study for ray refraction correction

The previously described results of the 128 element linear array were obtained without using the ray refraction correction algorithm. We will now first investigate our ray refraction correction approach on a numerical phantom. This gives us an idea for the required number of iterations and whether the method will work as predicted.

High resolution numerical phantoms were used to generate the data used in this study. The numerical phantoms are displayed in Figure 4.8. For the generation of speed of sound and acoustic attenuation projection measurements, we calculated the ray paths based on the numerical phantom with the HAFMM method. Projections were then obtained by tracing the ray paths over the speed of sound and acoustic attenuation distributions. These result in the sinograms of time of flight and integrated attenuation.

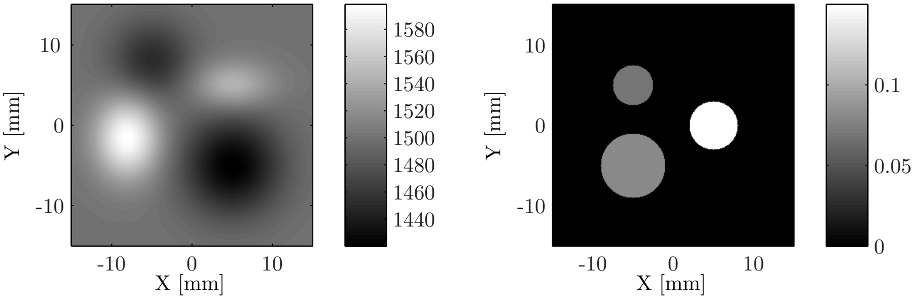

(a) Speed of sound phantom **(b)** Acoustic attenuation phantom

Figure 4.8 Overview of the numerical phantoms used in the ray refraction correction study.

To investigate the impact of the curved rays on the reconstructions of the acoustic parameters, we reconstructed the data using a straight ray approach and the proposed curved ray approach. The results of applying both approaches on the speed of sound and acoustic attenuation reconstructions are displayed in Figure 4.9. We can clearly see that using the straight ray approach we are unable to reconstruct both distributions correctly. The acoustic attenuation reconstruction, Figure 4.9b, is not anymore recognizable to the original phantom. The speed of sound reconstruction, Figure 4.9a, gives the correct trends, but the shape is very much distorted.

Next we investigated the iterative approach with ray refraction correction. The reconstruction from a previous iteration is now used to calculate the bend rays in the next iteration. The results look very successful. Both the speed of sound, Figure 4.9c, and the acoustic attenuation, Figure 4.9d, distribution are correctly distributed. Only minor artifacts remain visible in the acoustic attenuation reconstruction. The displayed results were obtained using 15 iterations which were enough for the algorithm to converge to a stable solution.

4.4.3 The curved 32 element array

Finally, an experiment on the 32 element curved array was performed which we used to investigate the multiple passive element method. A geometrical overview of the phantom used in this experiment is displayed in Figure 4.10. For this measurement, a set of nine passive elements was used. The positions of these passive elements, estimated using the algorithm described in Chapter 2, are displayed in Figure 4.11.

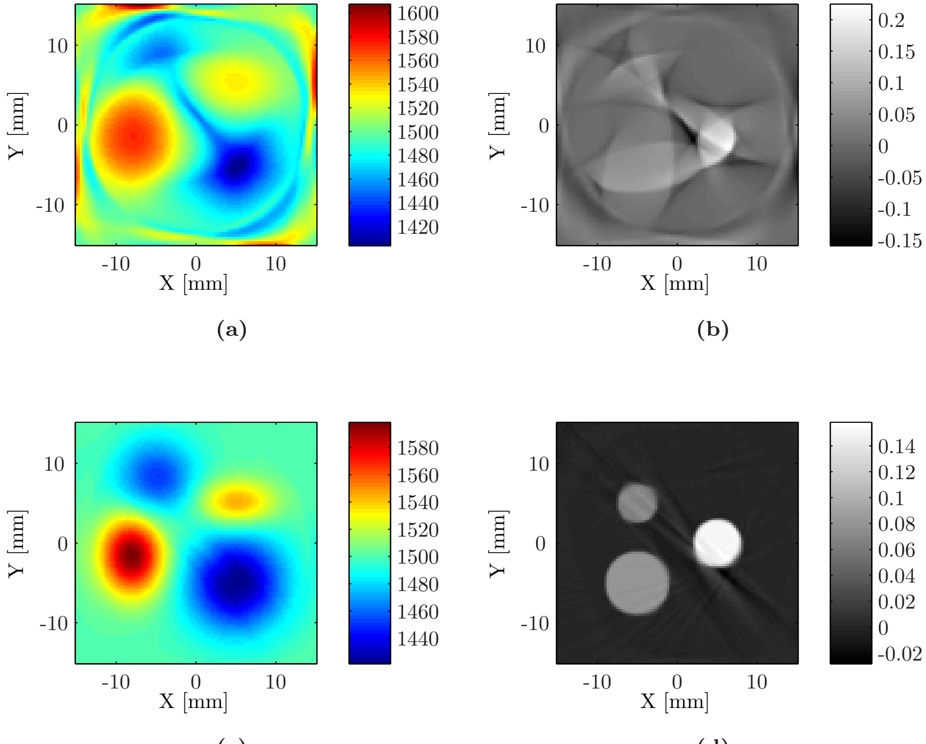

(a) **(b)**

(c) **(d)**

Figure 4.9 Speed of sound and acoustic attenuation map reconstruction results. The top row show the results of assuming linear propagation of sound rays and the bottom row shows the results of using the iterative correction algorithm with curved rays (15 iterations were used). The images on the left are the speed of sound reconstructions and the images on the right the acoustic attenuation reconstructions.

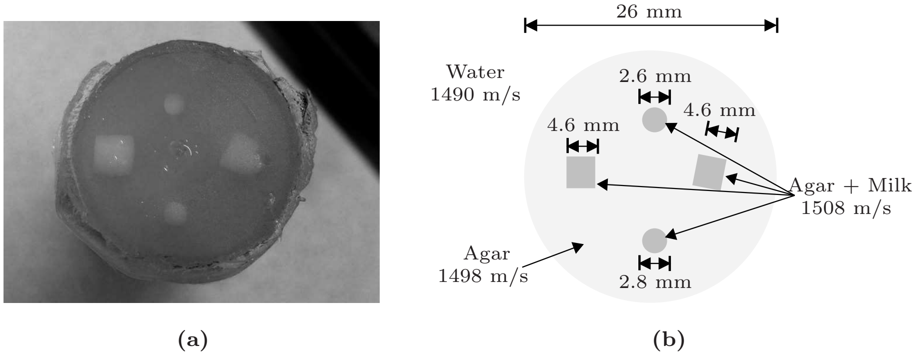

Figure 4.10 Photograph and geometrical layout of the phantom used in the 32 element linear array setup to test the multiple passive element approach.

Also displayed are the center of rotation and the position of the sensor array.

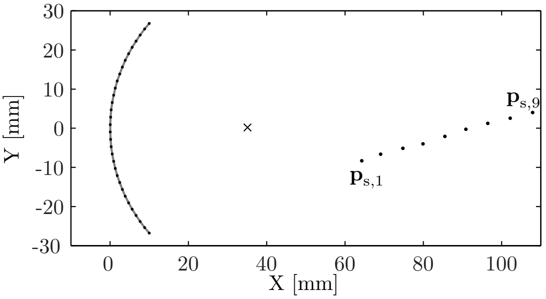

Figure 4.11 Positioning of the passive elements in the multiple passive element experiment. The nine passive elements are numbered from left (1) to right (9).

Speed of sound results

The time delay sinograms that have been extracted from the reference and object measurements of this experiment, using the techniques described in Chapter 3, are displayed for two different passive elements in Figure 4.12. From these sinograms it is clear that the furthest away from the object positioned passive element, number nine, has a full field of view that encapsulates the complete object. The closest to the object positioned passive element on the other hand, number one, has only a partial view of the object. Note that the element numbers 2, 10 and 18 are not working properly and as such do not contain the correct time delay.

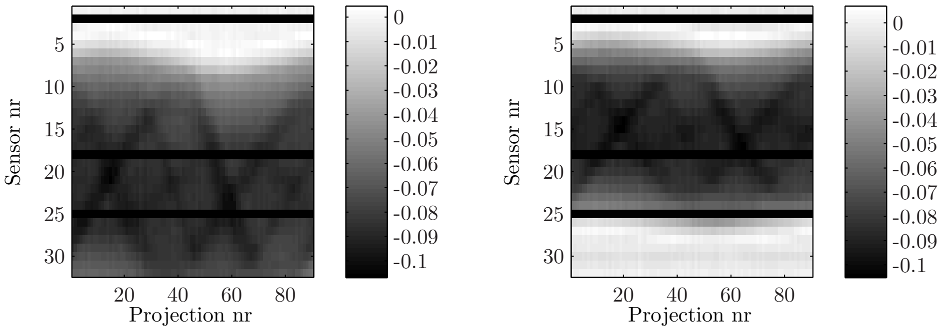

(a) Passive element nr 1 **(b)** Passive element nr 9

Figure 4.12 Extracted time delay sinograms from the measurement to test the multiple passive element approach. The units of the time delays are in μs.

Multiple passive elements with a limited number of projections The full experiment was performed with 90 projection over a full rotation of 360°. To investigate the advantage of using more passive elements, we started by using only a subset of nine projections, where the resulting rotation step size between the individual projections is 40°. The results of these limited projection reconstructions are displayed in Figure 4.13. In these results we see that there is obviously an improvement in the reconstruction when more passive elements are used. Using only one passive element, Figure 4.13a, only gives us a good reconstruction of the Agar phantom, but not of the four inner Agar/Milk structures. The result is much better with three passive elements, Figure 4.13b, then three of the four inner Agar/Milk structure are clearly visible. Doubling the number of passive elements to six in total, Figure 4.13c, makes also the fourth inner Agar/Milk structure visible. Finally, going to the full set of nine passive elements, Figure 4.13d gives a subtle improvement. For these reconstructions we used Tikhonov, L^2-norm, regularization. We can now conclude that for limited projection situations, which means less time is necessary to perform the measurement, having more passive elements is very useful and gives enormously improved reconstruction results.

Multiple passive elements with the full number of projections For a full set of 90 projections we also investigated the usefulness of having more passive elements. The reconstructions when using one and nine passive elements in this situation are displayed in Figures 4.14a and 4.14b. Overall both reconstructions in both cases are better then with the limited number of projections, there are less artifacts and the shapes of the structures are better visible. There is however not a big improvement in the reconstruction when comparing the reconstruction using only one passive element with the reconstruction using all passive elements. It can even be argued that the reconstruction using only one passive element is better than using all nine elements. This is possible when some of the passive elements have moved away from their initial

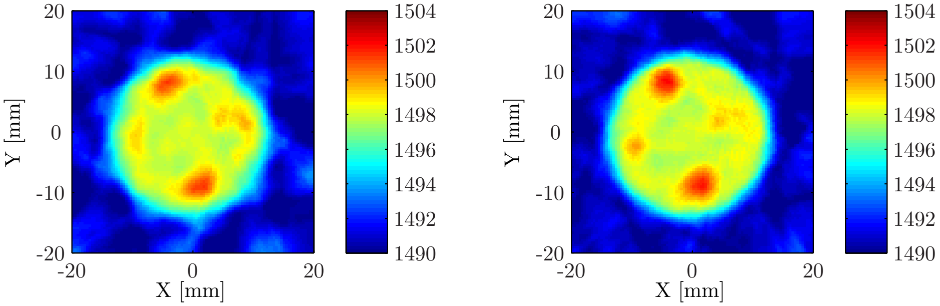

(a) Using passive element nr 1

(b) Using passive element nrs 1 to 3

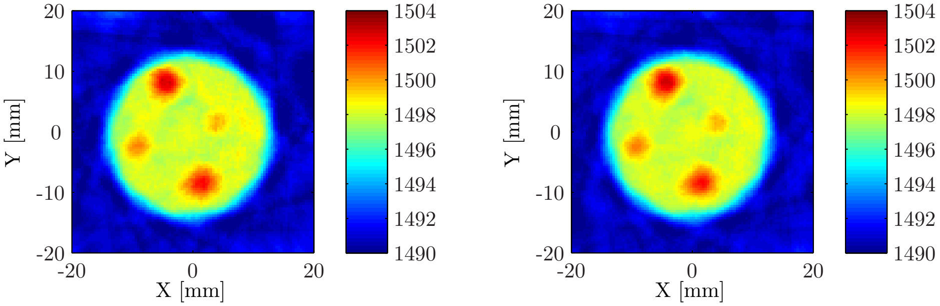

(c) Using passive element nrs 1 to 6

(d) Using passive element nrs 1 to 9

Figure 4.13 Speed of sound reconstructions from only nine projections and with an increasing number of passive elements used in the reconstruction.

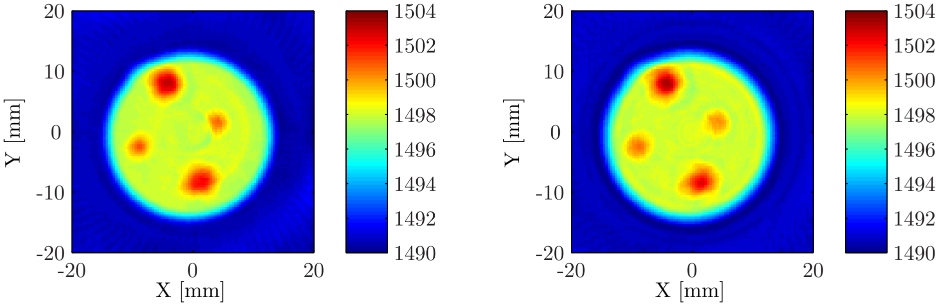

(a) Using passive element nr 1

(b) Using passive element nrs 1 to 9

Figure 4.14 Speed of sound reconstructions from the full 90 projections and with an increasing number of passive elements used in the reconstruction.

positions in the reference measurement or when there are other inconsistencies in the measurements. These inconsistencies can be so small that they are unnoticed in the the lower resolution reconstructions, such as in the limited projection reconstructions where more regularization is used. But for higher resolution reconstructions the negative effect of these inconsistencies can be higher than the positive effect of adding more information to the inverse problem, which is what we observe in Figure 4.14b. For a high number of projections we can thus conclude that there is no significant improvement to be expected from adding more passive elements to the setup. The best reconstructions have been obtained with passive element number one, which is positioned closest to the object and contains the most information in its measurement.

Total variation regularization Finally the effect of total variation, i.e., L^1-norm, regularization was tested on the speed of sound reconstructions. We expect that with this regularization the edges in the reconstruction will be preserved while the uniform areas will contain less noise. The result of applying this regularization is displayed in Figure 4.15. Compared to the L^2-normal regularization, Figure 4.14a, the expected improvements are clearly visible and it can be concluded that this regularization works very well.

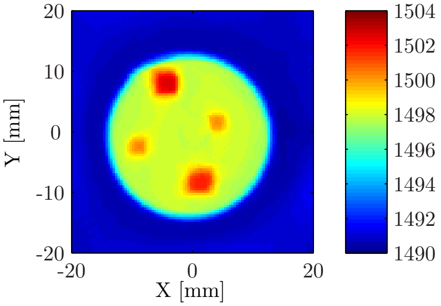

Figure 4.15 Speed of sound reconstruction from the full 90 projections using the first passive element. For this reconstruction Total Varation, L^1-norm, regularization is used.

Attenuation results

Attenuation sinograms, using the frequency dependent attenuation estimator which was introduced in Chapter 3, are displayed in Figure 4.16. The attenuation model used was based on the linear with frequency increasing attenuation function, $\alpha(\omega) = \alpha_0|\omega| + \alpha_\mathrm{r}$. What we see from these sinograms is that there is no clear transition from attenuation to no attenuation, which we would expect at the boundaries of the object. Instead we see that there is attenuation and amplification of the signal at the object boundary, which is visible around sensor element number five. The expected

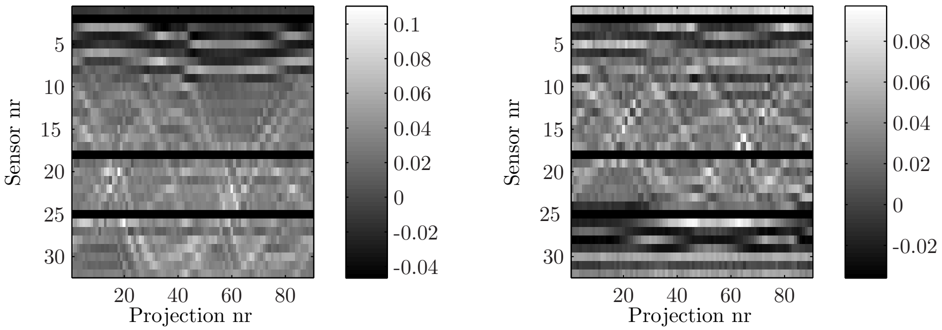

(a) Passive element nr 1 **(b)** Passive element nr 9

Figure 4.16 Extracted frequency dependent attenuation (linear increasing with frequency) sinograms from the measurement to test the multiple passive element approach. The units are in Np/MHz.

boundary can nicely be observed in the time delay sinograms in Figure 4.12. These attenuation and amplification effects happen at the boundary of the object, where ray refraction effects could occur. We expected that ray refraction would result in an amplitude effect of the propagated signal, because refraction changes the density of rays, resulting in signal amplitude attenuation and amplification, but not in a signal shape change. The frequency dependent part of the attenuation function, governing the signal shape, would therefore still be the same. Since the frequency dependent attenuation constant is not related to the signal amplitude, only to the signal shape, we expected to be insensitive to ray refraction effects. However, our experimental results indicate that the frequency dependent attenuation constant is changing at the boundary where ray refraction occurs. Therefore we think that the effects are caused by multipath propagation, an effect which we have not included in our model and therefore results in false attenuation and amplification measurements. When two paths between sensor and detector exist, one through the object and one around the object, which have a small propagation time difference, the two signals will interfere with each other so that the assumed model of a measuring a single signal is not valid anymore. To deal with these multipath propagation effects, a model including multipath propagation needs to be used. This multipath model is a recommendation for future work and falls out of the time scope of this research since this was discovered at the end of the project.

Instead of estimating frequency dependent attenuation, we also investigated signal amplitude attenuation and ignoring frequency dependency in the model. Thus all attenuating effects will now be related to a single frequency independent parameter, i.e., $\alpha(\omega) = \alpha_0$. The obtained sinograms for this measured attenuation parameter are displayed in Figure 4.17. Clearly the predicted amplitude effects near sensor element number five are visible. However the result looks quite reasonable and better than the result obtained using the frequency dependent attenuation model, Figure 4.16.

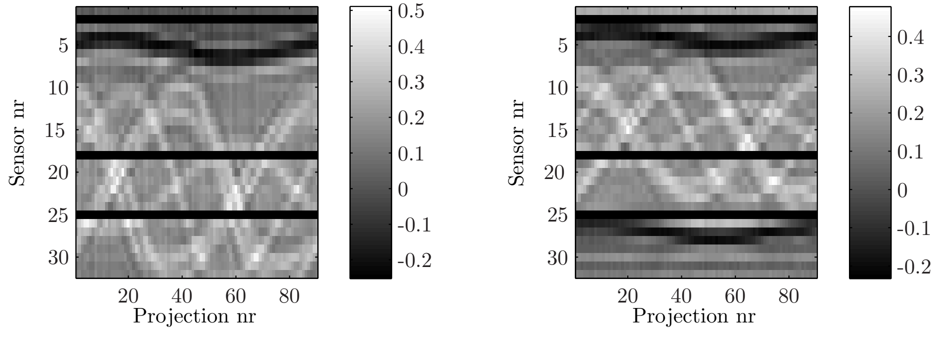

(a) Passive element nr 1

(b) Passive element nr 9

Figure 4.17 Extracted attenuation sinograms, assuming attenuation is frequency independent, from the measurement to test the multiple passive element approach. The units are in Np.

Reconstruction results We show the attenuation reconstructions on the measurements obtained with the first passive element and using Total Variation regularization, because this gave the best result for the reconstruction of speed of sound. The measurements obtained with both models, one assuming a frequency dependent and independent attenuation and one assuming only frequency independent attenuation, were reconstructed and the results are displayed in Figure 4.18. Both reconstructions show the four inner Agar/Milk structures and the outer Agar phantom, however the frequency independent model gives a much better reconstruction with almost no arti-

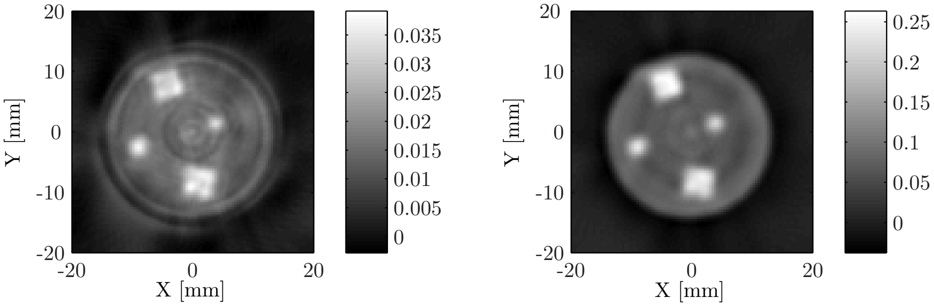

(a) Using frequency dependent attenuation

(b) Using only frequency independent attenuation

Figure 4.18 Attenuation reconstructions for the two attenuation models, only passive element number one was used on all 90 projections and with L^1-norm regularization. The units are in Np/(cm·MHz) and Np/cm respectively. The input sinograms for both reconstructions are displayed in Figures 4.16a and 4.17a.

facts. In the reconstruction using the frequency dependent attenuation, Figure 4.18a, there are artifacts at the boundary of the object caused by the previously discussed multipath effects. We can conclude that the frequency independent attenuation reconstruction is quite satisfactory, and expect that the frequency dependent attenuation reconstruction can be improved by using a multipath propagation model.

We also investigated the limited projection scenario with only nine projections. The reconstruction results when using only one and all the nine available passive elements are displayed in Figure 4.19. Also here it is visible that using more passive elements really enhances the image quality of the reconstructions.

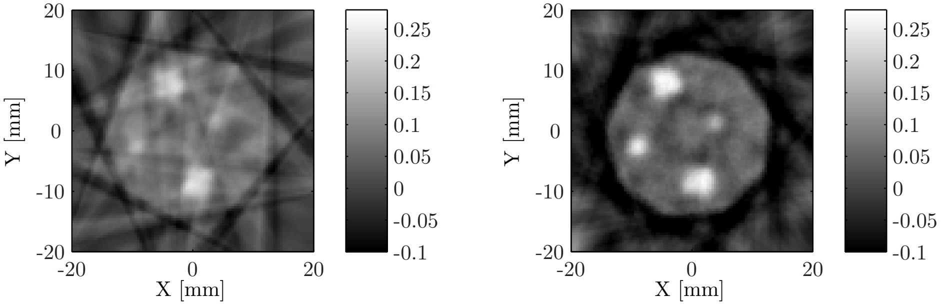

(a) Using passive element nr 1

(b) Using passive element nrs 1 to 9

Figure 4.19 Attenuation reconstructions from only nine projections and with an increasing number of passive elements used in the reconstruction.

4.5 Conclusion and future work

In this chapter we have presented a method to reconstruct both speed of sound and acoustic attenuation from projection measurements. These projection measurements are extracted from the reference and object measurements using the techniques described in Chapter 3. A measurement model was formulated which, once acoustic ray paths are known, linearly relates the projection measurements to the unknown acoustic property distributions. A reconstruction method is proposed by solving the resulting, large and sparse, linear system of equations using LSQR combined with proper regularization.

The influence of the number of passive elements on the inverse problem is investigated by analyzing the condition number of the projection matrix. Also the optimal geometrical placement of the passive elements was investigated. It was found that placement of the passive elements should always be on a line of sight between one side of the detector array and the element itself and that the elements positioned closest to the object contribute the most information.

An iterative procedure was proposed to correct for ray refraction effects, by switching between ray tracing through an estimated speed of sound map using the Fast

Marching Method and estimating the speed of sound map using the predicted refracted rays.

Using experimental evaluation we have shown that our proposed technique allows us to reconstruct speed of sound as well as acoustic attenuation distributions from photoacoustic measurements by adding one or more passive elements to our setup. The reconstruction results of both speed of sound and acoustic attenuation are good, the reconstructed distributions show the correct physical values. A noise filtering algorithm was successfully applied to the noisy measurement data obtained with the 128 element linear array. The best reconstruction results have been obtained with Total Variation, i.e., with an L^1-norm.

Problems have been encountered when reconstructing frequency dependent attenuation. We suspect that these problems are caused by multipath ray propagation effects which are not included in our current measurement model. An improvement for future work would be to extend the model to multipath ray propagation, this might however be difficult. Also we have obtained good results with the current model and using frequency independent attenuation. Finally for speed of sound reconstructions there is no problem with the current model.

5

Reconstruction of optical absorption[1]

Abstract

The reconstruction of the optical absorption distribution inside an object is the general problem that is considered in photoacoustic image reconstruction. A popular and widely used approach to solving this problem is the Filtered Back Projection (FBP) algorithm, invented originally for X-Ray CT imaging. With this algorithm an approximate solution, which can be calculated with very low computational complexity, is obtained. Solutions having a higher accuracy are possible by using iterative methods, which however require much more time to converge to a solution. We have investigated the general photoacoustic image reconstruction problem. An efficient way of representing the source distribution and calculating the required projection integral was proposed and an easy to calculate preconditioner to speed up the convergence speed of iterative algorithms was proposed. Furthermore we presented a new way to compensate for speed of sound corrections by making use of the Fast Marching method. Finally we outline an approach that can be used to correct for motion artifacts in photoacoustic imaging by attaching landmarks to the object that is being imaged.

---

[1] A part of this chapter is under communication as:
G.H. Willemink et al, “A fast iterative reconstruction method using preconditioning for photacoustic computed tomography”, IEEE Transactions on Medical Imaging

5.1 Introduction

This chapter consists of three different sections, all related to the reconstruction of the optical absorption distribution. In the first section, the general problem of photoacoustic image reconstruction is considered. The reconstruction can be done in either an iterative or a direct way, both have their advantages and disadvantages which will be discussed. Some new ideas on image representation and preconditioning to accelerate the iterative methods will be presented there as well. Then in the second and third sections two modifications of the reconstruction will be discussed. First we discuss how the reconstruction can be modified to include speed of sound inhomogeneities. After that we discuss how motion correction can be applied, when unknown motion has occurred to the object during measurement acquisition.

5.2 Photoacoustic image reconstruction

This section discusses solutions to solve the optical absorption reconstruction problem.

5.2.1 Photoacoustic measurement model

As seen in section 1.2, the generation and propagation of photoacoustic pressure waves in acoustically non-attenuating and homogeneous media, i.e. with a constant speed of sound, is governed by the following partial differential equation:

$$\nabla^2 p(\mathbf{r},t) - \frac{1}{c^2}\frac{\partial^2 p(\mathbf{r},t)}{\partial t^2} = -\frac{\beta}{C_\mathrm{p}}\frac{\partial I(t)}{\partial t}A(\mathbf{r}) \tag{5.1}$$

Here $A(\mathbf{r})$ represents the optical absorption distribution of the object as a function of spatial $\mathbf{r}$. $I(t)$ represents the illumination profile of the laser source as a function of time. β and C_p are the volume thermal expansion coefficient and the specific heat of the object. The pressure that will be generated is given by $p(\mathbf{r},t)$ as a function of both position and time. The speed of sound in the medium and the object is given by c. The solution to such a wave equation can be calculated by convolving the source term on the right with the Green's function of the wave equation. The Green's function represents the solution of the wave equation to an impulsive source and is given by, see Appendix A:

$$G(\mathbf{r},t) = \frac{-1}{4\pi\|\mathbf{r}\|}\delta\left(\tfrac{1}{c}\|\mathbf{r}\| - t\right) \tag{5.2}$$

Convolving this Green's function with the source term of the wave equation, $-\frac{\beta}{C_\mathrm{p}}\frac{\partial I(t)}{\partial t}A(\mathbf{r})$ gives the solution of the build up pressure function:

$$\begin{aligned} p(\mathbf{r},t) &= G(\mathbf{r},t) *_{\mathbf{r},t} \left(-\frac{\beta}{C_\mathrm{p}}\frac{\partial I(t)}{\partial t}A(\mathbf{r})\right) && (5.3)\\ &= -\frac{\beta}{C_\mathrm{p}}\Big(G(\mathbf{r},t) *_{\mathbf{r}} A(\mathbf{r})\Big) *_t \frac{\partial I(t)}{\partial t} && (5.4)\\ &= \frac{\beta}{4\pi C_\mathrm{p}}\iiint \frac{A(\mathbf{r}')}{\|\mathbf{r}-\mathbf{r}'\|}\delta\left(\tfrac{1}{c}\|\mathbf{r}-\mathbf{r}'\|-t\right)\mathrm{d}\mathbf{r}' *_t \frac{\partial I(t)}{\partial t} && (5.5)\\ &= \frac{\beta}{4\pi C_\mathrm{p}}\left(\frac{1}{t}\iint\limits_{\|\mathbf{r}-\mathbf{r}'\|=ct} A(\mathbf{r}')\mathrm{d}\mathbf{r}'\right) *_t \frac{\partial I(t)}{\partial t} && (5.6) \end{aligned}$$

Now suppose we position an ultrasound transducer at the spatial position $\mathbf{r}$. With the ultrasound transducer we can measure the generated pressure wave, which results in a measurement of:

$$\tilde{p}(\mathbf{r},t) = p(\mathbf{r},t) * h_\mathrm{IR}(t) \tag{5.7}$$

where $h_\mathrm{IR}(t)$ represents the impulse response of the transducer. In this model, diffraction effects have been ignored. Including diffraction effects, due to the finite size of the aperture of the transducer, would lead to an impulse response which is besides time dependent also spatially dependent, i.e. $h_\mathrm{IR}(\mathbf{r},t)$. In order to construct the model we need to have a description of the illumination profile $I(t)$ and the impulse response of the transducer $h_\mathrm{IR}(t)$. In practice it might be difficult to measure these functions directly. However, a practical solution to this problem was introduced by Wang et al[61], who propose to use the measured response of a photoacoustic point source to infer these functions. Now positioning a photoacoustic point source at $\mathbf{r}_\mathrm{p}$, i.e. $A(\mathbf{r}) = \delta(\mathbf{r}-\mathbf{r}_\mathrm{p})$, will result in a measured pressure, by using (5.7) and (5.5), of:

$$\tilde{p}_\delta(\mathbf{r},t) = \frac{\beta}{4\pi\|\mathbf{r}-\mathbf{r}_\mathrm{p}\|C_\mathrm{p}}\delta\left(\tfrac{1}{c}\|\mathbf{r}-\mathbf{r}_\mathrm{p}\|-t\right) *_t \frac{\partial I(t)}{\partial t} *_t h_\mathrm{IR}(t) \tag{5.8}$$

This means we can determine the convolution of the time derivative of the illumination profile with the transducer impulse response from this measured photoacoustic point source response, by rearranging the equation:

$$\frac{\partial I(t)}{\partial t} *_t h_\mathrm{IR}(t) = \frac{4\pi\|\mathbf{r}-\mathbf{r}_\mathrm{p}\|C_\mathrm{p}}{\beta}\tilde{p}_\delta\left(\mathbf{r}, t-\tfrac{1}{c}\|\mathbf{r}-\mathbf{r}_\mathrm{p}\|\right) \tag{5.9}$$

The measured pressure wave $\tilde{p}(\mathbf{r},t)$ of an optical absorption source $A(\mathbf{r})$ can thus be expressed as a function of the measured photoacoustic point source response:

$$\tilde{p}(\mathbf{r},t) = \|\mathbf{r}-\mathbf{r}_\mathrm{p}\| \times \left(\frac{1}{t}\iint\limits_{\|\mathbf{r}-\mathbf{r}'\|=ct} A(\mathbf{r}')\mathrm{d}\mathbf{r}'\right) *_t \tilde{p}_\delta(\mathbf{r},t') \tag{5.10}$$

with $t' = t - \frac{1}{c}\|\mathbf{r}-\mathbf{r}_\mathrm{p}\|$.

In our PER-PAT setup we use sliced light illumination of the object, resulting in a plane of illumination. The detector elements are all positioned in this plane and are surrounding the object. Furthermore, the sensitivity of the detector elements in the elevation (z) direction is restricted to this plane of illumination. Therefore we only have to take into account the contributions from the source distribution $A(\mathbf{r})$ in the plane of illumination, so that from now on the positions $\mathbf{r} = \left(r_x, r_y\right)$ are 2-d and indicate a position in the plane of illumination. The two dimensional integral over a spherical shaped surface can then be replaced by a one dimensional integral over a circular shaped contour:

$$\tilde{p}(\mathbf{r}, t) = \|\mathbf{r} - \mathbf{r}_\mathrm{p}\| \times \left(\frac{1}{t} \int\limits_{\|\mathbf{r}-\mathbf{r}'\|=ct} A(\mathbf{r}')\mathrm{d}\mathbf{r}' \right) *_t \tilde{p}_\delta(\mathbf{r}, t') \tag{5.11}$$

This model will be the basis of our reconstruction approach which we present in the next section.

5.2.2 Calculating the photoacoustic projection integral

The source distribution $A(\mathbf{r})$ is a continuous distribution of compact support. To make the inverse problem feasible, we will represent this source distribution using a limited number of degrees of freedom (pixels). Each pixel will be associated with a value $x_{i,j}$ and is linked to a 2-d basis function $h(\mathbf{r})$ at a shifted spatial location $\mathbf{r}_{i,j}$, so that the source distribution can be calculated as:

$$A(\mathbf{r}) = \sum_{i,j} x_{i,j} h(\mathbf{r} - \mathbf{r}_{i,j}) \tag{5.12}$$

The 2-d basis functions are typically of compact support and should make it possible to represent smooth (i.e. bandlimited) source distributions. We will come back to what basis functions are suitable for the representation of the source distributions later.

Evaluation of the projection integral

Evaluating the projection integral comes down to summing the contributions of each of the basis functions. Substituting the representation of our source distribution $A(\mathbf{r})$ in terms of basis functions (5.12) in the projection integral results in:

$$\begin{aligned} \int\limits_{\|\mathbf{r}_\mathrm{d}-\mathbf{r}'\|=ct} A(\mathbf{r}')\mathrm{d}\mathbf{r}' &= \int\limits_{\|\mathbf{r}_\mathrm{d}-\mathbf{r}'\|=ct} \sum_{i,j} x_{i,j} h(\mathbf{r}' - \mathbf{r}_{i,j})\mathrm{d}\mathbf{r}' && (5.13) \\ &= \sum_{i,j} x_{i,j} \int\limits_{\|\mathbf{r}_\mathrm{d}-\mathbf{r}'\|=ct} h(\mathbf{r}' - \mathbf{r}_{i,j})\mathrm{d}\mathbf{r}' && (5.14) \end{aligned}$$

where $\mathbf{r}_\mathrm{d}$ represents the detector position. We see that the integration can be performed independently of all the shifted basis functions and the result of all integrations

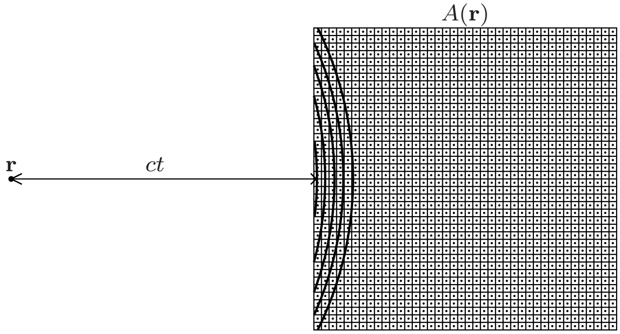

Figure 5.1 Illustration of the circular projection integral over the optical absorption distribution $A(\mathbf{r})$. The detector position is indicated with $\mathbf{r}$. The source distribution is represented on a grid, each of the grid points is coupled to a basis function and a value $x_{i,j}$.

simply has to be summed. An overview of the projection integral geometry is displayed in Figure 5.1. The projection integral is defined over curved paths through the basis function. However, on the scale of a single basis function, this curved path can be approximated as a linear path, which simplifies the actual calculation of the integral. This approximation holds when the distance from detector to a pixel, $\|\mathbf{r}_\mathrm{d} - \mathbf{r}_{i,j}\|$, is large compared to the scale of a basis function Δx, i.e. when $\|\mathbf{r}_\mathrm{d} - \mathbf{r}_{i,j}\| \gg \Delta x$. For example, when the closest distance of the detector to the object is 1 cm and the scale of a single basis function is set to 100 μm, then the deviation of the curved path from a straight line is at most 0.125 μm in the area of one pixel, showing that it is justified to make this approximation.

Going to a pixel centered coordinate system and applying the approximation of a projection line instead of a projection curve gives us:

$$\int\limits_{\|\mathbf{r}_\mathrm{d}-\mathbf{r}'\|=ct} h(\mathbf{r}' - \mathbf{r}_{i,j})\mathrm{d}\mathbf{r}' = \int\limits_{\|\mathbf{r}_\mathrm{d}-\mathbf{r}_{i,j}-\mathbf{r}'\|=ct} h(\mathbf{r}')\mathrm{d}\mathbf{r}' \approx \int\limits_{\|\mathbf{r}_\mathrm{d}-\mathbf{r}_{i,j}\|+\mathbf{r}_\varphi^T\mathbf{r}'=ct} h(\mathbf{r}')\mathrm{d}\mathbf{r}' \tag{5.15}$$

where $\mathbf{r}_\varphi = \frac{\mathbf{r}_{i,j}-\mathbf{r}_\mathrm{d}}{\|\mathbf{r}_{i,j}-\mathbf{r}_\mathrm{d}\|}$ is the unit vector pointing from the detector position to the pixel position. To clarify this, the projection line together with the geometry around the pixel $x_{i,j}$ is displayed in Figure 5.2a. If we rotate the basis function so that it aligns with the rotated coordinate system, as shown in Figure 5.2b, and refer to the rotated basis function as $h_\varphi(\mathbf{r})$ we get for the evaluation of the integral of each basis function:

$$\int\limits_{\|\mathbf{r}_\mathrm{d}-\mathbf{r}_{i,j}\|+\mathbf{r}_\varphi^T\mathbf{r}'=ct} h(\mathbf{r}')\mathrm{d}\mathbf{r}' = \int\limits_{-\infty}^{\infty} h_\varphi(ct - \|\mathbf{r}_\mathrm{d} - \mathbf{r}_{i,j}\|, \beta)\mathrm{d}\beta \tag{5.16}$$

Thus finally, using rotated basis function $h_\varphi(\mathbf{r})$ and linearization of the integral path,

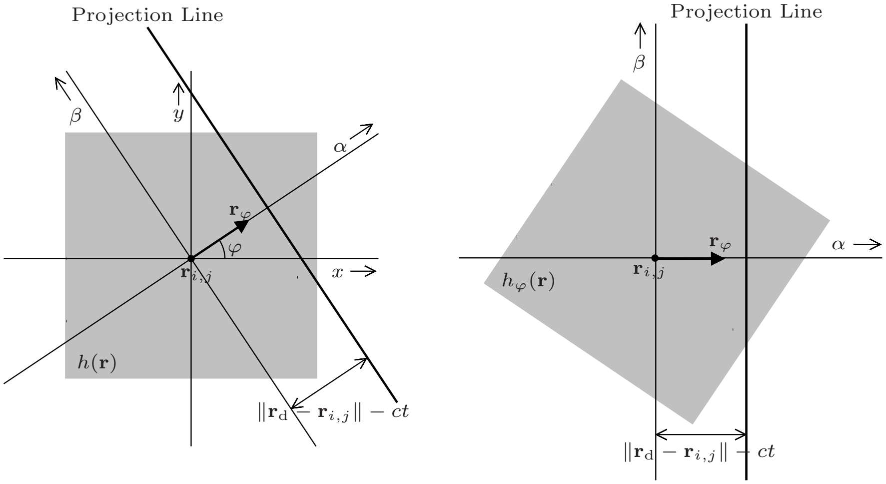

(a) Basis function projection geometry **(b)** Rotated basis function projection geometry

Figure 5.2 Geometry of the projection line with respect to the coordinate system defined around a single pixel $x_{i,j}$ positioned at $\mathbf{r}_{i,j}$.

we can write the projection as:

$$\int\limits_{\|\mathbf{r}_\mathrm{d}-\mathbf{r}'\|=ct} A(\mathbf{r}')\mathrm{d}\mathbf{r}' \approx \sum_{i,j} x_{i,j} \int\limits_{-\infty}^{\infty} h_\varphi(ct - \|\mathbf{r}_\mathrm{d} - \mathbf{r}_{i,j}\|, \beta)\mathrm{d}\beta \tag{5.17}$$

Rotation invariant basis functions

An interesting thing to further investigate is the situation of having a rotation invariant basis function. Such a basis function can be fully described from only its radial profile $h_r(r)$ using $h(\mathbf{r}) = h_r(\|\mathbf{r}\|)$. The required line integral is then independent of the orientation φ of the kernel and can be calculated from the radial profile using:

$$h_t(t) = \int\limits_{-\infty}^{\infty} h_r(\sqrt{(ct)^2 + x^2})\mathrm{d}x = 2\int\limits_{0}^{\infty} h_r(\sqrt{(ct)^2 + x^2})\mathrm{d}x \tag{5.18}$$

The required integration over the radial profile function $h_r(r)$ is an integral transform, also known as the Abel Transform, see Appendix E.4. By substituting $t' = ct$, such that $h_t(t) = h_{t'}(ct)$, we can express this transform as:

$$h_{t'}(t') = 2\pi \mathcal{F}^{-1}\mathcal{H}_0\{h_r(r)\} \tag{5.19}$$

and its inverse as:

$$h_r(r) = \frac{1}{2\pi}\mathcal{H}_0^{-1}\mathcal{F}\{h_{t'}(t')\} \tag{5.20}$$

where $\mathcal{F}$ is the Fourier transform and $\mathcal{H}_0$ the zeroth order Hankel transform, see Appendix E.4. The resulting time domain kernel function $h_t(t)$ is symmetric in its origin. Thus, using a rotation invariant basis function, calculating the projection integral comes down to a simple convolution in the time domain:

$$\begin{aligned} \int\limits_{\|\mathbf{r}_\mathrm{d}-\mathbf{r}'\|=ct} A(\mathbf{r}')\mathrm{d}\mathbf{r}' &\approx \sum_{i,j} x_{i,j} h_t(t - \tfrac{1}{c}\|\mathbf{r}_\mathrm{d} - \mathbf{r}_{i,j}\|) && (5.21) \\ &= h_t(t) * \left(\sum_{i,j} x_{i,j}\delta(t - \tfrac{1}{c}\|\mathbf{r}_\mathrm{d} - \mathbf{r}_{i,j}\|) \right) && (5.22) \end{aligned}$$

where the approximation again stems from the fact that we approximate the curved projection paths with linear projection paths. This is a very nice observation and it gives us insight in how to interpret different ways to calculate the projection integral in terms of the implicitly underlying basis function representation. Basically, this result already hints in the direction of an efficient pixel driven way to calculate the photoacoustic projection integral.

Simple pixel based calculation of the integral

Using the results of the previous section, we can give a meaning to simple pixel based methods to numerically calculate the photoacoustic projection integral. The simple schemes that we discuss here are based on calculating a time of flight for each pixel. Each time of flight value can be mapped to a certain location in the sampled time domain signal as shown in Figure 5.3. Due to the fact that the time domain signal is sampled, we have to use some form of interpolation to project the pixel value onto the sampled time domain signal. The most simple interpolation method is to just round the time of flight to the nearest sample, this method is called nearest neighbor interpolation (Figure 5.3a). A slightly better method would be to use linear interpolation to distribute the pixel value over the two nearest samples (Figure 5.3b) and an even better method would be to use cubic interpolation to distribute the value over the four nearest samples (Figure 5.3c). We will now see what the implications are when using such simple interpolation techniques to evaluate the photoacoustic projection integral.

Choosing a certain interpolation in the time domain can be related to the choice of a spatial basis function to represent the source distribution. The relation between these two is given by the Abel Transform as discussed in the subsection on rotation invariant basis function. Using (5.20) we can calculate the radial profile of the

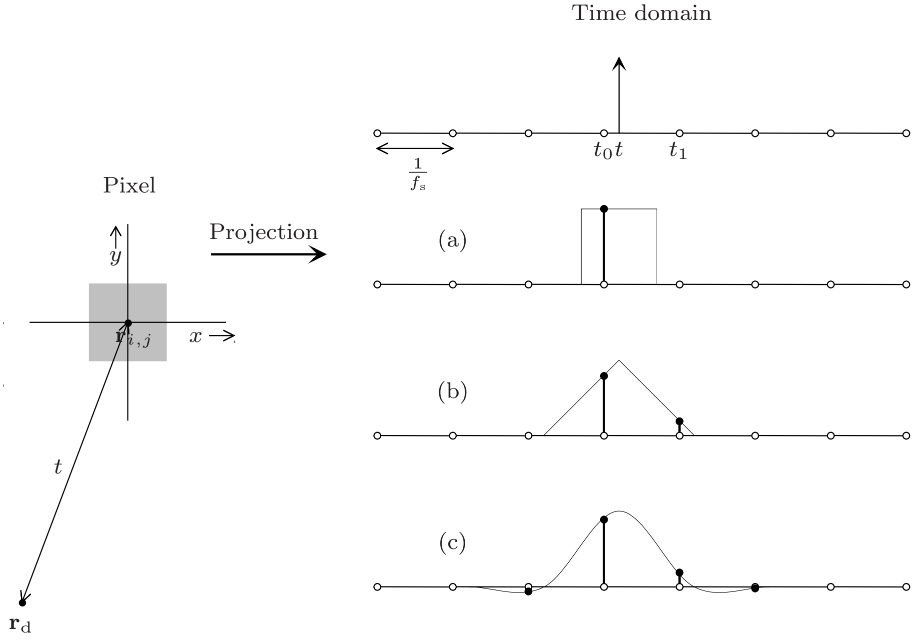

Figure 5.3 Calculation of the projection of a single pixel using a simple time domain interpolation scheme: (a) nearest neighbor interpolation, (b) linear interpolation and (c) cubic interpolation. The pixel is positioned at $\mathbf{r}_{ij}$ and the detector is positioned at $\mathbf{r}_\mathrm{d}$ resulting in a time of flight $t = \frac{1}{c}\|\mathbf{r}_{ij} - \mathbf{r}_\mathrm{d}\|$. The sampling frequency in the time domain is given by f_s.

corresponding spatial basis function for a certain interpolation method based on the convolution kernel that is used in that interpolation method. The convolution kernels for the chosen time domain interpolation methods are displayed in Table 5.1. The corresponding spatial basis functions that implicitly belong to these time domain interpolation kernels, numerically calculated using (5.20), are displayed in Figure 5.4. For convenience, in this figure we have displayed the temporal and spatial functions on the same scale, this can be done when the sampling in both domains is equal. In general, the relation between spatial and temporal grid spacing is determined by the sound speed and given by $\Delta r = c\Delta t$. From Figure 5.4a we see that using nearest neighbor interpolation to calculate the projection integral results in a valley shaped spatial basis function with very steep edges. This is an interesting result and it shows that nearest neighbor interpolation leads to a spatial basis function that will fail to properly represent smooth source distributions. Also in case of the linear interpolation, Figure 5.4b, we see a spikey function which will also fail to properly represent smooth source distributions. Finally in the case of the cubic interpolation scheme, Figure 5.4c, we see a basis function which is capable of representing smooth source

Method	Interpolation kernel
Nearest neighbor	$h_t(t) = \begin{cases} 1 & \lvert t\rvert < \frac{1}{2} \\ 0 & \text{otherwise} \end{cases}$
Linear	$h_t(t) = \begin{cases} 1 - \lvert t\rvert & \lvert t\rvert < 1 \\ 0 & \text{otherwise} \end{cases}$
Cubic	$h_t(t) = \begin{cases} \frac{3}{2}\lvert t\rvert^3 - \frac{5}{2}\lvert t\rvert^2 + 1 & \lvert t\rvert < 1 \\ -\frac{1}{2}\lvert t\rvert^3 + \frac{5}{2}\lvert t\rvert^2 - 4\lvert t\rvert + 2 & 1 < \lvert t\rvert < 2 \\ 0 & \text{otherwise} \end{cases}$

Table 5.1 Interpolation methods and corresponding convolution kernels, when the spacing between time points is set to $\Delta t = 1$

distributions. From this we can conclude, that when using these simple interpolation methods on its own to calculate the projection integeral, only the cubic interpolation scheme is a good choice. This conclusion however is only valid when the grid spacing in both the time domain and spatial domain are matched. The reason for this will be explained in the next paragraph.

Suppose the time domain measurements are sampled with a sampling frequency of f_s, then when using one of the simple time domain interpolation schemes the grid spacing in the spatial domain should be in the order of $\Delta r = \frac{c}{f_\mathrm{s}}$. When the grid spacing is larger, $\Delta r > \frac{c}{f_\mathrm{s}}$, thus the spatial resolution is lower, the resulting spatial basis function is not able to cover the complete spatial domain and gaps will appear in between the pixels. This will have an aliasing effect, the higher temporal frequencies will alias back into the spatial domain. When the grid spacing is made smaller $\Delta r < \frac{c}{f_\mathrm{s}}$, thus the spatial resolution is made higher, the resulting spatial basis function will start to overlap too much with its neighbors. This will have the effect of making the inverse problem more ill-conditioned. Due to the smoothing effect of the wider spatial basis functions there will be more sets of solutions resulting in the same (after applying the basis function) representations of the source distribution, i.e. the high frequencies of the pixel map will lie in the null space of the transformation.

Pixel based calculation of the integral using time domain convolution

Any time domain kernel function $h_t(t)$ can be chosen to evaluate the photoacoustic projection integral, each with its own implicitly corresponding spatial basis function $h_r(r)$. We have seen in the previous section what simple time domain kernels, based on an interpolating function, will do in terms of their corresponding basis functions. A limitation when using these interpolating basis functions alone is that the scale of the time spacing in the raw measurements should match the scale of the grid spacing in

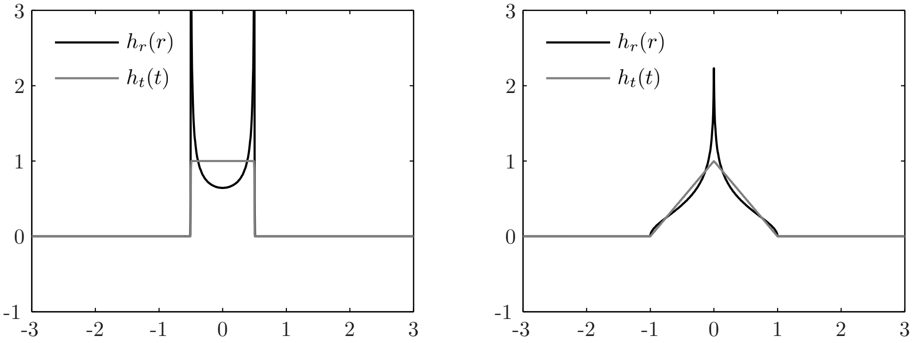

(a) Nearest neighbor **(b)** Linear

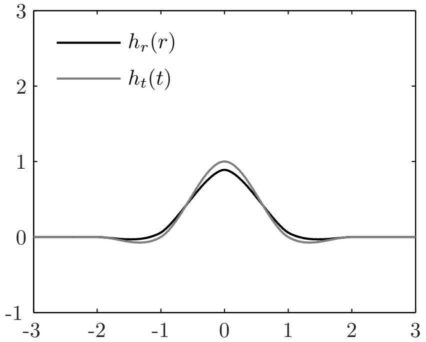

(c) Cubic

Figure 5.4 The effect of using a simple interpolation schemes in the time domain on the corresponding (implicitly assumed) spatial radial basis function $h_r(r)$. The spacing in the time domain was set to $\Delta t = 1$ and the speed of sound set to $c = 1$

the spatial domain. In a reconstruction problem like photoacoustic imaging, generally the grid spacing in the spatial domain will be wider, i.e. the resolution lower, than the matching time domain spacing. The reason for that is to limit the number of unknown pixels in the system of equations and has also to do with the bandwidth of the measuring transducer which does not allow for such high matching resolution reconstructions. For an arbitrary kernel function $h_t(t)$ still the approach sketched in Figure 5.3, but now using the wider kernel function $h_t(t)$ to sample from instead, can be used to calculate the necessary projection. However, with increasing kernel size it becomes less attractive do so in terms of computational efficiency. For wider kernels, a better method would be a two-step approach. First use one of the small interpolating functions to calculate the footprint of a certain pixel $x_{i,j}$ to a time position t and to splat and sample this smaller interpolating kernel on the time axis, as also shown in

Figure 5.3. Then in a next step, a simple convolution operation on the sampled time domain signal with the arbitrary kernel function $h_t(t)$, will give the aimed for result. Thus splatting and sampling of a wide kernel $h_t(t)$, i.e. discretizing the photoacoustic integral (5.21), can be approximated by splatting and sampling of a small interpolating kernel and convolving the result with the wider kernel $h_t(t)$. The convolution step can be implemented using FFT operations, resulting in a computationally efficient scheme.

The complete algorithms to calculate forward and backward projections of the discretized integral (5.21) are outlined in Figures 5.5 and 5.6 respectively. In these algorithms it is assumed that the source distribution $A(\mathbf{r})$ is represented on a grid of pixels $x_{i,j}$ and the projections are represented as a set of vectors $\mathbf{z}_d$ containing the time domain projection for a certain detector element. In the algorithms, a vector $\mathbf{p}$ is calculated which contains the coefficients resulting from interpolation of the time of flight t over the n_{coeff} neighboring time grid points. For nearest neighbor interpolation $n_{\text{coeff}} = 1$, for linear interpolation $n_{\text{coeff}} = 2$ and for cubic interpolation $n_{\text{coeff}} = 4$.

It is also possible to construct a sparse matrix once, which can then be used to calculate the necessary projections and back projections. In compressed column storage format, using 64 bits floating point coefficients and 64 bits integer representation (64 bits architecture), such a sparse matrix would occupy $16 n_{\text{coeff}} n_i n_j n_d + 8 n_i n_j$ bytes of memory, where n_i and n_j are the dimensions of the source image, n_d are the number of detector positions and n_{coeff} is the number of coefficients necessary for the interpolation method. For example, an image of dimensions 300×300 with 90 projections and using linear interpolation would result in a sparse matrix that occupies 247 Megabytes of memory. Depending on the dimensions of the image and the number of projections it can be advantageous to represent the projection as a sparse matrix, since forward and backward projections can be calculated faster in that case.

Algorithm Forward photoacoustic projection integral

```
For all detector element positions $\mathbf{r}_d$ in the measurement configuration
  For all pixels $(i, j)$ in the source distribution image $A(\mathbf{r})$
    Calculate the time of flight $t = \|\mathbf{r}_{i,j} - \mathbf{r}_d\|$
    Calculate interpolation coefficients $\mathbf{p}$ at neighboring time points of $t$
    Increase the measurement of each of the neighboring time points $t_k$
    with corresponding coefficient $p_k$ to $z_{d,t_k} = z_{d,t_k} + p_k \times x_{i,j}$
  End for
  Calculate convolution of $h_t(t)$ with $z_d(t)$ using the FFT operation
End for
```

Figure 5.5 The algorithm to calculate the forward photoacoustic projection integral for wide kernels $h_t(t)$ using convolutions (implemented with FFTs).

Algorithm Backward (transposed) photoacoustic projection integral

```
1. For all detector element positions $\mathbf{r}_d$ in the measurement configuration
2.   Calculate convolution of $h_t(-t)$ with $z_d(t)$ using the FFT operation
3.   For all pixels $(i,j)$ in the source distribution image $A(\mathbf{r})$
4.     Calculate the time of flight $t = \|\mathbf{r}_{i,j} - \mathbf{r}_d\|$
5.     Calculate interpolation coefficients $\mathbf{p}$ at neighboring time points of $t$
6.     Increase the pixel value $x_{i,j}$ by summing contributions from each of the
       neighboring time points $t_k$ with corresponding coefficient $p_k$:
       $x_{i,j} = x_{i,j} + p_k \times z_{d,t_k}$
7.   End for
8. End for
```

Figure 5.6 The algorithm to calculate the backward photoacoustic projection integral for wide kernels $h_t(t)$ using convolutions (implemented with FFTs).

5.2.3 Basis function realizations

We will discuss two possibilities for the rotation invariant spatial basis function $h(\mathbf{r})$. Requirements for these basis functions are that they have to be of limited spatial support and that they should allow smooth distributions to be represented. We have chosen two different basis functions that have this property. The first one is based on the Gaussian kernel and the second one is based on the Butterworth kernel. The Fourier transforms of the selected kernels, $H(\omega) = \mathcal{F}\{h_t(t)\}$, are displayed in Table 5.2. Both functions are defined for a certain scale, the Gaussian scale is controlled with the σ_ω parameter and the Butterworth scale is controlled by its cut-off frequency ω_c. Furthermore the steepness of the Butterworth kernel can be specified by its order n. A suitable order for the Butterworth kernel was experimentally determined to be $n = 6$. The scales should be such that they occupy the grid-size of one pixel. The scales that we used are displayed in the last row of Table 5.2. The scale parameters are chosen so that the cut-off frequency of the kernel is very close, and just below,

Name	Fourier transform of kernel $H(\omega)$	Scale parameter
Gaussian	$\exp\left[-\frac{1}{2}\left(\frac{\omega}{\sigma_\omega}\right)^2\right]$	$\sigma_\omega = \dfrac{c}{0.6\Delta x}$
Butterworth	$\dfrac{1}{1+\left(\frac{\omega}{\omega_c}\right)^{2n}}$	$\omega_c = 2\pi\dfrac{0.45\Delta x}{c}$

Table 5.2 Fourier transforms of the kernels belonging to the spatial basis functions used in this study to rerpesent the source distribtuion $A(\mathbf{r})$. The scale parameter, related to the grid spacing Δx and speed of sound c is also shown.

the Nyquist frequency belonging to the spatial grid spacing. In volume rendering, we have seen[62] the Gaussian kernel being used in a splatting and convolution process with a similar scale as we use. The selection of a basis function is not very crucial for image reconstruction, the chosen Gaussian and Butterworth kernels are an example to show how this works in practice and can easily replaced by other kernels.

The radial profile $h_r(r)$ of the resulting spatial basis function can be calculated from $H(\omega)$ via a zeroth order Hankel transform, as shown in (5.20). For the two chosen kernels, these basis functions are displayed in Figure 5.7.

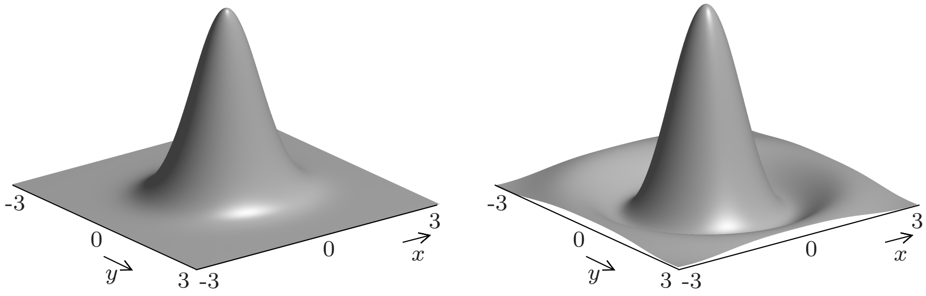

(a) Gaussian spatial basis function **(b)** Butterworth spatial basis function

Figure 5.7 Spatial basis functions shown on the size of the spatial grid spacing

5.2.4 Solving the image reconstruction problem

Having set the forward model that from a known source distribution $A(\mathbf{r})$, represented by a parameter vector $\mathbf{x}$ according to (5.12), it is now time to discuss strategies to solve the inverse problem. As we have seen, the forward model consists of several steps, which are all linear. From source distribution coefficients $\mathbf{x}$ to sampled ultrasound measurements $\mathbf{z}$ there are three linear operations that take place, as can be seen in Figure 5.8. The forward model can be compactly written in a linear equation with a

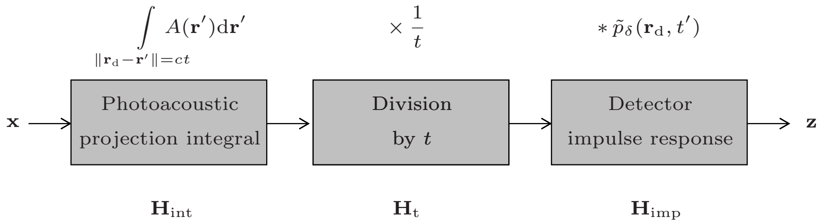

Figure 5.8 The three linear operations present in the forward model for photoacoustic signal generation

single linear operator $\mathbf{H}$ that represents the complete chain of linear operations:

$$\mathbf{H}\mathbf{x} = \mathbf{z} \tag{5.23}$$

The linear operator can thus be seen as the concatenation of three operators $\mathbf{H} = \mathbf{H}_{\mathrm{imp}}\mathbf{H}_{\mathrm{t}}\mathbf{H}_{\mathrm{int}}$. Finding the unknown source distribution coefficient $\mathbf{x}$ from a set of sampled ultrasound measurements $\mathbf{z}$ comes down to solving the system of linear equations. The least squares solution to this system is given by:

$$\hat{\mathbf{x}}_{\mathrm{LS}} = \left(\mathbf{H}^T\mathbf{H}\right)^{-1}\mathbf{H}^T\mathbf{z} \tag{5.24}$$

A stable solution to this least squares problem requires the term $\mathbf{H}^T\mathbf{H}$ to be well conditioned, since its inverse is required in the solution $\hat{\mathbf{x}}_{\mathrm{LS}}$. If the operator $\mathbf{H}$ is not well conditioned, regularization, i.e., prior assumptions on the solution $\mathbf{x}$, have to be included to make the problem solvable.

Filtered back projection

A popular technique to solve the reconstruction problem is called filtered back projection (FBP)[6]. It has its roots in x-ray CT imaging, in which a similar linear projection problem has to be solved[63, 64]. In parallel-ray CT imaging, a Radon transform, see Appendix E, describes the forward projection. To solve the CT inverse problem, an expression for the inverse Radon transform is required. This expression can be found analytically[63] and can be written as the concatenation of a filtering step $\mathbf{H}_{\mathrm{filt}}$ and a back projection step, $\mathbf{H}_{\mathrm{CT}}^T$, of the measured CT projections $\mathbf{z}_{\mathrm{CT}}$:

$$\mathbf{x}_{\hat{\mathrm{CT}}} = \mathbf{H}_{\mathrm{CT}}^T\mathbf{H}_{\mathrm{filt}}\mathbf{z}_{\mathrm{CT}} \tag{5.25}$$

The filtering operation represents a ramp filter in the time (projection) domain, $H(\omega) = |\omega|$. Applying a back projection without filtering with this ramp filter results in a blurred reconstruction. This blurring can be described by a convolution of the true image with a point spread function (PSF) of $\frac{1}{\sqrt{x^2+y^2}}$, as shown in Appendix E. Ramp filtering in the time domain is equivalent to deconvolving the blurred image with the PSF. This equivalence, however, is an analytical result without taking sampling and noise into account.

Kruger proposed a, similar to parallel beam x-ray CT, FBP algorithm for PA imaging[6, 20]. The idea is to first pre-process the measured ultrasound signals $\mathbf{z}$, so that we effectively step back two blocks in Figure 5.8, resulting in a pre-processed measurement $\mathbf{z}_{\mathrm{pre}}$. This pre-processing step typically consists of an integration step, when $\tilde{p}(\mathbf{r}_{\mathrm{d}}, t')$ is considered as a derivative operator, and a multiplication step. Or it consists of a deconvolution step and a multiplication step[61]. Effectively, according to (5.6) and (5.10), when $\tilde{p}(\mathbf{r}_{\mathrm{d}}, t')$ is considered to be a derivative operator, the transfer of the ultrasound transducer is implicitly assumed to be very flat and wide band and the laser pulse very short. The pre-processing step can be written as:

$$\mathbf{z}_{\mathrm{pre}} = \mathbf{H}_{\mathrm{t}}^{-1}\mathbf{H}_{\mathrm{deconv}}\mathbf{z} \tag{5.26}$$

Then what remains is the photoacoustic projection integral, $\mathbf{H}_{\text{int}}$, which has to be inverted. Here comes the analogy with x-ray parallel beam CT imaging into play. A filtering (with the ramp filter) and a back projection are used to obtain the final FBP reconstruction:

$$\hat{\mathbf{x}}_{\text{FBP}} = \mathbf{H}_{\text{int}}^T \mathbf{H}_{\text{filt}} \mathbf{z}_{\text{pre}} \tag{5.27}$$

This is a very fast, but approximate solution to the photoacoustic reconstruction problem. In the next section we will look at other ways to more accurately solve the reconstruction problem.

Iterative reconstruction methods

Besides doing a one-step FBP operation to reconstruct the source distribution, another approach for PA image reconstruction is to solve the linear system of equations. The linear operator, $\mathbf{H}$, involved in (5.23), is quite large. If for example an image size of 300 × 300 would be used, the number of rows in the operator would be 90,000. To solve such a large system of equations, iterative methods are needed. Methods that have been used in photoacoustic image reconstruction to solve the linear system are the Conjugate Gradient algorithm applied to the normal equations (CGNR)[65] and the LSQR[54] algorithm. Both these algorithms are Krylov subspace methods[66] and similar results, apart from numerical rounding errors, can be obtained.

In (5.25), we have assumed that we want to estimate the least squares solution to the linear system of equations in (5.23). This solution coincides with the maximum likelihood solution, when additive uncorrelated Gaussian noise on the measurements is assumed[67]. This is a good assumption for the noise which is seen on the measured ultrasound signals, because the main source of noise is electronic noise from the transducer, with no correlation between any two measurement samples[67].

Before we start, let us see what solution is actually calculated when using an iterative, Krylov subspace based method, such as CGNR or LSQR, to solve the linear system of equations. This solution depends on the number of iterations used and is given by:

$$\hat{\mathbf{x}}^{(j)} = \underset{x \in \mathcal{K}_j(\mathbf{H}^T\mathbf{H}, \mathbf{H}^T\mathbf{z})}{\arg\min} \|\mathbf{H}\mathbf{x} - \mathbf{z}\|^2 \tag{5.28}$$

where the Krylov space at the j^{th} iteration is given by:

$$\mathcal{K}_j(\mathbf{H}^T\mathbf{H}, \mathbf{H}^T\mathbf{z}) = \text{span}\big\{\mathbf{H}^T\mathbf{z},\, \big(\mathbf{H}^T\mathbf{H}\big)\mathbf{H}^T\mathbf{z},\, \ldots\,,\, \big(\mathbf{H}^T\mathbf{H}\big)^{j-1}\mathbf{H}^T\mathbf{z}\big\} \tag{5.29}$$

Thus a constrained solution to the least squares problems is found in every iteration of a Krylov subspace method, where the constraint is such that the solution in the j^{th} iteration is be contained in the associated j^{th} Krylov subspace. This implicitly provides a form of regularization to the solution by terminating the iterative method at a low number of iterations. The solutions tend to start off with low frequency content and the reconstructions get more and more high frequency contents as the iteration number increases. For example, the solution that is obtained after the first iterarion is the one that is obtained by simple back projection, i.e., $\hat{\mathbf{x}}^{(1)} \propto \mathbf{H}^T\mathbf{z}$, which is a very blurred reconstruction.

Implementation of the linear operators

Solving the linear system (5.23) using a Krylov based subspace method requires the evaluation of the linear operator $\mathbf{H}$ in forward and backward (transposed) mode, i.e., calculating $\mathbf{Hx}$ for any given $\mathbf{x}$ and calculating $\mathbf{H}^T\mathbf{z}$ for any given $\mathbf{z}$. As we have seen before, this operator is the concatenation of three linear operators. We will discuss efficient forward and backward evaluation of each of the three operators here.

The first operator, $\mathbf{H}_{\text{int}}$, has been discussed in section 5.2.2. An efficient algorithm to calculate the forward transform is displayed in Figure 5.5 and a similar algorithm to calculate the backward transform in Figure 5.6. The other two operators are square (same input and output dimensions) and operate on the time domain. The vector $\mathbf{z}$ represents the time domain signals in a single vector by vertically stacking the individual time domain measurements from the individual transducers.

The second operator $\mathbf{H}_{\text{t}}$ is a simple operator that results in an output vector which is obtained by element-wise division of the input vector with the time axis value that belongs to each of the elements of the input vector. This operator is diagonal, thus forward and backward mode are the same here.

The third operator $\mathbf{H}_{\text{imp}}$ applies the impulse response $\tilde{p}_\delta(\mathbf{r}_{\text{d}}, t')$ to each of the time domain measurements from the individual transducers present in the input vector. This is efficiently obtained by calculating the FFT of a sampled representation of $\tilde{p}_\delta(\mathbf{r}_{\text{d}}, t')$ and multiplying this with the FFT of each of the subvectors in the input vector. Then for each of the subvectors the IFFT is calculated. The backward operator $\mathbf{H}_{\text{imp}}^T$ is slightly different in the sense that the complex conjugate of the FFT of $\tilde{p}_\delta(\mathbf{r}_{\text{d}}, t')$ needs to be taken.

Preconditioning

Sometimes, due to the conditioning of the linear operator $\mathbf{H}$, solving the linear system with an iterative method may need a high number of iterations before convergence is obtained. A preconditioner matrix is often used to make the linear system better conditioned and subsequently improve the convergence rate of the iterative method. In our reconstruction problem, preconditioning can be applied to the normal equations associated with it. The normal equations are obtained by equating the gradient of the least squares formulation to zero, resulting in:

$$\mathbf{H}^T\mathbf{H}\mathbf{x} = \mathbf{H}^T\mathbf{z} \tag{5.30}$$

By preconditioning the system with a preconditioning matrix $\mathbf{M}$, the original linear system can be transformed to a system with the same solution, but which is likely to be easier to solve with an iterative solver [66]. The preconditioning matrix has to be chosen such that it is an approximation to $\mathbf{H}^T\mathbf{H}$, it should be nonsingular and the inverse should be readily available. This preconditioning matrix can be applied in several ways to transform the original system, such as left, right and split preconditioning. We have chosen for a split preconditioner, because it can be easily applied to the LSQR algorithm that we use to solve the linear system. In a split preconditioner, the preconditioner in split into $\mathbf{M}_1$ and $\mathbf{M}_2$ such that $\mathbf{M}^{-1} = \mathbf{M}_1^{-1}\mathbf{M}_2^{-1}$ and in our case, to apply it to the LSQR algorithm, we have that $\mathbf{M}_1 = \mathbf{M}_2$. The split preconditioned linear system is then given by:

$$\mathbf{H}\mathbf{M}_1^{-1}\mathbf{y} = \mathbf{z} \tag{5.31}$$

which will be solved for $\mathbf{y}$ and the solution is obtained from $\mathbf{x} = \mathbf{M}_1^{-1}\mathbf{y}$.

The question now is, what is a good preconditioner for the photoacoustic image reconstruction problem. This part heavily depends on the fact that for a photoacoustic projection, convolution operations in the time domain and spatial domain are related, as can be seen from (5.19) and (5.20). Our preconditioner $\mathbf{M}$ should be an approximation of:

$$\mathbf{H}^T\mathbf{H} = \mathbf{H}_{\mathrm{int}}^T\mathbf{H}_{\mathrm{t}}^T\mathbf{H}_{\mathrm{imp}}^T\mathbf{H}_{\mathrm{imp}}\mathbf{H}_{\mathrm{t}}\mathbf{H}_{\mathrm{int}} \tag{5.32}$$

The matrix $\mathbf{H}_{\mathrm{t}}$ is a diagonal matrix, which is very well conditioned, its condition number can be seen as the ratio between the time of flight of the last measurement sample of interest $t_{\max}$ and the first measurement sample of interest $t_{\min}$. Therefore we ignore this matrix in our approximation of $\mathbf{H}^T\mathbf{H}$. We are then left with the product $\mathbf{H}_{\mathrm{imp}}^T\mathbf{H}_{\mathrm{imp}}$, which actually represents the convolution $\tilde{p}_\delta(\mathbf{r}_{\mathrm{d}}, -t) *_t \tilde{p}_\delta(\mathbf{r}_{\mathrm{d}}, t)$. This convolution in the time domain, can be moved over to the spatial domain where the equivalent effect can be applied by convolution with a 2-d radially symmetric kernel. The transformation from time to spatial domain is given by the inverse Abel transform and has been shown in the previous section in (5.20). As mentioned before, this relation is an approximation which is valid for kernels which have small spatial support. This approximation is good enough for our preconditioner which is only supposed to approximate the behavior of $\mathbf{H}^T\mathbf{H}$ in some sense. Moving the convolution from time to spatial domain leaves us with the following form of the matrix:

$$\mathbf{H}_{\mathrm{int}}^T\mathbf{H}_{\mathrm{imp}}^T\mathbf{H}_{\mathrm{imp}}\mathbf{H}_{\mathrm{int}} \approx \mathbf{H}_{\mathrm{int}}^T\mathbf{H}_{\mathrm{int}}\mathbf{H}_{\mathrm{imp}^2,\mathrm{sp}} \tag{5.33}$$

where $\mathbf{H}_{\mathrm{imp}^2,\mathrm{sp}}$ represents the 2-d spatial convolution operation with a PSF of the radially symmetric kernel obtained from the inverse Abel transform of $\tilde{p}_\delta(\mathbf{r}_{\mathrm{d}}, -t) *_t \tilde{p}_\delta(\mathbf{r}_{\mathrm{d}}, t)$. What we are left now with is the $\mathbf{H}_{\mathrm{int}}^T\mathbf{H}_{\mathrm{int}}$ term, representing the chain of applying the forward then the backward photoacoustic projection integral. The photoacoustic projection integral can approximately be seen as a Radon transform. This mean we can approximate the operation by a forward and backward radon transform. In Appendix E we show that this comes down to a 2-d spatial convolution with a PSF of $\frac{2}{r}$. A similar approach was performed in x-ray CT image reconstruction[68] where a spatial PSF was numerically calculated and its inverse used as a preconditioner. Representing this spatial convolution with the operator $\mathbf{H}_{\mathrm{r}}$, would then give us the following preconditioner:

$$\mathbf{M} = \mathbf{H}_{\mathrm{r}}\mathbf{H}_{\mathrm{imp}^2,\mathrm{sp}} \tag{5.34}$$

which is the spatial convolution of two, radially symmetric, PSFs. Now in order for $\mathbf{M}$ to be a good preconditioner, the last requirement is that it is nonsingular. The preconditioner can easily be changed to be nonsingular by enforcing it with a certain condition number κ, which can be accomplished by limiting the lowest eigenvalues to have a value of at least $\kappa\sigma_{\max}$. Because the preconditioner represents the spatial convolution of a radially symmetric PSF and because it will be well conditioned, the preconditioner is symmetric positive definite. In the end we work with the split preconditioner $\mathbf{M}_1^{-1}$ which can be derived from $\mathbf{M}$ by square rooting and inverting its eigenvalues, i.e., $\mathbf{M} = \mathbf{M}_1\mathbf{M}_1$.

The practical implementation of the proposed split preconditioner $\mathbf{M}_1^{-1}$ is very simple, and the actual matrix never needs to be formed explicitly. In matrix form, it would have been a block-circulant matrix consisting of blocks which are circulant matrices[69] also called BCCB matrices[70]. We can efficiently apply the operator $\mathbf{M}_1^{-1}$ using a 2-d FFT and 2-d IFFT operation. The input image has to be transformed to the FFT domain, then a multiplication with a kernel representing $\mathbf{M}_1^{-1}$ is applied and the result is transformed back to the image domain via an IFFT operation. Now we come to the representation of $\mathbf{M}_1^{-1}$ in the 2-d FFT domain. A radially symmetric PSF is a real and even function, which has a real and even Fourier transform[71]. It turns out that the (real) coefficients of the 2-d Fourier transform represent the eigenvalues of the underlying BCCB matrix[70]. The radial FFT profile belonging to the forward/backward radon transform, $\mathbf{H}_\mathrm{r}$, can be obained by an inverse Hankel transform according to (5.20), of the radial profile of the 2-d spatial kernel $\frac{2}{r}$ which is given by $\frac{2}{k}$[72]. The radial FFT profile of the forward/backward impulse response, $\mathbf{H}_{\mathrm{imp}^2,\mathrm{sp}}$, can be obtained by a Fourier transform of the time domain kernel according to (5.20). Our time domain kernel is obtained by forward and backward applying the impulse response $\tilde{p}_\delta(\mathbf{r}_\mathrm{d}, t)$, which results in a real valued Fourier transform of $\left|\mathcal{F}\{\tilde{p}_\delta(\mathbf{r}_\mathrm{d}, t)\}\right|^2$. The unconditioned eigenvalues, and FFT coefficients, of $\mathbf{M}$ would then be given by:

$$\sigma_\mathrm{uc}(\omega) = \frac{2\left|\mathcal{F}\{\tilde{p}_\delta(\mathbf{r}_\mathrm{d}, t)\}\right|^2}{|\omega|} \tag{5.35}$$

To make $\mathbf{M}$ well conditioned with condition number κ, we have to add a small value of $\beta = \frac{1}{\kappa}\max\big(\sigma_\mathrm{uc}(\omega)\big)$ to all eigenvalues $\sigma_\mathrm{uc}(\omega)$. Now inverting and square rooting the eigenvalues, we find the radial FFT profile of the well conditioned inverse of our split preconditioner $\mathbf{M}_1^{-1}$:

$$\sigma(\omega) = \frac{\sqrt{|\omega|}}{\sqrt{2\left|\mathcal{F}\{\tilde{p}_\delta(\mathbf{r}_\mathrm{d}, t)\}\right|^2 + \beta|\omega|}} \tag{5.36}$$

This guarantees that the condition number of $\mathbf{M}_1^{-1}$ is at most $\sqrt{\kappa}$, but can be lower when the unmodified preconditioner already had a better condition number. Note that this is a continuous specification of the Fourier coefficients, the spatial sampling frequency and image size have to be taken into account to properly calculate the eigen values/FFT coefficients.

Data space preconditioning The above described preconditioning works on the object space, in the spatial domain, and as such it does not change the least squares solution that is being calculated in (5.24). Preconditioning can also be performed on the data space, or time domain, which, however, does change the value and meaning of the obtained solution[67]. We will come back to this later. If we take the preconditioner $\mathbf{M}_1^{-1}$ with the earlier discussed eigenvalues and Fourier coefficients (5.36), it is easy to convert this preconditioner to the time domain. Let us call the time domain preconditioner $\tilde{\mathbf{M}}_1^{-1}$. The Fourier coefficients which used to reside on radial profiles through the 2-d FFT description of $\mathbf{M}_1^{-1}$ can then be seen as 1-d FFT coefficients which have to be applied to the time domain signals. Also here the time domain sampling frequency and sample length have to be taken propertly into account. So instead of the preconditioner being a 2-d spatial PSF, as was the case for $\mathbf{M}_1^{-1}$, the data space preconditioner is a 1-d convolution kernel that operates on the time domain signals. If we refer to the time domain, or data space, preconditioner as $\tilde{\mathbf{M}}_1^{-1}$ then the data space preconditioned system of equations is given by:

$$\tilde{\mathbf{M}}_1^{-1}\mathbf{H}\mathbf{x} = \tilde{\mathbf{M}}_1^{-1}\mathbf{z} \tag{5.37}$$

The preconditioner, if explicitly formed as a matrix, would be the horizontal concatenation of a number of circulant matrices. The condition number of the data space preconditioner $\tilde{\mathbf{M}}_1^{-1}$ can be higher than the object space preconditioner $\mathbf{M}_1^{-1}$, because in general the sampling frequency in the spatial domain is lower than in the time domain. The condition number is however still bounded by $\sqrt{\kappa}$ as shown in (5.36).

Solving the data space preconditioned system is equivalent to minimizing:

$$\begin{aligned} \hat{\mathbf{x}} &= \arg\min_{\mathbf{x}} \|\tilde{\mathbf{M}}_1^{-1}\mathbf{H}\mathbf{x} - \tilde{\mathbf{M}}_1^{-1}\mathbf{z}\|^2 && (5.38) \\ &= \arg\min_{\mathbf{x}} \left(\mathbf{H}\mathbf{x} - \mathbf{z}\right)^T \tilde{\mathbf{M}}^{-1} \left(\mathbf{H}\mathbf{x} - \mathbf{z}\right) && (5.39) \end{aligned}$$

where $\tilde{\mathbf{M}}^{-1} = \tilde{\mathbf{M}}_1^{-1}\tilde{\mathbf{M}}_1^{-1}$. This is equivalent to assuming a covariance matrix of $\tilde{\mathbf{M}}$ on the data $\mathbf{z}$, and calculating the maximum likelihood solution for this assumed noise distribution. In reality however, the noise on $\mathbf{z}$ is considered to be white with a diagonal covariance matrix, thus a different solution is expected to be calculated when using the data space preconditioner then with the object space preconditioner or when no preconditioner is present.

Regularization

As seen in (5.24), calculating the least squares solution to the linear system involves the inversion given by $\left(\mathbf{H}^T\mathbf{H}\right)^{-1}$. When the projection $\mathbf{H}$ is ill-conditioned the inversion can be undefined, because a part of the singular values can be zero or close to zero. To solve this problem regularization is needed to stabilize this inversion, which means prior information about the solution $\mathbf{x}$ has to be added to the problem[73]. We will show three different regularization methods than can be applied to the reconstruction problem.

Tikhonov A well-known regularization scheme is Tikhonov regularization, where the following solution is calculated:

$$\hat{\mathbf{x}}_{\text{Tik}} = \arg\min_{\mathbf{x}} \|\mathbf{Hx}\|^2 + \lambda\|\mathbf{Lx}\|^2 \tag{5.40}$$

here **L** is an operator typically representing a high-pass filter which penalizes the high frequencies in the solution more than the low frequencies. The parameter λ controls the smoothness of the solution. The Tikhonov regularized solution can be seen in a statistical framework as the maximal a posteriori (MAP) estimate where $\mathbf{L}^T\mathbf{L}$ is the inverse of the covariance matrix of the prior information on the solution and λ balances the variances of the measurement noise and the prior information. An optimal choice for the λ parameter can be found by looking at the L-curve associated with the regularization. The L-curve is obtained[56] by plotting the regularized norm $\|\mathbf{Lx}\|$ against the residual norm $\|\mathbf{Hx}\|$ on a double logarithmic scale. The L-curve is shaped like the letter L and the optimal value for λ is found in the corner of the L-curve.

Total variation When using Tikhonov regularization, an L^2 norm, i.e., a quadratic criterion, is used to penalize the high frequencies in the solution. In image reconstruction it makes more sense to use a regularizer based on an L^1 norm[74] which instead of having only a smoothing effect has also an edge preserving effect. This kind of regularization is sometimes called Total Variation (TV) when the magnitude of the gradient is the quantity being regularized. The total variation regularized solution is then calculated from

$$\hat{\mathbf{x}}_{\text{TV}} = \arg\min_{\mathbf{x}} \|\mathbf{Hx}\|^2 + \lambda\text{TV}(\mathbf{x}) \tag{5.41}$$

where $\text{TV}(\mathbf{x}) = \sum_i \sqrt{(\partial_x x_i)^2 + (\partial_y x_i)^2 + \beta^2}$. Adding the constant $\beta > 0$ offers computational advantages, such as differentiability when the gradient approaches zero[55]. Effectively the β constant allows a smooth transition from a quadratic, L^2 cost function, for small gradients to a linear, L^1 cost function for large gradients. The transition point is found around $\sqrt{(\partial_x x_i)^2 + (\partial_y x_i)^2} = \beta$.

Krylov-subspace iteration number Another kind of regularization can be obtained by constraining the solution to lie in a lower dimensional subspace[56] $\mathcal{S}$:

$$\hat{\mathbf{x}}_{\text{Constr}} = \arg\min_{\mathbf{x}\in\mathcal{S}} \|\mathbf{Hx}\|^2 \tag{5.42}$$

this is effectively what happens when a Krylov-subspace method is used such as CGNR and LSQR. The solution space is then governed by the iteration number j and the associated Krylov subspace, i.e., $\mathcal{S} = \mathcal{K}_j\left(\mathbf{H}^T\mathbf{H},\, \mathbf{H}^T\mathbf{z}\right)$. When preconditioning with a preconditioner **M** is used, the associated Krylov space in which the solution is contrained to lie will also change according to $\mathcal{S} = \mathcal{K}_j\left(\mathbf{M}^{-1}\mathbf{H}^T\mathbf{H},\, \mathbf{M}^{-1}\mathbf{H}^T\mathbf{z}\right)$, which means that the regularizing properties of an iterative algorithm are also related to the chosen preconditioner. And finally, preconditioning in the data space results in yet another Krylov space, which is given by $\mathcal{S} = \mathcal{K}_j\left(\mathbf{H}^T\tilde{\mathbf{M}}^{-1}\mathbf{H},\, \mathbf{H}^T\tilde{\mathbf{M}}^{-1}\mathbf{z}\right)$.

5.2.5 Results

In this section we discuss the algorithms presented above.

The photoacoustic impulse response

Before we can use our methods, we need to have a description of the photoacoustic impulse response $\tilde{p}(\mathbf{r}_\mathrm{d}, t)$. In the calibration measurement, a measurement is taken of a calibration phantom consisting of several thin hairs (75 μm). The signal generated by such a hair can be seen as the signal coming from a photoacoustic point source. By aligning and averaging over all sensors for each individual hair, we can obtain photoacoustic point source signals from each of the hairs. A typical signal that is obtained from a hair in the calibration phantom is displayed in Figure 5.9a and the corresponding spectrum is displayed in Figure 5.9b. Because measurement conditions can change over time, for every PER-PAT measurement that is performed this photoacoustic impulse response is extracted again from the calibration measurement.

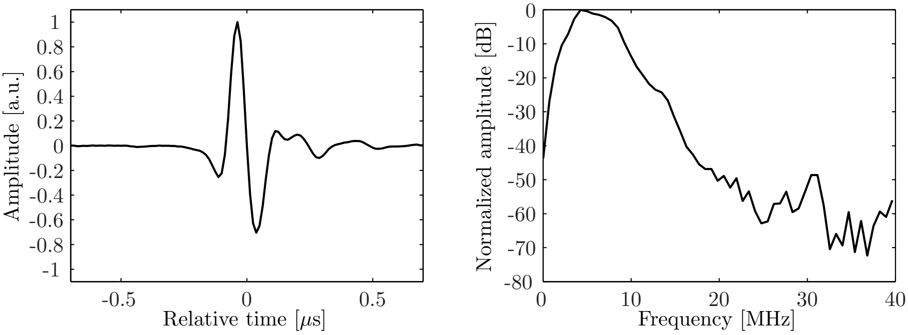

(a) Time domain **(b)** Frequency domain

Figure 5.9 Illustration of a measured photoacoustic impulse response $\tilde{p}(\mathbf{r}_\mathrm{d}, t)$. This response was obtained by illuminating a small hair such as is being done in the calibration measurement. The displayed signal is an average over all sensor elements.

Preconditioner eigenvalues/Fourier coefficients

The preconditioners that are being used, $\tilde{\mathbf{M}}_1^{-1}$ for data space preconditioning, and $\mathbf{M}_1^{-1}$ for object space preconditioning, are dependent on the photoacoustic impulse response. Both preconditioners consist of circulant matrices with eigenvalues dependent on the sampling frequency and domain size, the actual eigenvalue/Fourier coefficient distribution per frequency, valid for the photoacoustic impulse response shown in Figure 5.9, is displayed in Figure 5.10a. Especially the low frequency eigenvalues are important for the preconditioners. Therefore we show the low frequency filtered, cut-off frequency at around 7 MHz, convolution kernels belonging to $\tilde{\mathbf{M}}_1^{-1}$

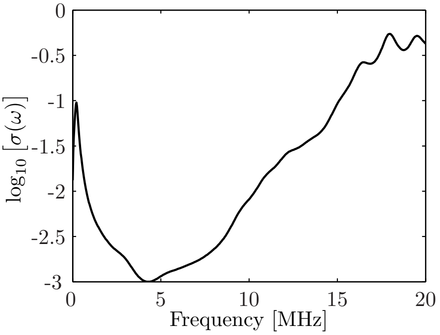

(a) Eigenvalues/Fourier coefficients $\sigma(\omega)$

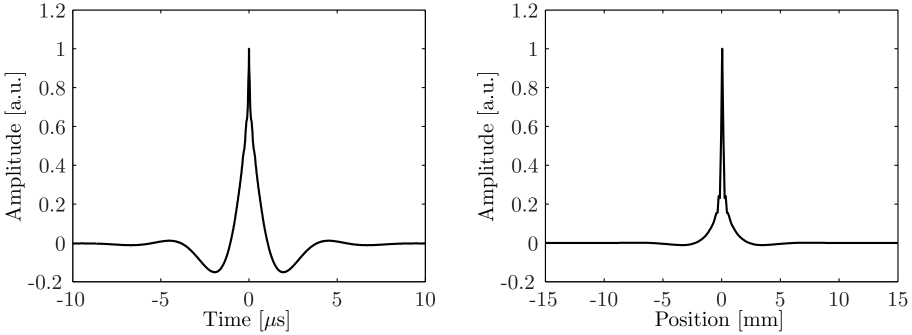

(b) Time domain convolution kernel

(c) Spatial domain convolution kernel (radial profile)

Figure 5.10 The top figure displays the eigenvalues/Fourier coefficients of the preconditioners $\tilde{\mathbf{M}}_1^{-1}$ (time domain/data space) and $\mathbf{M}_1^{-1}$ (spatial domain/object space). The low frequency content is the crucial part of the preconditioner, therefore the low pass content of the resulting convolution kernels are shown in (b) time domain and (c) spatial domain. The domain scaling is relevant for a speed of sound of 1500 m/s, i.e., 1.5 mm/μs.

and $\mathbf{M}_1^{-1}$ in Figures 5.10b and 5.10c. We see that the convolution kernels have a large support. The support of the spatial kernel of around 10 mm is clearly far more then what is considered to be small relative to the distances from object to the detector elements. This means the approximation of the object space preconditioner $\mathbf{M}$ to $\mathbf{H}^T\mathbf{H}$ will not be very accurate. This issue is not relevant for the data space preconditioner, which, however, has another issue, being the fact that it not minimizes the least squares residual but a differently weigted residual as was discussed before. In the upcoming section we will investigate what effects this all has on the performance of both preconditioners.

Numerical evaluation

First a numerical experiment was conducted to investigate the reconstruction performance of the algorithms with respect to a ground truth image. The numerical phantom that was being used is displayed in Figure 5.11. It consists of several lines, circles and a square. The dimensions and intensites of the labeled objects are displayed in Table 5.3. The small circles c_2/c_7 are chosen with increasing size so that resolution effects can be studied. The square s_1 and circle c_1 have a larger size to see how well larger objects can be reconstructed. The cross x_1 was added to study the reconstruction of line like structures.

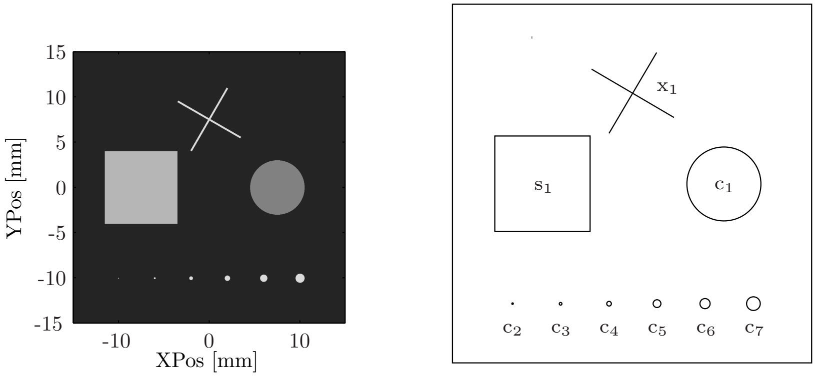

(a) Image representation **(b)** Object labels

Figure 5.11 Numerical phantom used in this evaluation.

Name	Size [mm]	Intensity [a.u.]
x_1	4.0 × 0.2	1.0
s_1	8.0	0.8
c_1	6.0	0.5
c_2	0.1	1.0
c_3	0.2	1.0
c_4	0.4	1.0
c_5	0.6	1.0
c_6	0.8	1.0
c_7	1.0	1.0

Table 5.3 Overview of the objects in the numerical phantom. The dimensions of the cross preserent the length of the line times its thickness. The dimensions of the circles represent their diameters.

A photoacoustic measurement was performed by numerical evaluation of the forward model, including the photoacoustic impulse response, at a high resolution. The grid spacing in the generation of these measurements was set to 10 μm. The sampling frequency in the time domain was set to 80 MHz, which is the frequency that is being used in our PER-PAT setup. Gaussian white noise, with a standard deviation of 5% of the maximum signal intensity was added to the measurements. The measurements were taken by positioning virtual detector elements, conform the 32 element circular array, rotated over five steps to cover a complete projection of 360 degrees, thus resulting in a set of 160 measurements roughly sampled over a circular trajectory surrounding the object. The radius of this circular trajectory was set to 45 mm.

Filtered back projection We start by having a look at a widely used method in photoacoustic image reconstruction, namely filtered back projection (FBP). This is a very fast method and only requires a filtering and a back projection step. We will test the FBP algorithm with and without taking the impulse response of the transducer into account. When the transducer response is taken into account, deconvolution is applied as pre-processing step and when not, integration of the raw pressure measurements is instead performed. When the deconvolution was applied, a proper deconvolution was carried out by regularizing the inversion. The results of the FBP algorithm on the numerical measurements, with and without impulse response taken into account are displayed in Figure 5.12. The obvious difference is that when not taking the transducer impulse response into account only the very small objects and the edges of the large objects can be reconstructed.

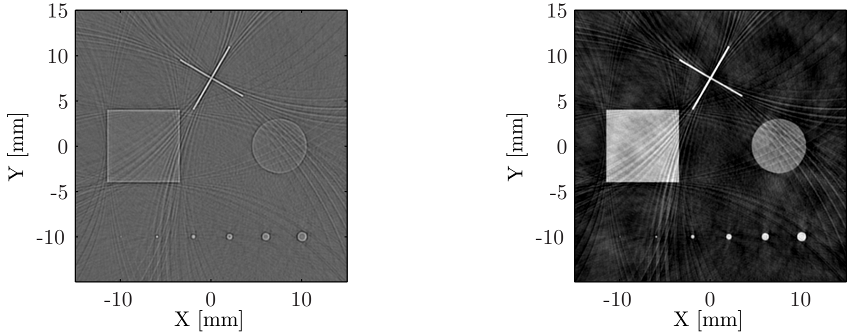

(a) No impulse response, integration in pre-processing

(b) With impulse response, deconvolution in pre-processing

Figure 5.12 Filtered back projection reconstruction results on the numerical optical absorption phantom.

Iterative algorithms The FBP algorithm was only an approximate solution to the reconstruction problem. With iterative algorithms we expect to get better image quality because the actual least squares solutions to the linear system of equations will be calculated instead of an approximation. This, however, comes at the cost of a computationally more demanding reconstruction algorithm.

We will start this section with the reconstruction performance of the linear system without explicit, i.e., Tikhonov or Total Varation, regularization. Three approaches were investigated here, the first one is without preconditioning, the second one is with object space preconditioning and the last one is with data space preconditioning. For every method, 400 iterations were calculated with the LSQR algorithm. The normalized RMS residuals, $\frac{1}{\sqrt{N_z}\sigma_z}\|\mathbf{H}\hat{\mathbf{x}}-\mathbf{z}\|$ and normalized RMSE of the solution, $\frac{\|\hat{\mathbf{x}}-\mathbf{x}_{\mathrm{GT}}\|}{\|\mathbf{x}_{\mathrm{GT}}\|}$, will be calculated at each iteration to evaluate the performance. A normalized RMS residual of one means that the residual has the same size as the standard deviation of the noise that was added to the measurements. A normalized RMSE of the solution having a value of one is what would be obtained when an all zero solution is assumed and a value of zero means the found solution is equal to the ground truth. The results of this test are displayed in Figure 5.13. It can be seen that the residual quickly approaches a limiting value for all methods. This residual is even below the expected value of one, which would correspond to a perfect fit with only noise left on the residual signal. The normalized RMSE of the solution shows a similar trend for all three methods, first it decreases after which is increases and rapidly expands. This clearly indicates that the linear system that is being solved is ill-conditioned. Also the regularizing property, which is obtained when terminating the iterative algorithm at a low number of iterations, is obvious from these curves. The optimal number of iterations would then correspond to the minimum of this curve. For the non-preconditioned system, it takes a long time, about 160 iterations, before this minimum is reached and the actual RMSE of this minimum is not very low when comparing it to the other two methods. The object space preconditioned system converges a lot faster, in about 33 iterations, then the non-preconditioned system and it has a substantially lower RMSE. Finally, the data space preconditioned system converges extremely fast in as little as five iterations, with a RMSE error similar to the

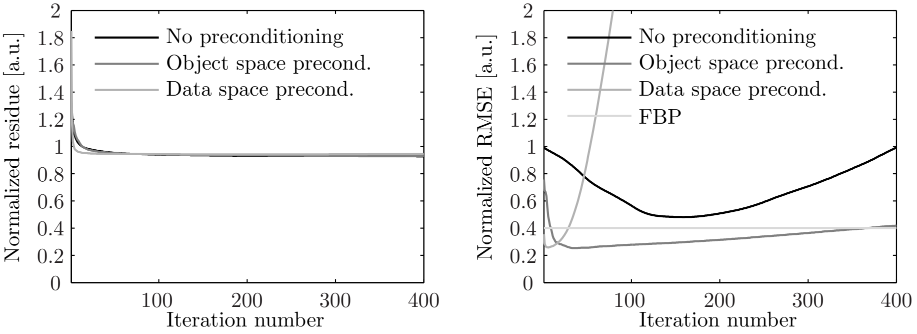

(a) Residual convergence **(b)** Image reconstruction convergence

Figure 5.13 Convergence plots of the not regularized system of equations..

object space preconditioned system. It also interesting to see that, although solving the data space preconditioned system does not aim at minimizing the sum of squared residuals, but a differently weighted residual, it still results in the same residual norm as the other two methods. The RMSE of the FBP method is also shown in the figure for comparison. Both iterative methods perform much better in terms of RMSE.

Besides the RMSE values it is interesting to look at the actual reconstructions of the methods at the optimal number of iterations. These reconstructions are displayed in Figure 5.14. Both preconditioned reconstructions look very similar and the differences are visually very difficult to see. The artifacts that are present in the FBP reconstruction are heavily reduced in the preconditioned reconstructions. The non-

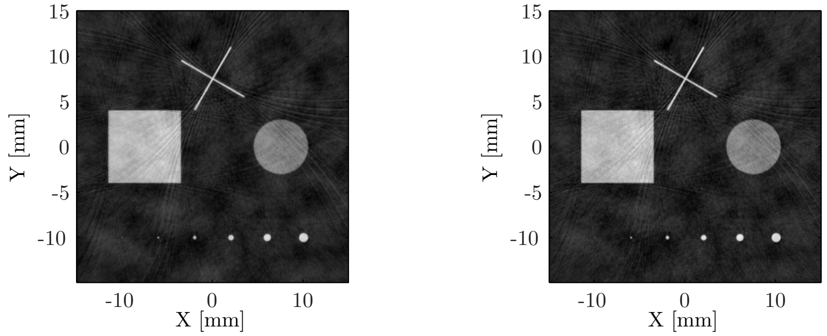

(a) Data space preconditioning **(b)** Object space preconditioning

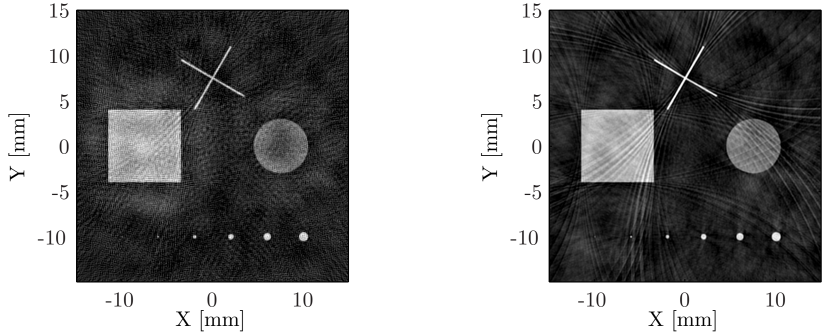

(c) No preconditioning **(d)** Filtered back projection

Figure 5.14 Reconstructed images of the iterative methods when no explicit regularization is used. The iterations were terminated according to minimum in the curves in Figure 5.13b. This means five iterations were used for the data space preconditioned system (a), 33 iterations were used for the object space preconditioned system (b), 160 iterations were used for the non-preconditioned system (c). The FBP reconstruction (d) is shown as a reference.

preconditioned reconstruction shows a lot of high frequency noise which is caused by the fact that the linear system is ill-conditioned. On the other hand, the self regularizing property of the iterative method, by limiting the number of iterations, seems to work very well on both preconditioned reconstructions.

To improve the conditioning of the linear system, explicit regularization can be used. We start off by using Tikhonov regularization, with an operator $\mathbf{L}$ that numerically calculates a first order x and y derivative on a 2×2 stencil with forward differences. A suitable value for the regularization parameter λ was found by trying a range of values and choosing the value that gives the best balance between smoothness and residual norm. It turned out that this value can quickly be found by trying just a few values and that the outcome is not extremely sensitive to this value. The convergence plots for the Tikhonov regularized system of equations are displayed in Figure 5.15. In the data space preconditioned system we have thus effectively solved the following regularized cost function:

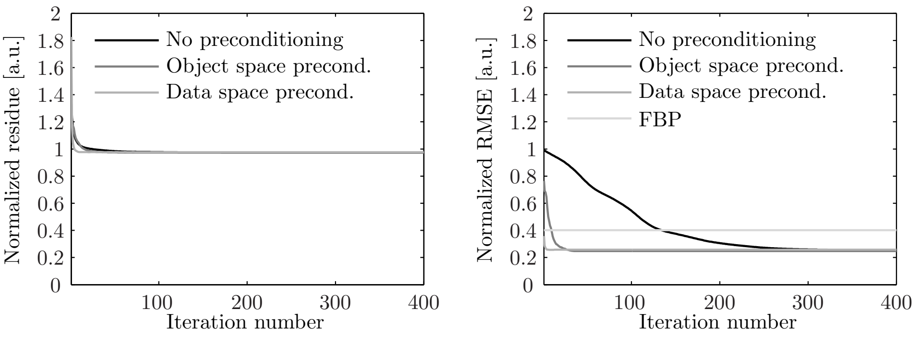

(a) Residual convergence **(b)** Image reconstruction convergence

Figure 5.15 Convergence plots of the Tikhonov regularized system of equations.

$$\hat{\mathbf{x}} = \arg\min_{\mathbf{x}} \|\tilde{\mathbf{M}}_1\big(\mathbf{H}\mathbf{x} - \mathbf{z}\big)\|^2 + \lambda\|\mathbf{L}\mathbf{x}\|^2 \tag{5.43}$$

and in the object space and non-preconditioned system:

$$\hat{\mathbf{x}} = \arg\min_{\mathbf{x}} \|\mathbf{H}\mathbf{x} - \mathbf{z}\|^2 + \lambda\|\mathbf{L}\mathbf{x}\|^2 \tag{5.44}$$

With these regularized systems, convergence is obtained with data space preconditioning after 10 iterations, with object space preconditioning after 40 iterations and without preconditioning it takes more than 400 iterations to fully converge. The normalized RMS residual is closer to one now which means the measurements are not over-fitted as was the case without regularization where a normalized RMS residual slightly lower then one was obtained. The reconstructed images that were obtained with Tikhonov regularization are very similar to the earlier obtained images without regularization, by using only a limited number of iterations as displayed in Figures 5.14a and 5.14b.

Finally, the reconstruction with TV (L^1 norm) regularization was investigated. Because this regularization yields a nonlinear system of equations, several iterations of different linearized system of equations are necessary to solve the problem. We used an approach where first the L^2 norm regularized solution is calculated and around that solution the $\mathrm{TV}(\mathbf{x})$ term is linearized for every pixel. This linearization around the newly obtained solution can be repeated until convergence is obtained. We found out that only one extra iteration was necessary to obtain good results with L^1 regularization, which means that compared to the L^2 norm regularization the amount of time needed for reconstruction is only twice as much. The reconstructions obtained with L^1 norm regularization, however, are visually much better than the ones obtained with L^2 regularization. In the data space preconditioned system, the following cost function is minimized:

$$\hat{\mathbf{x}} = \arg\min_{\mathbf{x}} \|\tilde{\mathbf{M}}_1\big(\mathbf{Hx} - \mathbf{z}\big)\|^2 + \lambda \mathrm{TV}\big(\mathbf{x}\big) \tag{5.45}$$

and in the object space and non-preconditioned system:

$$\hat{\mathbf{x}} = \arg\min_{\mathbf{x}} \|\mathbf{Hx} - \mathbf{z}\|^2 + \lambda \mathrm{TV}\big(\mathbf{x}\big) \tag{5.46}$$

The results of both approaches are displayed in Figure 5.16. Here we clearly see differences between the two approaches. Preconditioning in the data space, in which a modified system of equations is solved, results in low frequency noise corrupting the image, Figure 5.16a. This low frequency noise is not present in the reconstruction

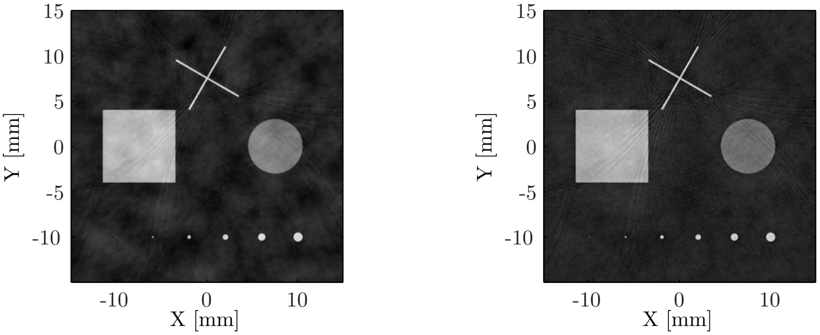

(a) Data space preconditioning **(b)** Object space preconditioning

Figure 5.16 Reconstructed images of the iterative methods when TV regularization is used. The iterations were terminated according to minimum in the curves in Figure 5.15b. This means 10 iterations were used for the data space preconditioned system (a) and 50 iterations were used for the object space preconditioned system.

using the unmodified system of equations, Figure 5.16b. Thus when TV regularization is used, improved image quality can be obtained when using the original system of equations.

A summary of the reconstruction qualities of all reconstruction methods is displayed in Table 5.4. In this table the normalized RMSE is the quality indicator. A good tradeoff between algorithm speed (number of required iterations) and reconstruction quality can be obtained with data space preconditioning using a limited number of iterations and no regularization. The best reconstruction quality can be obtained with object space preconditioning and TV regularization, it requires a 20-fold more amount of iterations and contains very much reduced noise and artifacts. This is however much less work then when solving the non-preconditioned system, which would require again an 8-fold more amount of iterations to attain the same result.

Method	# Iterations	NRMSE
FBP	1	0.4222
Data space / No regularization	5	0.2585
Object space / No regularization	33	0.2541
Data space / Tikhonov	10	0.2601
Object space / Tikhonov	50	0.2497
Data space / TV	2 × 10	0.2291
Object space / TV	2 × 50	0.2019

Table 5.4 Summary of the reconstruction results on the numerical phantom. The NRMSE is defined as $\frac{\|\hat{\mathbf{x}}-\mathbf{x}_{\mathrm{GT}}\|}{\|\mathbf{x}_{\mathrm{GT}}\|}$.

To illustrate the computational time that is needed: a reconstruction using the FBP method takes about 0.5 seconds, using the Data space / No regularization method takes about 4 seconds and using the Object space / TV method takes about 80 seconds. These times were obtained at an Intel Core2 Quad Q8200 running Matlab with multithreaded mex functions to calculate the photoacoustic projection integral. The number of pixels involved in a reconstruction is 300 × 300 and the number of measurement signals is 160.

Experimental evaluation

After these numerical simulations, we have performed an experiment with an optically absorbing square like structure in our PER-PAT experimental setup. The reconstruction we show here is with illumination from the right side only with one projection measurement, i.e., without rotating the object in the setup. The result of this left illuminated square is displayed in Figure 5.17. From these reconstructions we can see that the best result is obtained with the iterative approach, by using TV regularization. This gives a quite nice background with much less artifacts than using the FBP algorithm. Also the profile plots shows that the exponentially decreasing light

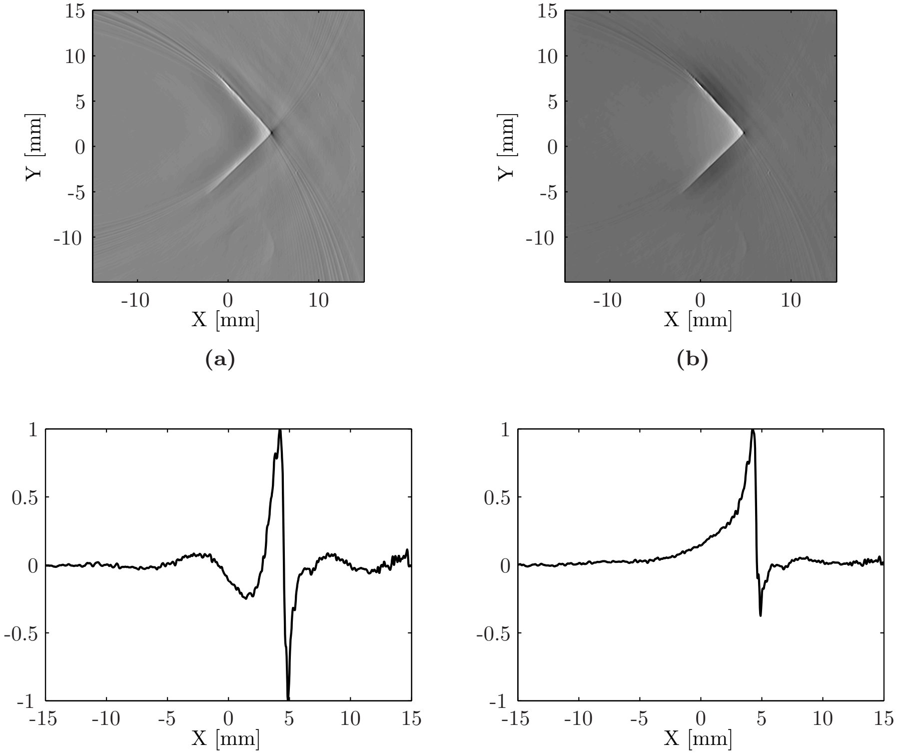

(a) **(b)** **(c)** **(d)**

Figure 5.17 Reconstruction results of a square object illuminated from the right side. The left column (a) and (c) contains the FBP reconstructions and the right column (b) and (d) the Object space preconditioning / TV regularization reconstructions. The top row shows the reconstructed images and the bottom row shows profile plots through the center of the image.

distribution as one would expect in an optically absorbing structure is much better reconstructed using the iterative approach, Figure 5.17d, than the FBP approach, Figure 5.17c.

A full reconstruction using illumination from 90 different angles spread over a full rotation of 360 degrees is displayed in Figure 5.18. Because in this case the optical absorption distribution is changing everytime a new projection is measured, it does not make sense to directly use the iterative approach based on the linear model, because this model assumes that a stationary optical absorption is present. When light illumination from different sides would be used, as is planned in the future, it would again be possible and make sense to use the iterative approach based on the linear model. Because of this, however, we used the simple FBP algorithm to obtain this reconstruction result. Now what we actually see in the reconstruction is the result of averaging of the different projections together. A better result would be possible by light illumination from more sides, which is something planned for the future, another possibility would be to extend the measurement model to take the (rotating) side illumination into account. This is further discussed in the final chapter on conclusions and discussion.

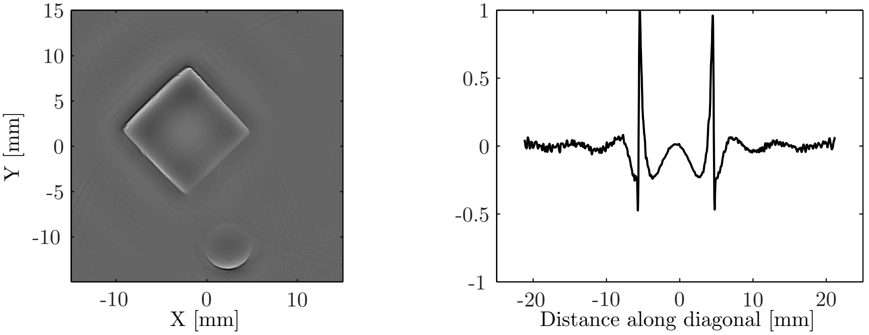

(a) **(b)**

Figure 5.18 Reconstruction results using 90 projections/rotations with the FBP algorithm.

5.2.6 Conclusions

In this section we have looked at the photoacoustic measurement model. An efficient way to calculate the projection integral that is part of this model has been proposed. The efficiency is caused by representing the optical absorption distribution using radial basis functions. The impulse response of the transducer and the laser pulse profile are also contained in the presented measurement model. A fast iterative reconstruction approach was presented, which uses preconditioning to attain reconstructions within an acceptable number of iterations. Too overcome the ill conditioning of the inverse problem associated with inversion of the measurement model, three different regularization methods were investigated. The best results were obtained with TV (Total Variation, based on an L1 norm) regularization.

5.3 Reconstruction using an inhomogeneous speed of sound

In this section we propose an algorithm for the reconstruction of optical absorption images where speed of sound inhomogeneities are taken into account. In our PER-PAT imaging setup, a speed of sound image can be reconstructed prior and independently of the optical absorption reconstruction process, as was discussed in chapter 4. The proposed algorithm will be based on this already known speed of sound distribution.

5.3.1 Previous work

In most of the existing photoacoustic reconstruction algorithms, the acoustic properties are assumed to be homogeneously distributed. Objects which do not satisfy this homogeneity cannot be accurately reconstructed with these algorithms and result in blurred and artifacted images. Several authors have considered the incorporation of speed of sound inhomogeneities in the reconstruction process. These methods can be divided into methods which require an a priori known speed of sound map and methods without this requirement.

Algorithms which require an a priori known speed of sound map

Anastasio et al.[75] demonstrated the reconstruction of photoacoustic measurements by assuming an a priori known speed of sound map. Using this speed of sound map, curved iso-time of flight (TOF) contours were calculated by assuming straight ray propagation of speed of sound. The photoacoustic measurement function, valid for homogeneous speed of sound distributions was modified to include inhomogeneous speed of sound distributions by specifying the integration over the curved iso-TOF contours instead of circles. The reconstruction was then accomplished by solving the positive linear photoacoustic measurement equation by using an EM-algorithm.

Jin and Wang[76] used a similar approach. The speed of sound map in this case was pre-calculated by performing a separate ultrasound transmission tomography (UTT) step. Here linear ray paths are assumed so that a filtered back projection reconstruction can be used in the UTT step. Curved iso-TOF contours were then calculated using the same algorithm as Anastasio et al[75], i.e. by assuming straight ray sound propagation. The inversion of the linear photoacoustic measurement equation was then performed by directly using the iterative LSQR method[54].

Algorithms which do not require an a priori known speed of sound map

Xu and Wang[77] studied the effects of acoustic heterogeneities in PA breast imaging. The acoustic property distribution was modeled with a speed of sound map consisting of two different areas, a boundary area and an inner part both with a different velocity.

Jiang et al[78] used a finite element discretized version of an inhomogeneous acoustic wave equation in the frequency domain. In the wave equation, terms representing the optical absorption distribution, acoustic property distributions and generated pressure are present. This results in a non-linear system of equations involving the unknown optical absorption and acoustic property distributions and the known pressure which is measured at the boundary of the imaging domain. The reconstruction algorithm is then implemented by iteratively solving a linearized system of equations. The linearization is done by calculating a first order Taylor expansion with respect to the unknown optical absorption and acoustic property distributions.

Jin Zhang et al[79] use the same photoacoustic measurement function as Anastasio et al[75] to relate the optical absorption distribution and curved iso-TOF contours to the measured ultrasound signals. The speed of sound distribution was not assumed to be known a priori, however a low dimensional parametrization was used. This parametrization allows the speed of sound distribution to be represented by a limited number of predefined areas with unknown constant speed of sound values. The actual values of the predefined areas are a priori unknown, but their boundaries are assumed to be known. A cost function was formulated that minimizes the difference between predicted and observed measurements and penalizes the roughness of the reconstructed speed of sound and optical absorption distributions. The nonlinear cost function was minimized by iteratively switching between solving for the speed of sound distribution with constant optical absorption and solving for the optical absorption distribution with constant speed of sound. In the first step, with constant optical absorption, a gradient descent step was performed where the direction of the cost function gradient was calculated numerically. In the second step, with constant speed of sound, a quadratic cost function is obtained which was solved using a conjugate gradient method.

Chi Zhang and Wang[80] also propose a method which does not assume any speed of sound distribution to be known a priori. In this method, curved iso-TOF contours are used again in the formulation of the photoacoustic measurement model. However, the calculation of these iso-TOF contours is completely different and does not involve tracing rays through an intermediate speed of sound distribution. Instead, the correlation between integrated photoacoustic signals from origin symmetric detector pairs is used. In the derivation of this method, several approximations were used which mainly involve the assumption that the imaged object is small or equivalently that the detectors are far away from the imaged object. Also, the speed of sound inhomogeneities should not be too high. The approach comes down to calculating a constant speed for each projection. Projections from detector pairs symmetrically with respect to the origin then share the same speed of sound.

5.3.2 Approach

Since we have already obtained a speed of sound map from our passive element measurements, as described in chapter 4, we will use this map in the optical absorption reconstruction. First we will look at the wave equation, in case of an inhomogeneous speed of sound distribution and use an approximate solution to this wave equation, exactly in accordance with [75]. The we propose a new way to calculate the time of flight values needed in the approximate solution. The optical absorption reconstruction is still a linear problem and reconstructions will be calculated using the techniques from section 5.2.

Photoacoustic wave propagation

The propagation of photoacoustic pressure waves in inhomogeneous speed of sound media, is governed by the following partial differential equation[76]:

$$\nabla^2 p(\mathbf{r},t) - \frac{1}{c^2(\mathbf{r})}\frac{\partial^2 p(\mathbf{r},t)}{\partial t^2} = -\frac{\beta}{C_p}\frac{\partial I(t)}{\partial t}A(\mathbf{r}) \tag{5.47}$$

Here, β is the volume thermal expansion coefficient, C_p is the specific heat, $p(\mathbf{r},t)$ is the generated pressure at location $\mathbf{r}$ and time t, $c(\mathbf{r})$ is the acoustic speed distribution, $I(t)$ is the laser pulse profile and $A(\mathbf{r})$ is the optical absorption distribution. A solution to this wave equation can be found for the constant speed case. The illumination function of the laser $I(t)$ will be seen as a delta pulse. In the case of an inhomogeneous speed of sound distribution, an approximate solution can be found as[77]:

$$p(\mathbf{r},t) = \eta\frac{\partial}{\partial t}\iint\limits_{t=t_f(\mathbf{r}',\mathbf{r})}\frac{A(\mathbf{r}')}{|\mathbf{r}-\mathbf{r}'|}\mathrm{d}\mathbf{r}' \tag{5.48}$$

where η is a constant and $t_f(\mathbf{r}',\mathbf{r})$ is the TOF for a pressure wave to travel from point $\mathbf{r}$ to point $\mathbf{r}'$. This function is dependent on the speed of sound distribution $c(\mathbf{r})$. Relation (5.48) shows that the generated pressure can be seen as the projections over iso-TOF contours, which are determined by the TOF function $t_f(\mathbf{r}',\mathbf{r})$. From this relation, we can see that given a speed of sound distribution, the relation between optical absorption $A(\mathbf{r})$ and the measured pressure $p(\mathbf{r},t)$ is linear. This relation has been used by the authors of other SOS compensated photoacoustic reconstruction[75, 76, 79, 80] methods. Their approaches differ in the way that the TOF function is calculated. The first three authors use a ray integral over the speed of sound distribution:

$$t_f(\mathbf{r}',\mathbf{r}) = \int_{l(\mathbf{r}',\mathbf{r})}\frac{1}{c(\mathbf{r}'')}\mathrm{d}\mathbf{r}'' \tag{5.49}$$

where the ray path is the straight line connecting $\mathbf{r}'$ and $\mathbf{r}$ directly. An other approach was used by Chi Zhang and Wang[80], which calculate the function based on the cross correlation between received signals of two opposite detector pairs:

$$t_f(\mathbf{r}',\mathbf{r}) = \frac{|\mathbf{r}'-\mathbf{r}|}{2|\mathbf{r}|}\arg\max_t R(\mathbf{r},t) \tag{5.50}$$

here $R(\mathbf{r},t)$ is the cross correlation function between the integrated measured signals of the detector at position $\mathbf{r}$ and the symmetrically opposite detector $-\mathbf{r}$.

We propose a different approach to calculate the TOF values, which takes refraction of rays into account. Our approach is based on solving the Eikonal equation:

$$|\nabla t(\mathbf{r})|^2 = \frac{1}{c(\mathbf{r})^2} \tag{5.51}$$

The Eikonal equation can be used to model acoustic wave front propagation with inhomogeneous speed of sound distributions. A computationable efficient method for calculation of the first arrival time solution to this equation can be obtained via the fast marching method (FMM)[57]. The effectiveness of the FMM method to incorporate refraction of rays has already been demonstrated in the application area of UTT by Li et al[81, 82].

Calculating the TOF values

For each detector position, TOF values have to be calculated for each of the points in the grid. As explained before, we will use the first arrival time solution to the Eikonal equation to obtain these TOF values using the FMM[57] method.

The FMM method is an algorithm that solves the Eikonal equation in a single pass using upwind finite differences. We have implemented the high accuracy FMM (HAFMM) which uses second order accurate approximations to the gradient. When a good initialization is used, the numerical errors that occur in the solution are very small. The grid that we will use to represent the TOF values will enclose the same area as the optical absorption map, but does not need to have a the same grid spacing (it can be coarser). The grid is the same as the grid in which we know the speed of sound distribution. In this section we assume that this speed of sound distribution is known and in the next section we will see how we obtain this distribution.

We initialize the FMM method by assuming that the speed of sound outside the defined speed of sound grid has a constant and known value. The boundaries of the TOF grid which are in sight from the detector position are then initialized by assuming we can calculate it directly from the distance to the detector and the background speed of sound value. The in sight boundary grid points and their direct neighbor grid points are then pre calculated. This gives a good initialization to start with the HAFMM (this method requires the two neighboring grid points to be known for second order accurate propagation). After initialization the algorithm is run until the TOF values at all grid points have been calculated.

This procedure is repeated for all different detector positions, resulting in n different TOF maps. Since the grids of the optical absorption map and the TOF maps are not necessarily the same, we use bicubic interpolation to obtain the TOF values at off grid points.

Reconstructing the optical absorption distribution

The difference in the measurement model where a homogeneous speed of sound distribution is assumed, as in section 5.2 and the measurement model for a homogeneous speed of sound distribution are very small. The only difference is in the projection integral. Recalling the projection integral from section 5.2, (5.13):

$$\int\limits_{\|\mathbf{r}_{\mathrm{d}}-\mathbf{r}'\|=ct} A(\mathbf{r}')\mathrm{d}\mathbf{r}' \tag{5.52}$$

which is now replaced with

$$\int_{t=t_f(\mathbf{r}_\mathrm{d},\mathbf{r}')} A(\mathbf{r}')\mathrm{d}\mathbf{r}' \tag{5.53}$$

Thus, instead of using $t_f(\mathbf{r}_\mathrm{d}, \mathbf{p}') = \frac{1}{c}\|\mathbf{r}_\mathrm{d} - \mathbf{r}'\|$, we now use the solution of (5.51) to determine the time of flight. For every detector element $\mathbf{r}_\mathrm{d}$, a time of flight map $t(\mathbf{r})$ can be calculated using the FMM. This time of flight map is then resampled at the correct grid points of the optical absorption map to obtain the needed values $t_f(\mathbf{r}_\mathrm{d}, \mathbf{p}')$. For the rest of the reconstruction algorithm, all the techniques discussed in section 5.2 can be used.

5.3.3 Evaluation

The evaluation of the speed of sound correction method consists of two parts. First a computer simulation study was conducted, with a numerical speed of sound phantom and a numerical optical absorption phantom. These results will give an impression of the performance of the algorithm and its performance compared to other algorithms. After that, a phantom object with a speed of sound contrast and optical absorption contrast was placed in the PER-PAT experimental setup. The measurements and results obtained from this phantom study are given in the second part of the evaluation.

Simulation study

The simulation data The geometrical parameters of our physical experimental setup were used in the generation of simulation data. To generate the measurements, we use high resolution numerical phantoms on which we apply the forward model (5.48) of the photoacoustic measurements. The numerical phantoms are displayed in Fig 5.19. This results in a generated sinogram as displayed in Fig.5.20.

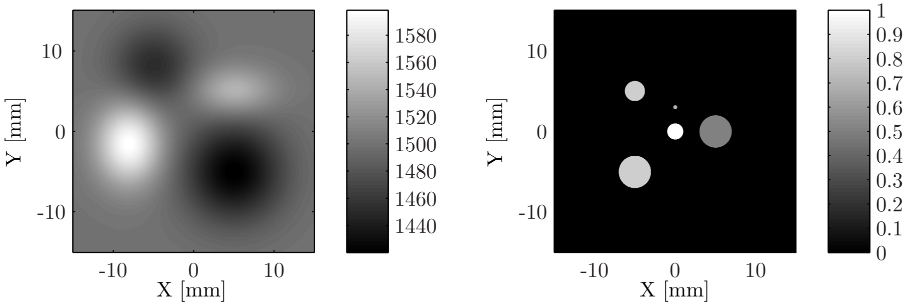

(a) Speed of sound phantom **(b)** Optical absorption phantom

Figure 5.19 Overview of the numerical phantoms used in this study

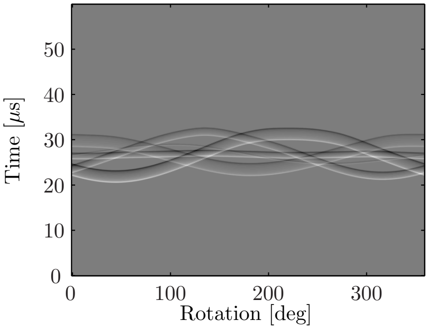

Figure 5.20 Photoacoustic pressure measurements obtained from the numerical phantoms

Reconstructions using the different algorithms After reconstructing the speed of sound distribution, using techniques from chapter 4, we proceeded with the reconstruction of the optical absorption distribution. Here we use the photoacoustic measurements displayed in Fig. 5.20. Different algorithms were tested.

Uniform speed of sound The first algorithm we implemented is based on a constant speed of sound distribution. It does not take into account curved iso-TOF contours. We set the speed of sound equal to 1500 m/s, which is the speed of sound of the background medium. The reconstruction result is displayed in Fig. 5.21a and a profile plot is displayed in Fig. 5.22a. We can see that there are blurring artifacts resulting from the incorrect speed of sound assumption. Especially the small structure above the center is distorted.

No speed of sound distribution We implemented the algorithm of Chi Zhang and Wang[80] which does not need an a priori known speed of sound distribution. For the reconstruction, we did not use their modified FBP approach, but used our approach to solve the resulting linear system of equations, which should give better results. The reconstructed image is displayed in Fig. 5.21b and a profile in Fig. 5.22b. The reconstructed image still contains artifacts, in fact it is not much better than using the assumption of a uniform speed of sound. The advantage, however, is that no speed of sound value needs to be given to the algorithm, which might not always be known accurately. The authors claim that the algorithm should be able to deal with small speed of sound inhomogenities of up to 10%. This is not true for our simulation study which also has inhomogenities of up to 10%, however the inhomogenities are above and below the background speed of sound. Their algorithm performs better when all inhomogenities are either all above or all below the background speed of sound.

Assuming straight ray propagation To investigate the effect of using straight ray propagation, we used the straight ray reconstruction result of the speed of sound

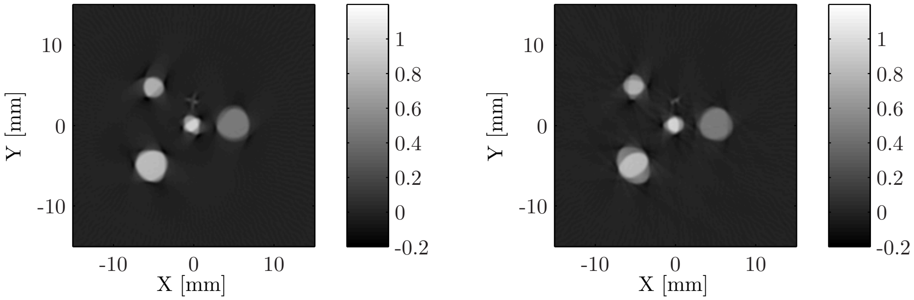

(a) RMSE = 0.0549 **(b)** RMSE = 0.0561

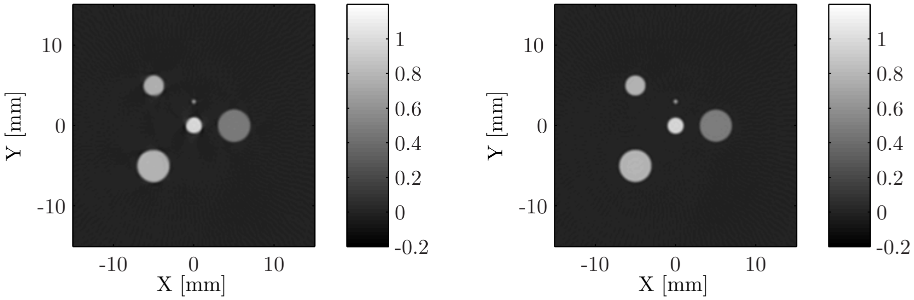

(c) RMSE = 0.0304 **(d)** RMSE = 0.0281

Figure 5.21 Optical absorption distribution reconstruction results. Shown here are the four different implementations with the corresponding RMSE with respect to the ground truth data. (a) Reconstruction assuming a uniform speed of sound of 1500 m/s. (b) Reconstruction assuming no sound speed distribution, with the correlation method of Chi Zhang and Wang[80]. (c) Reconstruction based on straight ray approximations. (d) Reconstruction using our proposed ray refraction correction method.

map. The iso-TOF contours were subsequently calculated by tracing straight rays through the obtained speed of sound map. The obtained linear system was solved and the solution is displayed in Fig. 5.21c. A profile of the reconstruction is displayed in Fig. 5.22c. The result is a lot improved compared to the uniform speed of sound reconstruction. The are hardly any artifacts visible anymore and most of the RMSE error is probably due to the limited bandwidth of the reconstructed image.

Assuming bent ray propagation Finally, our proposed method to reconstruct a speed of sound distribution with refraction corrections and using the result with the HAFMM method to calculate iso-TOF curves is tested. The results of the reconstruction are displayed in Fig. 5.21d and Fig. 5.22d. The results are artifact free and good reconstructions can be obtained.

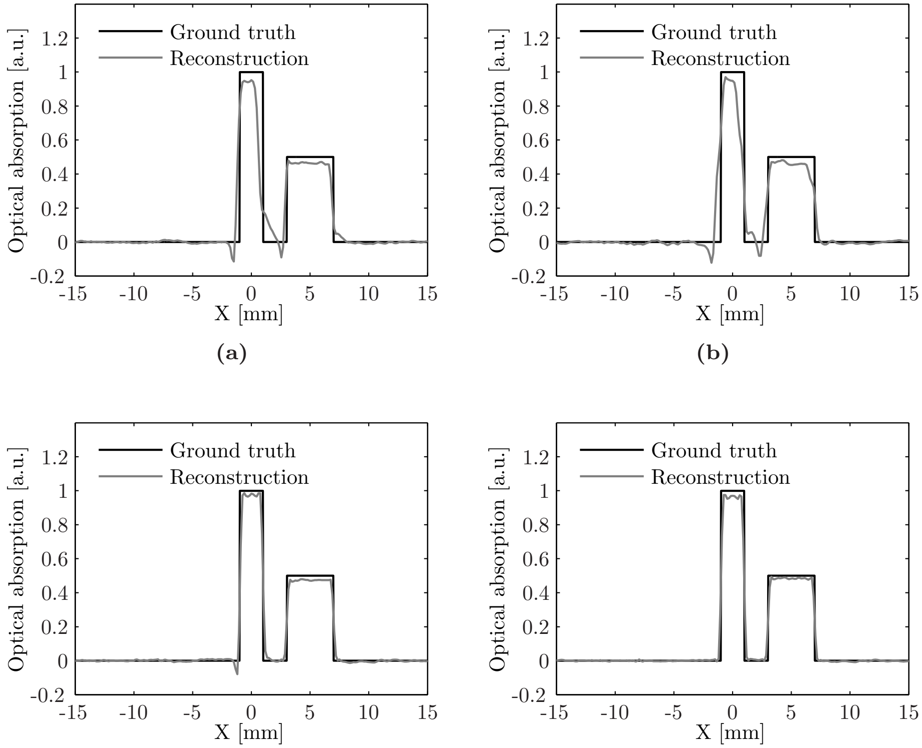

(a) (b) (c) (d)

Figure 5.22 Profile plots along the horizontal center of the images shown in Figure 5.21. (a) Reconstruction assuming a uniform speed of sound of 1500 m/s. (b) Reconstruction assuming no sound speed distribution, with the correlation method of Chi Zhang and Wang[80]. (c) Reconstruction based on straight ray approximations. (d) Reconstructions using our proposed ray refraction correction method.

Phantom study

In this following study, a hybrid phantom with speed of sound and optical absorption contrast was placed in the PER-PAT experimental setup. The layout of the cylindrically shaped phantom is displayed in Figure 5.23.

Measurements on this phantom were taken at five different heights. At the first height we expect to see only the intersection with vertically positioned hairs and at

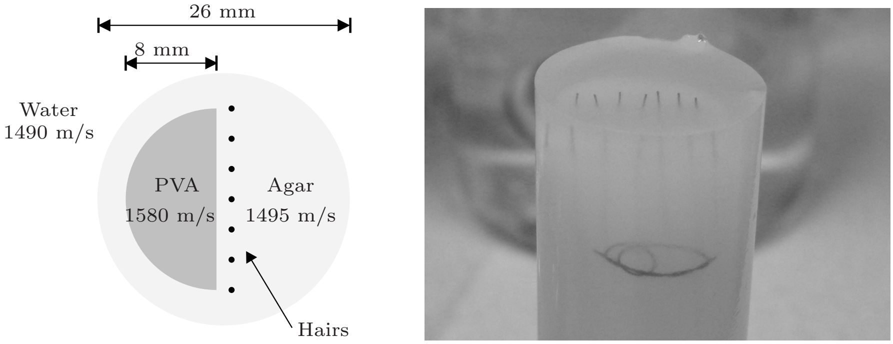

(a) Schematic drawing **(b)** Photograph

Figure 5.23 Images of the hybrid phantom used in the phantom study. The phantom consists of two materials, PVA and Agar each with a different speed of sound. Seven hairs are added for optical absorption contrast. Further down the phantom, some of the hairs are curved in the slice direction as can be seen in (b).

the final height we expect to see some of the curled up hairs in the slice itself. The reconstructions look similar, with the difference that at the final height the curled up hairs are visible, the reconstruction of this final height is displayed in Figure 5.24. From these reconstructions we clearly see that the uncorrected reconstructions suffer from the effect of a non-homogeneous speed of sound distributions. The correction by using the proposed speed of sound correction approach works very well, as can be seen in the right column of the figure.

5.3.4 Conclusions

In this section we presented a new method to reconstruct optical absorption distributions using a known speed of sound map. In our PER-PAT this speed of sound map can be estimated using the techniques described in chapter 4. Our method differs from existing methods that correct for speed of sound inhomogeneities in the way in which the iso-time of flight (TOF) contours are calculated. We use the Fast Marching method on the known speed of sound map to quickly calculate TOF values at each of the pixels in the reconstruction grid. By using the Fast Marching method, we take ray-refraction effects into account in this calculation. This is opposed to existing methods, which assume straight ray propagation in the TOF calculation. The improvements over existing methods are then a slight increase in accuracy and a computationally more efficient way to perform the reconstruction. Our proposed correction method, in combination with the techniques of chapter 4 to estimate the speed of sound map, has been shown to work well in practice by experimental evaluation.

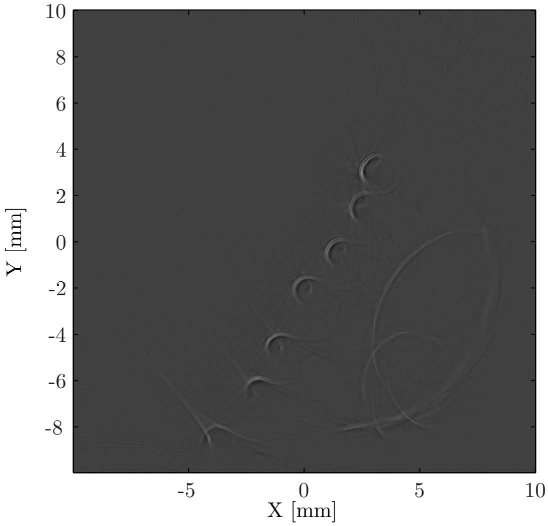

(a) Uncorrected reconstruction

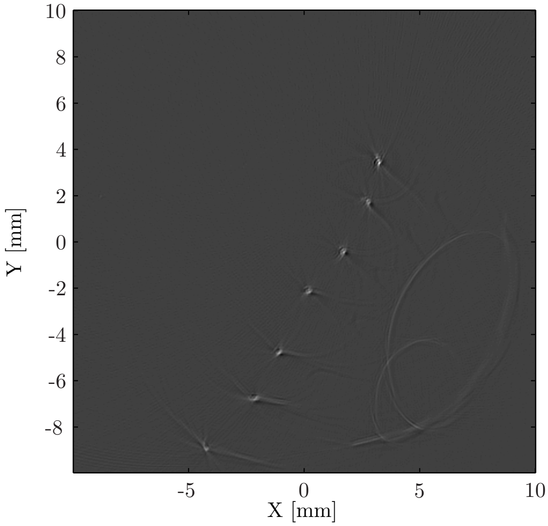

(b) SOS corrected reconstruction

Figure 5.24 Reconstructions of the hybrid phantom with and without the proposed speed of sound correction algorithm. The reconstruction on the top is reconstructed assuming a homogeneous speed of sound distribution, with a value equal to the surrounding water. The reconstruction on the bottom is reconstructed by using the speed of sound correction algorithm. The speed of sound map was obtained using the passive element based techniques in chapter 4.

5.4 Motion Correction

In this section we introduce an approach that can be used to estimate motion from an object measurement by using specific landmarks which are attached to this object. Once the motion is estimated, it is used in a modified reconstruction algorithm to correct for the motion artifacts.

5.4.1 Introduction

The approach and results used in this section are applied to photoacoustic measurement geometries where a single detector element is rotated around an object of interest. Which is in contrast with our PER-PAT imaging setup we have a complete array rotating around the object of interest. Effectively we are now only using the center sensor element from the array. The results of this section can be generalized to the complete rotating array scenario. An illustration of the measurement geometry for the single detector case is displayed in Figure 5.25.

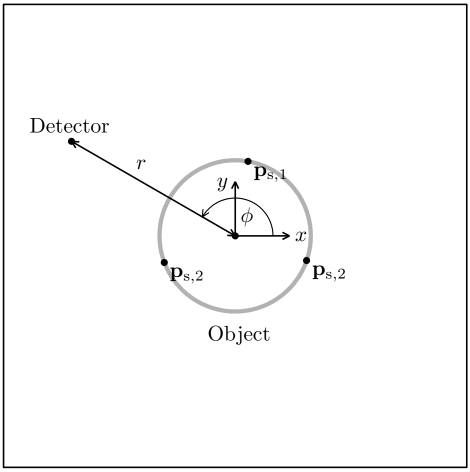

Figure 5.25 Schematical overview of the single element detector geometry. Also shown in this figure are the object and the landmark elements which have to be attached to the object to image.

In photoacoustic imaging, reconstruction of the optical absorption distribution involves back projection of ultrasound measurements in a spatial map. Different sets of ultrasound measurements are obtained by allowing the object (or the measurement system) to rotate in a computed tomography like way. However, unexpected movements of the object during the measurements can distort this reconstruction and result in blurred images. The aim of this section is to develop a technique that corrects for these unexpected and a priori unknown movements. Our approach is based on tracking known landmarks in the received signal. These landmarks have to be attached to the object under investigation as displayed in Figure 5.25. By assuming rigidity of the object under consideration, the tracking of landmarks in the PA signal can be used to estimate small translations of the object during signal acquisition. These estimated translations represent the unexpected object movement and can be used in the reconstruction phase to obtain a motion corrected image.

In our approach, we will take measurements at n different positions $\{\mathbf{r}_1, \ldots, \mathbf{r}_n\}$, which describe a circle in a plane according to

$$\mathbf{r}_i = r\left[\cos\left(\frac{i-1}{n}2\pi\right), \sin\left(\frac{i-1}{n}2\pi\right)\right]^T \tag{5.54}$$

where r is the radius of this circle and the measurements are numbered i and range from 1 to n. A measured signal at a position $\mathbf{r}_i$ consists of samples at distinct time points

$$\mathbf{s}_i = \begin{bmatrix} p(\mathbf{r}_i, t_0^{(i)}) \\ \vdots \\ p(\mathbf{r}_i, t_m^{(i)}) \end{bmatrix} \tag{5.55}$$

where the relation between the time points is given as $t_{j+1}^{(i)} = t_j^{(i)} + T$ with T the period of the sampling frequency. Since measurements at different positions are not taken at the same time (i.e. $t_0^{(i)} \neq t_0^{(i+1)}$), we have to take into account the dynamics of the system. The most important aspect here is the uncontrolled and unwanted movement of the object during measurement acquisition. The measurements $\mathbf{s}_i$ are not directly used, but first a pre-processing step is applied which extracts time of flight measurements $\mathbf{z}$ from these pressure measurements.

5.4.2 Problem formulation

Our problem can be defined as a state estimation problem of the unknown object motion (state) during measurement acquisition and to use the estimated object motion in the image reconstruction process. To solve this problem, we will formulate and test a method involving the tracking of object landmarks during image acquisition.

We assume that the structure of the object is rigid. The unwanted movement of the object during measurement acquisition can thus be described as a rigid transformation over time. In our setup, we take measurements in a 2-dimensional plane, and consequently we will reconstruct 2-dimensional images of the imaged structure. We will describe the rigid transformation of the object at each measurement step i using the state vector $\mathbf{x}_i$. For consecutive measurement steps, the changes in the transformation are small. The dynamics of the system can simply be captured as:

$$\mathbf{x}_{i+1} = \mathbf{x}_i + \mathbf{v}_i \tag{5.56}$$

where $\mathbf{v}_i$ is a random variable. Because we assume that the movement is smooth, and restricted by the variance of the random variable $\mathbf{v}_i$.

The landmarks in the object will help us to estimate the evolving state vector. Observations of these landmarks will be used to to decrease the uncertainty of the estimated state vector. A relation between observations and the current state $\mathbf{x}_i$ can in general be described as:

$$\mathbf{z}_i = h_i(\mathbf{x}_i, \boldsymbol{\varphi}, \mathbf{w}_i) \tag{5.57}$$

where $\mathbf{z}_i$ is a vector of observations, $\boldsymbol{\varphi}$ is a vector of parameters that influence the measurement function and $\mathbf{w}_i$ is a random variable describing the uncertainty in the observed measurements. The exact form of the measurement function $h_i()$ will be discussed in section 5.4.4. When tracking landmarks, time of flight values will be used as observations of the individual landmarks in the object. The exact value of the parameter vector $\boldsymbol{\varphi}$ is important for a good estimation of the state vector $\mathbf{x}_i$ but can sometimes still be uncertain a-priori. The a-priori knowledge available about the parameters can best be quantified in a probability density function (pdf) $p(\boldsymbol{\varphi})$. After all, what we are interested in are the values of $\mathbf{x}_{1:n}$ and $\boldsymbol{\varphi}$ that maximize the pdf

$$p(\mathbf{x}_{1:n}, \boldsymbol{\varphi} | \mathbf{z}_{1:n}) \tag{5.58}$$

representing the uncertainty on our estimate of $\mathbf{x}_{1:n}$ and $\boldsymbol{\varphi}$, given the observations $\mathbf{z}_{1:n}$. The problem here is that both the state vector and the parameters have to be estimated. We formulated this estimation as an iterative optimization process. By using Bayes theorem and dropping non-informative terms from the pdf, equation (5.58) can be written as

$$\frac{p(\mathbf{z}_1|\mathbf{x}_1, \boldsymbol{\varphi}) p(\mathbf{x}_1) p(\boldsymbol{\varphi})}{p(\mathbf{z}_1)} \prod_{i=2}^{n} \frac{p(\mathbf{z}_i|\mathbf{x}_i, \boldsymbol{\varphi}) p(\mathbf{x}_i|\mathbf{x}_{i-1})}{p(\mathbf{z}_i|\mathbf{z}_{i-1})} \tag{5.59}$$

using the relations (5.56) and (5.57).

5.4.3 Solution using linearization

We assume that the random variables $\mathbf{v}_i$ and $\mathbf{w}_i$, representing the uncertainty in the state dynamics and the observations respectively, are Gaussian distributed. If now both the state dynamics and the measurement function were linear, optimization of the posterior pdf (5.58) would result in determining the minimum of a quadratic function. This minimum is easily found and thus we try to base our solution to the problem on linearization of the measurement function.

The quadratic function that we now have to optimize consists of one part representing the prior knowledge of the unknown variables and another part representing knowledge on observations of the unknown variables. This function is derived from (5.58) which is, due to the linearization, a product of Gaussians. By taking the logarithm and removing terms which are not dependent on the unknown variables, we end up with the sum of squared Mahalanobis distances of each of the individual pdfs in (5.59):

$$g(\mathbf{x}_{1:n}, \boldsymbol{\varphi}) = g_{\text{obs}}(\mathbf{x}_{1:n}, \boldsymbol{\varphi}) + g_{\text{prior}}(\mathbf{x}_{1:n}, \boldsymbol{\varphi}) \tag{5.60}$$

This quadratic function can be written as (after substituting $\mathbf{x} = [\mathbf{x}_{1:n}^T, \boldsymbol{\varphi}^T]^T$)

$$g(\mathbf{x}) = g_0 + \mathbf{G}^T\mathbf{x} + \mathbf{x}^T\mathbf{H}\mathbf{x} \tag{5.61}$$

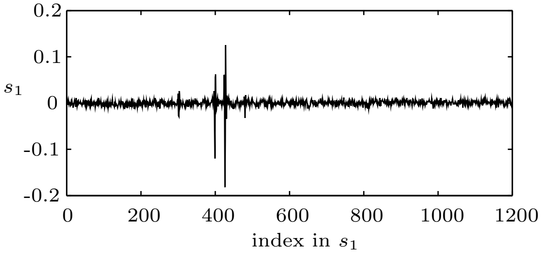

Figure 5.26 Measured pressure signal $\mathbf{s}_1$

where $\mathbf{H}$ is the Hessian matrix of g. This function has a unique minimum when the Hessian matrix is positive definite and thus invertible, which is guaranteed by including the prior knowledge on the unknown variables. The minimum can subsequently be found by setting the gradient of g to zero and solving the linear system of equations

$$\mathbf{G} + 2\mathbf{H}\mathbf{x} = 0 \quad \Leftrightarrow \quad \mathbf{x} = -\tfrac{1}{2}\mathbf{H}^{-1}\mathbf{G} \tag{5.62}$$

In combination with the linearization, this is an iterative optimization procedure, which is also known as Newton's method [35]. The solution to the linear system of equations is used as the linearization point in the next iteration. The optimization procedure will be initialized with the linearization point set at the expectation value of the unknown variables given the a-priori information

5.4.4 Implementation of the solution

In this section, the implementation of the motion correction algorithm will be described. To illustrate the individual steps in the algorithm, we show the results of each of the steps applied to measurements obtained from experiments on a phantom object.

The phantom object used here was a structure containing four landmarks, where each landmark is a human hair with a diameter of 150 μm. A series of measurements is made by rotating an ultrasound sensor around this structure, describing a full circle in 120 steps (i.e. an increase in angle of 3° each time). The phantom is illuminated by a laser pulse and the generated pressure wave is subsequently measured at these 120 positions in a circle around the phantom, which results in $n = 120$ vectors of measurements $\{\mathbf{s}_i\}_{i=1}^{n}$. The measurements are sampled at a frequency of 20 MHz, and the speed of sound c in the medium is assumed to be 1500 m/s. A single measurement vector $\mathbf{s}_1$ is displayed in Fig. 5.26. The whole set of measurement vectors (vertically stacked) is displayed in Fig. 5.27a.

Signature of the landmark

Landmarks in the imaged object will be visible in the measured signal as a distinctive waveform of a certain length. We term this distinctive waveform the *signature* of

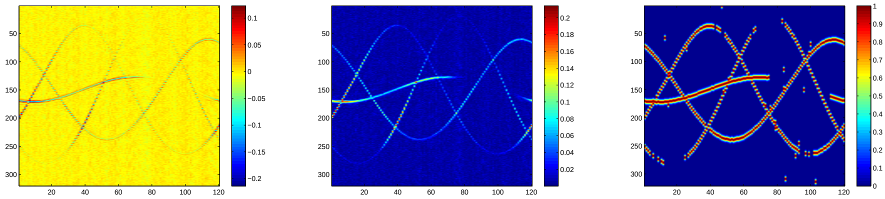

(a) Sinogram

(b) Envelope of sinogram

(c) Preprocessed envelope of sinogram

Figure 5.27 Measurements shown for a time domain region of interest.

the landmark and we have to determine this signature first, so that it can be used to extract time of flight (TOF) measurements of the landmarks from the measured signal. To extract these signatures from the measurements in a robust way, without being disturbed by other photoacoustic sources from inside the object, we will use the following approach. First we try to detect the presence of signals (landmark or not) by calculating the envelope of the signal. The envelope can be calculated by taking the absolute value of the analytic signal of the measurement[83]. The envelope of the phantom object measurements is displayed in Fig. 5.27b. The maxima in this envelope signal can subsequently be used to find potential realizations of the landmark signature in the neighborhood of those maxima. However, due to noise in the measurements, not all maxima found in the envelope signal are in reality caused by a landmark. To be robust and discard these outliers, we can use the fact that for one landmark the TOF trajectory is periodic and approximately sine shaped (this can also be observed in Fig. 5.27b). The maxima which are then too far away from one of the found sines can be marked as outliers. We can thus parametrize the TOF trajectory as a sine function with a known period, but unknown offset, amplitude and phase. However, the offset is the same for each of the sine functions generated by the different landmarks, and can be determined by taking the mean value of all TOFs on which maxima have been found in the envelope signal. This leaves us with two parameters – amplitude and phase – for each of the four sine waves (because we have four landmarks in our example). To discard signals from inside the object, we can set a threshold on the minimum amplitude that the sine shaped trajectory caused by a landmark should have.

The problem that now has to be solved is follows: Determine the most likely set of parameters that would generate an envelope image as we have observed it. The likelihood of a certain parameter vector can be evaluated by a Hough transform from the image to our parameter domain as

$$p(A,\theta) \propto \iint I(t,i)\delta\left(t - A\sin\left(\theta + i\frac{2\pi}{120}\right)\right)\mathrm{d}t\mathrm{d}i \qquad (5.63)$$

where $I(t,i)$ is the envelope image as displayed in Fig. 5.27b. Since we are not

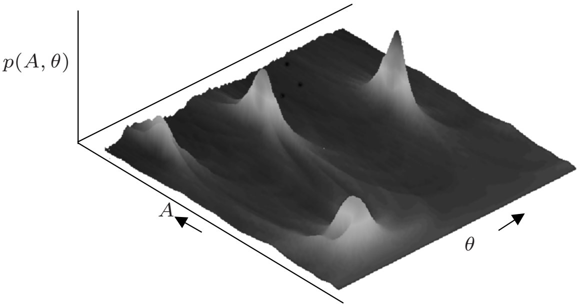

Figure 5.28 Probability density function $p(A,\theta)$

interested in the actual intensities of the produced sines, we first preprocess the image $I(t,i)$ so that only the positions of maxima in the envelope are of influence and the relative intensity of the maxima are discarded. This preprocessing is achieved by using the TOFs of the estimated maxima to generate a new image, where we use a Gaussian kernel to model some of the uncertainty involved in the estimation of the maximum. The preprocessed image is then obtained as the sum of Gaussian kernels around the estimated maxima positions

$$I_{\text{pre}}(t,i) = \sum_{j=1}^{4} e^{\frac{-(z_{ij}-t)^2}{2\sigma^2}} \tag{5.64}$$

where the vector $\mathbf{z}_i = [z_{i1},\ldots,z_{i4}]^T$ contains the TOFs of the maxima found in the envelope of each signal $\mathbf{s}_i$. The preprocessed image obtained from the envelope image by using a kernel width of $\sigma = 3$ is displayed in Fig. 5.27c. The pdf $p(A,\theta)$ can now be calculated by applying the Hough transform as given in (5.63) using the preprocessed image. The resulting pdf is displayed in Fig. 5.28. This pdf clearly contains four maxima, which are the parameters that generated the four sine waves. The four sets of parameters, being the four maxima in the pdf $p(A,\theta)$, can now be used to locate the outliers in the data.

Based on the positions of the estimated maxima, we now know which parts of the measured signal contain a realization of the landmark signature. These parts can be extracted from the signal and used for further estimation of the landmark signature. However, the exact location of the signature inside each extracted signal is not known. To align the extracted signals with respect to each other, we first increase the resolution by doing a cubic spline interpolation of the extracted signal and resampling this interpolated signal at a higher sample rate. This allows us to more accurately align the extracted signals. After observing the extracted signals, the alignment is based on the heuristic of aligning the zero crossing corresponding to the highest maximum-to-minimum difference in the signal.

It is possible that among the aligned signatures there are still outliers left, for example due to incorrect alignment or otherwise corrupted signals. These are removed

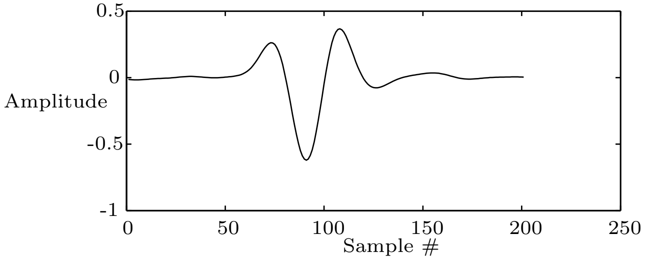

Figure 5.29 Estimated landmark signature (upsampled with a factor of 10 by interpolation)

by assuming that the aligned dataset is approximately Gaussian distributed. When any of the principal components in the dataset (based on eigenvector analysis of the covariance matrix) do not seem to be Gaussian distributed, the outliers are removed. The components are checked for conformity to the Gaussian by looking at the kurtosis of the dataset projected along the component. The finally estimated landmark signature is displayed in Fig. 5.29.

Extraction of landmark measurements

Having defined the landmark signature, the next task is to extract the locations (TOFs) of the landmark signatures from the measured pressure signals. This is done by correlation of the measured signal $\mathbf{s}_i$ with the landmark signature. The locations of the maxima in the correlated signal are taken as the TOF measurements. The number of correlation maxima that will be used is, at most, equal to the number of landmarks in the imaged object, but can be less if the value of a found maximum is below a certain threshold. This means that not all sensor measurements include an estimated TOF for each landmark.

Here again we have to cluster the TOF measurements according to their landmark source. To do this, we will use a Hough transform, exactly as was described in the previous section about the landmark signature. This Hough transform gives the most likely parameters that generated the four sines. The TOF measurements closest to the estimated sine of the specified source (below some threshold distance to remove outliers) will be assigned to the corresponding source.

Minimizing the cost function

With the TOF measurements available and each measurement assigned to the correct landmark source, the next task is to minimize our cost function. This involves the use of a measurement function that relates the measurements to the unknown state vector of the transformations (object motion) and the parameter vector containing information about the measurement geometry to the TOF measurements. We will model the state vector as the relative (in plane) translation of the object with respect to the first sensor reading

$$\mathbf{x}_i = \begin{bmatrix} T_x \\ T_y \end{bmatrix} \tag{5.65}$$

The parameter vector in our case contains the positions of the four landmarks ($\mathbf{p}^1, \ldots, \mathbf{p}^4$), the radius of the circle on which the sensors are positioned (r) and the synchronization time, being the difference between the time of firing of the laser pulse and time of receiving the first measurement sample (t_0), all placed in one parameter vector

$$\boldsymbol{\varphi} = \begin{bmatrix} p_x^1 \\ p_y^1 \\ \vdots \\ p_x^4 \\ p_y^4 \\ r \\ t_0 \end{bmatrix} \tag{5.66}$$

The measurement function relates the state vector and the parameter vector to the TOF measurements as

$$z_{ij} = h_{ij}(\mathbf{x}_i, \boldsymbol{\varphi}, \mathbf{w}_i) = \frac{\left\| \mathbf{p}_j + \mathbf{T}_i - r \begin{bmatrix} \cos\theta_i \\ \sin\theta_i \end{bmatrix} \right\|}{c} - t_0 + w_{ij} \tag{5.67}$$

where θ_i is the rotation of the ultrasound sensor at the i^{th} measurement, c is the known speed of sound and $\mathbf{w}_i$ is a Gaussian random vector with covariance $\mathbf{P}_{ww}$. The subscript j indicates for which landmark the measurement function is used (since not all landmarks might have a TOF measurement in each measurement $\mathbf{s}_i$).

Our cost function is based on the linearization of the measurement equation and contains the sum of the Mahalanobis distances of each of the pdfs in (5.59). The measurement function can be linearized as

$$h_{ij}(\mathbf{x}_i, \boldsymbol{\varphi}, \mathbf{w}_i) \approx z_{ij}^{(l)} + \mathbf{H}_x^{(l)} \mathbf{x}_i + \mathbf{H}_\varphi^{(l)} \boldsymbol{\varphi} + \mathbf{w}_i \tag{5.68}$$

with

$$z_{ij}^{(l)} = h_{ij}(\mathbf{x}_i^{(l)}, \boldsymbol{\varphi}^{(l)}, 0) \tag{5.69}$$

where linearization is done about the point $\mathbf{x}_i^{(l)}$ and $\boldsymbol{\varphi}^{(l)}$ and $\mathbf{H}_x^{(l)}$ and $\mathbf{H}_\varphi^{(l)}$ are the appropriate Jacobian matrices. Using this linearization, the measurement likelihood can be written as

$$p(z_{ij} | \mathbf{x}_i, \boldsymbol{\varphi}) \sim \mathcal{N}(z_{ij}^{(l)} + \mathbf{H}_x^{(l)} \mathbf{x}_i + \mathbf{H}_\varphi^{(l)} \boldsymbol{\varphi}, \mathbf{P}_{ww}) \tag{5.70}$$

The state transition function is already linear and has the simple form of

$$\mathbf{x}_{i+1} = \mathbf{x}_i + \mathbf{v}_i \tag{5.71}$$

with $\mathbf{v}_i$ a Gaussian random vector with covariance $\mathbf{P}_{vv}$, so that we can write the transition pdf as

$$p(\mathbf{x}_{i+1} | \mathbf{x}_i) \sim \mathcal{N}(\mathbf{x}_i, \mathbf{P}_{vv}) \tag{5.72}$$

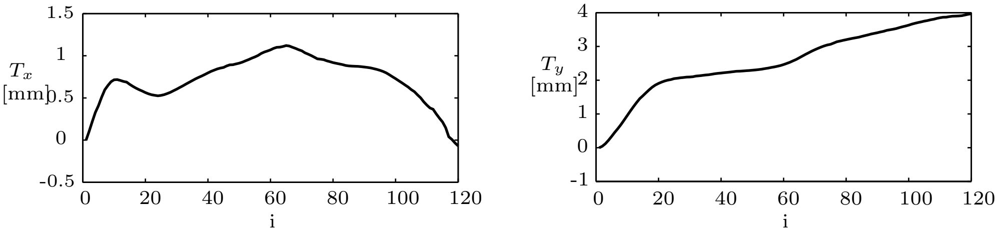

(a) Evolving state T_x **(b)** Evolving state T_y

Figure 5.30 Evolving state vector

From these two pdfs, the Mahalanobis distances can easily be extracted and summed, resulting in the quadratic cost function. Iterative optimization of this cost function using the phantom object measurements converged quickly in 13 iterations to a solution. The evolving state vector $\mathbf{x}_i$ in the final solution of the optimization is displayed in Fig. 5.30.

5.4.5 Image reconstruction

The final task is to reconstruct the image from the obtained pressure measurements. For this we use the filtered backprojection algorithm[6]. In the backprojection phase we will correct for the estimated motion, by shifting each image with the correct offset to compensate for the motion.

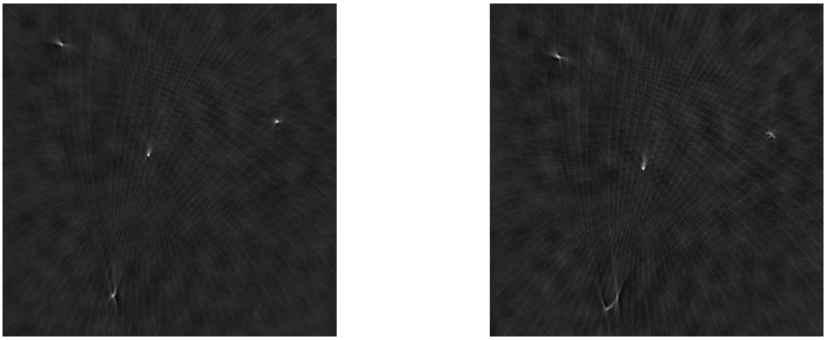

(a) Reconstructed image with motion correction **(b)** Reconstructed image without motion correction

Figure 5.31 Reconstructed image of the phantom object with motion present during the image acquisition phase.

Results of the image reconstruction are displayed in Fig. 5.31. Here we can clearly see the improvement that is obtained by correcting for the estimated object motion during the measurements acquisition. The uncorrected image clearly shows the motion. The reconstruction of the hairs does not result in four small dots, but instead we observe that the dots are somewhat distorted. This is shown more clearly in the zoomed in versions displayed in Fig. 5.32.

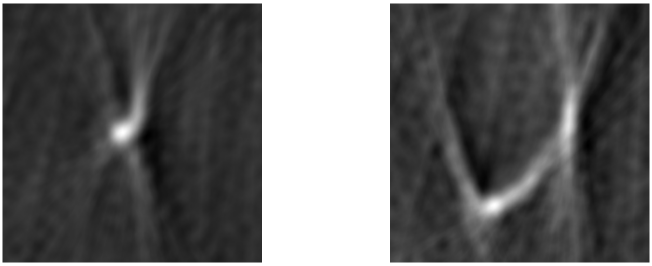

(a) Lowest hair, with motion correction

(b) Lowest hair, without motion correction

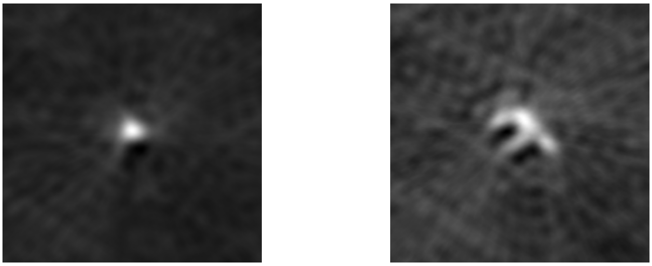

(c) Most right hair, with motion correction

(d) Most right hair, without motion correction

Figure 5.32 Zoomed reconstruction two hairs in the phantom object (width = 2mm)

5.4.6 Conclusion

In this section we have demonstrated that it is possible to correct for unwanted object motion during measurement acquisition. The image reconstruction was modified by a motion corrected backprojection algorithm. For this motion corrected image reconstruction to work, the unknown object motion has to be known. Therefore we proposed a motion estimation algorithm, which is based on tracking landmark signatures in the photoacoustic measurements. The landmark signatures are generated by landmark elements which have to be attached to the object. We have used small human hairs for this purpose, which gives good motion correction results.

6

Conclusion and recommendations

6.1 Conclusions

This thesis presented an analysis, description and experimental validation of the signal processing, i.e., calibration, post-processing, image reconstruction, needed in a Passive Element enRiched PhotoAcoustic Tomography (PER-PAT) imaging setup. In this chapter we will come to conclusions by answering the research questions posed in Chapter 1, section 1.4.1. The questions will be discussed for each topic separately.

6.1.1 Calibration

In the calibration chapter an analysis on the accuracy and the presentation of an algorithm that can be used in the PER-PAT setup to estimate the geometrical parameters needed for image reconstruction were presented.

Does the calibration problem have a unique solution and what are the conditions for having a unique solution?

Since the calibration problem consists of processing two measurements, the reference measurement and the calibration measurement, both with their own calibration procedure. We will answer the questions for each measurements separately.

Reference measurement When a single passive element is used in the PER-PAT setup, it is in some geometrical configurations possible that the reference calibration does not have a unique solution. In the linear array configuration this problem occurs when the passive element is positioned on, or close to, the axis of the sensor elements. This is in practice never the case, so for the linear array there will always be a unique solution to the calibration problem in the domain where the passive element is expected to be positioned. The situation is different, however, for the curved array. Whenever the passive element is positioned on, or close to, the virtual circle spanned by the curvature of the curved array, there can be an ambiguity as to whether the element was positioned inside or outside of this circle. This happens only when all three parameters, being speed of sound and the x- and y-positions of the passive element, are assumed to be unknown. When speed of sound is known and only the passive element position needs to be determined there is no ambiguity.

Calibration measurement From the calibration measurement we try to estimate the center of rotation and the speed of sound. The number of rotations necessary for a unique calibration was found to be at least two, one is obviously not enough because the center of rotation can only be determined when there is a rotation involved. Furthermore we found out that there is only one source needed to be present in the calibration phantom for a unique calibration.

What accuracy can we theoretically expect from a calibration and how does this depend on the chosen phantom and measurement configuration?

The accuracy of the calibration depends initially on how accurate the time of flight can be measured from each of the sources present in the calibration phantom. This accuracy is discussed in the time of flight estimator presented in Chapter 3. For a given time of flight uncertainty, the effects of using more rotations or more source in the phantom where simulated and displayed in Figure 2.4. There it is shown for example that using one source and five rotations gives an accuracy roughly equivalent to using four sources and two rotations. Furthermore, the effect of the geometrical configuration of the passive elements on the calibration accuracy, by varying the distance of the passive elements to the center of the calibration object, is also simulated and shown in the same figure.

How does a different speed of sound in the calibration phantom affect the calibration outcome and can we correct for this easily?

The calibration phantom is made of Agar which has a slightly higher (about 0.5%) speed of sound than the surrounding water. When this effect is not taken into account, depending on the position of the center of rotation, the resulting calibration will be biased. These biases can be heavily reduced by using a model that takes this higher speed of sound into account. This modified model requires that also the shape/radius of the calibration phantom needs to be known and specified to the algorithm. Refraction effects can be ignored in this modified model, since this introduces no significant improvement in accuracy.

Can we implement a robust calibration algorithm that performs well with a substantial amount of outliers?

We have proposed a calibration method that has been shown, from measurements with a lot of noise under far from ideal circumstances, to work very well in the presence of outliers. The robustness is obtained by using fuzzy clustering with an explicit outlier class using the Expectation-Maximization algorithm. Furthermore, a coarse to fine approach with four models of increasing complexity is used to make the optimization problem feasible.

6.1.2 Estimation of ultrasound parameters

In this chapter the estimation of ultrasound propagation parameters, i.e., time of flight and attenuation, is discussed. This can be seen as a pre-processing step, necessary before the image reconstruction of acoustic property distributions can take place. A maximum likelihood framework that can be used for the extraction of these projection measurement was presented in this chapter.

How accurate (with an accuracy possibly below the sampling frequency) can we theoretically extract time of flight measures from photoacoustic point source measurements and can we design a time of flight estimator that attains this accuracy in practice?

We have analyzed the problem of estimating the unknown time of flight from the measurement of a photoacoustic source signal with an ultrasound transducer. An estimator was derived which, for high SNR, equals the theoretically possible lower bound on the uncertainty of the estimate, the CRLB. This is an accuracy which can be far below the time period belonging to the sampling frequency, depending on the amount of noise present on the measurements. The result is visualized in Figure 3.7a.

Can we design an estimator that operates on ultrasound transmission mode measurements to estimate frequency dependent attenuation and the corresponding speed of sound dispersion?

We have developed several estimators to estimate ultrasound propagation parameters, three of which make it possible to estimate the frequency dependent attenuation and speed of sound dispersion. The developed estimators have been tested on two aspects, the statistical properties describing the accuracy using Monte-Carlo simulations and the correctness of the underlying models using experimentally obtained measurements. The signal shape change caused by the frequency dependent attenuation was observed in practice and could well be predicted by the proposed model. From the Monte-Carlo simulations we found that the performance of the best estimator was very close to the theoretically possible lower bound (CRLB).

How does including the Kramers-Kronig relation in the model increase the accuracy of the estimate with respect to existing estimator that do not use this extra information?

The increase in accuracy that is gained when using the Kramers-Kronig relation in the model depends very much on the SNR of the measurements. A low noise and high noise situation were investigated. In the low noise situation the effect is quite significant as can be seen in Figure 3.20a, there is a clear separation in accuracy between the estimators using the Kramers-Kronig relation (MLMagPhase and MLFFT/MLTDomain) and the other estimators for all propagation distances. In the high noise situation, Figure 3.20b, the result is a bit different for the MLMagPhase estimator, which performance becomes relatively worse with increasing distance. The MLFFT estimator however still performs better then other estimators which ignore the Kramers-Kronig information in their model. There is thus a clear accuracy increase when the Kramers-Kronig relation is included into the measurement model.

6.1.3 Reconstruction of ultrasound properties

Here we presented our approach and results for the reconstruction of speed of sound and attenuation distributions using our PER-PAT setup. An iterative procedure was proposed to correct for ray refraction effects, by switching between ray tracing through an estimated speed of sound map and estimating the speed of sound map using the predicted ray paths.

Can we reconstruct speed of sound and acoustic attenuation distributions from single passive element measurements?

Using experimental evaluation we have shown that our proposed technique allows us to reconstruct speed of sound and acoustic attenuation distributions from single passive element measurements. For single passive elements, a relatively high number of projections are needed to accurately reconstruct small structures in the object. For limited projection measurements, a single passive element is not be enough to reconstruct small structures in the object. However, when only a low resolution reconstruction is necessary, such as is the case for speed of sound inhomogeneity correction in photoacoustic image reconstruction, a single passive element might be enough.

Is there a benefit in using more than one passive element in the setup to increase the spatial resolution of the reconstruction?

For limited projection measurements, there is a very clear benefit in using multiple passive elements for the reconstruction of acoustic property distributions. The spatial resolution significantly increases when more passive elements are used, as can be observed in Figure 4.13. For measurements with a high number of projections, there is no improvement in reconstruction when using more than one passive element. In our setup there is always a very small independent motion in each of the passive elements, which introduces inconsistencies in the measurement model. Therefore the reconstruction using more passive elements is not necessarily better, since including some bad measurements can degrade the result. This effect is not noticable in the low projection measurements, because of the lower reconstruction resolution.

Can we deal with refraction effects, i.e., the bending of rays, that can occur in these ultrasound property measurements?

As mentioned, an iterative method has been proposed to deal with refraction effects. Experimental evaluation has shown that we can successfully deal with refraction effects. The objects that we measure typically have a higher speed of sound than the surrounding coupling medium (water). This results in ray bending towards and through the object at the boundaries of the object. Not taking ray refraction into account, i.e., assuming straight ray propagation results in reconstructions with increased dimensions of the object. After a couple of iterations of the method, the dimensions of the reconstructed object will decrease and match with the true object dimensions.

6.1.4 Reconstruction of optical absorption

Finally the image reconstruction of optical absorption, the main contrast in photoacoustic imaging, was discussed. Analysis and experimental evaluation of iterative and single step reconstruction approaches were presented. Also two additions to the reconstruction were proposed, being a speed of sound correction algorithm and a motion correction algorithm.

How much improvement can we expect from iterative reconstruction algorithms in image quality with respect to the much faster filtered back projection (FBP) type of algorithms?

A substantial improvement in image quality can be gained when using iterative reconstruction algorithms. The filtered back projection algorithm, which is indeed very fast, suffers from artifacts caused by the back projection over arcs. These artifacts can almost completely be removed by using a proper iterative reconstruction algorithm. A very important issue in the successful operation of iterative reconstruction algorithms is regularization. The best results can be obtained by using an L^1-norm term on the image gradient, such as Total Variation, which filters high frequency noise while having an edge preserving effect.

How can preconditioning help in improving the convergence speed of iterative reconstruction algorithms and how do we obtain a suitable preconditioner?

Iterative reconstruction algorithm can suffer from slow convergence, i.e., requiring a lot of iterations before converging to a good solution, when used without a preconditioner. We found out that this problem is a big problem in photoacoustic image reconstruction. This is mainly caused by the limited bandwith of the transducer which measures the photoacoustic signals, and manifests itself mostly in the low frequency content, i.e., the parts of the object with uniform absorption. We proposed a computationaly efficient preconditioner which can be implemented with FFT operations. The required number of iterations for finding a solution is enormously decreased when using this preconditioner.

How can we efficiently use an estimated speed of sound map to correct for blurring effects caused by the false assumption of an inhomogeneous speed of sound distribution?

Once a speed of sound map is available, as is the case in our PER-PAT setup with the techniques from chapter 4, it is possible to design a reconstruction algorithm that corrects for the blurring effects that would otherwise occur. We have proposed an algorithm that uses the Fast Marching Method (FMM) to calculate time of flight maps for each projection. The FMM implicitly takes ray refraction effects into account and is a very fast method to calculate time of flight maps. The calculated time of flight values are then used in the forward photoacoustic measurement model, and the resulting inverse problem can be solved with either an iterative method or the filtered back projection method. With experimental evaluation we have shown that the proposed approach works very well in practice.

Is unwanted motion a big problem in optical absorption reconstruction and is there an effective way to correct for this motion in the reconstruction?

In our first version of the photoacoustic measurement setup, we had some problems with motion of the phantom during the measurement acquisition process. This lead to blurred optical absorption reconstructions. A simple algorithm, based on tracking landmarks attached to the object was proposed, and was capable of completely reducing the motion artifacts in the reconstruction. In later versions of the PER-PAT measurement setup, we did not encounter motion artifacts anymore, so once a stable setup has been designed, motion of the phantom it is not an issue in optical absorption reconstruction anymore.

6.2 Recommendations

Estimation of ultrasound parameters To improve the robustness of our ultrasound parameter estimators, multipath effects have to be taken into account. When multipath propagation occurs, interference of the signals from the different paths can occur which results in a measured signal which can not be predicted with the currently used model. It could be possible to realize a model that sums the contributions of different time delays and attenuations, each corresponding to propagation over a single path. This is however difficult when the time delay differences become very small. Perhaps extra information, available from the speed of sound reconstruction, can be used in the ultrasound parameter estimation in an iterative manner. This requires the use of a multipath propagation model, instead of the fastest arrival time model that is being used now to trace rays through the speed of sound map.

Optical absorption reconstruction In our imaging setup we use side illumination of the object. The laser is rotated, together with the sensor array, around the object. This results in a different illumination direction for every projection, and thus a different light absorption profile for each projection. We currently assume in our model that the absorption profile, which is the unknown parameter of interest, is constant for all projections. A possible improvement could be made by using an iterative approach to model the light attenuation as a function of the absorbing structures for each projection individually. Thus instead of reconstructing the absorbed optical energy profile, we can try to reconstruct the optical absorbtion properties of the object and predict the absorbed optical energy profile with the knowledge of the direction of illumination of the light.

A

Green's function of the wave equation

We are looking here for solutions to the wave equation:

$$\nabla^2 p - \frac{1}{c^2}\frac{\partial^2 p}{\partial t^2} = S(\mathbf{r}, t) \tag{A.1}$$

where $S(\mathbf{r}, t)$ is a source term, c is the propagation speed in the medium and $p(\mathbf{r}, t)$ is the pressure function. This wave equation is a linear inhomogeneous partial differential equation. A solution to this equation can be found by determining the Green's function (impulse response) and convolve this with the excitation of the differential equation. The Green's function is determined by exciting the system with an impulsive source according to

$$\nabla^2 G(\boldsymbol{r}, t) - \frac{1}{c^2}\frac{\partial^2}{\partial t^2} G(\boldsymbol{r}, t) = \delta(\boldsymbol{r})\delta(t) \tag{A.2}$$

where $G(\boldsymbol{r}, t)$ is the Green's function we are interested in. An expression for the Green's function for our system can be derived by considering the boundary conditions of our problem which are given by

$$G(\boldsymbol{r}, t) = \begin{cases} 0 & \text{if } t < 0 \\ 0 & \text{if } t \to \infty \\ 0 & \text{if } |\boldsymbol{r}| \to \infty \end{cases} \tag{A.3}$$

Consequently we can Fourier transform the spatial domain and Laplace transform the time domain part of (A.2). We define the following Fourier transform

$$G(\boldsymbol{k}, t) = \mathcal{F}\{G(\boldsymbol{r}, t)\} = \int_{-\infty}^{\infty}\int_{-\infty}^{\infty}\int_{-\infty}^{\infty} G(\boldsymbol{r}, t) e^{-j\boldsymbol{k}\cdot\boldsymbol{r}} \mathrm{d}\boldsymbol{r} \tag{A.4}$$

and the following Laplace transform

$$G(\boldsymbol{k},s) = \mathcal{L}\big\{G(\boldsymbol{k},t)\big\} = \int_{0^-}^{\infty} G(\boldsymbol{k},t)e^{-st}\mathrm{d}t \tag{A.5}$$

By subsequently applying both transforms we obtain the transformed differential equation

$$-|\boldsymbol{k}|^2 G(\boldsymbol{k},s) - \frac{s^2}{c^2}G(\boldsymbol{k},s) = 1 \tag{A.6}$$

An algebraic solution to this equation can be found:

$$G(\boldsymbol{k},s) = \frac{-c^2}{|\boldsymbol{k}|^2c^2 + s^2} \tag{A.7}$$

and all we have to do is to inverse transform $G(\boldsymbol{k},s)$ back to the spatial and time domain.

The inverse Laplace transform is defined as

$$G(\boldsymbol{k},t) = \mathcal{L}^{-1}\big\{G(\boldsymbol{k},s)\big\} = \int_{0^-}^{\infty} G(\boldsymbol{k},s)e^{st}\mathrm{d}s \tag{A.8}$$

An expression for $G(\boldsymbol{k},t)$ can now be found by applying the inverse transform according to

$$\begin{aligned} G(\boldsymbol{k},t) =& \mathcal{L}^{-1}\left\{\frac{-c^2}{|\boldsymbol{k}|^2c^2+s^2}\right\} = \mathcal{L}^{-1}\left\{\frac{-c^2}{(s-j|\boldsymbol{k}|c)(s+j|\boldsymbol{k}|c)}\right\} = \\ =& \mathcal{L}^{-1}\left\{\frac{-c}{2j|\boldsymbol{k}|}\left(\frac{1}{(s-j|\boldsymbol{k}|c)} - \frac{1}{(s+j|\boldsymbol{k}|c)}\right)\right\} = \\ =& \mathcal{L}^{-1}\left\{\frac{-c}{2j|\boldsymbol{k}|}\left(e^{j|\boldsymbol{k}|ct} - e^{-j|\boldsymbol{k}|ct}\right)\right\} = \frac{-c}{|\boldsymbol{k}|}\sin(|\boldsymbol{k}|ct)\mathrm{u}(t) \end{aligned} \tag{A.9}$$

The inverse Fourier transform is defined as

$$G(\boldsymbol{r},t) = \mathcal{F}^{-1}\big\{G(\boldsymbol{k},t)\big\} = \frac{1}{(2\pi)^3}\int_{-\infty}^{\infty}\int_{-\infty}^{\infty}\int_{-\infty}^{\infty} G(\boldsymbol{k},t)e^{j\boldsymbol{k}\cdot\boldsymbol{r}}\mathrm{d}\boldsymbol{k} \tag{A.10}$$

When we look at $G(\boldsymbol{k},t)$ as derived in (A.9), we see that the function is rotationally invariant for $\boldsymbol{k}$, so that it is more convenient to go over to spherical coordinates. The spherical coordinates are related to the cartesian ones by

$$\boldsymbol{r}_s = [r\sin(\theta)\cos(\phi), r\sin(\theta)\sin(\phi), r\cos(\theta)]^T \tag{A.11}$$

and

$$\boldsymbol{k}_s = [k\sin(k_\theta)\cos(k_\phi), k\sin(k_\theta)\sin(k_\phi), k\cos(k_\theta)]^T \tag{A.12}$$

Because of our rotationally invariant $G(\boldsymbol{k}, t)$, we can align our spherical coordinate system in the direction of $\boldsymbol{r}$ by choosing $\theta = 0$, so that $\boldsymbol{r}_s$ reduces to $\boldsymbol{r}_s = [0, 0, r]^T$. Writing the inverse Fourier transform in spherical coordinates now leads to the following expression

$$\begin{aligned}
G(\boldsymbol{r}_s, t) =& \frac{1}{(2\pi)^3} \int_0^{2\pi}\int_0^{\pi}\int_0^{\infty} G(\boldsymbol{k}_s, t) k^2 \sin(k_\theta) e^{j\boldsymbol{k}_s \cdot \boldsymbol{r}_s} \mathrm{d}k \mathrm{d}k_\theta \mathrm{d}k_\phi = \\
=& \frac{1}{(2\pi)^3} \int_0^{2\pi}\int_0^{\pi}\int_0^{\infty} -c \sin(kct) \mathrm{u}(t) k \sin(k_\theta) e^{jkr\cos(k_\theta)} \mathrm{d}k \mathrm{d}k_\theta \mathrm{d}k_\phi = \\
=& \frac{-c\mathrm{u}(t)}{(2\pi)^2} \int_0^{\infty} \sin(kct) k \int_0^{\pi} \sin(k_\theta) e^{jkr\cos(k_\theta)} \mathrm{d}k_\theta \mathrm{d}k = \\
=& \frac{-c\mathrm{u}(t)}{(2\pi)^2} \int_0^{\infty} \sin(kct) k \frac{e^{jkr} - e^{-jkr}}{jkr} \mathrm{d}k = \\
=& \frac{-c\mathrm{u}(t)}{(2\pi)^2 jr} \int_{-\infty}^{\infty} \sin(kct) e^{jkr} \mathrm{d}k = \frac{-c\mathrm{u}(t)}{(2\pi)^2 jr} \frac{\pi}{j} \left(\delta(r + ct) - \delta(r - ct)\right) = \\
=& \frac{-c}{4\pi r} \delta(r - ct) = \frac{-1}{4\pi r} \delta\left(\frac{r}{c} - t\right) \qquad \text{(A.13)}
\end{aligned}$$

And finally written in cartesian coordinates this gives

$$G(\boldsymbol{r}, t) = \frac{-1}{4\pi|\boldsymbol{r}|} \delta\left(\frac{1}{c}|\boldsymbol{r}| - t\right) \qquad \text{(A.14)}$$

B

Definite Gaussian integrals of trigonometric functions

The results of this appendix are used in chapter 3, section 3.3 on the time of flight analysis. We will show here how Gaussian integrals of the form:

$$\int_{-\infty}^{\infty} f(x)e^{-a^2x^2}\mathrm{d}x \tag{B.1}$$

can be calculated. Where $f(x)$ is a trigonometric function. Hereby we will make use of the known integral relation:

$$\int_{-\infty}^{\infty} x^n e^{-a^2x^2}\mathrm{d}x = \begin{cases} 0 & \text{if } n \text{ is odd} \\ \dfrac{\sqrt{\pi}}{a}\dfrac{n!}{2^n\left(\frac{n}{2}\right)!}\left(\dfrac{1}{a}\right)^n & \text{if } n \text{ is even} \end{cases} \tag{B.2}$$

Furthermore we will make use of the Taylor series expansions given in Table B.1 and the double angle formulas in Table B.2.

We will now illustrate how the definite integral

$$\int_{-\infty}^{\infty} \cos^2(x)e^{-a^2x^2}\mathrm{d}x \tag{B.3}$$

can be calculated. We first apply the necessary double angle formula:

$$\int_{-\infty}^{\infty} \cos^2(x)e^{-a^2x^2}\mathrm{d}x = \frac{1}{2}\int_{-\infty}^{\infty}\left[1+\cos(2x)\right]e^{-a^2x^2}\mathrm{d}x \tag{B.4}$$

Function	Taylor series expansion
$\cos(x)$	$\sum_{n=0}^{\infty} \frac{(-1)^n}{(2n)!} x^{2n}$
$\sin(x)$	$\sum_{n=0}^{\infty} \frac{(-1)^n}{(2n+1)!} x^{2n+1}$
e^{-x^2}	$\sum_{n=0}^{\infty} \frac{(-1)^n}{n!} x^{2n}$

Table B.1 Taylor series expansions of useful functions

Function	Double angle formula
$\cos^2(x)$	$\frac{1}{2} + \frac{1}{2}\cos(2x)$
$\sin^2(x)$	$\frac{1}{2} - \frac{1}{2}\cos(2x)$
$\cos(x)\sin(x)$	$\frac{1}{2}\sin(2x)$

Table B.2 Double angle formulas

Next we fill in the Taylor series expansion of the remaining cosine function:

$$\int_{-\infty}^{\infty} \cos^2(x) e^{-a^2x^2} \mathrm{d}x = \frac{1}{2} \int_{-\infty}^{\infty} \left[1 + \sum_{n=0}^{\infty} \frac{(-1)^n 2^{2n}}{(2n)!} x^{2n} \right] e^{-a^2x^2} \mathrm{d}x \tag{B.5}$$

Then we rewrite the expression in terms of known integral relations:

$$\int_{-\infty}^{\infty} \cos^2(x) e^{-a^2x^2} \mathrm{d}x = \frac{1}{2} \int_{-\infty}^{\infty} e^{-a^2x^2} \mathrm{d}x + \sum_{n=0}^{\infty} \frac{(-1)^n 2^{2n}}{(2n)!} \int_{-\infty}^{\infty} x^{2n} e^{-a^2x^2} \mathrm{d}x \tag{B.6}$$

After substitution of the known integral relations in the obtained expression we get:

$$\int_{-\infty}^{\infty} \cos^2(x) e^{-a^2x^2} \mathrm{d}x = \frac{1}{2} \frac{\sqrt{\pi}}{a} \left[1 + \sum_{n=0}^{\infty} \frac{(-1)^n}{n!} \left(\frac{1}{a} \right)^{2n} \right] \tag{B.7}$$

Here we recognize the Taylor series expansion of the e^{-x^2} function so that the final expression will be:

$$\int_{-\infty}^{\infty} \cos^2(x) e^{-a^2x^2} \mathrm{d}x = \frac{1}{2} \frac{\sqrt{\pi}}{a} \left[1 + e^{-\frac{1}{a^2}} \right] \tag{B.8}$$

Similar operations can be applied to other combinations of trigonometric functions and the resulting integral relations are given in Table B.3.

Integral expression	Result
$\int_{-\infty}^{\infty} \cos^2(x) e^{-a^2x^2} \mathrm{d}x$	$\frac{1}{2}\frac{\sqrt{\pi}}{a}\left[1+e^{-\frac{1}{a^2}}\right]$
$\int_{-\infty}^{\infty} \sin^2(x) e^{-a^2x^2} \mathrm{d}x$	$\frac{1}{2}\frac{\sqrt{\pi}}{a}\left[1-e^{-\frac{1}{a^2}}\right]$
$\int_{-\infty}^{\infty} x\cos(x)\sin(x) e^{-a^2x^2} \mathrm{d}x$	$\frac{1}{2}\frac{\sqrt{\pi}}{a^3}e^{-\frac{1}{a^2}}$
$\int_{-\infty}^{\infty} x^2\sin^2(x) e^{-a^2x^2} \mathrm{d}x$	$\frac{1}{2}\frac{\sqrt{\pi}}{a^3}\left[\frac{1}{2}-\left(\frac{1}{2}-\frac{1}{a^2}\right)e^{-\frac{1}{a^2}}\right]$

Table B.3 Integral relations of trigonometric Gaussian integrals

C

Circular symmetry

Theorem Consider a circle with radius r, centered at the origin, and a point $\mathbf{p}_1$ inside the circle at a distance d_1 from the center and a point $\mathbf{p}_2$ outside the circle at distance d_2 from the center. Then when:

- both points $\mathbf{p}_1$ and $\mathbf{p}_2$ lie on the same line passing through the origin of the circle

- the distances d_1 and d_2 are related via $d_1 d_2 = r^2$

we have that for any point $\mathbf{p}_c$ on the circle the ratio between the distance from $\mathbf{p}_1$ to that point and the distance from $\mathbf{p}_2$ to that point is constant and equal to:

$$\frac{\|\mathbf{p}_1 - \mathbf{p}_c\|}{\|\mathbf{p}_2 - \mathbf{p}_c\|} = \frac{r}{d_2} \tag{C.1}$$

Proof With $\mathbf{p}_1 = d_1\mathbf{u}$, $\mathbf{p}_2 = d_2\mathbf{u}$ and $\mathbf{p}_c = r\mathbf{v}$ where $\mathbf{u}$ and $\mathbf{v}$ are arbitrary unit vectors we get for the ratio of distances:

$$\frac{\|\mathbf{p}_1 - \mathbf{p}_c\|}{\|\mathbf{p}_2 - \mathbf{p}_c\|} = \frac{\|d_1\mathbf{u} - r\mathbf{v}\|}{\|d_2\mathbf{u} - r\mathbf{v}\|} = \frac{\sqrt{d_1^2 + r^2 - 2d_1 r\mathbf{u}^T\mathbf{v}}}{\sqrt{d_2^2 + r^2 - 2d_2 r\mathbf{u}^T\mathbf{v}}} \tag{C.2}$$

which after substitution of $d_1 = \frac{r^2}{d_2}$ and keeping in mind that $r > 0$ and $d_2 > 0$ results in:

$$\begin{aligned}
\frac{\|\mathbf{p}_1 - \mathbf{p}_c\|}{\|\mathbf{p}_2 - \mathbf{p}_c\|} &= \frac{\sqrt{\left(\frac{r^2}{d_2}\right)^2 + r^2 - 2\frac{r^2}{d_2} r \mathbf{u}^T \mathbf{v}}}{\sqrt{d_2^2 + r^2 - 2 d_2 r \mathbf{u}^T \mathbf{v}}} && \text{(C.3)} \\
&= \frac{r\sqrt{\left(\frac{r}{d_2}\right)^2 + 1 - 2\frac{1}{d_2} r \mathbf{u}^T \mathbf{v}}}{\sqrt{d_2^2 + r^2 - 2 d_2 r \mathbf{u}^T \mathbf{v}}} && \text{(C.4)} \\
&= \frac{r\sqrt{r^2 + d_2^2 - 2 d_2 r \mathbf{u}^T \mathbf{v}}}{d_2\sqrt{d_2^2 + r^2 - 2 d_2 r \mathbf{u}^T \mathbf{v}}} && \text{(C.5)} \\
&= \frac{r}{d_2} && \text{(C.6)}
\end{aligned}$$

D

Accuracy of Monte Carlo simulations

An estimate of the mean of a random variable can be obtained by averaging over a large number (N) of independently drawn samples x_i from the random process:

$$\hat{\mu}_x = \frac{1}{N} \sum_{i=1}^{N} x_i \tag{D.1}$$

Associated with this estimate of the mean are an expected mean and expected variance of the estimate. The expected mean is given by:

$$E[\hat{\mu}_x] = E\left[\frac{1}{N} \sum_{i=1}^{N} x_i\right] = \frac{1}{N} \sum_{i=1}^{N} E[x_i] = \mu_x \tag{D.2}$$

and the expected variance is given by:

$$\begin{aligned}
\mathrm{Var}[\hat{\mu}_x] &= \mathrm{E}\left[(\hat{\mu}_x - \mu_x)^2\right] && \text{(D.3)} \\
&= \mathrm{E}\left[\left(\frac{1}{N} \sum_{i=1}^{N} x_i - \mu_x\right)^2\right] && \text{(D.4)} \\
&= \mathrm{E}\left[\left(\frac{1}{N} \sum_{i=1}^{N} x_i\right)^2\right] - \mu_x^2 && \text{(D.5)} \\
&= \frac{1}{N^2}\left(N\sigma_x^2 + N^2\mu_x^2\right) - \mu_x^2 = \frac{\sigma_x^2}{N} && \text{(D.6)}
\end{aligned}$$

According to the central limit theorem, which states that averaging over a sufficiently large number of independent random variables each with finite mean and variance will be Gaussian distributed, with the estimated value $\hat{\mu}_x$ will be Gaussian distributed:

$$\hat{\mu}_x \sim \mathcal{N}\left(\mu_x, \frac{\sigma_x^2}{N}\right) \tag{D.7}$$

where μ_x is the mean of the random variable and σ_x^2 is the variance of the random variable. This estimator gives us an unbiased estimate of the mean. The uncertainty of the estimate can be expressed by its variance of $\frac{\sigma_x^2}{N}$.

An estimate of the variance of a random variable can be obtained with the sample variance estimator:

$$\hat{\sigma}_x^2 = \frac{1}{N-1}\sum_{i=1}^{N}(x_i - \hat{\mu}_x)^2 \tag{D.8}$$

This is an unbiased estimator of the variance σ_x^2 of the random variable. To see that the estimated is unbiased, we take the expectation over the sum of squares and make use of the fact that the samples x_i are uncorrelated. This gives us:

$$\begin{aligned}
\mathrm{E}\left[\sum_{i=1}^{N}(x_i - \hat{\mu}_x)^2\right] &= \mathrm{E}\left[\sum_{i=1}^{N}\left(x_i - \frac{1}{N}\sum_{j=1}^{N}x_j\right)^2\right] && \text{(D.9)}\\
&= \mathrm{E}\left[\sum_{i=1}^{N}x_i^2 - \frac{1}{N}\left(\sum_{i=1}^{N}x_i\right)^2\right] && \text{(D.10)}\\
&= (N-1)\sigma_x^2 && \text{(D.11)}
\end{aligned}$$

From which we can conclude that the estimater is indeed unbiased and converges to true variance σ_x^2.

Furthermore, it is interesting to investigate the uncertainty associated with the estimate. To find this out we look at the sum of squared differences used in the estimator. This sum of N squared differences can be equivalently be written as a sum of $N-1$ squares of a transformed random variable with zero mean and the same variance. To see this, we start with the expression:

$$\begin{aligned}
\sum_{i=1}^{N}(x_i - \hat{\mu}_x)^2 &= \sum_{i=1}^{N}x_i^2 - \frac{1}{N}\left(\sum_{i=1}^{N}x_i\right)^2 && \text{(D.12)}\\
&= \mathbf{x}^T\left(\mathbf{I}_N - \frac{1}{N}\right)\mathbf{x} && \text{(D.13)}
\end{aligned}$$

This expression contains the $N-1$ rank matrix $\mathbf{I}_N - \frac{1}{N}$ which can be decomposed using eigenvector decomposition into:

$$\mathbf{I}_N - \frac{1}{N} = \mathbf{V}\begin{bmatrix}\mathbf{I}_{N-1} & \mathbf{0}\\ \mathbf{0} & 0\end{bmatrix}\mathbf{V}^T = \tilde{\mathbf{V}}\tilde{\mathbf{V}}^T \tag{D.14}$$

The $N-1$ rank matrix contains $N-1$ unit eigenvalues and one zero eigenvalue. An $N \times (N-1)$ submatrix $\tilde{\mathbf{V}}$ can be constructed from the matrix containing the eigenvectors $\mathbf{V}$ by removing the column corresponding to the zero eigenvalue. If we apply the transformation $\mathbf{y} = \tilde{\mathbf{V}}\mathbf{x}$ we obtain the transformed random vector $\mathbf{y}$ containing $N-1$ uncorrelated random variables with zero mean and variance σ_x^2. The sum of N squared differences can thus be written as a sum of $N-1$ squares:

$$\sum_{i=1}^{N}(x_i - \hat{\mu}_x)^2 = \mathbf{y}^T\mathbf{y} = \sum_{i=1}^{N-1} y_i^2 \tag{D.15}$$

If the random variables x_i are Gaussian distributed, then the sum of squared differences would be $\sigma_x^2\chi_{N-1}^2$-distributed. On the other hand, for a large number of samples, even in the case of non Gaussian distributed x_i, the sum of squared differences would be approximately Gaussian distributed as $\mathcal{N}\left((N-1)\sigma_x^2, 2(N-1)\sigma_x^4\right)$. Using these results in the expression of the estimator we find the following distributions of the sample variance estimator:

$$\hat{\sigma}_x^2 \sim \frac{\sigma_x^2}{N-1}\chi_{N-1}^2 \qquad \text{if } x_i \text{ is Gaussian distributed} \tag{D.16}$$

$$\hat{\sigma}_x^2 \sim \mathcal{N}\left(\sigma_x^2, \frac{2}{N-1}\sigma_x^4\right) \qquad \text{for large } N \tag{D.17}$$

so that for both cases, the variance of the sample variance estimator is given by:

$$\mathrm{Var}\left[\hat{\sigma}_x^2\right] = \frac{2}{N-1}\sigma_x^4 \tag{D.18}$$

From this we can also obtain an estimate of the variance of the sample standard deviation estimator. We do this by linearizing the relation between standard deviation and variance, $\sigma = \sqrt{\sigma^2}$ around the true value of the variance, σ_x^2, resulting in a multiplication of the original variance by $\left(\frac{1}{2\sqrt{\sigma_x^2}}\right)^2$. The expression for the variance of the sample standard deviation estimator is then given by:

$$\mathrm{Var}\left[\hat{\sigma}_x\right] \approx \left(\frac{1}{2\sigma_x}\right)^2 \mathrm{Var}\left[\hat{\sigma}_x^2\right] = \frac{1}{2(N-1)}\sigma_x^2 \tag{D.19}$$

E

Integral transforms

E.1 Radon transform

The Radon transform is a projection over lines of an input image $f(x, y)$ to a projection image (or sinogram) $g(r, \varphi)$ and is defined as:

$$g(r, \varphi) = \mathcal{R}\big\{f(x, y)\big\} = \int\limits_{-\infty}^{\infty}\int\limits_{-\infty}^{\infty} f(x, y)\delta(x\cos\varphi + y\sin\varphi - r)\mathrm{d}x\mathrm{d}y \tag{E.1}$$

The transposed Radon transform is a backprojection of the sinogram $g(r, \varphi)$ back to the image domain:

$$f_{\mathrm{bp}}(x, y) = \mathcal{R}^T\big\{g(r, \varphi)\big\} = \int\limits_{0}^{2\pi}\int\limits_{-\infty}^{\infty} g(r, \varphi)\delta(x\cos\varphi + y\sin\varphi - r)\mathrm{d}r\mathrm{d}\varphi \tag{E.2}$$

Applying the forward/backward transform to an impulsive source, i.e., $f(x, y) = \delta(x)\delta(y)$, gives us the point spread function of backprojection:

$$f_\delta(x, y) = \mathcal{R}^T\mathcal{R}\big\{\delta(x)\delta(y)\big\} = \int\limits_{0}^{2\pi} \delta\big(x\cos\varphi + y\sin\varphi\big)\mathrm{d}\varphi = \frac{2}{\sqrt{x^2 + y^2}} \tag{E.3}$$

E.2 Fourier transform

The Fourier Transform of a one dimensional signal $f(t)$ is defined as:

$$F(\omega) = \mathcal{F}\big\{f(t)\big\} = \int_{-\infty}^{\infty} f(t)e^{-j\omega t}\mathrm{d}t \tag{E.4}$$

and the inverse Fourier transform as:

$$f(t) = \mathcal{F}^{-1}\big\{F(\omega)\big\} = \frac{1}{2\pi}\int_{-\infty}^{\infty} F(\omega)e^{j\omega t}\mathrm{d}\omega \tag{E.5}$$

E.3 Zeroth-order Hankel transform

The zeroth-order Hankel Transform of a one dimensional signal $f(t)$ is defined as:

$$F(k) = \mathcal{H}_0\big\{f(t)\big\} = \int_{0}^{\infty} f(t)tJ_0(kt)\mathrm{d}t \tag{E.6}$$

and the inverse zeroth-order Hankel transform as:

$$f(t) = \mathcal{H}_0^{-1}\big\{F(k)\big\} = \int_{0}^{\infty} F(k)kJ_0(kt)\mathrm{d}k \tag{E.7}$$

where $J_0(t)$ is the zeroth-order Bessel function of the first kind:

$$J_0(t) = \frac{1}{2\pi}\int\limits_{-\pi}^{\pi} e^{jt\sin(\varphi)}\mathrm{d}\varphi \tag{E.8}$$

E.4 Abel transform

The Abel transform can be interpreted as the projection of a 2D radial symmetric function $h(\mathbf{r})$ onto a line. A 2D radially symmetric function is fully described by its radial profile according to $h_r(r) = h(\|\mathbf{r}\|)$. The projection of the radial symmetric function onto a line is then given by:

$$h_t(t) = \int\limits_{-\infty}^{\infty} h_r(\sqrt{t^2+y^2})\mathrm{d}y \tag{E.9}$$

where t parametrizes the position along the line onto which the projection is performed. Due to symmetry we can write:

$$h_t(t) = 2\int\limits_{0}^{\infty} h_r(\sqrt{t^2+y^2})\mathrm{d}y \tag{E.10}$$

The resulting projection $h_t(t)$ is even, i.e. $h(-t) = h(t)$. If we apply a coordinate transformation of $r = \sqrt{t^2 + y^2}$, then for $t > 0$ we obtain the Abel Transform:

$$h_t(t) = \mathcal{A}\{h_r(r)\} = 2\int_t^\infty \frac{h_r(r)r}{\sqrt{r^2 - t^2}}\mathrm{d}r \tag{E.11}$$

The Abel transform, the Zeroth-order Hankel transform and the Fourier transform are related to each other through the following relationship:

$$\mathcal{F}\mathcal{A} = 2\pi\mathcal{H}_0 \tag{E.12}$$

To see why this is true, we rewrite expression (E.9) for the zeroth-order Hankel Transform in polar coordinates:

$$\begin{aligned} h_t(t) &= \int_{-\infty}^{\infty} h_r(\sqrt{t^2 + y^2})\mathrm{d}y = \int_{-\infty}^{\infty}\int_{-\infty}^{\infty} h_r(\sqrt{x^2 + y^2})\delta(x - t)\mathrm{d}x\mathrm{d}y && \text{(E.13)} \\ &= \int_0^{\infty}\int_0^{2\pi} h_r(r)r\delta(r\cos(\varphi) - t)\mathrm{d}\varphi\mathrm{d}r && \text{(E.14)} \end{aligned}$$

Applying the Fourier transform and substituting the expression of the Abel Transform (E.14) then gives:

$$\begin{aligned} H_\omega(\omega) &= \int_{-\infty}^{\infty} h_t(t)e^{-j\omega t}\mathrm{d}t && \text{(E.15)} \\ &= \int_{-\infty}^{\infty}\int_0^{\infty}\int_0^{2\pi} h_r(r)r\delta(r\cos(\varphi) - t)\mathrm{d}\varphi\mathrm{d}re^{-j\omega t}\mathrm{d}t && \text{(E.16)} \\ &= \int_0^{\infty} h_r(r)r\int_0^{2\pi} e^{-j\omega r\cos(\varphi)}\mathrm{d}\varphi\mathrm{d}r && \text{(E.17)} \\ &= 2\pi\int_0^{\infty} h_r(r)rJ_0(\omega r)\mathrm{d}r && \text{(E.18)} \end{aligned}$$

which equals 2π times the zeroth-order Hankel Transform. The relationship can also be written as:

$$\mathcal{A} = 2\pi\mathcal{F}^{-1}\mathcal{H}_0 = \mathcal{F}\mathcal{H}_0 \tag{E.19}$$

E.5 Fourier slice theorem

$$G(\omega,\varphi) = \int\limits_{-\infty}^{\infty} g(r,\varphi)e^{-j\omega r}\mathrm{d}r \tag{E.20}$$

$$= \int\limits_{-\infty}^{\infty}\int\limits_{-\infty}^{\infty}\int\limits_{-\infty}^{\infty} f(x,y)\delta(x\cos\varphi + y\sin\varphi - r)e^{-j\omega r}\mathrm{d}x\mathrm{d}y\mathrm{d}r \tag{E.21}$$

$$= \int\limits_{-\infty}^{\infty}\int\limits_{-\infty}^{\infty} f(x,y)e^{-j\omega(x\cos\varphi + y\sin\varphi)}\mathrm{d}x\mathrm{d}y \tag{E.22}$$

$$= F(\omega\cos\varphi, \omega\sin\varphi) \tag{E.23}$$

Publications

Peer reviewed

- Manohar, Srirang and Willemink, Rene G.H. and van der Heijden, Ferdi and Slump, Cornelis. H.and van Leeuwen, Ton G. (2007) "Concomitant speed-of-sound tomography in photoacoustic imaging" In: *Applied Physics Letters*, Vol. 91

Peer reviewed under review, in preparation

- Willemink, Rene G.H. et al, "Calibration of a photoacoustic CT imager", IEEE Transactions on Medical Imaging
- Willemink, Rene G.H. and Manohar, Srirang et al, "Estimation of integrated ultrasound transmission parameters I: Speed of Sound", Physics in Medicine and Biology
- Willemink, Rene G.H. and Manohar, Srirang et al, "Estimation of integrated ultrasound transmission parameters II: Acoustic attenuation", Physics in Medicine and Biology
- Jose, Jithin and Willemink, Rene G.H. et al, "Passive element enriched photoacoustic computed tomography (PER-PACT) for hybrid imaging", Optics Express
- Resink, Steffen and Jose, Jithin and Willemink, Rene G.H. et al, "Multiple passive element enriched photoacoustic computed tomography (multi PER-PACT)", Journal of Biomedical Optics
- Willemink, Rene G.H. et al, "A fast iterative reconstruction method using preconditioning for photacoustic computed tomography", IEEE Transactions on Medical Imaging

Conference proceedings

- Willemink, Rene G.H.and Slump, C.H. and van der Heijden, F. (2006) "On image quality enhancement in photoacoustic image reconstruction by motion compensation.", In: *Proceedings of ProRISC the 17th Annual Workshop on Circuits, Systems and Signal Processing*, 23-24 Nov 2006, Veldhoven, The Netherlands

- Manohar, Srirang and Willemink, Rene G.H. and van Leeuwen, Ton G. (2007) "Speed-of-sound imaging in a photoacoustic imager." In: *Photons Plus Ultrasound: Imaging and Sensing 2007: The Eighth Conference on Biomedical Thermoacoustics, Optoacoustics, and Acousto-optics*, San Jose, United States
- Willemink, Rene G.H.and Manohar, Srirang and Slump, C.H. and van der Heijden, F. and van Leeuwen, Ton G. (2007) "Acoustic property measurements in a photoacoustic imager." In: *Proceedings of SPIE – Volume 6631, Novel Optical Instrumentation for Biomedical Applications III*, Munich, Germany
- Willemink, Rene G.H. and Manohar, Srirang and Purwar, Yashasvi and Slump, C.H. and van der Heijden, F. and van Leeuwen, Ton G. (2008) "Imaging of acoustic attenuation and speed of sound maps using photoacoustic measurements" In: *Proceedings of SPIE – Volume 6920, Medical Imaging 2008: Ultrasonic Imaging and Signal Processing*, San Diego, United States
- Manohar, Srirang and Willemink, Rene G.H. and J.C.G. van Hespen and Ton G. van Leeuwen (2008) "Hybrid photoacoustic - ultrasound transmission parameter imaging in a miniature photoacoustic imager." In: *Acoustics '08 Conference*, Paris, France
- Willemink, Rene G.H. and Manohar, Srirang and Slump, C.H. and van der Heijden, F. and van Leeuwen, Ton G. (2008) "A maximum likelihood method for obtaining integrated attenuation from ultrasound transmission mode measurements" In: *Acoustics '08 Conference*, Paris, France
- Willemink, Rene G.H. and Manohar, Srirang and Jose, Jithin and Slump, C.H. and van der Heijden, F. and van Leeuwen, Ton. G. (2009) "Simultaneous imaging of ultrasound attenuation, speed of sound, and optical absorption in a photoacoustic setup" In: *Proceedings of SPIE – Volume 7265, Medical Imaging 2009: Ultrasonic Imaging and Signal Processing*, Orlando, United States
- Willemink, Rene G.H. and Manohar, Srirang and Slump, C.H. and van Leeuwen, Ton. G. (2009) "Photoacoustic image reconstruction with a measurement model including the transducer impulse response" In: *Proceedings of the IEEE-EMBS Benelux Chapter 2009*, Enschede, The Netherlands

Bibliography

[1] L. V. Wang and H. I. Wu, *Biomedical Optics: principles and imaging.* Wiley-Interscience, 2007.

[2] A. Kharin, *Towards Photacoustic Mamography.* PhD thesis, University of Twente, 2005.

[3] C. Hoelen, *3-D Photoacoustic Tissue Imaging.* PhD thesis, University of Twente, 1998.

[4] M. W. Sigrist and F. K. Kneubhl, “Laser-generated stress waves in liquids,” *J. Acoust. Soc. Am.*, vol. 64, pp. 1652–1663, 1978.

[5] G. Paltauf and P. E. Dyer, “Photomechanical processes and effects in ablation,” *Chem. Rev.*, vol. 103, pp. 487–518, 2003.

[6] R. A. Kruger, P. Liu, Y. R. Fang, and C. R. Appledorn, “Photoacoustic ultrasound (PAUS)–reconstruction tomography,” *Med. Phys.*, vol. 22, no. 10, pp. 1605–1609, 1995.

[7] P. J. L. Rivière, “Image reconstruction in optoacoustic tomography for dispersive acoustic media,” *Opt. Lett.*, vol. 31, no. 6, pp. 781–783, 2006.

[8] Y. Xu, D. Feng, and L. V. Wang, “Exact frequency-domain reconstruction for thermoacoustic tomography–i: Planar geometry.,” *IEEE Trans Med Imaging*, vol. 7, no. 21, pp. 823–8, 2002.

[9] G. Paltauf, J. A. Viator, S. A. Prahl, and S. L. Jacques, “Iterative reconstruction algorithm for optoacoustic imaging,” *J. Acoust. Soc. Am.*, vol. 112, no. 4, pp. 1536–1544, 2002.

[10] R. I. Siphanto, K. K. Thumma, R. G. M. Kolkman, T. G. van Leeuwen, F. F. M. de Mul, J. W. van Neck, L. N. A. van Adrichem, and W. Steenbergen, “Serial noninvasive photoacoustic imaging of neovascularization in tumor angiogenesis,” *Opt. Express*, vol. 13, no. 1, pp. 89–95, 2005.

[11] D. Razansky, M. Distel, C. Vinegoni, R. Ma, N. Perrimon, R. W. Köster, and V. Ntziachristos, “Multispectral opto-acoustic tomography of deep-seated fluorescent proteins in vivo,” *Nature Photonics*, vol. 3, pp. 412 – 417, 2009.

[12] C. G. A. Hoelen, F. F. M. de Mul, R. Pongers, and A. Dekker, “Three-dimensional photoacoustic imaging of blood vessels in tissue,” *Opt. Lett.*, vol. 23, no. 8, pp. 648–650, 1998.

[13] K. P. Köstli and P. C. Beard, “Two-dimensional photoacoustic imaging by use of fourier-transform image reconstruction and a detector with an anisotropic response,” *Appl. Opt.*, vol. 42, no. 10, pp. 1899–1908, 2003.

[14] R. G. M. Kolkman, P. J. Brands, W. Steenbergen, and T. G. van Leeuwen, “Real-time in vivo photoacoustic and ultrasound imaging,” *Journal of Biomedical Optics*, vol. 13, no. 5, p. 050510, 2008.

[15] R. J. Zemp, R. Bitton, M.-L. Li, K. K. Shung, G. Stoica, and L. V. Wang, “Photoacoustic imaging of the microvasculature with a high-frequency ultrasound array transducer,” *Journal of Biomedical Optics*, vol. 12, no. 1, p. 010501, 2007.

[16] J. J. Niederhauser, M. Jaeger, R. Lemor, P. Weber, and M. Frenz, “Combined ultrasound and optoacoustic system for real-time high-contrast vascular imaging in vivo,” *IEEE Trans Med Imaging*, vol. 24, p. 436440, 2005.

[17] Y. Zeng, D. Xing, Y. Wang, B. Yin, and Q. Chen, “Photoacoustic and ultrasonic coimage with a linear transducer array,” *Opt. Lett.*, vol. 29, no. 15, pp. 1760–1762, 2004.

[18] S. Manohar, A. Kharine, J. C. G. Van Hespen, W. Steenbergen, and T. G. Van Leeuwen, “Photoacoustic mammography laboratory prototype: imaging of breast tissue phantoms,” *J. Biomed. Opt.*, vol. 9, no. 6, pp. 1172–1181, 2004.

[19] V. S, M. TJ, F. Y, W. IO, Z. X, D. L. Z. A, O. O, K. A, G. SS, J. R. Jr, and K.-Y. BT, “Three-dimensional photoacoustic imaging using a two-dimensional cmut array.,” *IEEE Trans Ultrason Ferroelectr Freq Control.*, vol. 56, pp. 2411–9, 2009.

[20] R. A. Kruger, D. R. Reinecke, and G. A. Kruger, “Thermoacoustic computed tomography – technical consideration,” *Med. Phys.*, vol. 26, pp. 1832 – 1837, 1999.

[21] X. Wang, Y. Pang, G. Ku, X. Xie, G. Stoica, and L.-H. Wang, “Noninvasive laser-induced photoacoustic tomography for structural and functional in vivo imaging of the brain,” *Nature Biotech*, vol. 21, p. 803, 2003.

[22] R. Ma, A. Taruttis, V. Ntziachristos, and D. Razansky, “Multispectral optoacoustic tomography (msot) scanner for whole-body small animal imaging,” *Opt. Express*, vol. 17, pp. 21414–21426, 2009.

[23] J. Gamelin, A. Aguirre, A. Maurudis, F. Huang, D. Castillo, L. V. Wang, and Q. Zhu, “Curved array photoacoustic tomographic system for small animal imaging,” *Journal of Biomedical Optics*, vol. 13, no. 2, p. 024007, 2008.

[24] S. Manohar, G. H. Willemink, F. Van der Heijden, C. H. Slump, and T. G. Van Leeuwen, “Concomitant speed-of-sound tomography in photoacoustic imaging,” *Appl. Phys. Lett.*, vol. 91, no. 13, p. 131911, 2007.

[25] J. Jose, T. Maalderink, G. H. Willemink, J. W. Van Neck, S. Manohar, and T. G. Van Leeuwen, “A Computed Tomography photoacoustic imager for imaging murine disease models,” *in prep.*

[26] V. Kozhushko, T. Khokhlova, A. Zharinov, I. Pelivanov, V. Solomatin, and A. Karabutov, “Focused array transducer for two-dimensional optoacoustic tomography,” *The Journal of the Acoustical Society of America*, vol. 116, no. 3, pp. 1498–1506, 2004.

[27] S. A. Ermilov, T. Khamapirad, A. Conjusteau, M. H. Leonard, R. Lacewell, K. Mehta, T. Miller, and A. A. Oraevsky, “Laser optoacoustic imaging system for detection of breast cancer,” *Journal of Biomedical Optics*, vol. 14, no. 2, p. 024007, 2009.

[28] G. Paltauf, R. Nuster, M. Haltmeier, and P. Burgholzer, “Photoacoustic tomography using a machzehnder interferometer as an acoustic line detector,” *Applied Optics*, vol. 46, pp. 3352 – 3358, 2007.

[29] M. Haltmeier, O. Scherzer, P. Burgholzer, and G. Paltauf, “Thermoacoustic computed tomography with large planar receivers,” *Inverse Problems*, vol. 20, pp. 1663 – 1673, 2004.

[30] P. Burgholzer, C. Hofer, G. Paltauf, M. Haltmeier, and O. Scherzer, “Thermoacoustic tomography with integrating area and line detectors,” *IEEE Transactions on Ultrasonics, Ferroelectrics and Frequency Control*, vol. 52, pp. 1577 – 1583, 2005.

[31] S. M. Kay, *Fundamentals of Statistical Signal Processing, Volume I: Estimation Theory.* Prentice Hall, 1993.

[32] M. A. Fischler and R. C. Bolles, “Random sample consensus: a paradigm for model fitting with applications to image analysis and automated cartography,” *Commun. ACM*, vol. 24, no. 6, pp. 381–395, 1981.

[33] P. Torr and A. Zisserman, “MLESAC: A new robust estimator with application to estimating image geometry,” *Computer Vision and Image Understanding*, vol. 78, no. 1, pp. 138–156, 2000.

[34] P. Torr, “Bayesian model estimation and selection for epipolar geometry and generic manifold fitting,” *International Journal of Computer Vision*, vol. 50, no. 1, pp. 35–61, 2002.

[35] R. Fletcher, *Practical methods of optimization.* John Wiley, 1987.

[36] N. Duric, P. Littrup, L. Poulo, A. B. andRoman Pevzner, E. Holsapple, O. Rama, and C. Glide, "Detection of breast cancer with ultrasound tomography: First resultswith the computed ultrasound risk evaluation (cure) prototype," *Med. Phys.*, vol. 34, no. 2, pp. 773–785, 2007.

[37] P. N. T. Wells, "Review: absorption and dispersion of ultrasound in biological tissue," *Ultrasound Med. Biol.*, vol. 1, no. 4, pp. 369–376, 1975.

[38] P. He, "Simulation of ultrasound pulse propagation in lossy media obeying a frequency power law," *IEEE Transactions on Ultrasonics, Ferroelectrics, and Frequency Control*, vol. 45, pp. 114–125, January 1998.

[39] R. S. C. Cobbold, *Foundations of biomedical ultrasound.* Oxford University Press, 2006.

[40] K. V. Gurumurthy and R. M. Arthur, "A dispersive model for the propagation of ultrasound in soft tissue," *Ultrason. Imaging*, vol. 4, pp. 355–377, 1982.

[41] K. R. Waters, M. S. Hughes, J. Mobley, G. H. Brandenburger, and J. G. Miller, "On the applicability of kramers-krönig relations for ultrasonic attenuation obeying a frequency power law," *J. Acoust. Soc. Am.*, vol. 108, no. 2, pp. 556–563, 2000.

[42] S. K. Patch and A. Greenleaf, "Ultrasound attenuation and thermo/photo/opto-acoustic tomography - theoretical foundation," in *SPIE Photons Plus Ultrasound*, vol. 6437, 2007.

[43] J. Pinkerton, "The absorption of ultrasonic waves in liquids and its relation to molecular constitution," in *Proc. Phys. Soc. London*, 1949.

[44] S. S. Soliman and M. D. Srinath, *Continuous and Discrete Signals and Systems.* Prentice Hall, 1990.

[45] K. A. Dines and A. C. Kak, "Ultrasonic attenuation tomography of soft tissues," *Ultrason. Imaging*, vol. 1, no. 1, pp. 16–33, 1979.

[46] R. Kuc, M. Schwartz, and L. V. Micsky, "Parametric estimation of the acoustic attenuation coefficient slope for soft tissue," in *Ultrasonics Symposium Proceedings*, pp. 44–47, 1976.

[47] A. C. Kak and K. A. Dines, "Signal processing of broadband pulsed ultrasound: Measurement of attenuation of soft biological tissues," *IEEE Trans. Biomed. Eng.*, vol. 25, no. 4, pp. 321–344, 1978.

[48] A. Papoulis, *Probability, Random Variables and Stochastic Processes.* McGraw-Hill, 1991.

[49] R. P. Brent, *Algorithms for Minimization without Derivatives.* Prentice-Hall, 1973.

[50] T. D. Rossing, *Springer handbook of acoustics.* Springer, 2007.

[51] S. J. Norton and M. Linzer, “Correcting for ray refraction in velocity and attenuation tomography: A pertubation approach,” *Ultrasonic Imaging*, vol. 4, pp. 201 – 233, 1982.

[52] S. A. Enright, S. M. Dale, V. A. Smith, R. D. Murch, and R. H. T. Bates, “Towards solving the bent-ray tomographic problem,” *Inverse Problems*, vol. 8, pp. 83 – 94, 1992.

[53] G. H. Golub and C. F. V. Loan, *Matrix Computations.* The John Hopkins University Press, 1996.

[54] C. C. Paige and M. A. Saunders, “LSQR: An algorithm for sparse linear equations and sparse least squares,” *ACM T. Math. Software*, vol. 8, no. 1, pp. 43–71, 1982.

[55] R. Acar and C. R. Vogel, “Analysis of bounded variation penalty methods for ill-posed problems,” *Inverse Problems*, vol. 10, pp. 1217 – 1229, 1994.

[56] P. C. Hansen and D. P. O’Leary, “The use of the l-curve in the regularization of discrete iii-posed problems,” *SIAM Journal on scientific computing*, vol. 14, pp. 1487 – 1503, 1993.

[57] J. A. Sethian, “Fast marching methods,” *SIAM Review*, vol. 41, pp. 199–235, June 1999.

[58] J. Butcher, *Numerical methods for ordinary differential equations.* Wiley, 2008.

[59] M. S. Hassouna and A. A. Farag, “Multistencils fast marching methods: A highly accurate solution to the eikonal equation on cartesian domains,” *IEEE Transaction on Pattern Analysis and Machine Intelligence*, vol. 29, pp. 1563 – 1574, 2007.

[60] M. M. Burlew, E. L. Madsen, J. A. Zagzebski, R. A. Banjavic, and S. W. Sum, “A new ultrasound tissue-equivalent material,” *Radiology*, vol. 134, pp. 517–520, 1980.

[61] Y. Wang, D. Xing, Y. Zeng, and Q. Chen, “Photoacoustic imaging with deconvolution algorithm,” *Phyisics in Medicine and Biology*, vol. 49, pp. 3117–3124, 2004.

[62] N. Neophytou and K. Mueller, “Post-convolved splatting,” in *IEEE TCVG Symposium on Visualization*, 2003.

[63] P. Toft, *The Radon Transform, Theory and Implementation.* PhD thesis, Technical University of Denmark, 1996.

[64] J. Hsieh, *Computed Tomography, Principles, Design, Artifacts and Recent Advances.* SPIE Press, 2003.

[65] A. Bjorck, *Numerical methods for least squares problems.* SIAM, 1996.

[66] Y. Saad, *Iterative methods for sparse linear systems.* PWS, 2000.

[67] J. Zhang, M. A. Anastasio, P. J. L. Riviere, and L. V. Wang, "Effects of different imaging models on least-squares image reconstruction accuracy in photoacoustic tomography," *IEEE Transactions on Medical Imaging*, vol. 28, pp. 1781–1790, 2009.

[68] N. H. Clinthorne, T.-S. Pan, P.-C. Chiao, W. L. Rogers, and J. A. Stamos, "Preconditioning methods for improved convergence rates in iterative reconstructions," *IEEE Transactions on Medical Imaging*, vol. 12, pp. 78 – 83, 1993.

[69] R. M. Rangayyan, *Biomedical Image Analysis.* CRC Press, 2005.

[70] P. C. Hansen, J. G. Nagy, and D. P. O'Leary, *Deblurring images: matrices, spectra, and filtering.* SIAM, 2006.

[71] R. C. González and R. E. Woods, *Digital Image Processing.* Prentice Hall, 2008.

[72] L. C. Andrews and B. K. Shivamoggi, *Integral Transforms for Engineers.* SPIE, 1999.

[73] P. C. Hansen, *Rank-Deficient and Discrete Ill-Posed Problems: Numerical Aspects of Linear Inversion.* SIAM, 1998.

[74] A. C. Bovik, *Handbook of image and video processing.* Elsevier, 2005.

[75] M. A. Anastasio, J. Zhang, and X. Pan, "Image reconstruction in thermoacoustic tomography with compensation for acoustic heterogeneities," in *SPIE Medical Imaging 2005*, vol. 5750, pp. 298–304, 2005.

[76] X. Jin and L. V. Wang, "Thermoacoustic tomography with correction for acoustic speed variations," *Phys. Med. Biol.*, vol. 51, no. 9, pp. 6437–6448, 2006.

[77] Y. Xu and L. V. Wang, "Effects of acoustic heterogeneity in breast thermoacoustic tomography," *IEEE Transactions on Ultrasonics, Ferroelectrics, and Frequency Control*, vol. 50, pp. 1134–1146, 2003.

[78] H. Jiang, Z. Yuan, and X. Gu, "Spatially varying optical and acoustic property reconstruction using finite-element-based photoacoustic tomography," *J. Opt. Soc. Am. A*, vol. 23, pp. 878–888, April 2006.

[79] J. Zhang, K. Wang, Y. Yang, and M. A. Anastasio, "Simultaneous reconstruction of speed-of-sound and optical absorption properties in photoacoustic tomography via a time-domain iterative algorithm," in *SPIE Photons Plus Ultrasound: Imaging and Sensing 2008*, vol. 6856, pp. 68561F–1–68561F–8, 2008.

[80] C. Zhang and Y. Wang, "A reconstruction algorithm for thermoacoustic tomography with compensation for acoustic speed heterogeneity," *Phyisics in Medicine and Biology*, vol. 53, pp. 4971–4982, 2008.

[81] S. Li, K. Mueller, M. Jackowski, D. P. Dione, and L. H. Staib, “Fast marching method to correct for refraction in ultrasound computed tomography,” in *3rd IEEE International Symposium on Biomedical Imaging: Nano to Macro, 2006*, pp. 896–899, 2006.

[82] S. Li, K. Mueller, M. Jackowski, D. P. Dione, and L. H. Staib, “Physical-space refraction-corrected transmission ultrasound computed tomography made computationally practical.,” in *MICCAI (2)* (D. N. Metaxas, L. Axel, G. Fichtinger, and G. Szkely, eds.), vol. 5242 of *Lecture Notes in Computer Science*, pp. 280–288, Springer, 2008.

[83] A. V. Oppenheim, *Discrete-Time Signal Processing.* Prentice-Hall, 1999.

Nawoord

Eindelijk begin ik dan aan de laatste pagina van mijn proefschrift, het is er een die niet meteen de hoogste prioriteit had, maar een die toch een keer geschreven moest worden. Op deze laatste pagina zal ik proberen iedereen te bedanken die, direct of indirect, heeft bijgedragen aan de vorming van dit proefschrift.

In eerste instantie bedank ik mijn promotor, Kees Slump. Zonder hem was dit allemaal niet gelukt, hij heeft er voor gezorgd dat ik aan deze promotie opdracht mocht beginnen en heeft me veel vrijheid gegeven in de precieze invulling hiervan. Daarnaast ben ik mijn assistent-promotor, Srirang Manohar, ook zeer dankbaar voor alles wat hij voor me gedaan heeft. Zonder hem was ik nooit zover gekomen, hij heeft veel tijd en moeite gestoken in de begeleiding en organisatie van het onderzoek, en hij wist me altijd goed te motiveren. Verder wil ik ook alle mensen uit het NIMTIK project, waaronder ik mijn opdracht heb uitgevoerd, bedanken. Het was altijd interessant om tijdens de drie maandelijkse lunchmeeting te horen waar iedereen in het project nu precies mee bezig was. Ook wil ik graag voor de goede samenwerking, vooral op het experimentele werk, Jithin Jose, Steffen Resink en Thijs Maalderink van de Biomedical Photonic Imaging groep bedanken. Zij hebben met veel succes de experimenten uitgevoerd waarop ik mijn algorithmes en methodes heb kunnen loslaten, het was een ideale samenwerking waarbij we veel aan elkaar hadden.

Binnen de vakgroep waar ik gewerkt heb, Signalen en Systemen, wil ik ook iedereen bedanken voor de leuke tijd, de goede ondersteuning en de goede samenwerking. Ondanks dat de verschillende onderzoeksgebieden en opdrachten binnen onze groep aan de buitenkant en qua applicatiegebied niet altijd veel overlap vertoonden, waren de technieken die we gebruikten om onze problemen oplossen toch weer erg aan elkaar verwant. Met name de medical imaging en biometrie subgroepen waren onder water vrijwel hetzelfde, een oplossing kon altijd gevonden worden met technieken uit de lineare algebra en parameterschatting. Veel heb ik ook gehad aan mijn kamergenoten Joost Kaufman en Dirk-Jan Kroon. Joost wist altijd overal wel wat vanaf, hij maakte zijn functie als kameroudste goed waar. Dirk-Jan was ook een enorm nuttige kamergenoot die zich erg snel in problemen kon inleven en altijd in Matlab binnen no time een oplossing in elkaar had gehacked. Daarnaast waren de conferentie bezoeken naar de Verenigde Staten met Dirk-Jan, Gerbert en Almar van het medical imaging team ook altijd een groot succes. Ook vond ik het leuk dat er altijd weer een delegatie van de vakgroep mee ging op wintersport, een traditie die ik nog wil blijven voortzetten. Verder wil ik de ondersteunende staf van de groep, Anneke, Geert-Jan en Henny, ook bedanken voor hun hulp, ze stonden altijd voor je klaar.

Mijn familie wil ik ook bedanken voor hun ondersteuning. Ze waren altijd erg nieuwsgierig naar wat ik nu precies aan het doen was, wat ik vervolgens erg moeilijk vond om duidelijk aan ze uit te leggen. Ik hoop dat na het lezen van dit proefschrift alles een stuk duidelijker is geworden, het staat hier uiteindelijk allemaal netjes op papier. Verder wil ik mama bedanken voor het controleren van de Nederlandse samenvatting op spelling en grammatica fouten en Martin bedanken voor het ontwerpen van de voorkant van het proefschrift.

De studentenflat NGTV, waar ik de eerste acht jaar van mijn periode in Enschede heb doorgebracht kan in dit nawoord natuurlijk niet ontbreken. Ik heb me er uitstekend vermaakt met de vele pokeravonden, feutenfeesten, kerstdiners, zomervakantiereizen, voetbalwedstrijden, sneakbezoeken, etc. Daarna heb ik nog een prima tijd gehad in huize Stinsburg, waar ik gewoond heb met Stijn en Steven. Het was er een stuk rustiger dan op de flat, wat me goed uitkwam tijdens mijn promotie periode. De leden van DAV Kronos, zowel de sprinters als de lappers als de trainers, wil ik ook bedanken voor de altijd weer competatieve trainingen, de recreatieve wedstrijden en alle andere mooie activiteiten. Ook bij DWV Hardboard heb ik een erg relaxte tijd gehad, het kitesurfen en wakeboarden was een prima aanvulling op mijn grootste hobby, het snowboarden. Tot slot wil ik natuurlijk iedereen bedanken voor de supervette wintersporten die ik gehad heb, vooral Stijn en Willie, die met negen weken en zes weken het vaakst met me zijn mee geweest.

Rene
Eindhoven, april 2010